
Enhancing the information content of geophysical data for nuclear site characterisation

by

Chak-Hau Michael Tso B.S. M.S.

Supervisor:

Prof. Andrew Binley

Thesis submitted in partial fulfilment for the
degree of *Doctor of Philosophy in Environmental Science*

September 2019

Lancaster Environment Centre

Enhancing the information of geophysical data for nuclear site characterisation

Chak-Hau Michael Tso

A thesis submitted for the degree of Doctor of Philosophy, Lancaster University

September 2019

Abstract

Our knowledge and understanding to the heterogeneous structure and processes occurring in the Earth's subsurface is limited and uncertain. The above is true even for the upper 100m of the subsurface, yet many processes occur within it (e.g. migration of solutes, landslides, crop water uptake, etc.) are important to human activities. Geophysical methods such as electrical resistivity tomography (ERT) greatly improve our ability to observe the subsurface due to their higher sampling frequency (especially with autonomous time-lapse systems), larger spatial coverage and less invasive operation, in addition to being more cost-effective than traditional point-based sampling. However, the process of using geophysical data for inference is prone to uncertainty. There is a need to better understand the uncertainties embedded in geophysical data and how they translate themselves when they are subsequently used, for example, for hydrological or site management interpretations and decisions. This understanding is critical to maximize the extraction of information in geophysical data. To this end, in this thesis, I examine various aspects of uncertainty in ERT and develop new methods to better use geophysical data quantitatively. The core of the thesis is based on two literature reviews and three papers.

In the first review, I provide a comprehensive overview of the use of geophysical data for nuclear site characterization, especially in the context of site clean-up and leak detection. In the second review, I survey the various sources of uncertainties in ERT studies and the existing work to better quantify or reduce them. I propose that the various steps in the general workflow of an ERT study can be viewed as a pipeline for information and uncertainty propagation and suggested some areas have been understudied. One of these areas is measurement errors. In paper 1, I compare various methods to estimate and model ERT measurement errors using two

long-term ERT monitoring datasets. I also develop a new error model that considers the fact that each electrode is used to make multiple measurements.

In paper 2, I discuss the development and implementation of a new method for geoelectrical leak detection. While existing methods rely on obtaining resistivity images through inversion of ERT data first, the approach described here estimates leak parameters directly from raw ERT data. This is achieved by constructing hydrological models from prior site information and couple it with an ERT forward model, and then update the leak (and other hydrological) parameters through data assimilation. The approach shows promising results and is applied to data from a controlled injection experiment in Yorkshire, UK. The approach complements ERT imaging and provides a new way to utilize ERT data to inform site characterisation.

In addition to leak detection, ERT is also commonly used for monitoring soil moisture in the vadose zone, and increasingly so in a quantitative manner. Though both the petrophysical relationships (i.e., choices of appropriate model and parameterization) and the derived moisture content are known to be subject to uncertainty, they are commonly treated as exact and error-free. In paper 3, I examine the impact of uncertain petrophysical relationships on the moisture content estimates derived from electrical geophysics. Data from a collection of core samples show that the variability in such relationships can be large, and they in turn can lead to high uncertainty in moisture content estimates, and they appear to be the dominating source of uncertainty in many cases. In the closing chapters, I discuss and synthesize the findings in the thesis within the larger context of enhancing the information content of geophysical data, and provide an outlook on further research in this topic.

Executive summary for the nuclear industry

Uncertainty in the subsurface characterisation of nuclear sites poses significant risks in terms of operational cost and environmental protection. Improved knowledge of the uncertainty of subsurface properties and processes is needed in order to enhance risk mitigation. Geophysical methods, such as electrical resistivity tomography (ERT), provide a cost-effective way to delineate variations in subsurface properties and monitor subsurface processes, however, the uncertainty in the results from such methods is often overlooked. A recent successful time-lapse ERT field trial conducted at Sellafield's Magnox Swarf Storage Silo (MSSS) highlights the potential of these methods [1] by showing 3D resistivity variations over time due to saline tracer injection. This PhD project explores various ways to better exploit information from ERT and to track the associated uncertainty in subsurface characterisation. This includes better understanding of the ERT data, and incorporating ancillary data sources to the ERT analysis.

We have studied the error structure in ERT data and proposed a new error model for geophysical measurements, which shows improved ERT inversion results and uncertainty estimation [2]. Recently, we have shown that there exists large variability in field petrophysical relationships and have developed a workflow quantifying pore water states (e.g. soil water content) derived from ERT. Even though different petrophysical relationships give consistent estimates of the change in total moisture, the estimates have large uncertainty bounds [3]. Our study also illustrates the joint use of coupled hydrogeophysical modelling and data assimilation to effectively estimate flow and transport properties in leak plumes. Our method proposes a range of hydrological models and then constrains them with time-lapse ERT data through data assimilation. The advantages of this method includes the flexibility to incorporate prior hydrogeological information and the ability to estimate flow and leak parameters of interest directly. The ensemble of hydrological model estimates also readily provides useful metrics for site management decisions, e.g. mass flux and mass discharge at any location or area within the model domain.

We have applied the above methods to the data collected from the Sellafield field trial and other sites. Overall, our work addresses the needs of the Nuclear Decommissioning Authority (NDA) by offering a suite of methods that can make geophysical methods more reliable and informative for site characterisation. Systematic application of ERT at NDA sites should contribute to a reduction in costs and risks in managing NDA's contaminated land portfolio.

References:

[1] Kuras et al. (2016) *Science of the Total Environment*.

DOI: 10.1016/j.scitotenv.2016.04.212

[2] Tso et al. (2017) *Journal of Applied Geophysics*. DOI: 10.1016/j.jappgeo.2017.09.009

[3] Tso et al. (2019) *Water Resources Research*. DOI: 10.1029/2019WR024964

Table of Contents

Contents

Abstract.....	i
Executive summary for the nuclear industry.....	iii
Table of Contents	v
Acknowledgment.....	vi
Declaration	viii
List of Figures	ix
List of Tables.....	xvi
List of Acronyms	xvii
1. Introduction	18
1.1 Background.....	18
1.2 Objectives and aims	18
1.3 Outline.....	20
2. Geophysical methods for nuclear site characterisation.....	23
3. Sources of uncertainties in electrical resistivity tomography (ERT): a review.....	59
4. Paper 1: Improved characterisation and modelling of measurement errors in electrical resistivity tomography (ERT) surveys.....	115
5. Paper 2: Integrated hydrogeophysical modelling and data assimilation for geoelectrical leak detection.....	166
6. Paper 3: On the field estimation of moisture content using electrical geophysics – the impact of petrophysical model uncertainty.....	210
7. Discussion summary	248
8. Conclusions and recommendations	255
8.1 Conclusions.....	255
8.2 Future work	256
Bibliography	257
Appendix 1: Instructions on using PFLOTRAN-E4D.....	300
Appendix 2: A guide to performing global sensitivity analysis using the Morris (1991) method.....	303
Appendix 3: Annotated bibliography for related textbooks.....	312
Vita	314

Acknowledgment

This thesis would not be possible without the help of many people and institutions.

My PhD experience has benefited from much input from my doctoral supervisor Andrew Binley. I thank him for challenging me with new ideas and opportunities and always providing insightful reviews of my work. I am grateful for his reassurance when I felt my work was not going anywhere. He has shown great patience, kindness, and forgiveness throughout my PhD. I also thank the members of the Binley group, Paul Mclachlan, Guillaume Blanchy, Tuvia Turkeltaub, Jimmy Boyd, Qinbo Cheng, John Ball and visitors to the group for their friendship and creating a stimulating and collaborative research environment. I also thank Lai Bun Lok (Engineering) and Andrew Curtis (Edinburgh Universtiy) for thoroughly examining this thesis and providing helpful comments during my viva.

My co-supervisor Oliver Kuras recruited me for this incredible opportunity. I thank him for his warm welcome, constant support and helpful comments throughout my PhD. I thank members of the BGS GTom team, especially Jon Chambers, Paul Wilkinson, and Seb Uhlemann for their helpful suggestions to many parts of my work.

This PhD is supported by a Faculty of Science and Technology studentship and a UK Nuclear Decommissioning Authority bursary. I thank my industry supervisor James Graham for his valuable experience in nuclear site characterisation and other NNL staff for planning activities that has deepened my understanding of the nuclear industry.

I am deeply grateful for the support and feedback from the wider hydrogeophysics community, especially our meetings in AGU and webinars. I thank my external collaborators Tim Johnson, Xingyaun Chen, Xuehang Song, Marco Iglesias, Andrew Curtis, Erica Galetti, Yuanyuan Zha, Chin Man Mok and Barbara Carrera for extra research opportunities that has broadened my PhD experience, and for hosting me during my visits.

Acknowledgment

I thank fellow members of the CEH Environmental Data Science Team, for their understanding while I have been finishing up my PhD. I thank Lancaster University Men's volleyball team for three memorable seasons and opportunities to play at the Roses. I thank my family and friends around the world for their love and encouragement. I thank my friends Welson, Roy, Richard, and Xichen for sharing their experience and encouraging me. I thank my parents Paul and Helen for always letting me choose a subject that I am interested in to study, and my brother Matthew for his companionship. I am indebted to my parents-in-law John and Melody, especially for allowing me to take their daughter to England. I thank my wife and best friend, Elizabeth, for her love, laughter, encouragement, patience, and sacrifices every day and going through the emotions of the PhD with me. I also thank our baby daughter, Jemimah, for big smiles to welcome "baba" home from work. Finally, I thank the greatest Giver of all my Lord Jesus Christ. I thank Moorlands Church for faithful Bible teaching and discipleship after we arrived in Lancaster. Thank you for growing my understanding of the Bible and my desire to bring people to Christ.

"Seek the Lord while he may be found; call to him while he is near. Let the wicked one abandon his way and the sinful one his thoughts; let him return to the Lord, so he may have compassion on him, and to our God, for he will freely forgive." (Isiah 55:6-7, Christian Standard Bible)

Declaration

Except where reference or is made to other sources, I declare that the work in this thesis is my own and has not been previously submitted, in part or in full, to any institution for any other degree or qualification.

Chapter 4 (Improved characterisation and modelling of measurement errors in electrical resistivity tomography (ERT) surveys, *Tso et al. 2017*) has been published in the peer reviewed publication *Journal of Applied Geophysics*, as described in the reference list below.

Chapter 6 (On the field estimation of moisture content using electrical geophysics – the impact of petrophysical model uncertainty, *Tso et al. 2019*) has been published in the peer reviewed publication *Water Resources Research*, as described in the reference list below.

For both of the abovementioned chapters, the co-authors contributed to the interpretation of results, design, or data provision of the studies and edited drafts. A.B. conceived the study and I wrote the manuscripts, developed scripts, and performed analysis. Chapter 2, 3, and 5 are prepared to be submitted to academic journals for peer-review.

Tso, C.-H.M., Kuras, O., Wilkinson, P., Uhlemann, S., Chambers, J., Meldrum, P., Graham, J., Sherlock, E., Binley, A. (2017): Improved modelling and characterisation of measurement errors in electrical resistivity tomography (ERT) surveys. *Journal of Applied Geophysics*, 145, 103--119, DOI:[10.1016/j.jappgeo.2017.09.009](https://doi.org/10.1016/j.jappgeo.2017.09.009).

Tso, C.-H.M., Kuras, O., Binley, A. (2019): On the field estimation of moisture content using electrical geophysics-the impact of petrophysical model uncertainty. *Water Resources Research*, 55, 2019, DOI:[10.1029/2019WR024964](https://doi.org/10.1029/2019WR024964).

X

Michael Tso

Chak-Hau Michael Tso B.S. (Texas) M.S. (Arizona)

Lancaster University, UK

List of Figures

Chapter 1

- Figure 1 The ERT workflow showing the various stages of conducting ERT survey and analysing its data. It also serves as a pipeline where information and uncertainty is propagated along. The annotation shows the relation between the chapters in this thesis and the workflow..... 20
- Figure 2 Snapshot showcasing coupled hydrogeophysical modelling using PFLOTTRAN-E4D. The 2D flow and transport model simulates tracer injection at an injector in the upper left of the domain. Groundwater movement is towards an extraction well to the lower right. An ERT imaging cell with 4 boreholes (20 electrodes each) is located at the centre of the domain. The animation shows that as the conductive tracer migrate through the ERT imaging cell, there is a corresponding increase in electrical conductivity in the ERT imaging cell..... 22

Chapter 2

- Figure 1 Aerial view of the Hanford Site (Johnson et al., 2015a)..... 29
- Figure 2 Estimated conductivity at the Hanford BY-Cribs (Johnson et al., 2010; Johnson and Wellman, 2013) 30
- Figure 3 A screenshot for the browser-based integrated data platform SOCRATES for the Hanford site. It serves as a centralized portal for all data collected at Hanford Site. It includes a wide variety of tools, such as those for filtering data and exporting data and model domain for flow and transport modelling..... 35
- Figure 4 An illustration of the iterative decision analysis framework (Paté-Cornell et al., 2010)..... 46

Chapter 3

- Figure 1 Various sources of errors and uncertainties propagate through the ERT workflow (Binley et al., 2015; Tran et al., 2016; Truex et al., 2013). The workflow begins with experimental design, where the objectives and details of the field campaign are laid out. It progresses to data collection in the field using a data acquisition system. Then the data is inverted to obtain results in a usable format for interpretations and discussions. Finally, the findings are used for decision making or prediction of future events..... 62
- Figure 2: Example of 3D borehole effects in 2D inversion reported in Nimmer et al. (2008), which shows the 2.5D inversion results from Slater et al. (1997). The heavily fractured zone at around 25-m depth can be seen as a low resistivity contrast to the background, but the large high resistivity ($>2 \times 10^5 \Omega \text{ m}$) in the centre of the image appears to be a result of the 2D resistivity model compensating for the low resistivity along the borehole. 66

List of Figures

- Figure 3 An outline of the Markov chain Monte Carlo (McMC) inversion algorithm.75
- Figure 4 Uncertainty quantification in Bayesian inversion (Iglesias and Stuart, 2014). The black dashed lines and red solid lines denote prior and posterior probabilities. Essentially, the data drives an updating of input probabilities (e.g. model parameters) and lead to an updating of model outputs, including quantities of interest that are not directly observable from data. 77
- Figure 5 This synthetic example shows that by disconnecting the smoothness constraint in a regularized ERT inversion, the fracture network (red and yellow) is much better recovered (Robinson et al., 2015). Compared with the smoothness constraint inversion, the smoothness disconnect case shows pronounced elongated fractures and recover the very high conductivities along them. 84
- Figure 6 A new Bayesian inversion method that jointly estimates both the interface of the two units and the sub-unit resistivity variations (de Pasquale et al., 2019). The approach estimates the resistivity field of both unit (assuming they span the entire model domain) and their interface. The resultant field is obtained by combining the two fields along the interface..... 85
- Figure 7 Illustration of different approaches for integrating multiple geophysical data sets for a hydrogeological interpretation (Doetsch, 2011). Individual processing invert each dataset individually before interpreting them together qualitatively. Joint inversion invert all available datasets together—explicit assumptions between different process models are required. A constrained inversion use parts of the inversion results from one inversion to constrain another..... 87
- Figure 8 The ERT workflow as a pipeline for information and uncertainty propagation is helpful for the experimental design of ERT surveys. It can be optimized to minimize uncertainty and maximize the extraction of information. 90

Chapter 4

- Figure 1 Synthetic problem for demonstration (a) Synthetic domain with a more conductive layer near the surface and a resistive area between $x = 15\text{m}$ and $x = 20\text{m}$. The synthetic data from running a forward model in (a) is perturbed with 5% Gaussian noise and then inverted by assuming (b) 10% linear error model (c) 5% linear error model (d) 2% linear error model. Note that rms error is defined as $\mathbf{i} = \mathbf{1n}(\mathbf{obs} - \mathbf{sim})^2/\mathbf{n}$, where obs and sim are vectors of observed/true and simulated transferred resistances of length n respectively. Note that the convergence target for all the inversions is a chi-squared statistic of 1. 122
- Figure 2 (a) Comparison of stacking errors, repeatability errors, and reciprocal errors for the Boxford dataset by plotting probability density functions. The PDFs of reciprocal errors and repeatability errors are comparable to each other. The stacking errors PDF, however, show very low mean and low variance. Using stacking errors for measurement errors characterisation may lead to significant underestimation of uncertainty and over-fitting of data. (b) Comparison of stacking errors, repeatability

errors, and reciprocal errors for the Sellafield dataset. The PDFs for Sellafield show greater variances than those for Boxford. Since a two-week repeatability cycle is used, the repeatability errors are much greater than reciprocal errors. In general, the stacking errors are more than an order-of-magnitude smaller than the reciprocal errors, indicating there may be significant underestimation of errors if they are used as error weights. The mean and standard deviation of each fitted normal distribution is shown next to the legend. 134

Figure 3 Autocorrelation of (a) departure from the mean (as a measure of repeatability errors) and (b) reciprocal errors for the 96 datasets collected continuously within 24h at the Boxford site. The number of lags is on the horizontal axis (here 1 lag = 15 minutes). Each grey translucent line plots the autocorrelation of one of the 516 ERT measurements as a function of lag. The red line denotes the mean autocorrelation. For each autocorrelation plot, 96 datasets are considered. The hashed region has insignificant correlation according to the critical Pearson’s test (around ± 0.2). 136

Figure 4 Autocorrelation of (a) departure from the mean (as a measure of repeatability errors) and (b) reciprocal errors for the 96 datasets collected continuously at the Sellafield site encompassing the three injection periods (22/1/2013 – 3/11/2013). The number of lags is on the horizontal axis (here 1 lag = ~2 to 3 days). Each grey translucent line plots the autocorrelation of one of the 12481 ERT measurements as a function of lag. The red line denotes the mean autocorrelation. For each autocorrelation plot, 96 datasets are considered. The hashed region has insignificant correlation according to the critical Pearson’s test (around ± 0.2). Similarly, (c) and (d) show the same for the long-term background monitoring period (i.e. no injection, 5/11/2013 – 31/3/2014). 136

Figure 5 Mean correlation coefficient of departure from the mean (as a measure of measurement errors) and reciprocal errors for measurement pairs from the Boxford dataset as a function of dipole separation multiplier n . For both departure from the mean and reciprocal errors, mean correlation coefficients are distinctively higher for measurements that share electrode(s) in their quadrupoles than the mean correlation coefficients for all measurements, indicating by considering the effect of using each electrode to make multiple measurements may improve error models. Also, note that the reciprocal errors have strikingly lower correlation coefficients than the departure from the mean. Note that electrode sharing only occurs in ~10% of all pairs. 138

Figure 6 Comparison of fitting reciprocal errors of time-lapse data as (a) individual datasets, fitting each dataset individually with a different LME model and (b) longitudinal data, fitting all data with one LME model. The above shows that it is much better not to treat errors as longitudinal data. 140

Figure 7 Synthetic surface ERT experiments to demonstrate the performance of the error models. For data involving 3 bad electrodes (marked by “X”), data is corrupted

by 10% white noise while for the rest of the data 2% white noise is added. (a) Inverted resistivity distribution using the 2% linear error model (b) Inverted resistivity distribution using a 4.52% (obtained from the Koestel et al. (2008) method) linear error model (c) Inverted resistivity distribution using the LME error model. Note that the convergence target for all the inversions is a chi-squared statistic of 1. 143

Figure 8 (a – c) Diagonal of resolution matrix for inversion using the following error models for inverting the synthetic data corrupted by “bad electrodes”: (a) 2% linear model (b) 4.52% linear model (c) LME model. (d - f) variance of element-wise log-resistivity estimates using each of the error models obtained from Monte Carlo experiments. The colour scale is the same for all three error models. Darker cells indicate more similar model estimates between Monte Carlo estimates. (g - i) mean model estimates from Monte Carlo experiments. The transparency is controlled linearly the variance shown in (d – f). With model averaging, the mean estimates of the three error models agree. It is noted, however, the deterministic results from the LME model agrees the best with its model-averaged results..... 144

Figure 9 Empirical model covariance matrix using the Monte Carlo uncertainty propagation procedure and the following error models: (a) 2% linear model (b) 4.52% linear model (c) LME model. The size of the matrix is $m \times m$, where m is the number of model parameters. By comparing (a) and (b), it is shown that assuming higher error levels, there is higher covariance between model parameters. With the LME error model, the model covariance is the lowest. While the spread of high covariance entries are quite even throughout the matrix, we can see that the spread for (c) is quite uneven: generally, elements on the left of the domain have higher spread..... 145

Figure 10 Inversion results from Boxford using (a) linear error model for stacking errors, (b) LME error model for stacking errors, (c) linear error model for reciprocal errors. 146

Figure 11 (a) 3-D static deterministic inversion results from Sellafeld on 5th February, 2013. Error weights are prescribed by fitting an LME error model. Black lines are boreholes installed with electrodes. (b) The corresponding uncertainty estimates obtained from Monte Carlo simulations, given by model standard deviation from Monte Carlo experiments. (c) The corresponding coefficient of variation of Monte Carlo model estimates. 147

Chapter 5

Figure 1 (a) Flowchart of the overall data assimilation framework used in this work. More details are found in the subsections. (b) The goal of this framework is that upon conditioning of geophysical data, the envelope of possible mass discharge time series will become less uncertain. 173

Figure 2 . (a) PFLOTTRAN model domain for the Sellafield MSSS. The grey area is the MSSS building, which is modelled as impermeable. The hashed area is the ERT imaging cell consisting of four ERT boreholes. (b) A snapshot of the simulated tracer concentration due to injection. (c) The corresponding distribution of electrical conductivity within the ERT imaging cell obtained via petrophysical transform. 180

Figure 3 Estimation of leak location. (a) The true leak location is within the ERT array (33.4534, -14.4303). (b) The true leak location is outside the ERT array (20, -10). In both cases, the data assimilation framework successfully identified the true leak location within a few iterations..... 183

Figure 4 Joint estimation of leak parameters: (x, y) location, leak rate, and onset time. (a) Violin plots showing the prior and posterior parameter distributions. The true values are marked with an orange lines. The posterior parameter values collapse around the true values (b) Prior and posterior tracer mass flux across the pre-defined plane. All the posterior curves collapse to nearly the true curve (green). Note that the sign of mass discharge denotes its direction across the plane..... 184

Figure 5 Joint estimation of leak and petrophysical parameters: the prior and posterior parameter distributions are shown as violin plots. The true values are marked with orange lines..... 185

Figure 6 (a) The estimation leak parameters under uncertain K values and $\log K$ variance = 1.0. The violin plots show the prior and posterior parameter distributions. The true value is marked with an orange line. (b) The estimation of leak parameters at variance of $\log_{10}(K)$ equal to 2, 3, 5, 7, 10 , while assuming the mean K values are known exactly and the K field is isotropic and is of unit correlation length. The violin plots show the posterior parameter distribution, while the true value is marked with an orange line..... 186

Figure 7 (a) Joint estimation of leak parameters and effective hydraulic conductivity. The violin plots show the prior and posterior parameter distributions. The true value is marked with an orange line. (b) Prior and posterior tracer mass flux across the pre-defined plane. The true curve is marked in green in the posterior plot... 187

Figure 8 Setup of the tracer injection test at Hatfield (H-I2 is the injection borehole and H-E1 to H-E4 are ERT boreholes) and the time-lapse resistivity images (iso-surfaces are plotted for 7.5% reduction of resistivity relative to baseline) obtained from a difference inversion of the ERT data (reproduced from Winship et al., 2006)..... 189

Figure 9 (a) Parameter scatterplots showing pairs of parameter values for the Hatfield example estimating leak and Archie parameters. The parameter symbols and units are defined in section 3. Grey squares indicate prior parameter values while black circles in date posterior values. The true leak parameters used in the field injection experiment is indicated by red triangles. (b) The prior and posterior mass discharge time series. The sign of mass discharge indicates the direction across the defined plane..... 192

Figure 10 Parameter scatterplots showing pairs of parameter values for the Hatfield example estimating leak and Archie parameters and hydraulic conductivities. The parameter symbols and units are defined in Table 3 and section 3. Grey squares indicate prior parameter values while black circles indicate posterior values. The true leak parameters used in the field injection experiment is indicated by red triangles. 193

Figure 11 Transfer resistance scatter plot between the observed and simulated data at Hatfield. The simulated data uses parameter values listed in Table 3. 195

Chapter 6

Figure 1 Moisture content θ estimation and petrophysical uncertainty propagation workflow used in this study. Rectangles indicate model inputs or data, while ovals represent modeling or analysis steps. We obtained synthetic ERT and θ data using PFLOTTRAN-E4D. Then we inverted the ERT data and used the Eggborough cores as different petrophysical models. They were passed through the moisture content estimation and uncertainty estimation framework to obtain ERT - estimated θ , which were compared against the θ data. ERT = electrical resistivity tomography. 218

Figure 2 (a) Cumulative density functions of grain size distribution of Eggborough cores and blocks. The legend shows the core or block ID. (b) Depth profiles of sand (blue), silt (red), and clay (yellow) percentages for Eggborough cores. 219

Figure 3 Archie's parameter estimation of individual Eggborough cores and blocks. The predictions using the best estimate of the parameters are shown in solid lines, while the 68% (i.e., ± 1 standard deviation) confidence intervals are shown in dashed lines. Note that the measurements are made at $\sigma_f = 1000 \mu S cm - 1$. Note that ρ , which is the dependent variable, is shown on the x-axis. 225

Figure 4 Summary of Archie model fits for the Eggborough/Hatfield cores and blocks. Note that values correspond to $\sigma_f = 1000 \mu S cm - 1$. The point label "synthetic" is the "true" solution considered in the synthetic study in section 3.2. 225

Figure 5 (a) Mean (log10) and (b) standard deviation (linear) of electrical resistivity for Day 18 obtained from Monte Carlo runs of electrical resistivity tomography inversion. (c) Extracted volume where there was a 5.5% reduction of resistivity relative to baseline on Day 18. The purple cubes are electrode locations. 227

Figure 6 (a) Total water volume within the extracted volume (with uncertainty bounds) using the different petrophysical models. The uncertainty bounds correspond to ± 1 standard deviation. The vertical lines show the true total water volume. (b) The corresponding changes in the amount of moisture within the extracted volume relative to baseline. The vertical lines show the true change in total water volume. (c) The contribution of different variables to the variance of total moisture of each petrophysical models. (d) Additional variance (i.e., uncertainty) caused by

List of Figures

- uncertain porosity values (0.32 ± 0.032). The contribution from uncertain porosity is significant in most cases, especially when the variance in saturation is low. 228
- Figure 7 (a) Electrical resistivity tomography estimated changes in volume of water in four selected cells. The vertical lines indicate the true change. (b) Scatter plots showing the fit for change in volume of water at individual cells using the 15 Archie models. The red dashed line in each plot is the best-fit line of the scatter points. 230

Chapter 7

- Figure 1 A diagram summarizing the major findings in this thesis and their relation to the ERT workflow. 250
- Figure 2 (Top) Parameter space of a 3-parameter layered ERT problem using 24 surface electrodes in dipole-dipole configuration. The axis represents the uniform parameter value of each layer in log scale. The true resistivity for all three layers are $100 \Omega \text{ m}$. The red cross indicate the true parameter value. The data misfit surface (left) and the derived streamlines to the data misfit minima (right) are plotted. (bottom) Gradient fields using 500 samples. The red polygons are the loops and the black cross is the true values. The gradient field somewhat point towards the true minima. 9 loops are identified, spanning a large fraction of the parameter space. 254

List of Tables

Chapter 3

Table 1 Table of error models reported in the literature..... 125

Chapter 4

Table 1 “True” coupled hydrogeophysical model parameters used for synthetic experiments. It is developed based on the Sellafeld field trial. *Only parameters for the main zone are listed below. #Leak location for some cases is (33.4534, -14.4303) instead. Note that for all cases the leak location is at the water table..... 181

Table 2 Summary of synthetic cases. All cases converge in seven iterations..... 182

Table 3 Baseline coupled hydrogeophysical model parameters used for the parameter estimation from the Hatfield field ERT data. *The domain consists of 3 meters of top soil and a uniform main zone. Only parameters of the main zone are listed below. 189

Table 4 Summary of cases for the Hatfield field example 191

Table 5 Global sensitivity analysis results using the Morris (1991) method on selected parameters on the Hatfield coupled hydrogeophysical model. The parameter ranges considered and the mean absolute elementary effect ($|EE|$) are reported. Parameter value combinations from ten realizations with the lowest RMSE are also reported. 195

Chapter 5

Table 1 Parameters used for the water injection experiment. 220

List of Acronyms

CO ₂	Carbon dioxide
DC	Direct current
EM or EMI	Electromagnetic induction
ER	Environmental remediation
ERT or ERI	Electrical resistivity tomography or Electrical resistivity imaging
GPR	Ground penetrating radar
HLW	High-level radioactive waste
IFRC	Integrated Field-Scale Subsurface Research Challenge
IP	Induced polarisation
McMC	Markov chain Monte Carlo
NRZ	Naturally- reduced zone
PRA	Probabilistic risk assessment
QoI	Quantity of interest
TCE	trichloroethylene
TDEM	Time domain EM
VOF	Value of flexibility
VOI	Value of information

1. Introduction

1.1 Background

Effective characterisation is essential to successful management of environmental sites (Artiola et al., 2004). They are, however, inherently labour- and cost-intensive because point samples are needed to be obtained from boreholes. It is often difficult to piece together the governing processes at the site based on the individual point samples. These challenges are exaggerated in nuclear sites where site access is restricted and risk of exposure of contamination is above average. Geophysical methods have been used in the last two decades to improve the effectiveness of site characterisation because they can “scan” the subsurface rapidly like hospital scanners do (Binley et al., 2015). Therefore, they can provide information about subsurface conditions at a spatial and temporal resolution that is not attainable by point measurements (French et al., 2014). Like hospital scanners, geophysical methods do not directly detect the quantity of interest (QoI) (e.g. pore water solute concentration). Therefore, we need to understand how geophysical responses are linked to the QoI. In order to make geophysics more useful for nuclear site characterisation, we also need to understand how to better extract site information from geophysical data, how errors and uncertainties propagate, and how to more closely tie geophysical data to site conceptualization.

1.2 Objectives and aims

Using electrical resistivity tomography (ERT) (Binley, 2015a; Daily et al., 2005) as an example, the primary objective of this work is to develop methods to better quantify and improve the amount of information ERT can provide to aid site characterisation. Electrical resistivity is related to subsurface material and fluid properties; yet this relationship is controlled by multiple material and rock properties and is uncertain. Moreover, all the data collection and interpretation stages in ERT propagate through the interpretation workflow and contribute to the uncertainty of the final interpretation of the ERT data to infer the quantity of interest (QoI), whether it is soil water content, hydraulic parameters, or parameters describing the leakage of

a potential contaminant from a storage facility. Prior to this study, little work had been undertaken to specifically address the potential issues with uncertainty in using ERT for hydrological predictions. Among the few work that attempted to address them, the focus has been on either improving the inversion method, or reducing the uncertainty in Bayesian model selection. None of them has undertaken a whole-system approach for uncertainty quantification, nor have they evaluated aspects of uncertainty propagation that does not depend on the choice of inversion methods (e.g. measurement errors, petrophysical relationships).

The specific aims identified to fulfil the above were to:

- Identify the sources of uncertainty in ERT data collection, modelling, inversion, and interpretation
- Assess the statistical distribution and correlation of ERT measurement errors
- Assess the benefit of leak parameter estimation using ERT data directly (i.e. without inversion)
- Examine the extent to which uncertain petrophysical relationships affect the estimation of soil water content (and its temporal changes)

To achieve the above aims the project objectives were to:

- Review the use of geophysical data for nuclear site characterisation worldwide (chapter 2)
- Introduce the sources of uncertainty in ERT (chapter 3)
- Conduct statistical analysis and develop a new model on ERT measurement errors (chapter 4)
- Develop a coupled hydrogeophysical data assimilation approach for leak parameter estimation without reliance of ERT images (chapter 5)
- Observe variability of petrophysical relationships in field soil samples, use it to populate a range of petrophysical models, and examine the variability in the estimated moisture content maps when ERT data is subjected the different petrophysical models (chapter 6)

We have traced the normal workflow for geophysical studies and consider it as a pipeline for the propagation of both information and uncertainty and it can be used to illustrate the relationship between the chapters (Figure 1). The chapters correspond to three areas of interest for further investigation. An ERT study begins with designing the survey and then collecting the measurements. Then the data collected is inverted to obtain images of geophysical properties. The images are interpreted to understand the cause of the behaviour observed in the images. Finally, such interpretation may be applied for prediction of future events.

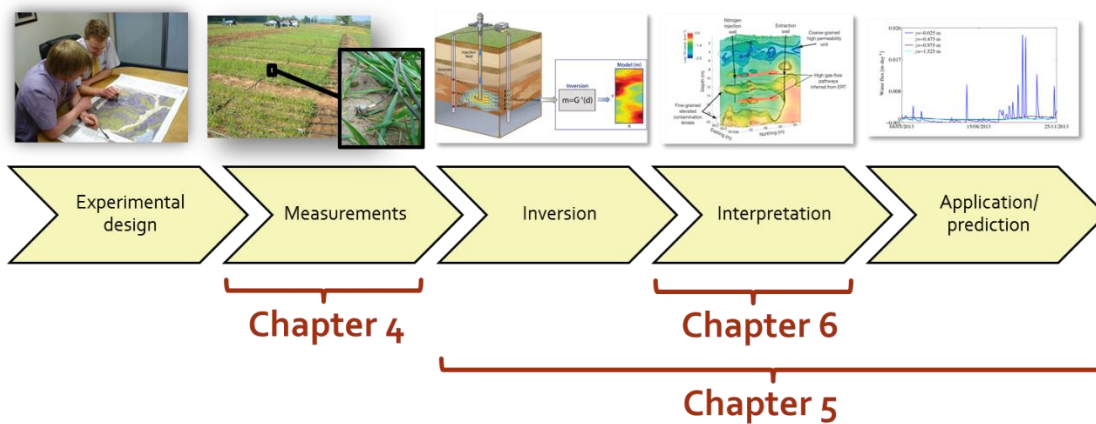


Figure 1 The ERT workflow showing the various stages of conducting ERT survey and analysing its data. It also serves as a pipeline where information and uncertainty is propagated along. The annotation shows the relation between the chapters in this thesis and the workflow.

Funded in part by the Nuclear Decommissioning Authority (NDA), this project has a focus on leak detection using ERT at nuclear sites. However, it was thought that some of the findings and conclusions from this study would improve the general understanding of using ERT for site characterisation and monitoring, and would be applicable for the deployment of ERT at other sites. It was also thought that some of the findings are applicable to the use of other geophysical methods for site characterisation.

1.3 Outline

Chapter 2 and 3 includes two literature review on the subject matter discussed in the thesis. The first one provides details on the context of the application of near-

surface geophysical methods for nuclear site characterisation. The second review provides a detail discussion on the various sources of uncertainties in ERT by summarizing existing research and identifying knowledge gaps.

Chapter 4 (Tso et al., 2017) describes an analysis of ERT measurement errors using permanently installed ERT arrays. Various types and formulation of measurement errors are assessed. A new model for ERT measurement errors is proposed to handle potential bias of faulty electrodes. This work is an essential first step to handle uncertainty propagation from ERT data in the hydrogeophysics workflow.

Chapter 5 describes a novel geoelectrical leak detection method using coupled hydrogeophysical modelling and data assimilation techniques. The ERT data corresponding to the leak is used to provide information of the leak parameters and reduce uncertainty in the geological conceptualization of the site. This work highlights that in previously characterized sites (as in most nuclear sites), geophysical data can be a powerful tool to estimate leak parameters using a minimal amount of boreholes.

Chapter 6 (also as Tso et al., 2019) explores the utility of inversion-based estimates of moisture content from ERT under the influence of uncertain petrophysical relationships. Field data shows that even cores within the same unit can show significant variation in petrophysical relationships and if the full range is considered, moisture content estimates can be highly uncertain. We advocate for the improved consideration of petrophysical uncertainty in future work.

The above is followed by the discussion summary and conclusion sections.

Part of this work has been conducted using the coupled hydrogeophysical code PFLOTRAN-E4D (Johnson et al., 2017), as illustrated in Figure 2. It was part of the PFLOTRAN software releases until the end of this PhD. An alternative approach to perform coupled hydrogeophysical simulation by running PFLOTRAN and E4D separately is outlined in the Appendix.

Introduction

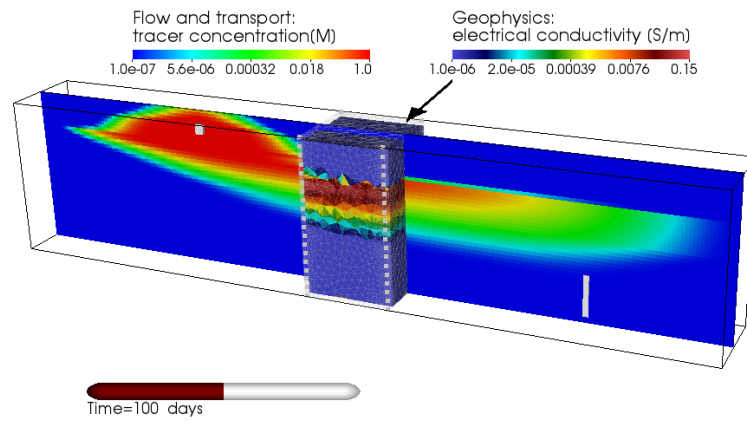


Figure 2 Snapshot showcasing coupled hydrogeophysical modelling using PFLOTRAN-E4D. The 2D flow and transport model simulates tracer injection at an injector in the upper left of the domain. Groundwater movement is towards an extraction well to the lower right. An ERT imaging cell with 4 boreholes (20 electrodes each) is located at the centre of the domain. The animation shows that as the conductive tracer migrate through the ERT imaging cell, there is a corresponding increase in electrical conductivity in the ERT imaging cell.

2. Geophysical methods for nuclear site characterisation

Manuscript prepared for journal submission as **Tso, C.-H.M.**, Kuras, O., Binley, A.
(201x) Geophysical methods for nuclear site characterisation

Background

Site characterisation, in the context here, involves desktop analysis of historic studies, making observations and collecting data in the field and interpreting them in order to build up a conceptual understanding of the geology, hydrogeology, hydrology, and contaminant transport processes at the site. This understanding allows assessments of exposure pathways and provides justification for clean-up decisions at the site. Geophysical methods allow mapping and monitoring subsurface properties and processes at resolutions and coverages that would otherwise be impossible to attain by other point-scale methods. The chapter summarizes the current applications of geophysical methods at nuclear sites and identifies critical gaps to be addressed in future work.

Improved understanding of a site's surface and subsurface conditions can greatly reduce the costs and risks of decommissioning. In particular, uncertainty in the site conditions contributes to tremendous financial and safety risks for multi-decade, multi-billion pound decommissioning projects. Conventional methods are cost- and labour-intensive because, traditionally, they rely on invasive, numerous local-scale measurements. The interpretation drawn from these methods may not represent the site-scale behaviour of the contaminant transport process. The above underpins a major discrepancy between the principle and implementation of contaminated land legislation. For example, in the U.K. contaminated land law, source-pathway-receptor linkage of the contaminant needs to be established in order to determine risk and responsibility ([Environmental Protection Act 1990 - Part IIA Contaminated Land: statutory guidance](#)). This has been proved to be very difficult to achieve in the subsurface environment. Geophysical methods offer a promising alternative as they provide much greater site coverage. Their short data collection cycle also allows time-lapse monitoring of transport processes. Much of the development in inversion has been focused on improving the resolution of estimates or joint inversion of different data types. Our understanding of a site, however, is always subject to uncertainty and complicated by inconsistent scales of measurements. More robust methods to reduce uncertainty in interpreting different site data is needed to improve site characterisation.

Site characterisation on nuclear sites (and ultimately the need for geophysics) can have very diverse drivers, often associated with different regulatory issues, different environmental hazards, and also different funding streams. More importantly, the different needs of characterisation are often related to different spatial and temporal scales of the problem. At the same time, some needs arise from a 'civil/nuclear engineering' angle, while others from a more holistic 'environmental assurance' perspective. For example, the recent Sellafield leak monitoring work fell under 'decontamination & decommissioning (D&D)', which addresses immediate risks and often precedes more strategic 'site restoration' and 'environmental remediation (ER)' tasks (timescales = many decades). There is also the (separate) issue of long-term geological disposal, which requires characterization of the deeper subsurface. At Sellafield and other NDA sites, all near-surface issues fall under the responsibility of a 'Land Quality' directorate, and UK regulatory oversight comes from the Environment Agency (EA) and the Office for Nuclear Regulation (ONR).

In this review, some conventional methods used in nuclear site characterisation are outlined. Then, the application of geophysics at a number of selected nuclear sites is reviewed. Finally, problems and aspects missing in current geophysical approaches are summarized, and suggestions made for possible solutions. This report only focuses on near-surface site characterisation (e.g. the shallowest 200 m). Geophysics can also be used in deep repositories, but they are used to address different needs. For a review of the technological development in characterizing potential deep repositories, the reader is referred to the work of [Tsang et al. \(2015\)](#).

Conventional Methods

Nuclear site characterisation requires careful planning. Desk studies and site walk-overs allow building up of knowledge of the site's history and current condition. They include surface mapping of geology, studying previous site records and investigation reports, and obtaining information from nationally held databases ([Bayliss and Langley, 2003](#)). They can provide the first evidence of site condition and can help determine the feasibility of a field study proposal. Once preliminary site

conditions are understood, and health, safety, and logistical issues are resolved, intrusive surveys can be arranged.

Typically, conventional characterisation of nuclear sites involves the drilling of boreholes, pitting and logging of rocks, single- and cross-hole hydraulic testing, and monitoring of water levels (Bayliss and Langley, 2003). Groundwater sampling is often considered as the most important aspect of contaminated land assessment since they provide direct evidence of the radioactive level and the presence of other chemical constituents in groundwater.

Tracer methods have also been used extensively to evaluate the contaminant transport behaviour at sites, for example, the US sites at Hanford (Ahlstrom et al., 1977) and Savannah River (Webster et al., 1970). They are often used to infer solute advection and dispersion properties of a site, which controls the rate at which a contaminant plume spreads. Stochastic methods (e.g. Gelhar and Axness, 1983; Zhang and Neuman, 1990) can be used to relate small-scale tracer test results to large-scale displacements of contaminants.

Geophysical surveys, such as surface and cross-borehole seismic and surface electromagnetic (EM), are common practice in conventional site characterisation. Common methods include electromagnetic conductivity mapping and sounding, resistivity profiling, and ground penetrating radar. The conventional use of geophysics distinguishes itself from its successors, not in the measurement techniques but its role in the investigation. Geophysics was thought to only provide a secondary, indirect means of characterizing a site prior to or in conjunction with intrusive work (Bayliss and Langley, 2003). Likewise, down-hole geophysical logging is also often used during the installation of boreholes. Again, conventional site characterisation does not consider it as a part of the formal investigation. For example, natural gamma logs are seen to assist overall approximation of hydraulic conductivity and allow data to be cross-correlated with other field data (Bayliss and Langley, 2003). In recent applications, however, both borehole and surface geophysics play a much more important role in nuclear site characterisation. A detailed discussion is provided in the next section.

As an illustration, all of the conventional characterisation tasks mentioned above were completed for part of the Sellafield site before 2000 (Bowden et al., 1998). The site was one of the two potential areas (the other being Dounreay, Scotland) to construct a low- and intermediate-level waste repository (Norton et al., 1997). Their results are reported respectively in thirty-some NIREX reports published between 1993 and 1998.

Geophysical Methods

The use of geophysics for site characterization in nuclear sites can be traced back to the 1970s (e.g. Edwards, 1977; Robins, 1979). However, its potential use for characterising and monitoring nuclear sites was not recognized until the 1980s (Morrison et al., 1987). An idealized 2-D nuclear waste repository was used to show the effectiveness of surface-borehole ERT (Asch and Morrison, 1989). This review uses two U.S. Department of Energy legacy sites—the Hanford site and the Savannah River Site as case studies to discuss the development of applications of geophysical methods in nuclear sites. This review also covers sites from the U.S. Department of Energy's (DOE's) Integrated Field-Scale Subsurface Research Challenge (IFRC), a new program that commits multi-investigator teams to perform large, benchmark-type experiments on formidable field-scale science issues. IFRC consists of three legacy sites: Hanford 300 areas, Washington, Rifle, Colorado, and Oak Ridge, Tennessee. Finally, a summary of applications in the United Kingdom and other countries are provided.

Hanford Site and Hanford 300 Area IFRC Site

The Hanford Site is located in south-central Washington State, the United States. It was selected in 1943 as part of the secretive project to build an atomic weapon (the Manhattan project) and was later expanded to produce weapon-grade and fuel-grade plutonium. From 1945 to 1986, Hanford produced 65% of the plutonium produced in US government-owned reactors (67 metric tons) and reprocessed 96,900 metric tons of Uranium (Gephart, 2010, 2003). It is among the largest open sites which the US Department of Energy is obligated to clean-up according to US environmental

laws. A more detailed review of the near-surface work done at Hanford is provided by [Johnson et al. \(2015a\)](#).

The Hanford Site is built along a section of the Columbia River and is divided into the 100, 200, and 300 Areas. The 300 Area was responsible for producing uranium fuel rods. The fuel rods were then sent to the five chemical separation plants in the 200 Area to extract plutonium. Each of the separation and extraction processes used complex, toxic, and corrosive chemicals that ultimately produced large amounts of high-level radioactive waste (HLW), though the process has improved significantly over the years. The extracted plutonium was sent to the nine plutonium production reactors in the 100 Area. Currently, the 200 Area stores most of the site's legacy waste facilities.

The 300 Area is located at the east reach of Columbia River, while the 100 Area aligns with the River's north reach, and the 200 Area is located in Hanford's Central Plateau. Figure 1 shows a map of the Hanford site. The geology of Hanford mainly consists of two formations: (1) the upper, Hanford Formation hosting the unconfined aquifer in which groundwater flows; (2) the underlying, semi-confining Ringold Formation. The interface between the permeable Hanford Formation and the relatively impermeable Ringold Formation is a critical hydrogeological contact controlling the vertical flow and transport of contaminated groundwater into the Columbia River ([Mwakanyamale et al., 2012](#)).

The use of electrical potential variations to detect leaks at Hanford can be traced back to the 1970s ([Key, 1977](#)). At the turn of the century, virtually all types of surface-based geophysical methods have been tested at Hanford, including electrical resistance tomography (ERT), ground-penetrating radar (GPR), numerous electromagnetic, magnetic, seismic, and gravity methods. Over 250 geophysical surveys have been conducted in portions of every "Area" of the Hanford Site ([Last and Horton, 2000](#)).

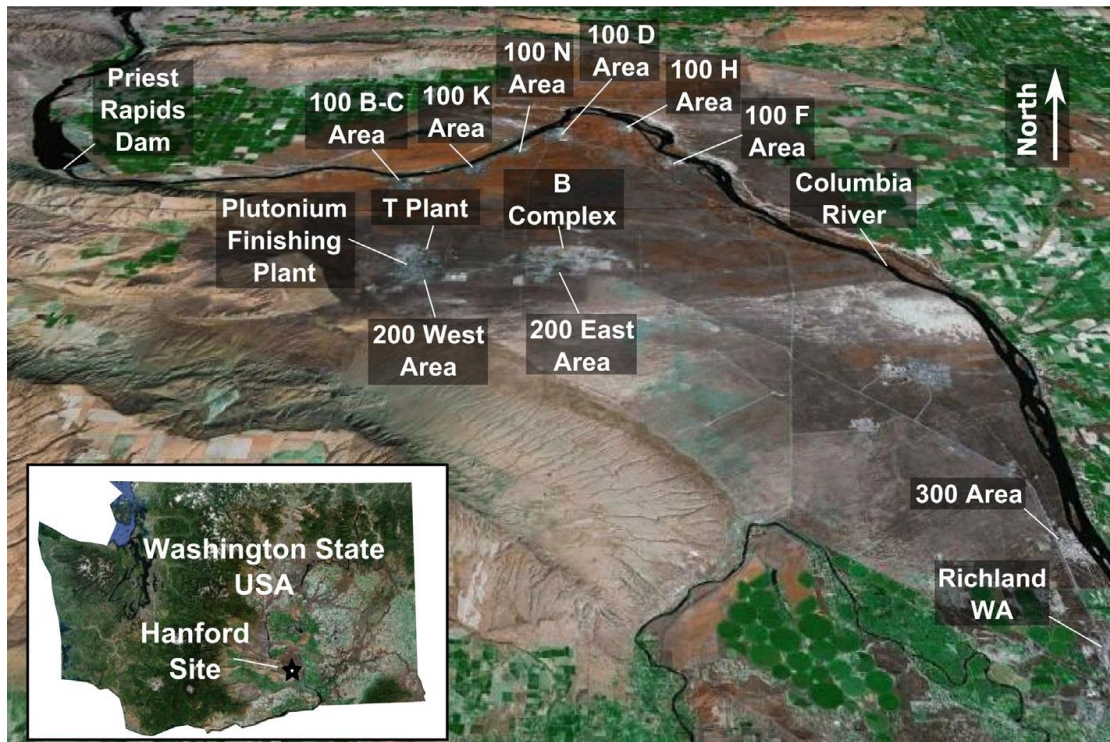


Figure 1 Aerial view of the Hanford Site (Johnson et al., 2015a)

The 200 Area is located away from the river and its major concern is the potential that contaminated water reaches regional groundwater or discharge to the adjacent Columbia River. A basalt unit underlying the Ringold Formation can be seen as a flow barrier yet its extent is unknown. Williams et al. (2012a, 2012b, 2012c, 2012d) combined seismic reflection, vertical seismic profile, geologic cross-section, and well control data to infer the subsurface basalt topography and showed that there is a significant gap known as the Gable Gap in the basalt flow barrier (up to a few km across), which provides a possible flow path for contaminants originating from the 200 Area.

Closer to the land surface, there are 40 single-shell HLW storage tanks in the B-complex (the oldest one in Hanford) of the 200 Area, many of which have leaked or experienced overfill episodes, and several outlying subsurface infiltration galleries. The waste streams introduced to the vadose zone were highly saline and created zones of elevated electrical conductivity. The waste poses a significant risk to groundwater quality, and determining the distribution of vadose zone contamination remains one of the most significant challenges limiting remediation and closure of Hanford Site

waste disposal facilities. ERT surveys were conducted to determine the distribution of highly conductive waste in the subsurface. Electrodes were laid parallel and perpendicular to the tanks, trenches, and cribs (Rucker et al., 2007). A comparison between the tank release history and groundwater sampling shows that higher disposal volumes were generally accompanied by more dilute waste. One exception is at the BY-Cribs Area, which was subjected to high waste volumes with high ionic strengths. The inverted results are consistent with the contaminant release history (Johnson and Wellman, 2013). They identify a main plume for the BY-Cribs Area which is oriented directly beneath the cribs (i.e. unlined underground box-like structures to dispose of liquid contaminants (Gephart, 2003)) have not only migrated vertically but also laterally. An eastward trending lobe that dips downward at $\sim 30^\circ$ appears to originate from the northeastern-most crib and a southeast trending lobe that appears to be an extension of the main plume beneath the cribs. Figure 2 shows the estimated plume for the BY-Cribs Area.

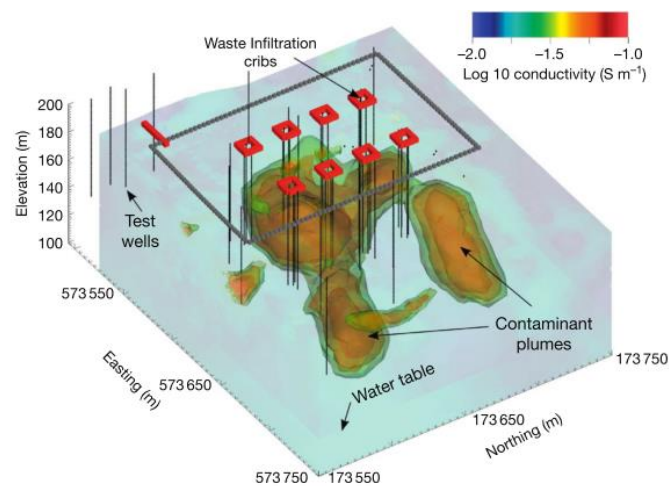


Figure 2 Estimated conductivity at the Hanford BY-Cribs (Johnson et al., 2010; Johnson and Wellman, 2013)

Within a tank farm there is typically extensive metallic infrastructure including pipes, tanks, wells, electrical lines, distribution manifolds, and fences that complicates the use of geophysical methods that aim to estimate electrical properties in the subsurface. For example, previous studies in the 200 Area show poor ERT resolution within the tank farm (Johnson and Wellman, 2013). Given the strong influence of metallic infrastructure on electrical resistivity response, it may be advantageous to

incorporate the infrastructure directly into the acquisition and modelling approaches (Johnson et al., 2014). The steel-cased wells originally used for drywell geophysical logging, for example, can be used as long electrodes in an electrical resistivity survey – the concept was first tested by Ramirez (Ramirez et al., 1996). Recently, the method is applied using a pilot-scale field experiment (Rucker, 2012) and within an actual tank farm to image suspected releases from a tank (Rucker et al., 2013).

Ramirez et al. (1996) compared the pre-spilt and after-spilt ERT images of a contaminant plume as it develops in soil under a tank already contaminated by previous leakage. They concluded the new contaminant plume can still be detected without the benefit of background data. Binley et al. (1997) tested the method of electrical current imaging for leak detection at a mock tank set up in the 200 East Area in Hanford. Both leaks from the centre of the tank and from the side were considered. Unlike ERT, electrical current imaging aims to resolve the distribution of the percentages of applied current within the electrode array and it can be sensitive to small leaks. Daily et al. (2004) pioneered the near-real-time and remote monitoring of leaks in underground storage tanks using ERT at the Hanford 200 East Area, as part of a 5-party “mock tank” demonstration study for geophysical leak detection technologies (Barnett et al., 2003, 2002). Based on the ERT images, a “leak/no-leak” decisions is made daily. The ‘blind test’ yielded a 57% success rate, which is further improved to 87% after defining a new criteria during re-analysis. The single-shell tank used is characteristic of the 177 of them at Hanford and another 51 at Savannah River currently containing waste. A number of steel-cased wells adjacent to the tank are used as ‘long’ electrodes to sense bulk resistivity beneath the tank as well as depth-averaged images of resistivity variation. 54,000 litres of sodium thiosulfate were episodically released from a steel tank in a blind test lasting 110 days. Each day during the test a leak or no-leak condition was declared based solely on analysis of the electrical data. The summary diagnostic measure proposed therein, the mean logarithmic ratio (MLR), is later used for value of information (VOI) studies to evaluate the benefit of using different ERT array to monitor possible leakage from geological storage of carbon dioxide (Trainor-Guitton et al., 2013b). The dataset from this study (Daily et al., 2004) is later used for the first stochastic Markov-chain Monte Carlo (MCMC) inversion of

time-lapse ERT data (Ramirez et al., 2005). This technique combines prior information, measured data, and forward models to produce subsurface resistivity distribution that is most consistent with all available data. It allows quantification of the uncertainty of a generated estimate, and allows alternative model estimates to be identified, compared, ranked, and rejected. Similar leak detection systems are also used in later studies at the site (Calendine et al., 2011; Glaser et al., 2008). The above is a good example to illustrate how nuclear applications can set trends in geophysical methodology.

The US Department of Energy (DOE) also initiated a treatability test program to desiccate a portion of the vadose zone to minimize migration of contaminants towards the water table, usually achieved by injection of non-reactive gas. The promise of the technology relies on reducing the moisture content of the vadose zone, and therefore monitoring its evolution over time is essential. A field test of using time-lapse ERT to monitor desiccation of the 100-m thick vadose zone at the Hanford 200 Area BC-Cribs and Trenches was conducted. The geophysical results show the creation of a desiccation plume and map its evolution over time (Truex et al., 2013a). The moisture content at the final time step agrees generally with independent neutron logging measurements. Neutron logging and other methods, however, cannot map the change in moisture content before and after the gas injection.

Finally, geophysical methods have also been used to assist the engineering aspect of the remediation effort at the Hanford 200 Area. Specifically, they can be used to map pipelines in the subsurface. Since high-density GPR over a large area is not economically feasible nor necessary, electromagnetic induction (EM) and magnetic gradiometry surveys were conducted by towing the equipment behind an all-terrain vehicle outside TX and TY tank farms, covering ~40 hectares (Myers et al., 2008a, 2008b). The identification of pipes in the subsurface can help minimize false-positive interpretation related to a potential contaminant disposed to the ground.

The Hanford 300 Area contains infiltration ponds that were used to dispose of waste from uranium fuel rods production. It is adjacent to part of the Columbia River,

the largest river in the US by volume. There exist many uranium hot spots within the groundwater that vary with seasonal fluctuations in Columbia River stage levels (Williams et al., 2008). The highest desorption of uranium occurs when the river stage is as high as the smear zone beneath former ponds and trenches. As stage decreases, groundwater flow moves towards the river and carries the desorbed uranium.

One of the challenges at the Hanford 300 Area is to understand the potential connectivity of contaminant plume to the Columbia River. Slater et al. (2010) used waterborne electrical resistivity and induced polarization surveys to map the thickness of the Hanford unconfined aquifer at the river bed, which is indicative of paleochannel structures that cause preferential groundwater flow. Using the temperature difference between groundwater and river water as a proxy, they also used fibre-optic distributed temperature sensing methods to map groundwater discharge along a 1.5 km stretch of shoreline adjacent to the 300 Area. Their results reveal variable, time-dependent, stage-driven groundwater discharge and river water intrusion along the shoreline. Mwakanyamale et al. (2012) conducted further resistivity and IP surveys using seven profiles running approximately parallel to the Columbia River and ~20m apart to estimate the elevation of the Hanford-Ringold contact connecting the aquifer and the Columbia River.

Johnson et al. (2012b) installed a 3-D electrode array near the 300 Area bank to monitor stage-driven river water intrusion and retreat using 4-D ERT. In particular, they capitalize on the distinctive contrast between groundwater and river water conductance. Methods of distilling data such as time-series and time-frequency analysis help improve the results. Correlation analysis between stage and bulk conductivity at several depths validates the location of a dominant groundwater/river water exchange zone along the shoreline previously identified by Slater et al. (2010).

River water is commonly detected 250 m inland to the IFRC well field during spring runoff peak flow. Three 2-D ERT lines were deployed to monitor intrusion during the 2011 peak flow event. The moving water table boundary becomes problematic when smoothness-constrained inversion is used. Wallin et al. (2013) show

that removing regularization constraints between neighbouring elements near the water table boundary can effectively enable the inversion to map sharp contrast at the water table boundary. Using ERT and borehole electrical conductivity (EC) data collected from the IFRC well field in 2008, [Johnson et al. \(2012b\)](#) devised a new constrained inversion method that allows incorporation of known geostatistical, discontinuous boundary, and known conductivity constraints. The results are compared to borehole flowmeter data. Building upon these efforts, [Johnson et al. \(2015b\)](#) devised a warping mesh inversion to monitor the 2013 spring runoff at the IFRC well field. The computational mesh warps to the known water table boundary without changing mesh topology, thereby facilitating consistent regularization constraints in the time dimension. The inversion is highly effective that it is conducted near-real-time via wireless transfer. The real-time imaging provided information concerning the onset of river water intrusion to scientists conducting time-sensitive microbial sampling at the site.

[Kowalsky et al. \(2005\)](#) described a method to jointly use borehole time-lapse GPR traveltimes data and neutron probe data to estimate unsaturated hydraulic properties fields, which they applied it to an infiltration experiment at the Hanford 200 Area 'Sisson and Lu site'. Their method has jointly estimated petrophysical parameters and it corrects for initial over-prediction near the edge of the water plume. Their work is an excellent example of how the combined use of geophysics and point-based monitoring data can improve both coverage and accuracy of the estimates of field-scale soil hydraulic parameters and the related moisture distribution.

Lastly, the reader has referred also to a few other joint inversion studies at the Hanford 300 Area, which may be extended to include geophysical data in the future. For example, [Murakami et al. \(2010\)](#) assimilated large-scale constant-rate injection data with small-scale borehole flowmeter data using a Bayesian geostatistical inversion framework, the method of anchored distributions (MAD) ([Rubin et al., 2010](#)). [Chen et al. \(2012\)](#) expanded the study of [Murakami et al. \(2010\)](#) by using MAD to assimilate also results from two field-scale nonreactive tracer tests. Using the same dataset, [Chen](#)

et al. (2013) compare several ensemble-based data assimilation techniques for aquifer characterisation, which was the first study of its kind using field data.

Finally, data management and visualization have become an important topic in nuclear site management and characterization. The Pacific Northwest National Laboratory has recently launched an online platform called SOCRATES (<https://socrates.pnnl.gov/>) (Truex, 2018), where all well logs, remote sensing images and historical groundwater monitoring data of the Hanford site is available for plotting and download on a user-friendly browser application (Figure 3). It includes options to visualize selected wells only and several useful tools to visualize plume evolution over time. Of relevance to geophysics is that the SOCRATES platform also includes near-real-time ERT inversion images from the Hanford permanent monitoring network. Such integrated data management platform can be valuable for deciding the appropriate remediation strategy.

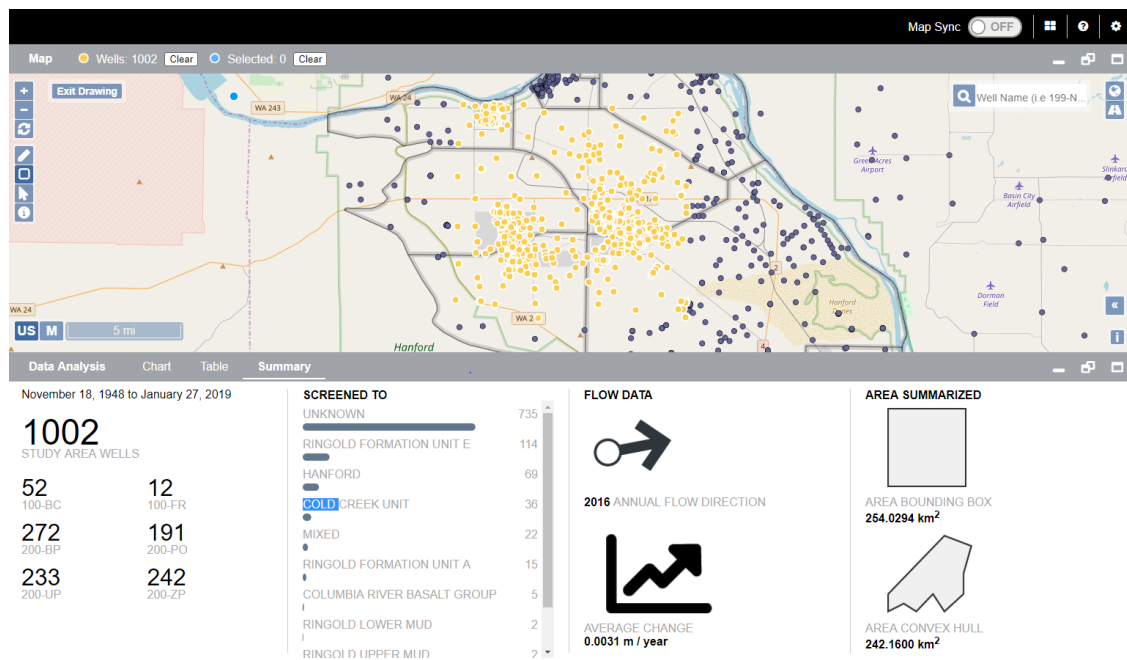


Figure 3 A screenshot for the browser-based integrated data platform SOCRATES for the Hanford site. It serves as a centralized portal for all data collected at Hanford Site. It includes a wide variety of tools, such as those for filtering data and exporting data and model domain for flow and transport modelling.

Savannah River Site

Most of the plutonium not produced at Hanford is produced at Savannah River Site near Aiken, South Carolina. The main contaminants of concern, however, are

chlorinated solvents such as trichloroethylene (TCE). One of the first time-lapse electrical resistivity tomography studies was conducted at the site by [Daily and Ramirez \(1995\)](#), to test the monitorability of methane air sparging for *in-situ* enhanced bioremediation of TCE. They used a differential tomography method to remove all static features of formation resistivity and found that the flow paths are confined to a complex three-dimensional network of channels. Another series of tests obtained images of water infiltration from the surface gives a similar conclusion, indicating the flow regime is minimally modified by infiltration.

Subsequently, time-domain electromagnetic soundings were used to define the electrical conductance of a clayey confining unit (aquitar), and shear-wave seismic reflection was used to define the stratigraphic framework ([Eddy-Dilek et al., 1997](#)). Later, three-dimensional (3-D) self-potential (SP) survey ([Minsley et al., 2007](#)) was conducted at part of the site and the data was inverted using the model of [Shi \(1998\)](#) to find an electrical current source model, taking into account the resistivity structure derived from a 3-D spectral induced polarization survey at the same field location. The sources and sinks of electrical current can be related to the zones of relatively high or low redox potential and are therefore interpreted in the context of contaminated areas. These results are reasonably correlated with contaminant concentration data obtained from several ground-truth well measurements, indicating that the SP sources can be an indicator of contaminated areas where electrochemical source mechanisms are active.

Taking advantage of the often-coupled physical-geochemical-microbiological properties of subsurface materials, [Sassen et al. \(2012\)](#) pioneered a reactive facies concept and applied it to the site's F-Area. The reactive facies concept is based on the hypothesis that subsurface units exist with distinct distributions of coupled physiochemical properties influencing reactive transport, such as effective surface area, mineralogy, and hydraulic conductivity. Applying Bayesian data mining algorithms to wellbore lithology, cone penetrometer testing, and cross-hole and surface seismic data, [Sassen et al. \(2012\)](#) identified two distinctive reactive facies, which were coincident to the two depositional facies at the site: a Barrier Beach and a Lagoonal

facies. [Wainwright et al. \(2014a\)](#) expanded the method over large scales at high resolution using a Bayesian hierarchical approach using recently acquired geochemical data in addition to the dataset from [Sassen et al. \(2012\)](#). The facies estimates are then used to obtain very high-resolution estimates of reactive facies-based transport properties, such as percentages of fines, hydraulic conductivity, and Al:Fe ratio. The modified approach is also a new formal methodology that quantifies the uncertainty of reactive-facies properties, as well as the uncertainty in the spatial distribution of reactive facies, using multiscale data sets.

Oak Ridge IFRC Site

At the Oak Ridge IFRC Site, Tennessee, the S-3 disposal ponds consisted of four ponds built in 1951. They received a yearly volume of 7.6 million litres of acidic (pH<2) liquid wastes consisting of nitric acid, uranium, technetium, cadmium, mercury, and chlorinated solvents for 32 years. In 1983, the ponds were drained and filled to neutralize the acidic wastewater, and they are covered with a multilayer cap to minimize leaching. The meteoric water falling on the cap is drained and diverted to a ditch surrounding the former S-3 ponds. The forced-gradient groundwater flow and the infiltration of meteoric water create a mixing zone for the contaminants down-gradient. The meteoric water has very different water chemistry than the plume. The complexity of the geology at the site—saprolite overlaying fractured shale bedrock and limestone interbeds – add challenge to the remediation of the site. Together, understanding the subsurface heterogeneity within the plume pathways and how recharge events affect the transport and attenuation of the plume are the major goals of the geophysical investigation at this site.

The first geophysical studies conducted at the site were standard surface resistivity tomography and seismic tomography along a survey line immediately downgradient of the former S-3 ponds ([Watson et al., 2005](#)). Combined with limited borehole data, they are used as a rapid and effective method for defining the location of the high-ionic-strength plume and defining the transition zone between the saprolite and bedrock so that a field plot can be established on-site to test microbially-mediated reduction and immobilization of uranium ([Wu et al., 2006](#)).

Subsequently, a Bayesian method was used to combine cross-hole seismic travel times and borehole flowmeter test data to estimate hydrogeological zonation (Chen et al., 2006). The Bayesian joint inversion approach permits information sharing between the hydrogeological and geophysical data. The study identifies an extended fracture zone along the primary axis of the plume. A later study inverts surface seismic refraction data with depth constraints (Chen et al., 2010) using boreholes drilled for the bioremediation pilot (Watson et al., 2005; Wu et al., 2006). They identify a zone of persistent seismic slowness along two transects, confirming the presence of a preferential flow path along the plume axis.

As more boreholes are drilled, more geochemical data are available. Joint interpretation of geochemical and geophysical data appears to be a valuable tool to study the hydrogeochemical processes in the heterogeneous subsurface at the site. Kowalsky et al. (2011) tested 10 coupled inversion cases using 1-D or 2-D hydrogeochemical models, combined with zero, one, or two ERT surveys from electrodes installed along two boreholes. Gasperikova et al. (2012) used difference inversion (Labrecque and Yang, 2001) to interpret data collected from 28 surface ERT datasets collected along the same profile, and 22 cross-well datasets spanning 5 boreholes. The time-lapse inversion results show the evolution of nitrate levels distribution in the subsurface, which is used to guide the site's large-scale modelling effort (Tang et al., 2010).

To better constrain geophysical inversion, detailed laboratory studies are conducted to study the petrophysical properties of the contaminated and flushed saprolites collected from the S-3 ponds (Revil et al., 2013a). A laboratory complex conductivity study is also conducted on samples from the S-3 ponds (Revil et al., 2013b), followed by inverting 15 time-lapse resistivity snapshots using the active time-constrained approach (ATC) (Karaoulis et al., 2011b). The inversion results capture the occurrence of an infiltration event during the winter of 2008–2009 with a dilution of the pore water chemistry and an increase of the pH.

Rifle IFRC Site

The Rifle, Colorado site is located on a floodplain adjacent to the Colorado River. It contains three major hydrostratigraphic units: the fill layer, the shallow unconfined aquifer Rifle Formation (~1-3 m below land surface), and the low-permeability Wastach Formation (~5-8 m below land surface). The site was previously used as a vanadium and uranium ore treatment facility. The Rifle site currently serves as a community field laboratory for research in biogeochemical characterization, bioremediation, subsurface microbial characterization and nutrient cycling. Recent studies at the site report the presence of a naturally-reduced zone (NRZ) within the aquifer sediments. The NRZ sediments had elevated concentrations of uranium, organic matter, and geochemically reduced mineral phases, such as metal sulfides, and were often associated with predominantly fine-grained sediment textures. The conceptual model of NRZ formation is that roots, twigs, and other plant materials accumulated during the river depositional process became buried and formed the reduced sediments and abundance of iron-reducing *Geobacteraceae* communities.

[Williams et al. \(2009\)](#) conducted a spectral induced polarization survey to resolve subsurface microbial activity at a high spatial resolution during bioremediation. Fluids and sediments recovered from regions exhibiting an anomalous phase response were enriched in Fe(II), dissolved sulfide, and cell-associated FeS nanoparticles. [Flores-Orozco et al. \(2011\)](#) extended the previous dataset and collected time-lapse induced polarization (IP) data during 100+ days of acetate injection, which was used to stimulate microbial growth and hence to immobilize U(VI) in the unconfined aquifer. The IP inversion identified zones with different redox characteristics, particularly an increase in polarization effect accompanying the precipitation of iron sulphide. These factors are critical in terms of controlling the rate and fate of bioremediation of uranium in the subsurface. A later, more detailed inversion of the data finds that the polarization effect of geochemically reduced, biostimulated sediment remains much higher than background aquifer materials over a broad frequency bandwidth (0.06-120 Hz) ([Flores-Orozco et al., 2013](#)). [Chen et al. \(2013\)](#) combined the IP and aqueous geochemistry time series using a hidden Markov model to estimate the timing of the most probable transitions of redox states, which cannot otherwise be inferred from

measurements directly. [Wainwright et al. \(2016\)](#) took a multi-step approach to map the NRZ and the two hydrostratigraphic contacts at the site. They first inverted ERT and time-domain IP (TDIP) data collected from ten of the surface lines. Statistical analysis was then used to find correlations between the inverted geophysical model and lithological logs information from 187 wells. Finally, the Bayesian reactive facies approach ([Sassen et al., 2012](#); [Wainwright et al., 2014a](#)) is used to map the most probable surfaces of the two contacts and volume of the NRZ. This is the first study that demonstrates the ability of TDIP imaging surveys for characterizing hotspots that have unique distributions of subsurface lithological and biogeochemical properties. A recent work by [Chen et al. \(2016\)](#) uses Bayesian methods to combine 47 years of streamflow data upstream of the site and large-scale climate information to predict future groundwater dynamics at the site. Results from this work can be used alongside those from geophysical investigations to better understand subsurface structures and processes at the site.

United Kingdom sites

Geophysical methods are also used extensively in sites in the United Kingdom for nuclear site characterisation. Regrettably, many of work are not available in the public domain. The use of electrical methods can be traced back to the 1970s ([Robins, 1979](#)) at Sellafield, Cumbria – U.K. 's most complex nuclear site. Since then, there has been a continuous effort to use different geophysical methods to map the subsurface at different areas of Sellafield ([Lean, 1998a, 1998b](#); [Ross, 2004](#); [Serco/Golder, 2010, 2009, 2008a, 2008b](#); [TERRADAT \(UK\) LTD., 2012, 2004, 1998](#)). Examples of methods used include micro-gravity, downhole geophysical logging, EM61 (time domain metal detector), GPR, and electrical resistivity imaging (ERI) surveys. In earlier years, gravity and aeromagnetic data had been used ([Kimbell, 1994](#)).

The potential use of different geophysical methods is considered at all U.K. nuclear sites ([Booth, 1997](#)), including the potential use of existing boreholes ([Cooper, 1997](#)). A comparative assessment among ten geophysical methods and case studies at seven U.K. nuclear sites was also made ([Cooper and Ross, 2005](#)), where the authors concluded that “the use of geophysical techniques at U.K. Nuclear Licensed Sites has

a number of advantages over intrusive surveys in terms of dose rate to workers, reduced time to obtain data, safety of workers and cost as intrusive surveys can be prohibitively expensive on such sites”.

Most of the geophysical applications at U.K. nuclear-licensed sites take a rather conventional approach. Geophysics plays only an assistive role in site characterisation programs and its use focuses on identifying geophysical anomalies. There are a few exceptions that explore the potential to monitor subsurface processes using borehole electrical methods. At the Low-Level Waste Repository in Cumbria, the United Kingdom, [Kemna et al. \(2004\)](#) has shown in a cross-hole ERT and IP survey that the image of imaginary conductivity reveals additional information that allows lithological decimation than the image of real conductivity. Throughout 2000, 2-D ERT had also been used to monitor a tracer injection test at Drigg and the plume arrival shows good agreement to background hydraulic gradient-based calculations (personal communication with Andrew Binley, Lancaster University).

A full-scale field experiment applying 4D (3D time-lapse) cross-borehole ERT to the monitoring of simulated subsurface leakage has been undertaken at a legacy nuclear waste silo at the Sellafield Site ([Kuras et al., 2016, 2015, 2014, 2011](#)), similar to the one at Hanford ([Daily et al., 2004; Ramirez et al., 2005](#)). A 4-D inversion ([Kim et al., 2009](#)) was used to estimate the time-lapse changes in conductivity, and they have revealed likely pathways of simulant flow in the vadose zone and upper groundwater system. The geophysical evidence was found to be compatible with historic contamination detected in permeable facies in borehole sediment cores, and with a geological model based on wider scale borehole stratigraphy. The results suggest that laterally discontinuous till units act as localized hydraulic barriers, which can substantially affect flow patterns and contaminant transport in the shallow subsurface at Sellafield.

In 2011, the Environment Agency reviewed the use of geophysical techniques for nuclear site characterization ([Environment Agency, 2011](#)). The report ranks the potential applicability of nine geophysical methods in nine different geological environments in terms of providing information in six areas (e.g. geotechnical,

hydrogeological, gas migration). The review's focus was on the siting a geological disposal facility (GDF). DC electrical resistivity method ranked low on the table, probably because (i.) only a single-line surface survey is considered, (ii.) static but not time-lapse surveys are considered, and (iii.) specific setups (such as leak detection or tracer injection monitoring) is not considered. As already demonstrated in this chapter, when used in the right context, DC electrical resistivity methods can be an extremely powerful tool for nuclear site characterization.

Sites in other countries

For other countries, information about decommissioning of military-grade nuclear facilities is often not available in the public domain. Previous work that is related to disposal or storage of nuclear waste is briefly reviewed in the following.

In Russia, little is known about their application of geophysics for nuclear site characterization. However, as an activity for a visit to Russia by a team of U.S. Lawrence Berkeley National Laboratory scientists through the Russian-American Center for Contaminant Transport, [Frangos and Ter-Saakian \(1996\)](#) performed resistivity and IP surveys at the Chelyabinsk Nuclear Waste Site. They attribute the anomalously low IP response recorded in some of the contaminated areas to a radiolytic reaction with the dissolved nitrate, yielding oxygen which, in turn, reacts to remove accessory pyrite from the host rocks.

At the French Institute of Radiological Protection and Nuclear Safety (IRSN) experimental platform at Touremire (Aveyron, France), surface ERT was performed for the underground research laboratory (for deep repository science) using two 2.5 km-long profiles to complement earlier 3-D seismic reflection investigations of limestone and clay-rock formations ([Gélis et al., 2010](#)). Several distinct vertical low-resistivity discontinuities were found, one associated with the regional Cernon fault, while others are consistent with the location of well-identified secondary faults.

In northern European countries, geophysics is widely used for potential deep waste repository characterisation, but not in near-surface remediation. Sweden is one of the earliest countries to recognize the benefit of geophysical methods in nuclear site

characterisation (Ahlbom et al., 1983). However, its work is mostly focused on deep repositories (e.g. > 1 km). Note that Sweden will be the first country to house a deep geological repository for its high-level radioactive waste (HLW). Borehole radar was used in an early SKB project to monitor tracer transport in fractured crystalline rock (Olsson et al., 1991; Olsson and Gale, 1995). Single-hole geophysics, as well as seismic cross-hole and reflection experiments were also conducted in the late 1980s and 1990s by the Swedish National Defense Institute and the Swedish Geological Co. Detailed surface ground magnetic and resistivity measurements were taken for a potential deep geologic repository for spent nuclear fuel in Oskarshamn (Stenberg, 2008). Similarly, in Finland 30 borehole seismic surveys were used to develop a complex site model alongside existing magnetic and EM mapping data (e.g. Enescu et al., 2004).

In recent years, China has recognized the benefit of geophysical methods in the design of disposal sites for its rapidly increasing number of nuclear power plants (Zheng et al., 2000). Unfortunately, most of them are published in Chinese journals. For example, a resistivity survey was conducted to select the disposal facility for the Daya Bay Nuclear power plant near Hong Kong (Zhao, 2000). In Taiwan, geophysics is also recognized as an important tool for nuclear site characterisation. For example, geophysical methods were used to assist the building of the conceptual site model and numerical transport models of the low-level nuclear waste repository in the western Pacific island of Lan-Yu (Huang, 2013). Surface electromagnetic survey and high-resolution audio-frequency magnetotelluric (AMT) surveys are used for the Xinchang site in Beishan area in Gansu province, which is China's proposed site for geological disposal of high-level radioactive waste (Wang et al., 2018).

Moving Forward

The wide range of applications of geophysical methods in nuclear sites has highlighted their utility and versatility in mapping subsurface facies and monitoring time-lapse changes in water and contaminants in the subsurface. Geophysical methods no longer only play an assistive role in identifying structural contrasts in the subsurface; they have also emerged to be a highly flexible and cost-effective suite of

tools to provide time-lapse monitoring of subsurface processes and high-resolution imaging of the subsurface.

A necessary first step to quantify uncertainty in geophysical data is to understand their errors. Like any measurements, basic research should be conducted to determine the error levels, which is currently lacking. For example, ERT measurements are generally taken using four electrodes, which may present some unique challenges. Similarly, varying resolution in a geophysical image is well recognized in the geophysical and hydrological community (e.g. [Day-Lewis et al., 2005](#); [Singha and Moysey, 2006](#)). Previous work has devised non-stationary calibration to compensate such variation. It remains unclear, however, how to translate variations in resolution to variations in uncertainty. When a geophysical property is translated to a quantity of interest (QoI, e.g. solute concentration, saturation), a conversion using petrophysical relationship needs to be assumed. The conversion is subject to uncertainty and its impact on the estimates of the QoI and its uncertainty remain unclear.

Nuclear site characterisation often spans decades and often lead to overlapping work. Because of a large amount of historical information available, it is easy for findings from previous characterization effort to be ignored. An effective, unifying uncertainty and image appraisal framework from design, data collection, to monitoring, is needed. It should take a sequential data collection approach that allows evaluation of uncertainty reduction since there are alternating tasks of data collection and interpretation. Data assimilation approaches can be used effectively to fuse information from various site characterisation efforts together.

Currently, there is a lack of a framework to compare the reliability of different characterisation options, particularly their ability to reduce risk and uncertainty. Forward simulations can be used to establish the data reliability of different methods ([Bratvold and Begg, 2010](#); [Nenna and Knight, 2013](#); [Trainor-Guitton, 2014](#); [Trainor-Guitton et al., 2013b, 2013a, 2011](#)). Decision analysis ([Bratvold and Begg, 2010](#)) and probabilistic risk assessment (PRA) (Figure 4) ([Paté-Cornell et al., 2010](#)), which has a

long history in evaluating nuclear reactor risks, can be used to rank different alternatives.

Installation of field monitoring programs should be able to justify its costs. The use of the value of information (VOI) (Eidsvik et al., 2015) to evaluate different alternatives, whether it is to decide on installation or monitoring strategies, is common practice in environmental applications. For example, they are used to decide the optimal number of point samples to be collected (Back, 2007), worth of hydraulic conductivity to determine maximum pumping in ecologically sensitive zones (Feyen and Gorelick, 2005) or alternatives to groundwater remediation (Lee et al., 2012; Liu et al., 2012). The VOI framework has also been applied to the use of geophysical methods to solve subsurface problems under uncertainty, including determining the monitorability of leak during geological storage of CO₂ (Trainor-Guitton et al., 2013b), placement of geothermal (Trainor-Guitton, 2014; Trainor-Guitton et al., 2014) wells, and the value of using TDEM to monitor a groundwater desalinisation project (Nenna et al., 2011). In CO₂ storage, long-term monitoring programs need to be in place before any data is collected. Some pioneering research on optimizing uncertainty reduction (Eslick et al., 2014) and VOI analysis (Sato, 2011) can be found.

Although there are many merits of VOI calculations, they are context-specific. Also, some characterization problems are more flexible than others to changes during their implementation. A solution is to incorporate the value of flexibility (VOF) (Begg et al., 2013) calculation when choosing characterisation alternatives. VOF has become popular in manufacturing operation research and oil and gas markets. Programs that can bring more side benefits to potential future uses and overall site objectives should be favoured.

Uncertainty quantification or reduction creates no value in or of itself and does not necessarily lead to better decision making (Bickel and Bratvold, 2008). Uncertainty quantification methods must be decision-focused. Modelling details, including uncertainty quantification, should only be included if it helps separate the alternatives under consideration. Therefore, a decision should be made as soon as there is enough information. An iterative decision analysis (Figure 4) is needed so that great detail is

built into the model only when it is relevant to an important area. This approach also accommodates learning and refinement, as well as a stopping rule that can reduce work that does not increase value. On a related note, very often investigations are not optimized to answer specific questions. The use of hypothesis-driven approaches (Leube et al., 2012; Nowak et al., 2012) and task-driven approach for Bayesian geostatistical design (Nowak et al., 2010) have emerged in recent work to address this. A selection of other work simply focuses on designing programs to minimize risks (de Barros et al., 2012; de Barros and Rubin, 2008; Tartakovsky, 2013; Varouchakis et al., 2016).

Advances in data analytics allow real-time and continuous monitoring and anomaly detection of data collected at nuclear site. For example, Schmidt et al. (2018) used Kalman filter for real-time and continuous estimation of tritium and uranium concentration from a live stream of specific conductance (SC) and pH data at Savannah River Site F-Area. This is achieved by building data correlation between the input and concentration data using principal component analysis (PCA) and coupling it with a concentration decay model. The current implementation is limited to point sensors in boreholes. Similar methods can be extended to incorporate geophysical data. If the inverted images are needed, near-real-time inversions will need to be set up, like the one that has been used to monitor and optimize remediation of contaminants real-time at the Hanford site (Pacific Northwest National Laboratory, 2016).

In summary, there is a need to better understand the errors, uncertainties, and information content of geophysical data and how they are translated and propagated in the various stages of analysis. There is also a need to continue developing flexible methods to incorporate different types of monitoring data from various characterisation efforts. These efforts are pivotal to make geophysical data more useful for nuclear site characterisation.

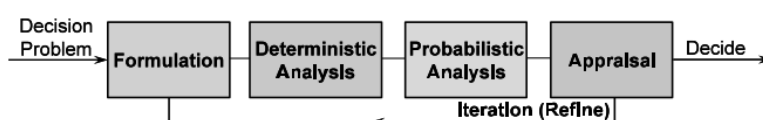


Figure 4 An illustration of the iterative decision analysis framework (Paté-Cornell et al., 2010).

References

- Ahlbom, K., Carlsson, L., Olsson, O., 1983. Final disposal of spent nuclear fuel - geological, hydrogeological and geophysical methods for site characterization. Stockholm.
- Ahlstrom, S.W., Foote, H.P., Arnett, R.C., Cole, C.R., Serne, R.J., 1977. Multicomponent mass transport model: theory and numerical implementation (discrete-parcel-random-walk version). Richland, Washington.
- Asch, T., Morrison, H.F., 1989. Mapping and monitoring electrical resistivity with surface and subsurface electrode arrays. *Geophysics* 54, 235–244.
- Back, P.-E., 2007. A model for estimating the value of sampling programs and the optimal number of samples for contaminated soil. *Environ. Geol.* 52, 573–585. <https://doi.org/10.1007/s00254-006-0488-6>
- Barnett, D.B., Gee, G.W., Sweeney, M.D., 2002. Results of Tank-Leak Detection Demonstration Using Geophysical Techniques at the Hanford Mock Tank Site – Fiscal Year 2001. Richland, Washington.
- Barnett, D.B., Gee, G.W., Sweeney, M.D., Johnson, M.D., Medina, V.F., Khan, F., 2003. Results of Performance Evaluation Testing of Electrical Leak-Detection Methods at the Hanford Site Mock Tank – FY 2002-2003. Richland, Washington.
- Bayliss, C.R., Langley, K.F., 2003. Nuclear Decommissioning, Waste Management, and Environmental Site Remediation, Nuclear Decommissioning, Waste Management, and Environmental Site Remediation. Elsevier. <https://doi.org/10.1016/B978-075067744-8/50027-8>
- Begg, S., Bratvold, R., Campbell, J., 2013. The value of flexibility in managing Uncertainty in oil and gas investments, in: SPE Annual Technical Conference and Exhibition. Society of Petroleum Engineers. <https://doi.org/10.2118/77586-MS>
- Bickel, E.J., Bratvold, R.B., 2008. From uncertainty quantification to decision making in the oil and gas industry. *Energy, Explor. Exploit.* 26, 311–325. <https://doi.org/10.1260/014459808787945344>
- Binley, A., Daily, W., Ramirez, A., 1997. Detecting leaks from environmental barriers using electrical current imaging. *J. Environ. Eng. Geophys.* 2 (March), 11–19. <https://doi.org/10.4133/JEEG2.1.11>
- Booth, P.M., 1997. Sellafield site characterisation project: an appraisal of site investigation techniques previously untried at BNFL's sites. Risley, United Kingdom.
- Bowden, R.A., Bumpus, C., Littleboy, A.K., 1998. An overview and update of the site

References

- characterization studies at Sellafield. *Proc. Yorksh. Geol. Soc.* 52, 125–137.
<https://doi.org/10.1144/pygs.52.2.125>
- Bratvold, R.B., Begg, S., 2010. *Making good decisions*. Society of Petroleum Engineers, Richardson, Texas, USA.
- Calendine, S., Rucker, D.F., Fink, J.B., Levitt, M.T., 2011. Automated leak detection of buried tanks using geophysical methods at the Hanford nuclear site, in: *SAGEEP 2011. Annual Meeting of the Environmental and Engineering Geophysical Society*. Charleston, South Carolina.
- Chen, J., Hubbard, S., Peterson, J., Williams, K., Fioren, M., Jardine, P., Watson, D., 2006. Development of a joint hydrogeophysical inversion approach and application to a contaminated fractured aquifer. *Water Resour. Res.* 42, 1–13.
<https://doi.org/10.1029/2005WR004694>
- Chen, J., Hubbard, S.S., Williams, K.H., 2013. Data-driven approach to identify field-scale biogeochemical transitions using geochemical and geophysical data and hidden Markov models: Development and application at a uranium-contaminated aquifer. *Water Resour. Res.* 49, 6412–6424.
<https://doi.org/10.1002/wrcr.20524>
- Chen, J., Hubbard, S.S., Williams, K.H., Ficklin, D.L., 2016. Estimating groundwater dynamics at a Colorado River floodplain site using historical hydrological data and climate information. *Water Resour. Res.* n/a-n/a.
<https://doi.org/10.1002/2015WR017777>
- Chen, J.S., Hubbard, S.S., Gaines, D., Korneev, V., Baker, G., Watson, D., 2010. Stochastic estimation of aquifer geometry using seismic refraction data with borehole depth constraints. *Water Resour. Res.* 46, 16. <https://doi.org/10.1029/2009wr008715>
- Chen, X., Hammond, G.E., Murray, C.J., Rockhold, M.L., Vermeul, V.R., Zachara, J.M., 2013. Application of ensemble-based data assimilation techniques for aquifer characterization using tracer data at Hanford 300 area. *Water Resour. Res.* 49, 7064–7076. <https://doi.org/10.1002/2012WR013285>
- Chen, X., Murakami, H., Hahn, M.S., Hammond, G.E., Rockhold, M.L., Zachara, J.M., Rubin, Y., 2012. Three-dimensional Bayesian geostatistical aquifer characterization at the Hanford 300 Area using tracer test data. *Water Resour. Res.* 48, W06501. <https://doi.org/10.1029/2011WR010675>
- Cooper, S., 1997. *Assessment of the potential for downhole geophysics within the BHP boreholes*. Risley, United Kingdom.
- Cooper, S., Ross, M.O., 2005. *Application and comparative assessment of non-intrusive site characterisation techniques*. Daresbury, United Kingdom.

References

- Daily, W., Ramirez, A., 1995. Electrical resistance tomography during in-situ trichloroethylene remediation at the Savannah River Site. *J. Appl. Geophys.* 33, 239–249. [https://doi.org/10.1016/0926-9851\(95\)90044-6](https://doi.org/10.1016/0926-9851(95)90044-6)
- Daily, W., Ramirez, A., Binley, A., 2004. Remote monitoring of leaks in storage tanks using electrical resistance tomography: Application at the Hanford Site. *J. Environ. Eng. Geophys.* 9, 11–24. <https://doi.org/10.4133/jee9.1.11>
- Day-Lewis, F.D., Singha, K., Binley, A.M., 2005. Applying petrophysical models to radar travel time and electrical resistivity tomograms: Resolution-dependent limitations. *J. Geophys. Res. B Solid Earth* 110, 1–17. <https://doi.org/10.1029/2004JB003569>
- de Barros, F.P.J., Ezzedine, S., Rubin, Y., 2012. Impact of hydrogeological data on measures of uncertainty, site characterization and environmental performance metrics. *Adv. Water Resour.* 36, 51–63. <https://doi.org/10.1016/j.advwatres.2011.05.004>
- de Barros, F.P.J., Rubin, Y., 2008. A risk-driven approach for subsurface site characterization. *Water Resour. Res.* 44, 1–14. <https://doi.org/10.1029/2007WR006081>
- Eddy-Dilek, C.A., Looney, B.B., Hoekstra, P., Harthill, N., Blohm, M., Phillips, D.B., 1997. Definition of a critical confining zone using surface geophysical methods. *Groundwater* 35, 451–462.
- Edwards, L.S., 1977. A modified pseudosection for resistivity and IP. *Geophysics* 42, 1020–1036. <https://doi.org/10.1190/1.1440762>
- Eidsvik, J., Mukerji, T., Bhattacharjya, D., 2015. Value of information in the earth sciences: Integrating spatial modeling and decision analysis. Cambridge University Press, Cambridge.
- Enescu, N., Ahokas, T., Heikkinen, E., Cosma, C., 2004. Integrated Geophysical Characterization of a Hard Rock Site, in: EAGE 66th Conference & Exhibition. Paris, France, pp. 7–10.
- Environment Agency, 2011. Geophysical surveying techniques to characterise a site for a geological disposal facility: A review of recent developments and NDA's proposals.
- Eslick, J.C., Ng, B., Gao, Q., Tong, C.H., Sahinidis, N. V., Miller, D.C., 2014. A framework for optimization and quantification of uncertainty and sensitivity for developing carbon capture systems. *Energy Procedia* 63, 1055–1063. <https://doi.org/10.1016/j.egypro.2014.11.113>
- Feyen, L., Gorelick, S.M., 2005. Framework to evaluate the worth of hydraulic

References

- conductivity data for optimal groundwater resources management in ecologically sensitive areas. *Water Resour. Res.* 41, 1–13. <https://doi.org/10.1029/2003WR002901>
- Flores-Orozco, A., Williams, K.H., Kemna, A., 2013. Time-lapse spectral induced polarization imaging of stimulated uranium bioremediation. *Near Surf. Geophys.* 11, 531–544. <https://doi.org/10.3997/1873-0604.2013020>
- Flores-Orozco, A., Williams, K.H., Long, P.E., Hubbard, S.S., Kemna, A., 2011. Using complex resistivity imaging to infer biogeochemical processes associated with bioremediation of an uranium-contaminated aquifer. *J. Geophys. Res. Biogeosciences* 116, 1–17. <https://doi.org/10.1029/2010JG001591>
- Frangos, W., Ter-Saakian, S., 1996. Resistivity and induced polarization survey at a Russian nuclear waste site. Berkeley, California, United States. <https://doi.org/10.1149/1.2221597>
- Gasperikova, E., Hubbard, S.S., Watson, D.B., Baker, G.S., Peterson, J.E., Kowalsky, M.B., Smith, M., Brooks, S., 2012. Long-term electrical resistivity monitoring of recharge-induced contaminant plume behavior. *J. Contam. Hydrol.* 142–143, 33–49. <https://doi.org/10.1016/j.jconhyd.2012.09.007>
- Gelhar, L., Axness, C., 1983. Three-dimensional stochastic analysis of macrodispersion in aquifers. *Water Resour. Res.* 19, 161–180.
- Gélis, C., Revil, A., Cushing, M.E., Jougnot, D., Lemeille, F., Cabrera, J., de Hoyos, A., Rocher, M., 2010. Potential of electrical resistivity tomography to detect fault zones in limestone and argillaceous formations in the experimental platform of Tournemire, France. *Pure Appl. Geophys.* 167, 1405–1418. <https://doi.org/10.1007/s00024-010-0097-x>
- Gephart, R.E., 2010. A short history of waste management at the Hanford Site. *Phys. Chem. Earth, Parts A/B/C* 35, 298–306. <https://doi.org/10.1016/J.PCE.2010.03.032>
- Gephart, R.E., 2003. A short history of Hanford waste generation, storage, and release. *Pnnl-13605* 1–39.
- Glaser, D.R., Fink, J.B., Levitt, M.T., Rucker, D.F., 2008. A summary of recent geophysical investigations at the Department of Energy Hanford Nuclear Facility, in: 2008 Chapman Conference on Biogeophysics. Portland, Maine.
- Huang, H.-T., 2013. Radionuclide Migration in Low-level Radioactive Waste Disposal at Lan-Yu Site (in Chinese). National Cheng Kung University.
- Johnson, T., Triplett, M., Wellman, D., Northwest, P., 2014. Modeling of electrical resistivity data in the presence of electrically conductive well casings and waste storage tanks, in: WM2014 Conference, March 2 – 6. Phoenix, Arizona, USA, p. 7.

References

- Johnson, T.C., Rucker, D.F., Glaser, D.R., 2015a. Near-Surface Geophysics at the Hanford Nuclear Site, the United States, in: *Treatise on Geophysics*. Elsevier, pp. 571–595. <https://doi.org/10.1016/B978-0-444-53802-4.00205-0>
- Johnson, T.C., Versteeg, R., Thomle, J., Hammond, G., Chen, X., Zachara, J., 2015b. Four-dimensional electrical conductivity monitoring of stage-driven river water intrusion: Accounting for water table effects using a transient mesh boundary and conditional inversion constraints. *Water Resour. Res.* 51, 6177–6196. <https://doi.org/10.1002/2014WR016129>
- Johnson, T.C., Versteeg, R.J., Rockhold, M., Slater, L.D., Ntarlagiannis, D., Greenwood, W.J., Zachara, J., 2012. Characterization of a contaminated wellfield using 3D electrical resistivity tomography implemented with geostatistical, discontinuous boundary, and known conductivity constraints. *Geophysics* 77, EN85. <https://doi.org/10.1190/geo2012-0121.1>
- Johnson, T.C., Versteeg, R.J., Ward, A., Day-Lewis, F.D., Revil, A., 2010. Improved hydrogeophysical characterization and monitoring through parallel modeling and inversion of time-domain resistivity and induced-polarization data. *Geophysics* 75, WA27. <https://doi.org/10.1190/1.3475513>
- Johnson, T.C., Wellman, D.M., 2013. Re-inversion of surface electrical resistivity tomography data from the Hanford Site B-Complex.
- Karaoulis, M., Revil, a., Werkema, D.D., Minsley, B.J., Woodruff, W.F., Kemna, a., 2011. Time-lapse three-dimensional inversion of complex conductivity data using an active time constrained (ATC) approach. *Geophys. J. Int.* 187, 237–251. <https://doi.org/10.1111/j.1365-246X.2011.05156.x>
- Kemna, A., Binley, A.M., Slater, L., 2004. Cross-borehole IP imaging for engineering and environmental applications. *Geophysics* 69, 97–107. <https://doi.org/10.1190/1.1649379>
- Key, K.T., 1977. Nuclear waster tank and pipeline external leak detection systems. Richland, Washington.
- Kim, J.-H., Yi, M.-J., Park, S.-G., Kim, J.G., 2009. 4-D inversion of DC resistivity monitoring data acquired over a dynamically changing earth model. *J. Appl. Geophys.* 68, 522–532. <https://doi.org/10.1016/j.jappgeo.2009.03.002>
- Kimbell, G.S., 1994. The interpretation of gravity and aeromagnetic data for the geological investigation of the Sellafield area, west Cumbria. *Proc. Yorksh. Geol. Soc.* 50, 103–112. <https://doi.org/10.1144/pygs.50.1.103>
- Kowalsky, M.B., Finsterle, S., Peterson, J., Hubbard, S., Rubin, Y., Majer, E., Ward, A., Gee, G., 2005. Estimation of field-scale soil hydraulic and dielectric parameters through joint inversion of GPR and hydrological data. *Water Resour. Res.* 41, n/a-

References

- n/a. <https://doi.org/10.1029/2005WR004237>
- Kowalsky, M.B., Gasperikova, E., Finsterle, S., Watson, D., Baker, G., Hubbard, S.S., 2011. Coupled modeling of hydrogeochemical and electrical resistivity data for exploring the impact of recharge on subsurface contamination. *Water Resour. Res.* 47, W02509. <https://doi.org/10.1029/2009WR008947>
- Kuras, O., Wilkinson, P.B., Meldrum, P.I., Oxby, L.S., Uhlemann, S., Chambers, J.E., Binley, A., Graham, J., Smith, N.T., Atherton, N., 2016. Geoelectrical monitoring of simulated subsurface leakage to support high-hazard nuclear decommissioning at the Sellafield Site, UK. *Sci. Total Environ.* 566–567, 350–359. <https://doi.org/10.1016/j.scitotenv.2016.04.212>
- Kuras, O., Wilkinson, P.B., Meldrum, P.I., Oxby, L.S., Uhlemann, S., Chambers, J.E., Binley, A.M., Graham, J., Dewey, G., Atherton, N., 2014. A trial of 4D Cross-hole electrical resistivity tomography (ERT) for detecting and monitoring subsurface leakage and contaminant transport, supporting the decommissioning of legacy silos at the Sellafield Site, UK, in: WM2014 Conference, March 2 – 6. Phoenix, Arizona, USA.
- Kuras, O., Wilkinson, P.B., Meldrum, P.I., Uhlemann, S., Chambers, J.E., 2015. Results of the GEMS ERT trial and extended baseline measurements at Sellafield. Keyworth.
- Kuras, O., Wilkinson, P.B., White, J.C., Chambers, J.E., Meldrum, P.I., Ogilvy, R.D., 2011. MSSS leak mitigation-leak detection phase 3: Desk study for ERT technology. Keyworth.
- Labrecque, D.J., Yang, X., 2001. Difference inversion of ERT data: a fast inversion method for 3-D in situ monitoring. *J. Environ. Eng. Geophys.* 6, 83–89. <https://doi.org/dx.doi.org/10.4133/JEEG6.2.83>
- Last, G. V, Horton, D.G., 2000. Review of geophysical characterization methods used at the Hanford Site.
- Lean, C., 1998a. The use of surface geophysics in the geological characterisation of Sellafield. Risley, United Kingdom.
- Lean, C., 1998b. TerraDat geophysical site investigation at the buried channel area of Sellafield. Risley, United Kingdom.
- Lee, J., Liu, X., Kitanidis, P.K., Kim, U., Parker, J., Bloom, A., Lyon, R., 2012. Cost optimization of DNAPL remediation at Dover Air Force Base Site. *Groundw. Monit. Remediat.* 48–56. <https://doi.org/10.1111/j1745>
- Leube, P.C., Geiges, A., Nowak, W., 2012. Bayesian assessment of the expected data impact on prediction confidence in optimal sampling design. *Water Resour. Res.*

References

- 48, 1–16. <https://doi.org/10.1029/2010WR010137>
- Liu, X., Lee, J., Kitanidis, P.K., Parker, J., Kim, U., 2012. Value of information as a context-specific measure of uncertainty in groundwater remediation. *Water Resour. Manag.* 26, 1513–1535. <https://doi.org/10.1007/s11269-011-9970-3>
- Minsley, B.J., Sogade, J., Morgan, F.D., 2007. Three-dimensional self-potential inversion for subsurface DNAPL contaminant detection at the Savannah River Site, South Carolina. *Water Resour. Res.* 43, 1–13. <https://doi.org/10.1029/2005WR003996>
- Morrison, H.F., Beckers, A., Lee, K.H., 1987. Measurements of electrical conductivity for characterizing and monitoring nuclear waste repositories. Berkeley, California, United States.
- Murakami, H., Chen, X., Hahn, M.S., Liu, Y., Rockhold, M.L., Vermeul, V.R., Zachara, J.M., Rubin, Y., 2010. Bayesian approach for three-dimensional aquifer characterization at the Hanford 300 Area. *Hydrol. Earth Syst. Sci.* 14, 1989–2001. <https://doi.org/10.5194/hess-14-1989-2010>
- Mwakanyamale, K., Slater, L., Binley, A., Ntarlagiannis, D., 2012. Lithologic imaging using complex conductivity: Lessons learned from the Hanford 300 Area. *Geophysics* 77, E397. <https://doi.org/10.1190/geo2011-0407.1>
- Myers, D.A., Cabbage, B., Brauchla, R., O'Brien, G., Bergeron, M., Henderson, C., 2008a. Surface geophysical exploration of TX-TY tank farms at the Hanford Site: Results of background characterization with ground penetrating radar. RPP-RPT-38104. Richland, Washington.
- Myers, D.A., Rucker, D.F., Levitt, M., Cabbage, B., Henderson, C., 2008b. Surface geophysical exploration of TX-TY tank farms at the Hanford Site: Results of background characterization with magnetics and electromagnetics. RPP-RPT-36893. Richland, Washington.
- Nenna, V., Knight, R., 2013. Demonstration of a value of information metric to assess the use of geophysical data for a groundwater application. *Geophysics* 79, E51–E60. <https://doi.org/10.1190/geo2012-0474.1>
- Nenna, V., Pidlisecky, A., Knight, R., 2011. Informed experimental design for electrical resistivity imaging. *Near Surf. Geophys.* 9, 469–482. <https://doi.org/10.3997/1873-0604.2011027>
- Norton, M.G., Arthur, J.C.R., Dyer, K.J., 1997. Geophysical survey planning for the Dounreay and Sellafield geological investigations. *Geol. Soc. London, Eng. Geol. Spec. Publ.* 12, 335–343. <https://doi.org/10.1144/GSL.ENG.1997.012.01.31>
- Nowak, W., de Barros, F.P.J., Rubin, Y., 2010. Bayesian geostatistical design: Task-

References

- driven optimal site investigation when the geostatistical model is uncertain. *Water Resour. Res.* 46, 1–17. <https://doi.org/10.1029/2009WR008312>
- Nowak, W., Rubin, Y., de Barros, F.P.J., 2012. A hypothesis-driven approach to optimize field campaigns. *Water Resour. Res.* 48, W06509. <https://doi.org/10.1029/2011WR011016>
- Olsson, O., Anderson, P., Gustafsson, E., 1991. PROJECT 9118 Site Characterization and Validation - Monitoring of Saline Tracer Transport by Borehole Radar Measurements, Final Report.pdf. Stockholm.
- Olsson, O., Gale, J.E., 1995. Site assessment and characterization for high-level nuclear waste disposal; results from the Stripa Project, Sweden. *Q. J. Eng. Geol.* 28, 17–30.
- Pacific Northwest National Laboratory, 2016. An Award-Winning Subsurface Software [WWW Document]. URL <https://energyenvironment.pnnl.gov/highlights/highlight.asp?id=2556> (accessed 9.16.19).
- Paté-Cornell, E., Cochran, J.J., Cox, L.A., Keskinocak, P., Kharoufeh, J.P., Smith, J.C., Assessment, F.R., 2010. An introduction to probabilistic risk analysis for engineered systems. *Wiley Encycl. Oper. Res. Manag. Sci.* <https://doi.org/10.1002/9780470400531.eorms0680>
- Ramirez, A., Daily, W., 1996. Detection of leaks in underground storage tanks using electrical resistance methods:1996 results. Livermore, California.
- Ramirez, A., Daily, W., Binley, A., LaBrecque, D., Roelant, D., 1996. Detection of Leaks in Underground Storage Tanks Using Electrical Resistance Methods. *J. Environ. Eng. Geophys.* 1, 189–203. <https://doi.org/10.4133/JEEG1.3.189>
- Ramirez, A.L., Nitao, J.J., Hanley, W.G., Aines, R., Glaser, R.E., Sengupta, S.K., Dyer, K.M., Hickling, T.L., Daily, W.D., 2005. Stochastic inversion of electrical resistivity changes using a Markov Chain Monte Carlo approach. *J. Geophys. Res.* 110, B02101. <https://doi.org/10.1029/2004JB003449>
- Revil, A., Skold, M., Hubbard, S.S., Wu, Y., Watson, D.B., Karaoulis, M., 2013a. Petrophysical properties of saprolites from the Oak Ridge Integrated Field Research Challenge site, Tennessee. *Geophysics* 78, D21–D40. <https://doi.org/10.1190/geo2012-0176.1>
- Revil, A., Wu, Y., Karaoulis, M., Hubbard, S.S., Watson, D.B., Eppheimer, J.D., 2013b. Geochemical and geophysical responses during the infiltration of fresh water into the contaminated saprolite of the Oak Ridge Integrated Field Research Challenge site, Tennessee. *Water Resour. Res.* 49, n/a-n/a. <https://doi.org/10.1002/wrcr.20380>
- Robins, N.S., 1979. Electrical resistivity survey at the Windscale Works, Cumbria.

References

- Oxfordshire, United Kingdom.
- Ross, M., 2004. Consideration of available geophysical techniques for non-intrusive survey of B291 trenches. Sellafield, United Kingdom.
- Rubin, Y., Chen, X., Murakami, H., Hahn, M., 2010. A Bayesian approach for inverse modeling, data assimilation, and conditional simulation of spatial random fields. *Water Resour. Res.* 46, 1–23. <https://doi.org/10.1029/2009WR008799>
- Rucker, D., Levitt, M., O'Brien, G., Henderson, C., 2007. Surface geophysical exploration of B , BX , and BY Tank Farms at the Hanford Site : Results of background characterization with ground penetrating radar.
- Rucker, D.F., 2012. Enhanced resolution for long electrode ERT. *Geophys. J. Int.* 191, 101–111. <https://doi.org/10.1111/j.1365-246X.2012.05643.x>
- Rucker, D.F., Myers, D.A., Cubbage, B., Levitt, M.T., Noonan, G.E., McNeill, M., Henderson, C., Lober, R.W., 2013. Surface geophysical exploration: Developing noninvasive tools to monitor past leaks around Hanford's tank farms. *Environ. Monit. Assess.* 185, 995–1010. <https://doi.org/10.1007/s10661-012-2609-x>
- Sassen, D.S., Hubbard, S.S., Bea, S.A., Chen, J., Spycher, N., Denham, M.E., 2012. Reactive facies: An approach for parameterizing field-scale reactive transport models using geophysical methods. *Water Resour. Res.* 48, 1–20. <https://doi.org/10.1029/2011WR011047>
- Sato, K., 2011. Value of information analysis for adequate monitoring of carbon dioxide storage in geological reservoirs under uncertainty. *Int. J. Greenh. Gas Control* 5, 1294–1302. <https://doi.org/10.1016/j.ijggc.2011.07.010>
- Schmidt, F., Wainwright, H.M., Faybishenko, B., Denham, M., Eddy-Dilek, C., 2018. In Situ Monitoring of Groundwater Contamination Using the Kalman Filter. *Environ. Sci. Technol.* 52, 7418–7425. <https://doi.org/10.1021/acs.est.8b00017>
- Serco/Golder, 2010. Sellafield contaminated land and groundwater management project – geophysical survey – micro-gravity, downhole logging, EM61, GPR and ERI.
- Serco/Golder, 2009. Sellafield contaminated land and groundwater management project – Report for B291 Trench Area investigation.
- Serco/Golder, 2008a. Sellafield contaminated land and groundwater management project – geophysics survey – B291 Trench Area.
- Serco/Golder, 2008b. Sellafield contaminated land and groundwater management project – Geophysical data collection plan.
- Shi, W., 1998. Advanced modeling and inversion techniques for three-dimensional

References

- geoelectrical surveys. Massachusetts Institute of Technology.
- Singha, K., Moysey, S., 2006. Accounting for spatially variable resolution in electrical resistivity tomography through field-scale rock-physics relations. *Geophysics* 71, A25. <https://doi.org/10.1190/1.2209753>
- Slater, L.D., Ntarlagiannis, D., Day-Lewis, F.D., Mwakanyamale, K., Versteeg, R.J., Ward, A., Strickland, C., Johnson, C.D., Lane, J.W., 2010. Use of electrical imaging and distributed temperature sensing methods to characterize surface water-groundwater exchange regulating uranium transport at the Hanford 300 Area, Washington. *Water Resour. Res.* 46, 1–13. <https://doi.org/10.1029/2010WR009110>
- Stenberg, L., 2008. Detailed ground magnetic and resistivity measurements for a potential deep geologic repository for spent nuclear fuel in Oskarshamn, in: Ahlbom, K., Stephens, M. (Eds.), *Investigations of Potential Repository Sites for Spent Nuclear Fuel at Forsmark and Laxemar-Simpevarp, Sweden*. SKB, Stockholm, p. 43.
- Tang, G., D’Azevedo, E.F., Zhang, F., Parker, J.C., Watson, D.B., Jardine, P.M., 2010. Application of a hybrid MPI/OpenMP approach for parallel groundwater model calibration using multi-core computers. *Comput. Geosci.* 36, 1451–1460. <https://doi.org/10.1016/j.cageo.2010.04.013>
- Tartakovsky, D.M., 2013. Assessment and management of risk in subsurface hydrology: A review and perspective. *Adv. Water Resour.* 51, 247–260. <https://doi.org/10.1016/j.advwatres.2012.04.007>
- TERRADAT (UK) LTD., 2012. Geophysical survey to locate subsurface features and services at B38, Sellafield, Cumbria. Cardiff, United Kingdom.
- TERRADAT (UK) LTD., 2004. Geophysical investigations into the subsurface deposits and structures. Cardiff, United Kingdom.
- TERRADAT (UK) LTD., 1998. Geophysical survey trials carried out at Sellafield, West Boundary. Cardiff, United Kingdom.
- Trainor-Guitton, W.J., 2014. A geophysical perspective of value of information: Examples of spatial decisions for groundwater sustainability. *Environ. Syst. Decis.* 34, 124–133. <https://doi.org/10.1007/s10669-013-9487-9>
- Trainor-Guitton, W.J., Caers, J.K., Mukerji, T., 2011. A Methodology for Establishing a Data Reliability Measure for Value of Spatial Information Problems. *Math. Geosci.* 43, 929–949. <https://doi.org/10.1007/s11004-011-9367-0>
- Trainor-Guitton, W.J., Hoversten, G.M., Ramirez, A., Roberts, J., Juliusson, E., Key, K., Mellors, R., 2014. The value of spatial information for determining well placement: A geothermal example. *GEOPHYSICS* 79, W27–W41.

References

- <https://doi.org/10.1190/geo2013-0337.1>
- Trainor-Guitton, W.J., Mukerji, T., Knight, R., 2013a. A methodology for quantifying the value of spatial information for dynamic Earth problems. *Stoch. Environ. Res. Risk Assess.* 27, 969–983. <https://doi.org/10.1007/s00477-012-0619-4>
- Trainor-Guitton, W.J., Ramirez, A., Yang, X., Mansoor, K., Sun, Y., Carroll, S., 2013b. Value of information methodology for assessing the ability of electrical resistivity to detect CO₂/brine leakage into a shallow aquifer. *Int. J. Greenh. Gas Control* 18, 101–113. <https://doi.org/10.1016/j.ijggc.2013.06.018>
- Truex, M.J., 2018. Groundwater and Vadose Zone Remedy Management Strategies at DOE Sites, in: SERDP ESTCP Symposium. Washington, D.C.
- Truex, M.J., Johnson, T.C., Strickland, C.E., Peterson, J.E., Hubbard, S.S., 2013. Monitoring Vadose Zone Desiccation with Geophysical Methods. *Vadose Zo. J.* 12. <https://doi.org/10.2136/vzj2012.0147>
- Tsang, C.-F., Neretnieks, I., Tsang, Y., 2015. Hydrologic issues associated with nuclear waste repositories. *Water Resour. Res.* 51, 1–50. <https://doi.org/10.1002/2014WR016259>
- Varouchakis, E.A., Palogos, I., Karatzas, G.P., 2016. Application of Bayesian and cost benefit risk analysis in water resources management 534, 390–396.
- Wainwright, H.M., Chen, J., Sassen, D.S., Hubbard, S.S., 2014. Bayesian hierarchical approach and geophysical data sets for estimation of reactive facies over plume scales. *Water Resour. Res.* 50, 4564–4584. <https://doi.org/10.1002/2013WR013842>
- Wainwright, H.M., Flores Orozco, A., Bücker, M., Dafflon, B., Chen, J., Hubbard, S.S., Williams, K.H., 2016. Hierarchical Bayesian method for mapping biogeochemical hot spots using induced polarization imaging. *Water Resour. Res.* 52, 533–551. <https://doi.org/10.1002/2015WR017763>
- Wallin, E.L., Johnson, T.C., Greenwood, W.J., Zachara, J.M., 2013. Imaging high stage river-water intrusion into a contaminated aquifer along a major river corridor using 2-D time-lapse surface electrical resistivity tomography. *Water Resour. Res.* 49, 1693–1708. <https://doi.org/10.1002/wrcr.20119>
- Wang, J., Chen, L., Su, R., Zhao, X., 2018. The Beishan underground research laboratory for geological disposal of high-level radioactive waste in China: Planning, site selection, site characterization and in situ tests. *J. Rock Mech. Geotech. Eng.* 10, 411–435. <https://doi.org/10.1016/j.jrmge.2018.03.002>
- Watson, D.B., Doll, W.E., Gamey, T.J., Sheehan, J.R., Jardine, P.M., 2005. Plume and lithologic profiling with surface resistivity and seismic tomography. *Ground Water* 43, 169–77. <https://doi.org/10.1111/j.1745-6584.2005.0017.x>

References

- Webster, D.S., Proctor, J.F., Marine, I.W., 1970. Two -Well Tracer Test in Fractured Crystalline Two-Well Tracer Test in Fractured Crystalline. Washington DC.
- Williams, B.A., Thompson, M.D., Miller, S.F., 2012a. Integrated surface geophysical investigation results at Liquid Effluent Retention Facility, 200 East Area, Washington. Richland, Washington.
- Williams, B.A., Thompson, M.D., Miller, S.F., 2012b. Interpretation and integration of seismic data in the Gable Gap. Richland, Washington.
- Williams, B.A., Thompson, M.D., Miller, S.F., 2012c. Land streamer and gimbaled geophones phase II-200 Areas: high-resolution seismic reflection suvey at the Hanford Site. Richland, Washington.
- Williams, B.A., Thompson, M.D., Miller, S.F., 2012d. Seismic reflection investigation at the Liquid Effluent Retention Facility, 200 East Area, Hanford Site Richland, Washington. Richland, Washington.
- Williams, K.H., Kemna, A., Wilkins, M.J., Druhan, J., Arntzen, E., N'Guessan, A.L., Long, P.E., Hubbard, S.S., Banfield, J.F., 2009. Geophysical Monitoring of Coupled Microbial and Geochemical Processes During Stimulated Subsurface Bioremediation. *Environ. Sci. Technol.* 43, 6717–6723. <https://doi.org/10.1021/es900855j>
- Williams, M.D., Rockhold, M.L., Thorne, P.D., Chen, Y., 2008. Three-dimensional groundwater models of the 300 Area at the Hanford Site, Washington State. Richland, Washington.
- Wu, W.M., Carley, J., Fienen, M., Mehlhorn, T., Lowe, K., Nyman, J., Luo, J., Gentile, M.E., Rajan, R., Wagner, D., Hickey, R.F., Gu, B., Watson, D., Cirpka, O. a., Kitanidis, P.K., Jardine, P.M., Criddle, C.S., 2006. Pilot-scale in situ bioremediation of uranium in a highly contaminated aquifer. 1. Conditioning of a treatment zone. *Environ. Sci. Technol.* 40, 3978–3985. <https://doi.org/10.1021/es051954y>
- Zhang, Y.-K., Neuman, S.P., 1990. A quasi-linear theory of non-Fickian and Fickian subsurface dispersion: 2. Application to anisotropic media and the Borden site. *Water Resour. Res.* 26, 903–913. <https://doi.org/10.1029/WR026i005p00903>
- Zhao, Z., 2000. Application of geophysical exploration to site selection for waste disposal of the Guangdong nuclear power plant. *Geol. Prospect.* (in Chinese) 36, 51–53.
- Zheng, J., Zhang, Z., Dong, L., 2000. Environmental geophysics and its advance. *Adv. Earth Sci.* (in Chinese) 15, 40–47.

3. Sources of uncertainties in electrical resistivity tomography (ERT): a review

Manuscript prepared for journal submission as **Tso, C.-H.M.**, Kuras, O., Binley, A. (201x) Sources of uncertainties in electrical resistivity tomography (ERT): a review

Abstract

The use of near-surface geophysics methods has become prevalent in many areas, including environmental investigations, engineering, agriculture, archaeology, forensic science, mineral exploration and hydrogeology. With improvements in infrastructure, equipment, and modelling software and tools, near-surface geophysical techniques have become more accessible. These developments allow the methods to be readily used, in some cases, with limited background understanding of the theoretical principles and limitations.

Like any other kind of measurement or interpretation, the near-surface geophysical methods are subject to errors and uncertainties. To maximise the benefits of such methods and reduce over-interpretation or failure to capture the maximum information content they can provide, it is necessary to understand and manage the various sources of errors and uncertainties, particularly to quantify them and assess how they propagate through the various stages of interpretation. Using electrical resistivity tomography (ERT) as an example, we review the various sources of uncertainty and discuss approaches to handle them in practice. These sources include measurement errors, inversion, petrophysical relationships, and application-specific uncertainties.

In this review, we outline the advances made in characterizing and reducing uncertainty along the various stages of the workflow and reveal that most approaches focus their effort at a particular stage and rarely considers multiple sources of uncertainties. Potential directions for future research includes: (i) reducing overall prediction uncertainty through experimental design optimization; (ii) value of information that considers uncertainty in the entire workflow; (iii) consider jointly multiple sources of uncertainty and their effect downstream of the workflow; (iv) propose alternative workflows to bypass certain high uncertainty steps in certain applications.

1) Introduction

Geophysical methods often provide a cost-effective and relatively rapid means of collecting data on the properties of subsurface. The use of near-surface geophysics methods has become prevalent and widely accessible due to improvements in infrastructure, equipment, and modelling tools. These developments allow the methods to be readily used, in some cases, with limited background understanding of the theoretical principles and limitations. This draws many new users from different fields. The geophysical properties returned from such surveys are often not the quantity of interest (QoI) in these applications. Rather, the geophysical properties are used as a proxy or are then converted to the QoI. For example, an electrical resistivity tomography (ERT) survey returns a (smoothed or blocky) image of electrical resistivity while monitoring the movement of a saline tracer (e.g. [Cassiani et al., 2006](#); [Kemna et al., 2004](#); [Wilkinson et al., 2010b](#)). However, a hydrologist is interested in the soil moisture content or solute concentration, which are converted from resistivity using petrophysical relationships. Likewise, time-lapse resistivity images during CO₂ injection monitoring needs to be converted to changes in CO₂ concentrations ([Carrigan et al., 2013](#); [Doetsch et al., 2013](#); [Schmidt-Hattenberger et al., 2016](#); [Yang et al., 2015](#)).

Like any other kind of measurement or interpretation, the use of near-surface geophysics involves errors and uncertainties. To maximise the benefits of using near-surface geophysics there is a need, therefore, to understand and manage the various sources of errors and uncertainties, in particular to quantify them and assess how they propagate through the various stages of interpretation. The issue of uncertainty in near-surface geophysics has become more relevant in recent years because these methods have been increasingly used in a quantitative manner for prediction of properties or state variables, or for decision making after being converted to QoIs. A comprehensive appraisal of their various sources of uncertainties and their impact on making predictions and decision making is desperately needed.

We focus our review on ERT, one of the most commonly used near surface geophysical methods, with an emphasis on hydrogeophysics. In general, an ERT survey follows the following five-step workflow: experimental design (i.e. desk study),

data collection, inversion, interpretation, and prediction (Figure 1). While this serves as a pipeline where information is passed along from measurements to prediction, it also allows the propagation of uncertainties along it. Each part of the workflow presents its own sources of uncertainties. Therefore, our review is organized as follows. We will first discuss measurement and data errors in section 2 and inversion in section 3. We will then discuss interpretation of ERT results (section 4) before revisiting inversion, this time focusing on incorporation of auxiliary information (section 5), which is followed by a discussion on experimental design and emerging methods. We then offer some conclusions and recommendations. Our review is limited to discussing the various sources of uncertainties along the ERT workflow. Specialized reviews on selected topics are available: for example, electrical imaging (Falzone et al., 2018), time-lapse electrical imaging (Singha et al., 2015), geophysical imaging for surface water-groundwater interaction and the critical zone (McLachlan et al., 2017; Parsekian et al., 2015), landslide monitoring (Whiteley et al., 2019), and soil structure mapping (Romero-Ruiz et al., 2018). A more general review on the uncertainty quantification in hydrogeology and hydrogeophysics can be found in Linde et al. (2017).

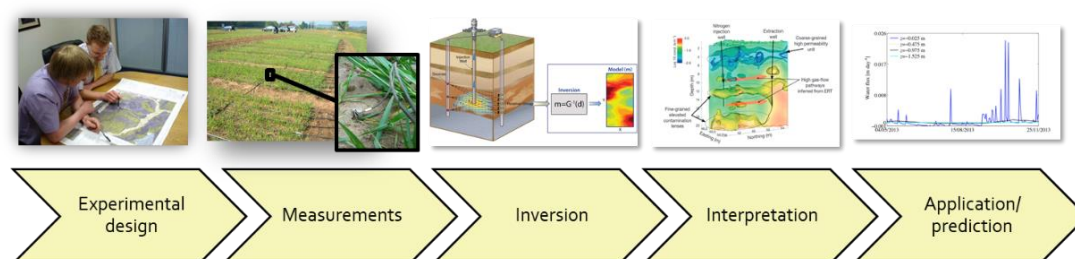


Figure 1 Various sources of errors and uncertainties propagate through the ERT workflow (Binley et al., 2015; Tran et al., 2016; Truex et al., 2013a). The workflow begins with experimental design, where the objectives and details of the field campaign are laid out. It progresses to data collection in the field using a data acquisition system. Then the data is inverted to obtain results in a usable format for interpretations and discussions. Finally, the findings are used for decision making or prediction of future events.

2) Measurement and data errors

In most ERT inversion approaches an objective function incorporating a weighted misfit is used, allowing data value to be inversely weighted according to their errors. It is important to recognise that such errors are not just measurement errors – they

should also recognise modelling errors due to imperfections of the forward model to represent the physics of electrical current flow.

2.1. Measurement errors and data quality

Measurement errors are often ignored (or poorly estimated) and yet they propagate through the workflow. There are three ways to quantify measurement errors: (i) stacking errors, which is returned by the ERT equipment based on averaging the voltage signal caused by the injection of a low frequency alternating current; (ii) repeatability errors, which are obtained by repeating the measurement sequence; (iii) reciprocal errors, which are obtained by repeating measurement sequence but the current and potential electrodes are swapped.

If we follow the classical approach and consider that all measurement errors follow a normal distribution (i.e. assuming the measurements are independent and identically distributed (i.i.d.) random variables and follow the central limit theorem), then, for a given electrode quadrupole, each of the error quantities we obtain is only a point on the normal distribution. Therefore, these errors need to be fitted into an error model to predict the error weights to be used in an inversion, and also to identify any outlier data that one may wish to discard (or, ideally, repeat after addressing the source of error, e.g. high contact resistance). Most error models recognize the proportionality effect of ERT transfer resistance data, meaning the magnitude of the error in a transfer resistance should be more or less proportional to the magnitude of the measurement. It is important to note that such information on error trends cannot be established from measurements expressed as apparent resistivity, since the measurements (and associated errors) are scaled according to a geometrical factor. The simplest transfer resistance error model, therefore, is a straight line between the transfer resistance and the measurement errors (or variances) recorded (Binley et al., 1995; Slater et al., 2000). This may be done in the linear, semi-log, or log-log space. The scatter in such a data-error plot from such a process can make error model determination challenging. To alleviate this issue, the data-error pairs may be grouped into logarithmically equally distributed bins of transfer resistance before fitting (Koestel et al., 2008). It is normal to consider measurement errors as uncorrelated. Recognizing the different electrodes

used in a ERT survey may contribute differently to measurement errors; [Tso et al. \(2017\)](#) devised a linear mixed effect model to fit a linear model to the errors, while using the electrode number as an additional grouping variable.

There has been other studies of specific ERT applications focussed on improving data quality. For example, [Deceuster et al. \(2013\)](#) developed an algorithm to automatically detect changes in electrode contact properties for long-term permanent ERT monitoring surveys. [Mitchell and Oldenburg \(2016\)](#) developed a new data quality control methodology for large ERT datasets to identify and characterize highly contaminated data from different noise sources. [Lesparre et al. \(2017\)](#) suggested when performing difference inversion on time-lapse data (see section 3.4 for details), reciprocal errors should be computed using difference in data between time steps. [Wilkinson et al. \(2008\)](#) identified some electrode configurations that are highly sensitive to geometric displacement in crosshole surveys.

One practical concern is that whether different ERT equipment gives comparable response and whether their inverted resistivity results agree. The study of [Parsekian et al. \(2017\)](#) compared six commercially available ERT equipment on the same line of electrodes and showed that they give statistically similar apparent resistivity results. They also showed by measuring the full waveform of a 4-electrode array that systematic errors might be introduced due to poor electrode contact and instrument-specific recording settings. In practice, some sources of systematic errors, such as incorrectly swapping the connection of two electrodes, may be identified and corrected in the data processing stage. In spite of the equipment used, at least one error estimate should be recorded for error modelling and uncertainty propagation.

2.2. Forward modelling errors

In most ERT applications, current flows are not modelled analytically but are approximated by finite difference or finite element models. Both methods require discretization in space. The quality of the mesh (i.e. discretization) affects the quality of the modelling of current flow and the discrepancy between the data generated by the forward model and analytical solution (usually for a homogeneous domain) is a forward modelling error. This can be especially important for surface surveys

conducted in areas with rough or uneven topography (e.g. slopes). In general, the mesh should be highly refined near electrode locations since the potential gradient is highest. In field studies, the mesh should also extend laterally and downwards from the survey area to satisfy the infinite earth assumption, or appropriate accounting should be made. Forward modelling errors can also exist due to the effect of 3-D variability not accounted for in a 2-D representation. Resistivity variation orthogonal to the survey line (in a 2-D survey) can influence measurements but will not be correctly modelled in a 2-D model. An example of this is where an ERT survey is used to monitor the migration of a solute plume. Another example of 3-D effects is a borehole used for deployment of electrodes in a cross-borehole configuration. [Nimmer et al. \(2008\)](#) demonstrate the various scenarios where 3-D effects may be dominant in 2-D borehole ERT studies (Figure 2): large diameter boreholes, borehole backfills with contrasting conductivities to the formation, non-centered targets, and heterogeneity outside the imaging plane. [Doetsch et al. \(2010a\)](#) cautioned against the potential borehole-fluid effects in borehole ERT studies, especially for shorter dipole spacing. [Wagner et al. \(2015a\)](#) suggested using an explicit discretization of the borehole completion to mitigate borehole-related effects for CO₂ monitoring. Large forward modelling error is most likely to occur in media containing complex fracture networks. To account for this issue, a number of authors have proposed discrete fracture forward models as an alternative ([Beskardes and Weiss, 2018](#); [Demirel et al., 2019](#); [Roubinet and Irving, 2014](#)) to conventional finite element forward models. Electrode position errors are also known to contribute to ERT data errors ([Oldenborger et al., 2005](#)), with recent work focusing on accounting for movement of electrodes in landslide studies ([Wilkinson et al., 2016, 2010a](#)). A further source of forward modelling error is failure to treat electrodes as non-point sources or sensors, which can be significant for small scale studies.

Inversion

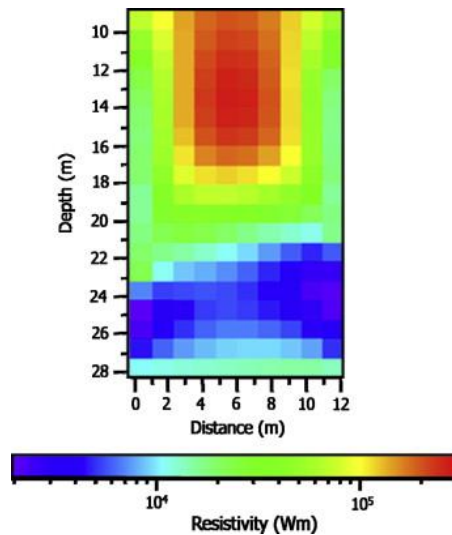


Figure 2: Example of 3D borehole effects in 2D inversion reported in Nimmer et al. (2008), which shows the 2.5D inversion results from Slater et al. (1997). The heavily fractured zone at around 25-m depth can be seen as a low resistivity contrast to the background, but the large high resistivity ($>2 \times 10^5 \Omega \text{ m}$) in the centre of the image appears to be a result of the 2D resistivity model compensating for the low resistivity along the borehole.

3) Inversion

In order to convert raw geophysical measurements (e.g. transfer resistances or apparent resistivities) into useful products to interpret (e.g. spatial distribution of electrical resistivity), data have to be converted to some parameter distribution that can reproduce the measured data using a forward problem that describes the underlying geophysical process, i.e. inversion. Inversion almost always suffer from ill-posedness: Hadamard (1902) states that a well-posed problem must: (1) have a solution, (2) the solution is unique, and (3) the solution's behaviour changes continuously with the initial conditions. Consequently, identifying a solution in the parameter space is challenging.

When analysing a geophysical inverse problem, obtaining an optimal model is usually not sufficient (Shi, 1998). Normally we also wish to have an estimation of uncertainties and resolutions in the information content of the images. In other words, we wish to know to what degree the inversion results represent the true (unknown) structure. Any inversion procedure is considered to be incomplete without any uncertainty or resolution analysis (*ibid.*). Taking a multi-hypothesis viewpoint, one

would also hope to use geophysical data to falsify or corroborate hydrological models (Linde, 2014). The Popper-Bayes philosophy proposed by Tarantola (2006) even argues that data should be used *first* to falsify models. Regrettably, the above tasks have rarely been undertaken due to heavy computational demand, difficulty in defining and segregating sources of uncertainty, and the lack of framework to do so.

For most geophysical applications, the goal is to estimate spatial variability and patterns of geophysical properties. This is challenging because of ill-posedness and this is addressed either by regularization or computationally intensive Bayesian inversion.

3.1. Regularized Inversion

The most common approach to tackling the problem of ill-posedness is to use a Tikhonov-type regularization function, which makes such problems solvable by minimizing the roughness of an image. Not surprisingly, the resultant images are smooth. Philosophically, this approach can be considered as using an Occam's razor or adopting the law of parsimony, which argues "among competing hypotheses, the one with the fewest assumptions should be selected" (note that "use the smoothest image" is a strong assumption). This philosophy can be problematic in geophysical inversion because maximum smoothness is often not justified, for example, in fractured or layered systems, or when the subsurface is stimulated, e.g. by solute injection.

To obtain the baseline resistivity structure, we seek to find a model solution that minimizes the following objective function:

$$\Phi = \Phi_d + \Phi_m = (d - F(m))^T W_d^T W_d (d - F(m)) + \alpha m^T R_m m \quad (1)$$

where d are the data (e.g. measured apparent resistivities), $F(m)$ is the set of simulated data using the forward model and estimated parameters m . W_d is a data weight matrix, which, if we consider the uncorrelated measurement error case and ignore forward model errors, is a diagonal matrix with entries equal to the reciprocal of the errors of each measurement. Forward modelling errors are also added to the diagonal of W_d . α

is the scalar regularisation factor, while R_m is a roughness matrix that describes the spatial connectedness of the parameter cell values.

Using a Gauss-Newton procedure (see derivation in [Appendix 1](#)), the above is solved iteratively using the following solution:

$$(J^T W_d^T W_d J + \alpha R_m) \Delta m = J^T W_d^T W_d (d - F(m)) - \alpha R_m m_k \quad (2)$$

$$m_{k+1} = m_k + \Delta m$$

where J is the Jacobian (or sensitivity) matrix, given by $J_{i,j} = \partial d_i / \partial m_j$; m_k is the parameter set at iteration k ; and Δm is the parameter update at iteration k . The derivation of equation (2) can be found in the appendix. For the case of ERT, the inverse problem is typically parameterized using log-transformed resistivities. The computation of the Jacobian (or sensitivity) matrix J can be a computationally demanding task. Adjoint-state methods ([Skyes et al., 1985](#)) are normally applied to greatly improve the computation of sensitivity matrices by efficiently computing the gradient. Massive improvements have also been made in terms of computational power. Highly parallelized codes (e.g. [Johnson et al., 2010](#)) have been developed to greatly speed up computation by splitting matrix computations across multiple nodes.

3.2. Image appraisal

The model resolution matrix (\mathbf{R}) is a matrix derived from the forward operator of an inverse problem, which describes the quality of mapping in the model space. It is given by:

$$\mathbf{R} = (J^T W_d^T W_d J + \alpha W_m^T W_m)^{-1} J^T W_d^T W_d J \quad (3)$$

A well-posed inverse problem would have a model resolution matrix that is a diagonal matrix of 1. Strictly speaking, \mathbf{R} can only be derived for linear inverse problems. For weakly non-linear problems, it is common practice to approximate \mathbf{R} by linearization. Many methods have been proposed to evaluate the attributes of \mathbf{R} for image appraisal. [Ramirez et al. \(1995\)](#) used the diagonal elements of \mathbf{R} as estimates of spatial resolution of ERT images for cross-hole ERT surveys. More recently, [Friedel \(2003\)](#) used the concept of averaging kernels (i.e. truncated singular value

decomposition) to analyse attributes of \mathbf{R} . [Alumbaugh and Newman \(2000\)](#) analysed individual columns of \mathbf{R} (also termed as PSFs for Point Spread Functions) in order to estimate the spatial variation of the resolution in the horizontal and vertical directions for 2-D and 3-D electromagnetic conductivity inversions. Their study was later extended by [Oldenborger and Routh \(2009\)](#) to detect artefacts and study model dependence of resolution. [Day-Lewis and Lane \(2004\)](#) and [Day-Lewis et al. \(2005\)](#) used \mathbf{R} combined with random field averaging and spatial statistics of the geophysical property to predict the correlation loss between geophysical properties and hydrological parameters. They showed that the correlation varies greatly within the tomogram and direct application of petrophysical models to tomograms may yield misleading estimates of hydrological properties. [Caterina et al. \(2013\)](#) reviewed the use of \mathbf{R} for image appraisal and edge detection techniques and proposed a new image appraisal procedure that combines both methods. More details on edge detection is given in section 4.1.

The computation of \mathbf{R} is very expensive ([Nolet et al., 1999](#); [Oldenborger et al., 2007](#)) as it solves for the inverse of a matrix that contains the sums and products of roughness and sensitivity matrices. \mathbf{R} is a full matrix so sparse matrix solvers cannot be used to improve computation efficiency. Alternative approaches are taken to estimate resolution (or a proxy) at a considerably lower cost: some uses data error-weighted cumulative sensitivity ([Kemna, 2000](#)), while other uses the depth-of-investigation (DOI) concept ([Oldenburg and Li, 1999](#)). The latter essentially compares how different the estimates are given two different prior models. These approaches have inherent problems: for the prior, high sensitivity is not always correlated with good resolution, while for the latter the DOI evaluates only a small subspace of \mathbf{R} and often sends false alarms of high or low resolutions.

Commonly used Tikhonov-type methods (i.e. regularizations), although sufficient to produce a mathematically unique solution, do not really eliminate uncertainty ([Kitanidis, 2011](#)). Their estimates are associated with errors, but these errors are only measures of the discrepancy between the forward model and the “true”

model, which does not contain much information on their uncertainty. Since the model is deterministic, model structure uncertainty is assumed to be negligible.

In most practical cases, there exists information that may be helpful to better solve an inverse problem in addition to the measurements. For example, the layering of the subsurface from regional scale geological studies may be helpful to improve estimates from a local ERT studies. Strictly speaking, such features cannot be incorporated to the deterministic framework because unlike Bayesian methods, there is no way within this framework to incorporate information that is not described by the inverse model. The only option is to introduce some bias to the regularizations. For example, one may force stronger regularization in one direction than the others, which can be achieved at various degree of sophistication (Elwaseif and Slater, 2012; Farquharson, 2008; Günther et al., 2006; Lelièvre and Farquharson, 2013). One may even remove regularization in a certain region (e.g. Doetsch et al., 2012a; Johnson et al., 2012b), such decision is usually informed from other data sources such as ground penetrating radar (GPR) reflection data. This approach is common and practical as it is a simple way to improve the estimates. In many cases, different regularization makes dramatic changes in the estimate. An alternative to incorporate *a priori* geological information is to use geostatistical regularization operators, which has recently been extended to irregular mesh (Jordi et al., 2018). Sometimes regularization information comes in the form of structural orientation information, which a recent study has offered a couple of strategies to incorporate them in regularized inversion (Ross, 2004). The problem with *any* regularization in deterministic inversion is that it is difficult to evaluate whether its choice is justified. Even though the computation of sensitivity and resolution matrix incorporates the regularization, these two measures only describe the mapping of data on the model space. Again, a deterministic model assumes there is no model uncertainty, which in many case this assumption is not justified.

A common misconception is to equate improved resolution to uncertainty reduction—the two are not necessarily related. It is common in the literature to use “uncertainty” and “resolution” interchangeably, as if they are the exact opposite. Generally, resolution of an *image* is referred to its quality or its sharpness or its ability

to identify features. Some geophysical literature, however, refers resolution analysis to the analysis of non-uniqueness and uncertainty of solutions to inverse problems (Gouveia and Scales, 1997; Mosegaard, 1999). Such a definition originates from the Backus-Gilbert method (Backus and Gilbert, 1970, 1968)—the first attempt to quantify uncertainty in geophysics because this method poses the inverse problem as finding the optimal trade-off between variance (i.e. a measure for uncertainty) and spread (i.e. a measure for spatial resolution). Subsequent articles are often not very clear whether they are referring to the resolution of the recovered *image* (i.e. or model) or that of the *inverse problem*. Even though subsequent work does not always link spatial resolution and uncertainty, this confusion in terminology gives the wrong impression that the two are necessarily the same. As an illustration of the problem, it is possible to get a very sharp image of the subsurface properties but not know whether they are artefacts or true features. Perhaps more critically, the sharper images may not change our ability and confidence to answer the scientific questions of interest. On a related note, the model resolution matrix (\mathbf{R}) in geophysical inverse theory (Menke, 1989) is a measure of mapping information from the data space to the model space. A more diagonal \mathbf{R} only means that such mapping is better. In the most extreme case, the subsurface can be treated as homogeneous, making the *inverse problem* well-posed and thus well-resolved but such formulation of the inverse problem will produce an *image* that does not show any features of interest. Also, the computation of \mathbf{R} requires the error level of each data point to be known. Therefore, care must be taken to relate improved resolution and uncertainty reduction. Nevertheless, the use of \mathbf{R} is very useful to guide and optimize geophysical survey design, which will be discussed in section 6.1.

Another metric to consider the uncertainty of inversion results is through the examination of the posterior model covariance matrix \mathbf{MCM} . There are two methods to obtain the \mathbf{MCM} . The first one is through computing it from the sensitivity matrix obtained in the linearized inversion equations itself (Alumbaugh and Newman, 2000; Ruggeri et al., 2014), which is given by

$$\mathbf{MCM} = (J^T W_d^T W_d J + \alpha W_m^T W_m)^{-1} \quad (4)$$

The second method is to perturb the data with its noise level and run Monte Carlo simulations of the inversion (Aster et al., 2005; Tso et al., 2017). The **MCM** is given by

$$\mathbf{MCM} = \frac{\mathbf{A}^T \mathbf{A}}{q} \quad (5)$$

where q is the number of realizations and rows of \mathbf{A} contains the difference between the model estimate of each realizations and the average model. The diagonal terms are the variances of the estimated model parameters, while the off-diagonal terms represent smoothing between pairs of parameters. Examination of the **MCM** can provide insights to the uncertainty trade-off among different model parameters. Notice that this method tends to return low uncertainty estimates in low resolution areas (e.g. away from electrodes). The perturbed measurements mostly affect the high-resolution region while the low-resolution regions are mainly controlled by regularization, which causes the latter to show low variability. A variant of the Monte Carlo approach is the data kit inversion (Fernández-Muñiz et al., 2019) which borrows the idea of random sampling with replacement from bootstrapping. Instead of using the entire dataset for inversion in each realization, a random subset of random size is drawn at each realization. A similar idea of using bootstrapping for uncertainty quantification was applied to the CO₂ saturation samples derived directly from time-lapse ERT at the Cranfield Pilot Site (Yang et al., 2014).

Uncertainty quantification of resistivity models recovered from deterministic methods is one of the most poorly understood issues in geophysics. Only an inversion based on a statistical approach provides a systematic framework to quantify such uncertainties (Pankratov and Kuvshinov, 2015).

The regularized inversion suffers a number of shortcomings. Ideally, our goal is not to obtain a unique solution (i.e. usually the smoothest model), but all the possible models. In the next section, we change philosophy and introduce a number of other approaches to invert ERT data.

3.3. Global optimization approaches and Bayesian inversion

Regularized inversion smooths the model space to arrive at a single solution which is a local minimum. This solution may not be a global minimum of the objective function. In this case, global optimization approaches can be useful. This is usually achieved by Monte Carlo methods such as particle swarm optimization or particle filter (Fernández-Martínez et al., 2019). The advantage of these methods is that unlike regularized inversion, it does not require the gradient of the problem, thus it does not require the objective function to be differentiable nor the computation of the Jacobian matrix.

Bayesian inversion relies on Bayes rule to relate prior model probabilities $P(m)$ to posterior ones $P(m|\tilde{d})$ by a likelihood function $L(m|\tilde{d}) = P(\tilde{d}|m)$ given observed data \tilde{d} :

$$P(m|\tilde{d}) = \frac{P(m)P(\tilde{d}|m)}{P(\tilde{d})} \quad (6)$$

Assuming Gaussian probabilities, the likelihood function becomes

$$L(m|\tilde{d}) \propto \exp\left(-\frac{1}{2}(d - \mathbf{G}(m))^T C_{dd}^{-1}(d - \mathbf{G}(m))\right) \quad (7)$$

where $\mathbf{G}(m)$ is the forward model, while the *a priori* model distribution becomes

$$P(m) \propto \exp\left(-\frac{1}{2}(m - m_{prior})^T C_M^{-1}(m - m_{prior})\right) \quad (8)$$

where C_{DD}^{-1} and C_M^{-1} are the data and model covariance matrices respectively. The maximum *a posteriori* (MAP) solution m_{MAP} is commonly computed, and it is where the following objective function is minimized:

$$m_{MAP} = (d - \mathbf{G}(m))^T C_{dd}^{-1}(d - \mathbf{G}(m)) + (m - m_{prior})^T C_M^{-1}(m - m_{prior}) \quad (9)$$

The prior or model regularization is often simplified by replacing C_m with a matrix that quantifies the first derivative of the proposed model (flatness), the second derivative (roughness) or its deviation from m_{prior} (damping) multiplied by a model regularization weight. Notice that it is common practice for both the deterministic and the Bayesian approach to apply model regularizations. However, they have important distinctions. For the deterministic approach, regularization is applied directly to the

estimated model. For the Bayesian approach, regularization is through the probability density of the prior model assumed. Note that although there is striking resemblance between the formulation of Tikhonov regularization and that of Bayesian MAP inference and perhaps the solutions obtained are similar, the goals and interpretations of the two methods are rather different (Shi, 1998). The former determine maximum model smoothness that allows for data fitting, while the latter sample a probability distribution of models that are consistent with both the data and prior information. In fact the regularizing terms of the two (i.e. $m^T R_m m$ and C_M^{-1}) can never be equal because the inverse of $m^T R_m m$ is ill-posed.

Similar to the resolution matrix in deterministic methods, the resolution of the inverse model is given by the posterior covariance matrix (Tarantola, 2005). However, it is rarely computed because to define it often requires assumption such as Gaussian prior probability density of the model, and linear relationship between model parameters and data. Recently, Gunning et al. (2010) shows that resolution of controlled-source electromagnetic (CSEM, a type of CSAMT method) data can be inferred by either hierarchical models with free parameters for effective correlation lengths (“Bayesian smoothing”), or model-choice frameworks applied to variable resolution spatial models (“Bayesian splitting/merging”) (Kaipio and Somersalo, 2006). Such evaluation of resolution for Bayesian inversion, however, has never been done for near-surface geophysics applications.

Moving beyond the MAP solution, a major challenge for applying Bayesian inversion rigorously is the evaluation of posterior distribution. In many cases, one needs to approximate the full posterior probability distribution. Markov chain Monte Carlo methods (MCMC) build Markov chains in the parameter space formed of a sequence of random variables that are drawn proportional to the posterior distribution (i.e. importance sampling). Although many samples (or in many cases, model runs) are needed, it nonetheless provides a means to sample high dimension and very complicated posterior distributions accurately. More importantly, they allow alternative model estimates to be identified, compared, ranked, and rejected. The posterior distribution is obtained when a chain “forgets” its initial states and converge

to a unique and stationary distribution. With some simplifications, the algorithm to construct a McMC chain is outlined in Figure 3.

For geophysical applications, since complex model proposals are not described by a functional form, the extended Metropolis rule (Mosegaard and Tarantola, 1995) is often used to determine the acceptance probability α :

$$\alpha = \min \left\{ 1, \frac{L(m_{prop}, \eta | \vec{d})}{L(m_{curr}, \eta | \vec{d})} \right\} \quad (10)$$

For more information on the Bayesian approach and McMC, the readers are referred to Brunetti (2019).

-
1. Randomly select a point in the model space as the initial position, m_0 . Decide on the total number of $nstep$ steps to run.

FOR $i = 1:nstep$

2. Set $m_{curr} = m_{i-1}$
3. Propose a random move in the parameter space to generate m_{prop}
4. Draw a value u from the uniform distribution between 0 and 1, $U(0,1)$
5. Accept or reject m_{prop} based on an acceptance probability α : if $U < \min(1, \alpha)$ then m_{prop} is accepted and the chain moves to the new position, $m_i = m_{prop}$; otherwise, m_{prop} is rejected and the chain does not move, $m_i = m_{curr}$

ENDFOR

Figure 3 An outline of the Markov chain Monte Carlo (McMC) inversion algorithm.

An additional strength of Bayesian inversion is the ability to perform trans-dimensional inversion. Conventional inversion algorithms require the user to define the number of resistivity values to be estimated and the locations to which they correspond. Trans-dimensional inversion, however, jointly estimates the number of cells that discretize the model domain, sizes and shapes of the cells, and their resistivity values. Generally, they utilize McMC algorithm for inversion and Metropolis-Hasting

method for sampling the prior. [Andersen et al. \(2003\)](#) used a random coloured polygonal model to jointly estimate shapes of different resistivity zones within a model domain and the resistivity values of each zone. Sometimes it is preferable to consider electrical resistivity changes, such as the delineation of plume caused by saline tracer release. [Ramirez et al \(2005\)](#) used MCMC to estimate the resistivity distribution from the ratio of two ERT datasets. Using a base representation algorithm, their method proposes subvolumes of varying sizes, shapes and resistivity values. Taking advantage of Voronoi cells and the reversible-jump Markov chain Monte Carlo algorithm, [Galetti and Curtis \(2018\)](#) developed a more robust and practical method for trans-dimensional ERT inversion (TERT). They have also shown that TERT yield superior uncertainty estimates than those obtained from conventional methods (e.g. resolution and sensitivity matrix). Trans-dimensional inversion is advantageous over fixed-dimensional inversion because it alleviates the “curse of dimensionality” (i.e. computational demands of stochastically exploring higher-dimensional spaces (i.e. more unknowns) explode exponentially) ([Curtis and Lomax, 2001](#); [Scales and Snieder, 1997](#)) and it takes advantage of the natural parsimony for Bayesian inference, meaning the posterior models are only as complex as is required by data or prior information. In a way, this is the result of a trade-off between Occam Factor (i.e. the ratio of posterior to prior accessible volume) and high likelihood (low misfit). A mathematical proof of this concept is given by [Ray et al. \(2018, 2016\)](#).

Bayesian methods treat uncertainties as probabilities and imply a multiplicative relationship between different sources of uncertainty. Figure 4 shows the framework of Bayesian inversion and their effect on uncertainty, as manifested in the spread of probability density functions. In Tikhonov-type methods, all input uncertainties are lumped to the starting model, making other sources of uncertainty intractable. Bayesian methods, in contrast, allow one to disentangle or segregate sources of uncertainty using multiplicative error models and sequential data assimilation models ([Rojas et al., 2008](#); [Salamon and Feyen, 2010](#)) or Bayesian hierarchical models ([Tsai and Elshall, 2013](#)).

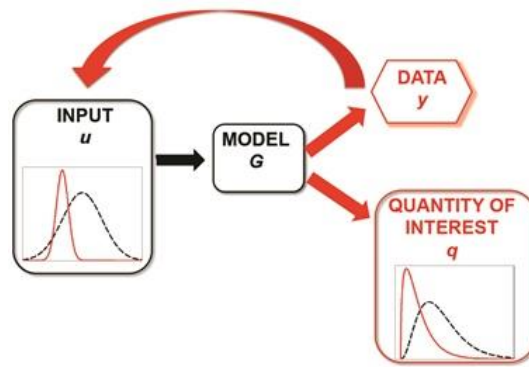


Figure 4 Uncertainty quantification in Bayesian inversion (Iglesias and Stuart, 2014). The black dashed lines and red solid lines denote prior and posterior probabilities. Essentially, the data drives an updating of input probabilities (e.g. model parameters) and lead to an updating of model outputs, including quantities of interest that are not directly observable from data.

3.4. Time-lapse inversion

The fast collection cycle of geophysical methods makes them suitable to monitor subsurface processes. Sequences of images can be used to evaluate the temporal evolution of subsurface properties. Hayley et al. (2011) summarizes the various approaches used for time-lapse inversion. The most straightforward one is to invert each image individually (i.e. absolute inversion). The initial model for starting the inversion in absolute imaging is often the same for each time step, though the conductivity model from the previous time step has also been used, as in Oldenborger et al. (2007). The ratio inversion (Daily et al., 1992; Ramirez et al., 2005) inverts the ratio of the resistivity between two times, while difference inversion (Labrecque and Yang, 2001) seeks to minimize the misfit between the difference in two datasets and the difference between two model responses. The cascaded inversion (Miller et al., 2008; Oldenborger et al., 2007) adds the constraint that the second inversion result should be similar to the first. The 4-D inversion (Kim et al., 2009) seeks to invert data from all times using a single system of equation. To do so, time regularization is added so that changes from one time to another are smooth. A variety of the method is the active time constraint approach (Karaoulis et al., 2011b, 2011a), which allows the time regularization to vary depending on the degree of spatial resistivity changes occurring between different monitoring stages. In simultaneous time-lapse inversion (Hayley et al., 2011), time-lapse inversion for two time steps are done simultaneously and constraints of smoothness and closeness to a reference model are applied to the

difference image produced. It produces images of similar resolution to difference inversion while needing less tailoring of regularization parameters. Following the same idea of focusing (section 6.1), comparing \mathbf{R} from different times also allow one to anticipate areas where model parameters change most in time, thus allowing temporal focusing (Wagner et al., 2015b; Wilkinson et al., 2015). The feature is particularly attractive for long-term monitoring systems where resistivity in only part of the inversion domain is expected to change significantly over time. The above approaches have all applied some smoothness constraints between datasets in the inversion and they yield inferior results in zones where sensitivity is low and resistivity change is abrupt. Hermans et al. (2016a) suggested a covariance-constrained difference inversion, which computes the covariance between datasets and use it instead of arbitrary smoothing functions to constrain the inversion.

An alternative approach to invert absolute time-lapse electrical resistivity data is to use the extended Kalman filter (Lehikoinen et al., 2009; Mitchell et al., 2011; Nenna et al., 2011). Kalman filter approaches, which have been successful for electrical impedance tomography in medical imaging (Kaipio et al., 1999; Trigo et al., 2004; Vauhkonen et al., 1998) and is rapidly gaining its popularity in hydrology (e.g. Reichle et al., 2008; Schöniger et al., 2012; Xue and Zhang, 2014), allows inclusion of information from previous time steps. Interesting properties of Bayesian filtering approaches like Kalman filter include (i) both source terms and data can be taken as uncertain; (ii) allows joint estimation of sources and model parameters. Ward et al. (2014) combined Kalman filter and edge detection algorithms to track the movement and evolution of saline tracer in 2-D and 3-D time-lapse experiments. Other methods to improve time-lapse inversion includes time-series and time-frequency analysis (Johnson et al., 2012a), as well as the data-domain correlation approach (Johnson et al., 2009).

Resolution analysis and image appraisal methods for individual inversion are also used for time-lapse inversion. Measures have not been developed specifically for time-lapse inversion. For uncertainty analysis, one may follow either a frame-by-frame analysis or a MCMC approach as in individual inversion. The mean-log ratio (MLR) is

commonly used to assess the amount of added information of a new image (Ramirez et al., 2005; Trainor-Guitton et al., 2013b).

4) Interpretation, application, and prediction

4.1. Interpretation of ERT images

Interpretation of inverted ERT images is not straightforward because they are smoothed representation of the actual system and their appearance are governed by the inversion algorithm used. This task is further complicated when the resolution of the survey is low. Dumont et al. (2018) studied the effects of smoothed resistivity changes, pore water dilution, temperature, and initial water distribution on the interpretation of infiltration depth, area, and volume at a landfill site and found that the failure to consider these effects can lead to misestimating the infiltration metrics. Carey et al. (2017) used forward modelling to investigate inversion artefacts resulting from time-lapse ERT during rainfall simulations under three moisture contrast scenarios and eight array configurations and showed that both factors contribute to artefact development.

In some applications, the goal of conducting an ERT survey is to infer interfaces from the resistivity images. Most studies identify the interfaces by visual interpretation, while a few have attempted to do so using some automatic algorithms. The most common one is the steepest gradient method (Chambers et al., 2013, 2012; Nguyen et al., 2005), which assumes the interface is located at the point where resistivity is steepest along a depth profile. Bouchedda et al. (2012) used parallel ERT and radar travel time inversion and a Canny edge detector to exchange structural information between them at every iteration to jointly estimate resistivity and slowness distribution. Alternatively, an iso-resistivity surfaces approach can be used when the resistivity at the interface is known through an independent measurement (Chambers et al., 2013). Chambers et al. (2014b) applied a fuzzy c-means clustering approach (Ward et al., 2014) to assign each cell within a ERT image to its most likely population and calculate the resistivity at the interface. They found that it shows superior performance at a

catchment site where the assumptions of the steepest gradient method break down. [Wainwright et al. \(2016\)](#) took a multi-step approach to map the naturally-reduced zone and the two hydrostratigraphic contacts at the Rifle IRFC site in Colorado. They first inverted ERT and time-domain induced polarisation data collected from ten surface lines. A Bayesian hierarchical analysis was then used to find correlations between the inverted geophysical model and lithological logs information from 187 wells. There exists another class of methods where the interface is inferred in the inversion and they are discussed in section 5.1.

In some other applications, the goal of ERT is to calibrate hydrological models and derive its parameters. Earlier studies focus on user ERT to capture tracer breakthrough and derive vadose zone parameters ([Binley et al., 2002a](#); [Cassiani and Binley, 2005](#)). More recent study extends such use to more complex problems. For example, [Doetsch et al. \(2013\)](#) found that including the reservoir boundaries as structural constraints significantly improves the images of increasing supercritical CO₂ saturation. They then used ERT-derived changes in subsurface electrical resistivity along with gas composition data to constrain and calibrate hydrological models.

4.2. Petrophysical uncertainty

Petrophysical relationship converts geophysical data or parameter to hydrological parameter of interest. They are largely considered as uncertain and can impact any hydrological applications that uses geophysical data. A large number of previous field and laboratory studies, however, has applied petrophysical relationships deterministically (e.g. [Chambers et al., 2014a](#); [Dumont et al., 2018, 2016](#); [Miller et al., 2008](#); [Wehrer and Slater, 2015](#)). Among them, some studies compared ERT-derived moisture contents with point-based moisture measurements (e.g. theta probes, neutron probes, or Time domain reflectometry (TDR)) ([Beff et al., 2013](#); [Hübner et al., 2015](#)). Many review articles for hydrogeophysics and near-surface geophysics have highlighted it as an outstanding challenge ([Binley et al., 2015](#); [Linde and Doetsch, 2016](#)). Two studies have considered uncertain petrophysical relationships in their analysis: [Huisman et al. \(2010\)](#) estimated a few Archie parameters alongside with other parameter of interest, while [Irving and Singha \(2010\)](#) considered a range of Archie

parameters in their MCMC updating scheme. Recently, [Tso et al. \(2019\)](#) shows that the natural variability in petrophysical parameters can lead to high uncertainty in moisture content estimates derived from inverted ERT images.

There have been attempts to overcome this issue by estimating some form of non-stationary petrophysical relations. [Day-Lewis et al. \(2005\)](#) uses a random field averaging analysis, where an assumed covariance is used to describe the spatial structure of the geophysical parameter and generate a realization for the geophysical model, and together with an assumed petrophysical model, generate a realization of the hydrological parameter of interest. Through analysing the model resolution matrix of the geophysical inversion, random field averaging is used for upscaling and generating ensemble variance tomograms and correlation coefficient between estimated and true geophysical parameter. With them, probabilistic pixel-specific petrophysical between hydrologic and estimated geophysical parameters can be established for inversion of lab or field data. [Moysey et al. \(2005\)](#) and [Singha and Gorelick \(2006\)](#) devise a full inverse statistical (FIS_t) calibration. Their method starts with generating realizations of hydrogeological model. Passing the hydrogeological models through a petrophysical model and geophysical forward model, realizations of geophysical synthetic data are produced. Inverting each of the geophysical synthetic data deterministically, the resultant images can be used to upscale hydrogeological property models and develop non-stationary apparent petrophysical relations to better estimate hydrologic properties.

5) Inversion continued

5.1. Incorporation of prior information and facies/interface detection

Introducing prior knowledge (or assumed knowledge) of the subsurface in the inversion can have a dramatic effect on the resultant images: the spatial structure can be significantly enhanced. This can be done in both the regularized inversion framework where model roughness matrix is modified, and in the Bayesian framework where prior knowledge of the spatial variability of properties can be prescribed as prior probabilities (e.g. [Andersen et al., 2003](#); [Linde et al., 2006](#)). The

effects of incorporating prior information in inversion of ERT data is demonstrated by [Caterina et al. \(2014\)](#), where they compare smoothness constrained inversion, reference model inversion, structural inversion, and geostatistical inversion under various settings.

Among Bayesian methods, geostatistical approaches ([Linde et al., 2006](#); e.g. [Yeh et al., 2002](#)) can be very robust and effective. They treat spatial properties as a random field conditioned on data. For example, [Linde et al. \(2006\)](#) invert DC resistivity and ground-penetrating radar traveltime data with a regularized least squares algorithm but use stochastic regularization operators based on geostatistical models to constrain the solution. The successive linear estimator ([Yeh et al., 2002](#); [Yeh and Liu, 2000](#)) uses a perturbation method to yield conditional expectation and the associate variance of the subsurface conductivity field. At the end of each iteration, the covariance matrices are updated. For the quasi-linear geostatistical approach ([Kitanidis, 1995](#)), the trend of the data is updated instead. [Kitanidis \(2015a\)](#) reports that using the highly parallelized forward code of [Johnson et al. \(2010\)](#) as a black box in lieu of the principal component geostatistical approach (PCGA) ([Lee and Kitanidis, 2014](#)), which utilizes the leading principal components from the prior covariance, a good approximation of the solution can be obtained at a fraction of the cost. Latest approaches devise the use of multi-point geostatistics ([Hu and Chugunova, 2008](#); [Linde et al., 2015a](#); [Mariethoz and Caers, 2014](#)) or the Matérn covariance family in their inversion ([Bouchedda et al., 2015](#)). The advantages of these methods is that they can better handle non-stationarity of spatial variation and the geostatistics parameters can be estimated in the inversion. There is potential to take advantage of the advances in ensemble Kalman inversion ([Chada et al., 2018](#)), such as using a combination of level set methods, Matern covariance functions and ensemble Kalman inversion for ERT data. The advantages of this method are: (i.) can perform Bayesian inversion at a fraction of the cost of MCMC, (ii.) allows joint estimation of spatially varying correlation scales of the resistivity field, (iii.) level set method allows the delineation of sharp contrast without the need to impose constraints *a priori*.

The roughness matrix in deterministic smoothness-constrained inversion can be replaced by a model covariance matrix determined by geostatistical model (Hermans et al., 2012). The approach yields superior results than conventional inversion because it only smooths the model parameters to a level that is controlled by the correlation length. The same approach can be extended to difference inversion of time-lapse data (Hermans et al., 2016a). Alternatively, the model covariance matrix can be determined using an image-guided approach. For example, structural information from a seismic or GPR image can be extracted by first converting it to a greyscale guiding image and then infer the coefficients of the model covariance matrix based on structure oriented semblance (Zhou et al., 2014). Such approach has also been applied to stochastic inversion (Zhou et al., 2016). It should also be noted that besides the commonly used Tihonov regularization for smoothness-constrained inversion, the total variation (TV) which favours a piecewise constant solution is another popular choice. A total generalized variation scheme which alternate between the two is recently proposed to avoid bias towards one of the two without any noticeable extra computational cost (Sibbertt et al., 2017).

If there are known interfaces in the model domain, the roughness matrix can be modified by disconnecting the regularization between two neighbouring model parameters, with the option to prescribe known resistivity values. This approach is particularly useful in fractured medium (Robinson et al., 2015) (see example in Figure 5), segregating known zones (e.g. bedrock and sediments) (Bazin and Pfaffhuber, 2013; Coscia et al., 2011; Johnson et al., 2012b), and engineered barriers with known boundaries (Slater and Binley, 2003). The regularization disconnect approach requires prior knowledge of the interfaces. In some applications, there may be a sharp target in the domain of which its location is not known (e.g. tracking a moving plume). In this situation, focusing approaches that penalize changes in a certain way is preferred. One example is the minimum gradient support (MGS) functional (Portniaguine and Zhdanov, 1999), which minimizes the area where strong model variation and discontinuity occur. An issue of this method is that the solution is very sensitive to the MGS parameter. Nguyen et al. (2016) developed a data-driven approach to optimally select the MGS parameter for time-lapse data. Finally, Fiandaca et al. (2015) proposed

a generalized focusing method for time-lapse changes, which allows joint tuning of the sharpness of the timeless changes and the size of the area/volume influenced by such changes.

We have mentioned methods to interpret interfaces from ERT images (section 4.1). A potentially more reliable alternative is to estimate the interface within the ERT data inversion. Irving and Singha (2010) used a sequential MCMC approach for (i) tracer concentration data, (ii) ERT data, and (iii) both to estimate the membership probability of a binary facies systems. This approach can be extended to estimate heterogeneous resistivity fields within each facies or zones using a Metropolis-within-Gibbs method in which the model proposals are symmetric and the interface and physical properties are updated alternately within the Gibbs framework (de Pasquale et al., 2019; Iglesias et al., 2014). For a critical zone-bedrock problem (Figure 6), two heterogeneous field for the entire model domain are generated (which are cropped to match terrain) and then the two fields and the interface between them are sequentially updated using a MCMC algorithm. This resultant resistivity image clearly resolves both the interface boundary and the in-zone heterogeneity.

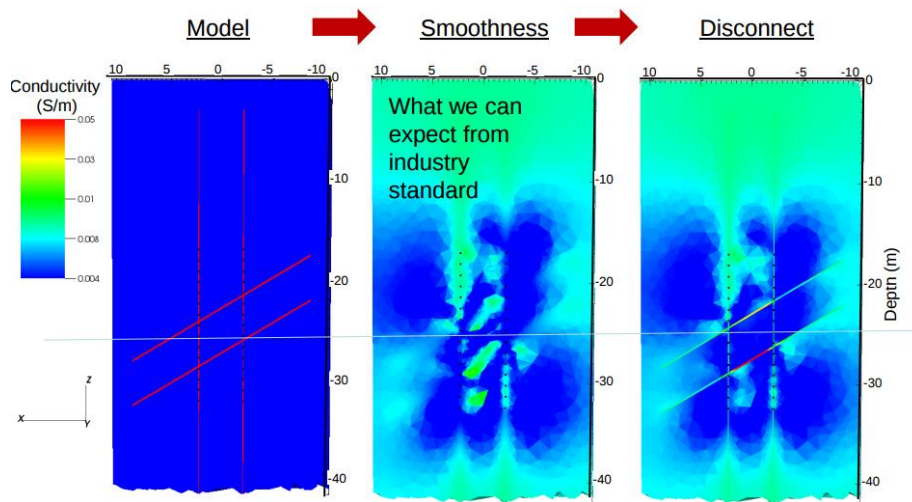


Figure 5 This synthetic example shows that by disconnecting the smoothness constraint in a regularized ERT inversion, the fracture network (red and yellow) is much better recovered (Robinson et al., 2015). Compared with the smoothness constraint inversion, the smoothness disconnect case shows pronounced elongated fractures and recover the very high conductivities along them.

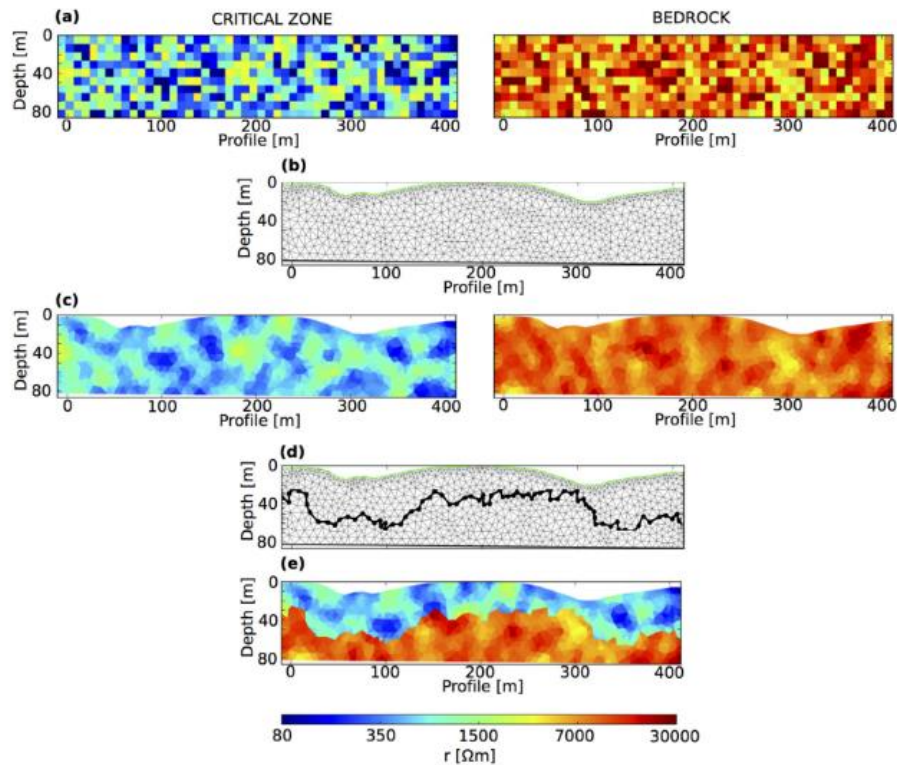


Figure 6 A new Bayesian inversion method that jointly estimates both the interface of the two units and the sub-unit resistivity variations (de Pasquale et al., 2019). The approach estimates the resistivity field of both unit (assuming they span the entire model domain) and their interface. The resultant field is obtained by combining the two fields along the interface.

5.2. Coupled (joint and constrained) and uncoupled methods, and process-based methods

The ultimate goal of geophysical inversion is rarely just the mapping of geophysical properties. Usually it is used to gain understanding of other processes, for instance, hydrogeology or hydrological processes. As shown already in section 4), the process of interpreting an ERT image or to translate an ERT image to quantities of interest can be a source of significant uncertainty. Coupled inversion or coupled modelling can be an effective means to handle such issues because (i.) the inverse problem is formulated in such a way that it returns the quantities of interests directly and (ii.) usually the underlying process model that drives the geophysical response is incorporated in the forward models used for inversion.

Traditionally, a geophysical image is used as a proxy for the spatial distribution of interest. This approach is termed ‘un-coupled hydrogeophysical inversion’. An alternative is to use a ‘coupled hydrogeophysical inversion’ (Hinnell et al., 2010; Huisman et al., 2010; Irving and Singha, 2010; Kowalsky et al., 2005; Looms et al., 2008;

Pollock and Cirpka, 2010), where feedback between geophysical and hydrology is explicitly defined (as prior hydrological conceptualization). There are also situations where multiple geophysical datasets are available to describe the same process. For example, Lochbühler et al. (2013) used the structure-coupled approach (Doetsch, 2011; Gallardo and Meju, 2011) to jointly invert multilevel crosshole slug interference tests, temporal moments of tracer breakthrough curves, and cross-hole ground penetrating radar data. Doetsch et al. (2010b) used the structural constraint to jointly invert ERT and GPR data so that the geophysics-derived moisture content honours both modalities. Huisman et al. (2010) used the DREAM algorithm (Vrugt et al., 2009), which runs multiple Markov Chains simultaneously at the same time, to jointly use ERT data and moisture content data from time-domain reflectometry (TDR) to estimate soil hydraulic parameters of a model dykes. They also used AMALGAM (Vrugt and Robinson, 2007) to approximate the Pareto front of parameter pairs. Jardani et al. (2013) devised a stochastic MCMC approach to invert hydraulic conductivity distribution between two wells using ERT, self-potential and salt tracer concentration data jointly. Notice that the application of coupled approaches is not limited to near-surface processes. For example, transient pressure pulses and dc resistivity acquired at permanent borehole sensors can be jointly inverted (Alpak et al., 2004). Similarly, the combined use of electrical and gas composition data are used to constrain CO₂ simulations (Doetsch et al., 2013).

When there are multiple geophysical data sets, the relationship between two geophysical modalities may not be known for certain. In this case, the inversion may benefit from not enforcing strict feedback between them. This is termed the constrained inversion. Figure 7 shows the different strategies to invert multiple geophysical data sets. Similarly, to relate geophysical and hydrological properties, some petrophysical relationships are needed. These relationships can be determined in the laboratory but they can be unreliable when applied to field problems. It may be desirable to impose some “soft” process constraint instead so that uncertain inversion results are related to one another in a more flexible sense. One idea is to use Monte Carlo simulations using flow and transport models to generate training images that are used as prior information to constrain geophysical inversion (Owari et al., 2013).

While fully coupled approaches assume strict feedback between two modalities, and individual inversion uses some possibly ambiguous regularization constraints, process-based inversion can be viewed as an intermediate approach that allows physically based regularization.

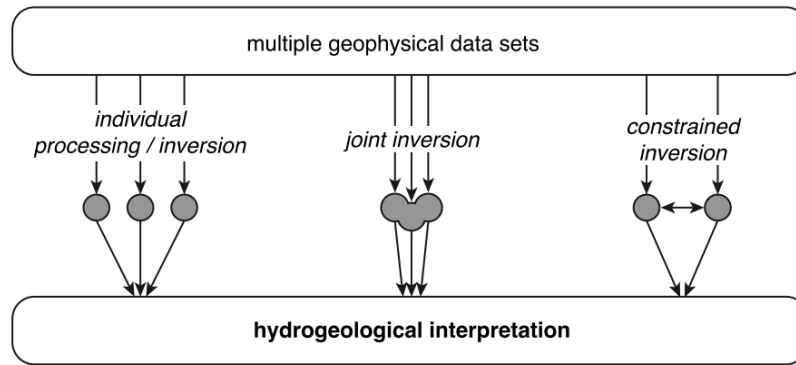


Figure 7 Illustration of different approaches for integrating multiple geophysical data sets for a hydrogeological interpretation (Doetsch, 2011). Individual processing invert each dataset individually before interpreting them together qualitatively. Joint inversion invert all available datasets together—explicit assumptions between different process models are required. A constrained inversion use parts of the inversion results from one inversion to constrain another.

5.3. Data assimilation and data fusion of multiple data types

A straightforward way to enhance the information content in geophysical measurements is to integrate hydrological and geophysical data from different sources. This integration, however, is never as straightforward as it seems because different data are measured in different spatial and temporal scales (Kitanidis, 2015b). This is a problem because most integration would require the use of a Bayesian framework, but the scales issues violate the “consistency” requirement for Bayesian updating. Nevertheless, there have been many attempts to integrate data of different scales, mostly relying on bringing all measurements to the same manageable scale. Ruggeri et al. (2013) uses a two-step Bayesian sequential simulation approach: they first link the low- and high-resolution geophysical data via a stochastic downscaling procedure, followed by relating the downscaled geophysical data to the high-resolution hydraulic conductivity distribution. JafarGandomi and Binley (2013) develop a trans-dimensional geophysical data fusion workflow that first transform all geophysical data into 1-D. Then they run stochastic joint inversion using Markov chain Monte Carlo

methods to obtain discrete 1-D models. Subsequently, the information of the 1-D models are quantified using entropy measures, which can be used to improve survey design. Finally, the discrete 1-D models are fused using the Bayesian maximum entropy approach (Christakos, 2000) to obtain 2-D or 3-D spatial distribution of geophysical properties.

Localized averages can sometimes help assess and distinguish the information embedded in different images. Miller and Routh (2007) and Routh (2009) use funnel function analysis to provide a formalism to compute upper and lower bounds of localized averages of the image. This framework can be helpful to determine scale dependent (target-oriented) uncertainties taking into account the resolution of the geophysical data. This idea can also be used probabilistically as adaptive kernel smoothing to estimate the probability density of the data variable for each training image at a much lower dimension (Hermans et al., 2015; Park et al., 2013).

As discussed in previous sections, prior information plays a dramatic role in modifying inversion results. Better incorporation of prior information gives more and better information for an inverse problem to start with. We should continue exploring methods to improve incorporation of prior information. Moreover, the goal of inversion is to obtain more accurate posterior estimates and their uncertainty bounds. Better incorporation of prior and other sources of information means more information to constrain the posterior solution, and thus it is key to the uncertainty quantification in ERT.

6) Discussion

6.1. Experimental design

Once we understand the geophysical workflow and how errors and uncertainties enter and propagate along it, this knowledge can be used to design experiments with the aim to maximize the extraction of information or minimization of uncertainty. Current work focusses mostly on inversion and examine whether particular inversion algorithms and survey design to resolve the target feature.

However, after understanding how uncertainty propagates along the ERT workflow, future work should consider also other sources of uncertainty in experimental design.

For regularized inversion, the resolution matrix \mathbf{R} can be used to confirm whether a proposed survey can resolve model parameters of interest, as well as ranking the merits of competing survey proposals (Friedel, 2003; Furman et al., 2007, 2004; Leube et al., 2012; Loke et al., 2014; Maurer et al., 2010). The ‘Compare \mathbf{R} ’ method seeks to incrementally add measurements that would lead to the greatest resolution improvement to the measurement scheme (Stummer et al., 2004; Wilkinson et al., 2012, 2006). Its variant combines the optimization for time-lapse studies (Wilkinson et al., 2015) and electrode placement (Uhlemann et al., 2018). Similar approaches, some work in the other direction (i.e. incrementally reduce measurements from a full set), can be found in the literature (Blome et al., 2011; Maurer et al., 2000).

Bayesian approach also allows optimization of survey design. However, it does not take a model resolution viewpoint as in deterministic inversion. Classical approaches are based on the expected utility of data (de Barros and Rubin, 2008; Feyen and Gorelick, 2005; Fu and Jaime Gómez-Hernández, 2009; Neuman et al., 2012; Shi et al., 2013). Alternatives have been proposed such as the use of multi-objective optimization (Nowak et al., 2015, 2012).

Existing literature only consider optimizing the design based on inversion outputs. However, recognizing uncertainty stems from and propagates through the ERT workflow (Figure 1), future work should strive to reduce the overall prediction uncertainty instead and consider uncertainty sources at all steps along the workflow (Figure 8). This approach can be used in conjunction with value of information (VOI) analysis, which has been applied to ERT data previously (Nenna et al., 2011; Trainor-Guitton et al., 2013b), to provide an estimate on whether the proposed field campaign leads to added value or whether it is cost-effective.

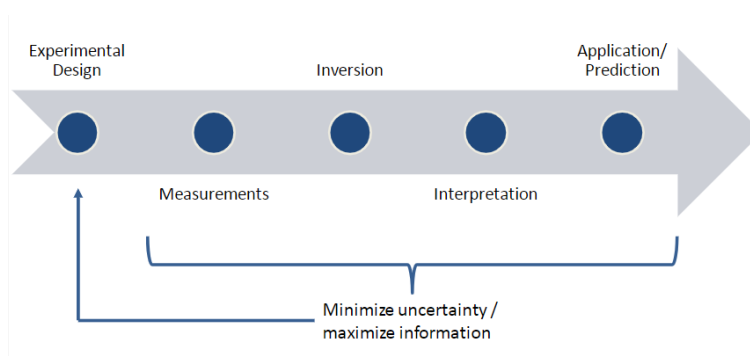


Figure 8 The ERT workflow as a pipeline for information and uncertainty propagation is helpful for the experimental design of ERT surveys. It can be optimized to minimize uncertainty and maximize the extraction of information.

6.2. Emerging methods and future work

The quantification of uncertainty in ERT is an important research topic challenged by computational time constraints. Recently, [Fernández-Martínez \(2019\)](#) developed an algorithm based on singular value decomposition and an exploratory member of the particle swarm optimization family to speed up the estimation of ERT model parameter uncertainty. Computation time reductions can also be achieved by speeding up the forward model. Surrogate models or support vector machines can be used to approximate model response at a fraction of the normal computation cost and has been applied to many sub-disciplines of hydrology ([Asher et al., 2015](#)), yet there has not been any application to near-surface geophysics.

The rapid advances of data science has provided new tools to approach the inversion and uncertainty quantification problems ([Scheidt et al., 2018](#)). In particular, the idea of Bayesian evidential learning is proposed as a new scientific protocol for uncertainty quantification. It does not rely on traditional inversion methods but instead rely on machine learning from Monte Carlo simulations. Meanwhile, some authors argue for more geological realism in hydrogeophysics ([Linde, 2014](#); [Linde et al., 2015b](#)) and stress the importance of falsifying models that are inconsistent to data. Machine learning are also applied to the estimation of moisture content variation from ERT images ([Moghadas and Badorreck, 2019](#)). The authors built artificial neural networks using the time series of soil moisture measurements at five depths and they argue that the use of artificial neural networks better captures the nonlinear

spatiotemporal behaviour of the wetting front than traditional petrophysical models from the ERT data. With the rapid growth of automated ERT monitoring systems deployed worldwide, key environmental data science challenges such as data interoperability and real-time data analytics on cloud computing platforms will become highly relevant.

This review has focused on using ERT as the main source of information. However, it is noteworthy that ERT information are often used as “soft” data to constrain other models, such as groundwater models. There is increased use of such approach to constrain realizations of groundwater models generated using multi-point geostatistics ([Gottschalk et al., 2017](#); [Hermans et al., 2015](#)).

Recent work has extended coupled hydrogeophysical inversion to include even more processes. In this situation, usually ERT data is used directly without inversion. [Tran et al. \(2016\)](#) devised a coupled thermal-mechanical-hydrogeophysical inversion to simultaneously estimate subsurface hydrological, thermal and petrophysical parameters using hydrological, thermal and electrical resistivity tomography (ERT) data. To reduce the number of unknown parameters, they screen the parameters using global sensitivity analysis ([Wainwright et al., 2014b](#)) and fixed parameters that are found to have negligible effect on the observation. The [Morris \(1991\)](#) method is generally suitable for hydrogeophysical problems because of the relatively small number of forward model runs required. More computationally intensive global sensitivity analysis with the [Sobol \(2001\)](#) indices requires more forward runs and is usually performed using surrogate modelling techniques (e.g. polynomial chaos expansion), as demonstrated in a recent study on travel time of radionuclides ([Deman et al., 2016](#)). There are a number studies that compares the two global sensitivity analysis methods (e.g. [Gan et al., 2014](#); [Hermans et al., 2014](#)). [Tran et al. \(2017\)](#) uses soil liquid water content, temperature and electrical resistivity tomography (ERT) data and a MCMC inversion scheme to estimate the vertical distribution of soil organic carbon content during a freeze-thaw event in the Arctic tundra. Even though the models used to model ERT response are ever more complex, the principles discussed above are relevant and can be used to guide future advances in data collection and

modelling. Another example is the coupled inversion of CO₂ and hydraulic pressure, CO₂ arrival times and ERT data at the Ketzin site (Wagner and Wiese, 2018; Wiese et al., 2018), where singular value decomposition and PEST (Christensen and Doherty, 2008) are used in combination to estimate parameters for a multi-physical reservoir model.

7) Conclusion

We have reviewed the various sources of uncertainties in ERT along its workflow. Each of the steps along the workflow presents its unique challenges to represent and reduce its uncertainties, while these uncertainties propagate downstream along the workflow. Significant effort has been put to characterize and reduce uncertainty at each step. While majority of the literature has focused on reducing inversion uncertainty, we also see an emergence of techniques focusing on better handling of uncertainties in the interpretation or experimental design of ERT surveys. We have shown that the inverse problem formulations for deterministic and Bayesian inversion are similar but their meaning are not identical. We also highlight that the ERT inverse problem, in general, is not a simple trade-off between resolution and uncertainty. Future work needs to better address the apparently low uncertainty (due to low resolution) away from electrodes in smoothness constrained inversions. Incorporation of prior information, coupled inversions, and data assimilation are key areas of research to improve the applicability and reliability of ERT results. Currently, it is uncommon to consider uncertainty propagation along the entire ERT workflow. Future work can focus on better describing such uncertainty propagation and perhaps proposing alternative workflows to bypass certain high uncertainty steps.

Acknowledgement

This paper is published with the permission of the Executive Director of the British Geological Survey (NERC) and Sellafield Ltd. (on behalf of the Nuclear Decommissioning Authority). The first author is supported by a Lancaster University Faculty of Science and Technology PhD studentship and a Nuclear Decommissioning Authority PhD bursary.

References

- Alpak, F., Torres-Verdín, C., Habashy, T.M., 2004. Joint inversion of transient pressure and dc resistivity measurements acquired with in-situ permanent sensors: A numerical study. *Geophysics* 69, 1173–1191. <https://doi.org/10.1190/1.1801935>
- Alumbaugh, D.L., Newman, G.A., 2000. Image appraisal for 2-D and 3-D electromagnetic inversion. *Geophysics* 65, 1455. <https://doi.org/10.1190/1.1444834>
- Andersen, K.E., Brooks, S.P., Hansen, M.B., 2003. Bayesian inversion of geoelectrical resistivity data. *J. R. Stat. Soc. Ser. B Stat. Methodol.* 65, 619–642. <https://doi.org/10.1111/1467-9868.00406>
- Asher, M.J.J., Croke, B.F.W.F.W., Jakeman, A.J.J., Peeters, L.J.M.J.M., 2015. A review of surrogate models and their application to groundwater modeling. *Water Resour. Res.* 51, 5957–5973. <https://doi.org/10.1002/2015WR016967>
- Aster, R., Borchers, B., Thurber, C.H., 2005. *Parameter estimation and inverse problems*. Elsevier, Burlington, Massachusetts, USA.
- Backus, G.E., Gilbert, F., 1970. Uniqueness in the Inversion of inaccurate Gross Earth Data. *Philos. Trans. R. Soc. London A* 266, 123–192.
- Backus, G.E., Gilbert, F., 1968. The Resolving power of Gross Earth Data. *Geophys. J. R. Astron. Soc.* 16, 169–205.
- Bazin, S., Pfaffhuber, A.A., 2013. Mapping of quick clay by electrical resistivity tomography under structural constraint. *J. Appl. Geophys.* 98, 280–287. <https://doi.org/10.1016/J.JAPPGEO.2013.09.002>
- Beff, L., Günther, T., Vandoorne, B., Couvreur, V., Javaux, M., 2013. Three-dimensional monitoring of soil water content in a maize field using Electrical Resistivity Tomography. *Hydrol. Earth Syst. Sci.* 17, 595–609. <https://doi.org/10.5194/hess-17-595-2013>
- Beskardes, G.D., Weiss, C.J., 2018. Modelling dc responses of 3-D complex fracture networks. *Geophys. J. Int.* 214, 1901–1912. <https://doi.org/10.1093/gji/ggy234>
- Binley, A., Cassiani, G., Middleton, R., Winship, P., 2002. Vadose zone flow model parameterisation using cross-borehole radar and resistivity imaging. *J. Hydrol.* 267, 147–159. [https://doi.org/10.1016/S0022-1694\(02\)00146-4](https://doi.org/10.1016/S0022-1694(02)00146-4)
- Binley, A., Hubbard, S.S., Huisman, J.A., Revil, A., Robinson, D.A., Singha, K., Slater, L.D., 2015. The emergence of hydrogeophysics for improved understanding of

References

- subsurface processes over multiple scales. *Water Resour. Res.* 51, 3837–3866. <https://doi.org/10.1002/2015WR017016>
- Binley, A., Ramirez, A.L., Daily, W., 1995. Regularised image reconstruction of noisy electrical resistance data, in: *Proceedings of the 4th Workshop of the European Concerted Action on Process Tomography*,. Bergen, pp. 401–410.
- Blome, M., Maurer, H., Greenhalgh, S., 2011. Geoelectric experimental design — Efficient acquisition and exploitation of complete pole-bipole data sets. *GEOPHYSICS* 76, F15–F26. <https://doi.org/10.1190/1.3511350>
- Bouchedda, A., Chouteau, M., Binley, A., Giroux, B., 2012. 2-D joint structural inversion of cross-hole electrical resistance and ground penetrating radar data. *J. Appl. Geophys.* 78, 52–67. <https://doi.org/10.1016/j.jappgeo.2011.10.009>
- Bouchedda, A., Giroux, B., Gloaguen, E., 2015. Bayesian ERT Inversion using Non-Stationary Inverse Matérn Covariance Matrix, in: *SEG Annual Meeting*. New Orleans.
- Brunetti, C., 2019. Bayesian model selection in hydrogeophysics and hydrogeology. Université de Lausanne.
- Carey, A.M., Paige, G.B., Carr, B.J., Dogan, M., 2017. Forward modeling to investigate inversion artifacts resulting from time-lapse electrical resistivity tomography during rainfall simulations. *J. Appl. Geophys.* 145, 39–49. <https://doi.org/10.1016/J.JAPPGEO.2017.08.002>
- Carrigan, C.R., Yang, X., LaBrecque, D.J., Larsen, D., Freeman, D., Ramirez, A.L., Daily, W., Aines, R., Newmark, R., Friedmann, J., Hovorka, S., 2013. Electrical resistance tomographic monitoring of CO₂ movement in deep geologic reservoirs. *Int. J. Greenh. Gas Control* 18, 401–408. <https://doi.org/10.1016/j.ijggc.2013.04.016>
- Cassiani, G., Binley, A., 2005. Modeling unsaturated flow in a layered formation under quasi-steady state conditions using geophysical data constraints. *Adv. Water Resour.* 28, 467–477. <https://doi.org/10.1016/j.advwatres.2004.12.007>
- Cassiani, G., Bruno, V., Villa, A., Fusi, N., Binley, A.M., 2006. A saline tracer test monitored via time-lapse surface electrical resistivity tomography. *J. Appl. Geophys.* 59, 244–259. <https://doi.org/10.1016/j.jappgeo.2005.10.007>
- Caterina, D., Beaujean, J., Robert, T., Nguyen, F., 2013. A comparison study of different image appraisal tools for electrical resistivity tomography. *Near Surf. Geophys.* 11, 639–657. <https://doi.org/10.3997/1873-0604.2013022>

References

- Caterina, D., Hermans, T., Nguyen, F., 2014. Case studies of incorporation of prior information in electrical resistivity tomography: comparison of different approaches. *Near Surf. Geophys.* 12, 451–465. <https://doi.org/10.3997/1873-0604.2013070>
- Chada, N.K., Iglesias, M.A., Roininen, L., Stuart, A.M., 2018. Parameterizations for ensemble Kalman inversion. <https://doi.org/10.1088/1361-6420/aab6d9>
- Chambers, J.E., Gunn, D.A., Wilkinson, P.B., Meldrum, P.I., Haslam, E., Holyoake, S., Kirkham, M., Kuras, O., Merritt, A., Wragg, J., 2014a. 4D electrical resistivity tomography monitoring of soil moisture dynamics in an operational railway embankment. *Near Surf. Geophys.* 12, 61–72. <https://doi.org/10.3997/1873-0604.2013002>
- Chambers, J.E., Wilkinson, P.B., Penn, S., Meldrum, P.I., Kuras, O., Loke, M.H., Gunn, D.A., 2013. River terrace sand and gravel deposit reserve estimation using three-dimensional electrical resistivity tomography for bedrock surface detection. *J. Appl. Geophys.* 93, 25–32. <https://doi.org/10.1016/j.jappgeo.2013.03.002>
- Chambers, J.E., Wilkinson, P.B., Uhlemann, S., Sorensen, J.P.R., Roberts, C., Newell, A.J., Ward, W.O.C., Binley, A., Williams, P.J., Gooddy, D.C., Old, G., Bai, L., 2014b. Derivation of lowland riparian wetland deposit architecture using geophysical image analysis and interface detection. *Water Resour. Res.* 50, 5886–5905. <https://doi.org/10.1002/2014WR015643>
- Chambers, J.E., Wilkinson, P.B., Wardrop, D., Hameed, A., Hill, I., Jeffrey, C., Loke, M.H., Meldrum, P.I., Kuras, O., Cave, M., Gunn, D.A., 2012. Bedrock detection beneath river terrace deposits using three-dimensional electrical resistivity tomography. *Geomorphology* 177–178, 17–25. <https://doi.org/10.1016/j.geomorph.2012.03.034>
- Christakos, G., 2000. *Modern Spatiotemporal Geostatistics*. Oxford University Press, New York.
- Christensen, S., Doherty, J., 2008. Predictive error dependencies when using pilot points and singular value decomposition in groundwater model calibration. *Adv. Water Resour.* 31, 674–700. <https://doi.org/10.1016/J.ADVWATRES.2008.01.003>
- Coscia, I., Greenhalgh, S.A., Linde, N., Doetsch, J., Marescot, L., Günther, T., Vogt, T., Green, A.G., 2011. 3D crosshole ERT for aquifer characterization and monitoring of infiltrating river water. *Geophysics* 76, G49–G59. <https://doi.org/10.1190/1.3553003>

References

- Curtis, A., Lomax, A., 2001. Prior information, sampling distributions, and the curse of dimensionality. *GEOPHYSICS* 66, 372–378. <https://doi.org/10.1190/1.1444928>
- Daily, W., Ramirez, A., LaBrecque, D., Nitao, J., 1992. Electrical resistivity tomography of vadose water movement. *Water Resour. Res.* 28, 1429–1442. <https://doi.org/10.1029/91WR03087>
- Day-Lewis, F.D., Lane, J.W., 2004. Assessing the resolution-dependent utility of tomograms for geostatistics. *Geophys. Res. Lett.* 31, 2–5. <https://doi.org/10.1029/2004GL019617>
- Day-Lewis, F.D., Singha, K., Binley, A.M., 2005. Applying petrophysical models to radar travel time and electrical resistivity tomograms: Resolution-dependent limitations. *J. Geophys. Res. B Solid Earth* 110, 1–17. <https://doi.org/10.1029/2004JB003569>
- de Barros, F.P.J., Rubin, Y., 2008. A risk-driven approach for subsurface site characterization. *Water Resour. Res.* 44, 1–14. <https://doi.org/10.1029/2007WR006081>
- de Pasquale, G., Linde, N., Doetsch, J., Holbrook, W.S., 2019. Probabilistic inference of subsurface heterogeneity and interface geometry using geophysical data. *Geophys. J. Int.* <https://doi.org/10.1093/gji/ggz055>
- Deceuster, J., Kaufmann, O., Camp, M. Van, 2013. Automated identification of changes in electrode contact properties for long-term permanent ERT monitoring experiments. *Geophysics* 78, E79–E94. <https://doi.org/10.1190/GEO2012-0088.1>
- Deman, G., Konakli, K., Sudret, B., Kerrou, J., Perrochet, P., Benabderrahmane, H., 2016. Using sparse polynomial chaos expansions for the global sensitivity analysis of groundwater lifetime expectancy in a multi-layered hydrogeological model. *Reliab. Eng. Syst. Saf.* 147, 156–169. <https://doi.org/10.1016/j.ress.2015.11.005>
- Demirel, S., Irving, J., Roubinet, D., 2019. Comparison of REV size and tensor characteristics for the electrical and hydraulic conductivities in fractured rock. *Geophys. J. Int.* 216, 1953–1973. <https://doi.org/10.1093/gji/ggy537>
- Doetsch, J., 2011. Joint and constrained inversion of geophysical data for improved imaging of aquifer structure and processes. ETH Zurich.
- Doetsch, J., Coscia, I., Greenhalgh, S., Linde, N., Green, A., Gunther, T., 2010a. The borehole-fluid effect in electrical resistivity imaging. *Geophysics* 75, F107–F114. <https://doi.org/10.1190/1.3467824>

References

- Doetsch, J., Kowalsky, M.B., Doughty, C., Finsterle, S., Ajo-Franklin, J.B., Carrigan, C.R., Yang, X., Hovorka, S.D., Daley, T.M., 2013. Constraining CO₂ simulations by coupled modeling and inversion of electrical resistance and gas composition data. *Int. J. Greenh. Gas Control* 18, 510–522. <https://doi.org/10.1016/j.ijggc.2013.04.011>
- Doetsch, J., Linde, N., Binley, A., 2010b. Structural joint inversion of time-lapse crosshole ERT and GPR traveltime data. *Geophys. Res. Lett.* 37, 1–6. <https://doi.org/10.1029/2010GL045482>
- Doetsch, J., Linde, N., Pessognelli, M., Green, A.G., Gunther, T., 2012. Constraining 3-D electrical resistance tomography with GPR reflection data for improved aquifer characterization. *J. Appl. Geophys.* 78, 68–76. <https://doi.org/10.1016/j.jappgeo.2011.04.008>
- Dumont, G., Pilawski, T., Dzaomuh-Lenieregue, P., Hiligsmann, S., Delvigne, F., Thonart, P., Robert, T., Nguyen, F., Hermans, T., 2016. Gravimetric water distribution assessment from geoelectrical methods (ERT and EMI) in municipal solid waste landfill. *Waste Manag.* 55, 129–140. <https://doi.org/10.1016/J.WASMAN.2016.02.013>
- Dumont, G., Pilawski, T., Hermans, T., Nguyen, F., Garré, S., 2018. The effect of initial water distribution and spatial resolution on the interpretation of ERT monitoring of water infiltration in a landfill cover. *Hydrol. Earth Syst. Sci. Discuss.* 1–26. <https://doi.org/10.5194/hess-2018-163>
- Elwaseif, M., Slater, L., 2012. Improved Resistivity Imaging of Targets with Sharp Boundaries Using an Iterative Disconnect Procedure. *J. Environ. Eng. Geophys.* 17, 89–101. <https://doi.org/10.2113/JEEG17.2.89>
- Falzone, S., Robinson, J., Slater, L., 2018. Characterization and Monitoring of Porous Media with Electrical Imaging: A Review. *Transp. Porous Media* 1–26. <https://doi.org/10.1007/s11242-018-1203-2>
- Farquharson, C.G., 2008. Constructing piecewise-constant models in multidimensional minimum-structure inversions. *GEOPHYSICS* 73, K1–K9. <https://doi.org/10.1190/1.2816650>
- Fernández-Martínez, J.L., Fernández-Muñiz, Z., Xu, S., Cernea, A., Sirieix, C., Riss, J., 2019. Efficient uncertainty analysis of the 3D electrical tomography inverse problem. *GEOPHYSICS* 1–62. <https://doi.org/10.1190/geo2017-0729.1>
- Fernández-Muñiz, Z., Khaniani, H., Fernández-Martínez, J.L., 2019. Data kit inversion and uncertainty analysis. *J. Appl. Geophys.* 161, 228–238. <https://doi.org/10.1016/j.jappgeo.2018.12.022>

References

- Feyen, L., Gorelick, S.M., 2005. Framework to evaluate the worth of hydraulic conductivity data for optimal groundwater resources management in ecologically sensitive areas. *Water Resour. Res.* 41, 1–13. <https://doi.org/10.1029/2003WR002901>
- Fiandaca, G., Doetsch, J., Vignoli, G., Auken, E., 2015. Generalized focusing of time-lapse changes with applications to direct current and time-domain induced polarization inversions 1101–1112. <https://doi.org/10.1093/gji/ggv350>
- Friedel, S., 2003. Resolution, stability and efficiency of resistivity tomography estimated from a generalized inverse approach. *Geophys. J. Int.* 153, 305–316. <https://doi.org/10.1046/j.1365-246X.2003.01890.x>
- Fu, J., Jaime Gómez-Hernández, J., 2009. Uncertainty assessment and data worth in groundwater flow and mass transport modeling using a blocking Markov chain Monte Carlo method. *J. Hydrol.* 364, 328–341. <https://doi.org/10.1016/j.jhydrol.2008.11.014>
- Furman, A., Ferré, T.P. a., Heath, G.L., 2007. Spatial focusing of electrical resistivity surveys considering geologic and hydrologic layering. *Geophysics* 72, F65. <https://doi.org/10.1190/1.2433737>
- Furman, A., Ferré, T.P.A., Warrick, A.W., 2004. Optimization of ERT Surveys for Monitoring Transient Hydrological Events Using Perturbation Sensitivity and Genetic Algorithms. *Vadose Zo. J.* 3, 1230. <https://doi.org/10.2136/vzj2004.1230>
- Galetti, E., Curtis, A., 2018. Transdimensional Electrical Resistivity Tomography. *J. Geophys. Res. Solid Earth.* <https://doi.org/10.1029/2017JB015418>
- Gallardo, L.A., Meju, M.A., 2011. Structure-coupled multiphysics imaging in geophysical sciences. *Rev. Geophys.* 49, RG1003. <https://doi.org/10.1029/2010RG000330.24>
- Gan, Y., Duan, Q., Gong, W., Tong, C., Sun, Y., Chu, W., Ye, A., Miao, C., Di, Z., 2014. A comprehensive evaluation of various sensitivity analysis methods: A case study with a hydrological model. *Environ. Model. Softw.* 51, 269–285. <https://doi.org/10.1016/j.envsoft.2013.09.031>
- Gottschalk, I.P., Hermans, T., Knight, R., Caers, J., Cameron, D.A., Regnery, J., McCray, J.E., 2017. Integrating non-colocated well and geophysical data to capture subsurface heterogeneity at an aquifer recharge and recovery site. *J. Hydrol.* 555, 407–419. <https://doi.org/10.1016/j.jhydrol.2017.10.028>

References

- Gouveia, W.P., Scales, J. a, 1999. Resolution of seismic waveform inversion: Bayes versus Occam. *Inverse Probl.* 13, 323–349. <https://doi.org/10.1088/0266-5611/13/2/009>
- Gunning, J., Glinsky, M.E., Hedditch, J., 2010. Resolution and uncertainty in 1D CSEM inversion: A Bayesian approach and open-source implementation. *Geophysics* 75, F151. <https://doi.org/10.1190/1.3496902>
- Günther, T., Rücker, C., Spitzer, K., 2006. Three-dimensional modelling and inversion of dc resistivity data incorporating topography - II. Inversion. *Geophys. J. Int.* 166, 506–517. <https://doi.org/10.1111/j.1365-246X.2006.03011.x>
- Hadamard, J., 1902. Sur les problèmes aux dérivées partielles et leur signification physique. *Princet. Univ. Bull.* 13, 49–52.
- Hayley, K., Pidlisecky, A., Bentley, L.R., 2011. Simultaneous time-lapse electrical resistivity inversion. *J. Appl. Geophys.* 75, 401–411. <https://doi.org/10.1016/j.jappgeo.2011.06.035>
- Hermans, T., Kemna, A., Nguyen, F., 2016. Covariance-constrained difference inversion of time-lapse electrical resistivity tomography data. *GEOPHYSICS* 81, E311–E322. <https://doi.org/10.1190/geo2015-0491.1>
- Hermans, T., Nguyen, F., Caers, J., 2015. Uncertainty in training image-based inversion of hydraulic head data constrained to ERT data: Workflow and case study. *Water Resour. Res.* 51, 5332–5352. <https://doi.org/10.1002/2014WR016259>
- Hermans, T., Nguyen, F., Robert, T., Revil, A., 2014. Geophysical methods for monitoring temperature changes in shallow low enthalpy geothermal systems. *Energies* 7, 5083–5118. <https://doi.org/10.3390/en7085083>
- Hermans, T., Vandenbohede, A., Lebbe, L., Martin, R., Kemna, A., Beaujean, J., Nguyen, F., 2012. Imaging artificial salt water infiltration using electrical resistivity tomography constrained by geostatistical data. *J. Hydrol.* 438–439, 168–180. <https://doi.org/10.1016/J.JHYDROL.2012.03.021>
- Hinnell, A.C., Ferr, T.P.A., Vrugt, J.A., Huisman, J.A., Moysey, S., Rings, J., Kowalsky, M.B., 2010. Improved extraction of hydrologic information from geophysical data through coupled hydrogeophysical inversion. *Water Resour. Res.* 46, 1–14. <https://doi.org/10.1029/2008WR007060>
- Hu, L.Y., Chuginova, T., 2008. Multiple-point geostatistics for modeling subsurface heterogeneity: A comprehensive review. *Water Resour. Res.* 44, 1–14. <https://doi.org/10.1029/2008WR006993>

References

- Hübner, R., Heller, K., Günther, T., Kleber, A., 2015. Monitoring hillslope moisture dynamics with surface ERT for enhancing spatial significance of hydrometric point measurements. *Hydrol. Earth Syst. Sci.* 19, 225–240. <https://doi.org/10.5194/hess-19-225-2015>
- Huisman, J.A., Rings, J., Vrugt, J.A., Sorg, J., Vereecken, H., 2010. Hydraulic properties of a model dike from coupled Bayesian and multi-criteria hydrogeophysical inversion. *J. Hydrol.* 380, 62–73. <https://doi.org/10.1016/j.jhydrol.2009.10.023>
- Iglesias, M.A., Lin, K., Stuart, A.M., 2014. Well-posed Bayesian geometric inverse problems arising in subsurface flow. *Inverse Probl.* 30, 114001. <https://doi.org/10.1088/0266-5611/30/11/114001>
- Iglesias, M.A., Stuart, A.M., 2014. Inverse problems and uncertainty quantification. *SIAM News* 2–3.
- Irving, J., Singha, K., 2010. Stochastic inversion of tracer test and electrical geophysical data to estimate hydraulic conductivities. *Water Resour. Res.* 46, W11514. <https://doi.org/10.1029/2009WR008340>
- JafarGandomi, A., Binley, A., 2013. A Bayesian trans-dimensional approach for the fusion of multiple geophysical datasets. *J. Appl. Geophys.* 96, 38–54. <https://doi.org/10.1016/j.jappgeo.2013.06.004>
- Jardani, A., Revil, A., Dupont, J.P., 2013. Stochastic joint inversion of hydrogeophysical data for salt tracer test monitoring and hydraulic conductivity imaging. *Adv. Water Resour.* 52, 62–77. <https://doi.org/10.1016/j.advwatres.2012.08.005>
- Johnson, T.C., Slater, L.D., Ntarlagiannis, D., Day-Lewis, F.D., Elwaseif, M., 2012a. Monitoring groundwater-surface water interaction using time-series and time-frequency analysis of transient three-dimensional electrical resistivity changes. *Water Resour. Res.* 48, 1–13. <https://doi.org/10.1029/2012WR011893>
- Johnson, T.C., Versteeg, R.J., Huang, H., Routh, P.S., 2009. Data-domain correlation approach for joint hydrogeologic inversion of time-lapse hydrogeologic and geophysical data. *Geophysics* 74, F127. <https://doi.org/10.1190/1.3237087>
- Johnson, T.C., Versteeg, R.J., Rockhold, M., Slater, L.D., Ntarlagiannis, D., Greenwood, W.J., Zachara, J., 2012b. Characterization of a contaminated wellfield using 3D electrical resistivity tomography implemented with geostatistical, discontinuous boundary, and known conductivity constraints. *Geophysics* 77, EN85. <https://doi.org/10.1190/geo2012-0121.1>
- Johnson, T.C., Versteeg, R.J., Ward, A., Day-Lewis, F.D., Revil, A., 2010. Improved hydrogeophysical characterization and monitoring through parallel modeling

References

- and inversion of time-domain resistivity and induced-polarization data. *Geophysics* 75, WA27. <https://doi.org/10.1190/1.3475513>
- Jordi, C., Doetsch, J., Günther, T., Schmelzbach, C., Robertsson, J.O., 2018. Geostatistical regularization operators for geophysical inverse problems on irregular meshes. *Geophys. J. Int.* 213, 1374–1386. <https://doi.org/10.1093/gji/ggy055>
- Kaipio, J.P., Karjalainen, P.A., Somersalo, E., Vauhkonen, M., 1999. State estimation in time-varying electrical impedance tomography. *Ann. N. Y. Acad. Sci.* <https://doi.org/10.1111/j.1749-6632.1999.tb09492.x>
- Kaipio, J.P., Somersalo, E., 2006. *Statistical and computational inverse problems.* Springer-Verlag, New York.
- Karaoulis, M., Kim, J.-H., Tsourlos, P.I., 2011a. 4D active time constrained resistivity inversion. *J. Appl. Geophys.* 73, 25–34. <https://doi.org/10.1016/j.jappgeo.2010.11.002>
- Karaoulis, M., Revil, A., Werkema, D.D., Minsley, B.J., Woodruff, W.F., Kemna, A., 2011b. Time-lapse three-dimensional inversion of complex conductivity data using an active time constrained (ATC) approach. *Geophys. J. Int.* 187, 237–251. <https://doi.org/10.1111/j.1365-246X.2011.05156.x>
- Kemna, A., 2000. *Tomographic inversion of complex resistivity.* Ruhr-Universität Bochum.
- Kemna, A., Binley, A.M., Slater, L., 2004. Cross-borehole IP imaging for engineering and environmental applications. *Geophysics* 69, 97–107. <https://doi.org/10.1190/1.1649379>
- Kim, J.-H., Yi, M.-J., Park, S.-G., Kim, J.G., 2009. 4-D inversion of DC resistivity monitoring data acquired over a dynamically changing earth model. *J. Appl. Geophys.* 68, 522–532. <https://doi.org/10.1016/j.jappgeo.2009.03.002>
- Kitanidis, P.K., 2015a. Three-dimensional ERT imaging by the geostatistical approach, in: *American Geophysical Union Fall Meeting.* San Francisco, California.
- Kitanidis, P.K., 2015b. Persistent questions of heterogeneity, uncertainty, and scale in subsurface flow and transport. *Water Resour. Res.* 51, 5888–5904. <https://doi.org/10.1002/2015WR017639>
- Kitanidis, P.K., 2011. Bayesian and Geostatistical Approaches to Inverse Problems, in: Biegler, L., Biros, G., Ghattas, O., Heinkenschloss, M., Keyes, D., Mallick, B., Marzouk, Y., Tenorio, L., van Bloemen Waanders, B., Willcox, K. (Eds.), *Large-*

References

- Scale Inverse Problems and Quantification of Uncertainty. John Wiley & Sons, Ltd, Chichester, UK, pp. 71–85. <https://doi.org/10.1002/9780470685853>
- Kitanidis, P.K., 1995. Quasi-linear geostatistical theory for inversing. *Water Resour. Res.* 31, 2411–2419.
- Koestel, J., Kemna, A., Javaux, M., Binley, A., Vereecken, H., 2008. Quantitative imaging of solute transport in an unsaturated and undisturbed soil monolith with 3-D ERT and TDR. *Water Resour. Res.* 44, 1–17. <https://doi.org/10.1029/2007WR006755>
- Kowalsky, M.B., Finsterle, S., Peterson, J., Hubbard, S., Rubin, Y., Majer, E., Ward, A., Gee, G., 2005. Estimation of field-scale soil hydraulic and dielectric parameters through joint inversion of GPR and hydrological data. *Water Resour. Res.* 41, n/a-n/a. <https://doi.org/10.1029/2005WR004237>
- Labrecque, D.J., Yang, X., 2001. Difference inversion of ERT data: a fast inversion method for 3-D in situ monitoring. *J. Environ. Eng. Geophys.* 6, 83–89. <https://doi.org/dx.doi.org/10.4133/JEEG6.2.83>
- Lee, J., Kitanidis, P.K., 2014. Large-scale hydraulic tomography and joint inversion of head and tracer data using the Principal Component Geostatistical Approach (PCGA). *Water Resour. Res.* 50. <https://doi.org/10.1002/2014WR015483>
- Lehikoinen, A., Finsterle, S., Voutilainen, A., Kowalsky, M.B., Kaipio, J.P., 2009. Dynamical inversion of geophysical ERT data: state estimation in the vadose zone. *Inverse Probl. Sci. Eng.* 17, 715–736. <https://doi.org/10.1080/17415970802475951>
- Lelièvre, P.G., Farquharson, C.G., 2013. Gradient and smoothness regularization operators for geophysical inversion on unstructured meshes. *Geophys. J. Int.* 195, 330–341. <https://doi.org/10.1093/gji/ggt255>
- Lesparre, N., Nguyen, F., Kemna, A., Robert, T., Hermans, T., Daoudi, M., Flores-Orozco, A., 2017. A new approach for time-lapse data weighting in electrical resistivity tomography. *GEOPHYSICS* 82, E325–E333. <https://doi.org/10.1190/geo2017-0024.1>
- Leube, P.C., Geiges, A., Nowak, W., 2012. Bayesian assessment of the expected data impact on prediction confidence in optimal sampling design. *Water Resour. Res.* 48, 1–16. <https://doi.org/10.1029/2010WR010137>
- Linde, N., 2014. Falsification and corroboration of conceptual hydrological models using geophysical data. *Wiley Interdiscip. Rev. Water* 1, 151–171. <https://doi.org/10.1002/wat2.1011>

References

- Linde, N., Binley, A., Tryggvason, A., Pedersen, L.B., Revil, A., 2006. Improved hydrogeophysical characterization using joint inversion of cross-hole electrical resistance and ground-penetrating radar traveltime data. *Water Resour. Res.* 42, WR005131. <https://doi.org/10.1029/2006WR005131>
- Linde, N., Doetsch, J., 2016. Joint Inversion in Hydrogeophysics and Near-Surface Geophysics, in: Moorkamp, M., Lelievre, P., Linde, N., Khan, A. (Eds.), *Integrated Imaging of the Earth*. John Wiley & Sons, Inc., Hoboken, New Jersey, pp. 117–135. <https://doi.org/10.1002/9781118929063.ch7>
- Linde, N., Ginsbourger, D., Irving, J., Nobile, F., Doucet, A., 2017. On uncertainty quantification in hydrogeology and hydrogeophysics. *Adv. Water Resour.* 110, 166–181. <https://doi.org/10.1016/J.ADVWATRES.2017.10.014>
- Linde, N., Lochbühler, T., Dogan, M., Van Dam, R.L., 2015a. Tomogram-based comparison of geostatistical models: Application to the Macrodispersion Experiment (MADE) site. *J. Hydrol.* 531, 543–556. <https://doi.org/10.1016/j.jhydrol.2015.10.073>
- Linde, N., Renard, P., Mukerji, T., Caers, J., 2015b. Geological Realism in Hydrogeological and Geophysical Inverse Modeling: a Review. *Adv. Water Resour.* 86, 86–101. <https://doi.org/10.1016/j.advwatres.2015.09.019>
- Lochbühler, T., Doetsch, J., Brauchler, R., Linde, N., 2013. Structure-coupled joint inversion of geophysical and hydrological data. *Geophysics* 78, ID1–ID14. <https://doi.org/10.1190/geo2012-0460.1>
- Loke, M.H., Wilkinson, P.B., Uhlemann, S.S., Chambers, J.E., Oxby, L.S., 2014. Computation of optimized arrays for 3-D electrical imaging surveys. *Geophys. J. Int.* 199, 1751–1764. <https://doi.org/10.1093/gji/ggu357>
- Looms, M.C., Binley, A., Jensen, K.H., Nielsen, L., Hansen, T.M., 2008. Identifying Unsaturated Hydraulic Parameters Using an Integrated Data Fusion Approach on Cross-Borehole Geophysical Data. *Vadose Zo. J.* 7, 238. <https://doi.org/10.2136/vzj2007.0087>
- Mariethoz, G., Caers, J., 2014. *Multiple-Point Geostatistics*. John Wiley & Sons, Ltd, Chichester, UK.
- Maurer, H., Boerner, D.E., Curtis, A., 2000. Design strategies for electromagnetic geophysical surveys. *Inverse Probl.* 16, 1097–1117. <https://doi.org/10.1088/0266-5611/16/5/302>
- Maurer, H., Curtis, A., Boerner, D.E., 2010. Recent advances in optimized geophysical survey design. *Geophysics* 75, A177–A194. <https://doi.org/10.1190/1.3484194>

References

- McLachlan, P.J., Chambers, J.E., Uhlemann, S.S., Binley, A., 2017. Geophysical characterisation of the groundwater–surface water interface. *Adv. Water Resour.* 109, 302–319. <https://doi.org/10.1016/j.advwatres.2017.09.016>
- Menke, W., 1989. *Geophysical Data Analysis: Discrete Inverse Theory*. Academic Press.
- Miller, C.R., Routh, P.S., 2007. Resolution analysis of geophysical images: Comparison between point spread function and region of data influence measures. *Geophys. Prospect.* 55, 835–852. <https://doi.org/10.1111/j.1365-2478.2007.00640.x>
- Miller, C.R., Routh, P.S., Brosten, T.R., McNamara, J.P., 2008. Application of time-lapse ERT imaging to watershed characterization. *Geophysics* 73, G7. <https://doi.org/10.1190/1.2907156>
- Mitchell, M.A., Oldenburg, D.W., 2016. Data quality control methodology for large , non-conventional DC resistivity datasets. *J. Appl. Geophys.* 3, 948–953. <https://doi.org/10.1016/j.jappgeo.2016.09.018>
- Mitchell, V., Knight, R., Pidlisecky, A., 2011. Inversion of time-lapse electrical resistivity imaging data for monitoring infiltration. *Lead. Edge* 140–144.
- Moghadas, D., Badorreck, A., 2019. Machine learning to estimate soil moisture from geophysical measurements of electrical conductivity. *Near Surf. Geophys.* <https://doi.org/10.1002/nsg.12036>
- Morris, M.D., 1991. *Factorial Sampling Plans for Preliminary Computational Experiments*, Technometrics.
- Mosegaard, K., 1999. Resolution analysis of general inverse problems through inverse Monte Carlo sampling. *Inverse Probl.* 14, 405–426. <https://doi.org/10.1088/0266-5611/14/3/004>
- Mosegaard, K., Tarantola, A., 1995. Monte Carlo sampling of solutions to inverse problems. *J. Geophys. Res. (Solid Earth)* 100, 12431–12448. <https://doi.org/10.1029/94JB03097>
- Moysey, S., Singha, K., Knight, R., 2005. A framework for inferring field-scale rock physics relationships through numerical simulation. *Geophys. Res. Lett.* 32, 1–4. <https://doi.org/10.1029/2004GL022152>
- Nenna, V., Pidlisecky, A., Knight, R., 2011. Informed experimental design for electrical resistivity imaging. *Near Surf. Geophys.* 9, 469–482. <https://doi.org/10.3997/1873-0604.2011027>

References

- Neuman, S.P., Xue, L., Ye, M., Lu, D., 2012. Bayesian analysis of data-worth considering model and parameter uncertainties. *Adv. Water Resour.* 36, 75–85. <https://doi.org/10.1016/j.advwatres.2011.02.007>
- Nguyen, F., Garambois, S., Jongmans, D., Pirard, E., Loke, M.H., 2005. Image processing of 2D resistivity data for imaging faults. *J. Appl. Geophys.* 57, 260–277. <https://doi.org/10.1016/j.jappgeo.2005.02.001>
- Nguyen, F., Kemna, A., Robert, T., Hermans, T., 2016. Data-driven selection of the minimum-gradient support parameter in time-lapse focused electric imaging. *Geophysics* 81, A1–A5. <https://doi.org/10.1190/geo2015-0226.1>
- Nimmer, R.E., Osiensky, J.L., Binley, A.M., Williams, B.C., 2008. Three-dimensional effects causing artifacts in two-dimensional, cross-borehole, electrical imaging. *J. Hydrol.* 359, 59–70. <https://doi.org/10.1016/j.jhydrol.2008.06.022>
- Nolet, G., Montelli, R., Virieux, J., 1999. Explicit, approximate expressions for the resolution and a posteriori covariance of massive tomographic systems. *Geophys. J. Int.* 138, 36–44. <https://doi.org/10.1046/j.1365-246X.1999.00858.x>
- Nowak, W., Bode, F., Loschko, M., 2015. A Multi-objective Optimization Concept for Risk-based Early-warning Monitoring Networks in Well Catchments. *Procedia Environ. Sci.* 25, 191–198. <https://doi.org/10.1016/j.proenv.2015.04.026>
- Nowak, W., Rubin, Y., de Barros, F.P.J., 2012. A hypothesis-driven approach to optimize field campaigns. *Water Resour. Res.* 48, W06509. <https://doi.org/10.1029/2011WR011016>
- Oldenborger, G.A., Knoll, M.D., Routh, P.S., LaBrecque, D.J., 2007. Time-lapse ERT monitoring of an injection/withdrawal experiment in a shallow unconfined aquifer. *Geophysics* 72, F177–F187. <https://doi.org/10.1190/1.2734365>
- Oldenborger, G.A., Routh, P.S., 2009. The point-spread function measure of resolution for the 3-D electrical resistivity experiment. *Geophys. J. Int.* 176, 405–414. <https://doi.org/10.1111/j.1365-246X.2008.04003.x>
- Oldenborger, G.A., Routh, P.S., Knoll, M.D., 2005. Sensitivity of electrical resistivity tomography data to electrode position errors. *Geophys. J. Int.* 163, 1–9. <https://doi.org/10.1111/j.1365-246X.2005.02714.x>
- Oldenburg, D.W., Li, Y., 1999. Estimating depth of investigation in dc resistivity and IP surveys. *Geophysics* 64, 403. <https://doi.org/10.1190/1.1444545>

References

- Oware, E.K., Moysey, S.M.J., Khan, T., 2013. Physically based regularization of hydrogeophysical inverse problems for improved imaging of process-driven systems. *Water Resour. Res.* 49, 6238–6247. <https://doi.org/10.1002/wrcr.20462>
- Park, H., Scheidt, C., Fenwick, D., Boucher, A., Caers, J., 2013. History matching and uncertainty quantification of facies models with multiple geological interpretations. *Comput. Geosci.* 17, 609–621. <https://doi.org/10.1007/s10596-013-9343-5>
- Parsekian, A.D., Claes, N., Singha, K., Minsley, B.J., Carr, B., Voytek, E., Harmon, R., Kass, A., Carey, A., Thayer, D., Flinchum, B., 2017. Comparing Measurement Response and Inverted Results of Electrical Resistivity Tomography Instruments. *J. Environ. Eng. Geophys.* 22, 249–266. <https://doi.org/10.2113/JEEG22.3.249>
- Parsekian, A.D., Singha, K., Minsley, B.J., Holbrook, W.S., Slater, L., 2015. Multiscale geophysical imaging of the critical zone. *Rev. Geophys.* 53, 1–26. <https://doi.org/10.1002/2014RG000465>
- Pollock, D., Cirpka, O.A., 2010. Fully coupled hydrogeophysical inversion of synthetic salt tracer experiments. *Water Resour. Res.* 46, W07501. <https://doi.org/10.1029/2009WR008575>
- Portniaguine, O., Zhdanov, M.S., 1999. Focusing geophysical inversion images. *GEOPHYSICS* 64, 874–887. <https://doi.org/10.1190/1.1444596>
- Ramirez, A.L., Daily, W.D., Newmark, R.L., 1995. Electrical resistance tomography for steam injection monitoring and process control. *J. Environ. Eng. Geophys.* 1, 39. <https://doi.org/10.4133/JEEG1.A.39>
- Ramirez, A.L., Nitao, J.J., Hanley, W.G., Aines, R., Glaser, R.E., Sengupta, S.K., Dyer, K.M., Hickling, T.L., Daily, W.D., 2005. Stochastic inversion of electrical resistivity changes using a Markov Chain Monte Carlo approach. *J. Geophys. Res.* 110, B02101. <https://doi.org/10.1029/2004JB003449>
- Ray, A., Kaplan, S., Washbourne, J., Albertin, U., 2018. Low frequency full waveform seismic inversion within a tree based Bayesian framework. *Geophys. J. Int.* 212, 522–542. <https://doi.org/10.1093/gji/ggx428>
- Ray, A., Sekar, A., Hoversten, G.M., Albertin, U., 2016. Frequency domain full waveform elastic inversion of marine seismic data from the Alba field using a Bayesian trans-dimensional algorithm. *Geophys. J. Int.* 205, 915–937. <https://doi.org/10.1093/gji/ggw061>

References

- Reichle, R.H., Crow, W.T., Keppenne, C.L., 2008. An adaptive ensemble Kalman filter for soil moisture data assimilation. *Water Resour. Res.* 44, 1–13. <https://doi.org/10.1029/2007WR006357>
- Robinson, J., Johnson, T., Slater, L., 2015. Challenges and opportunities for fractured rock imaging using 3D cross borehole electrical resistivity. *Geophysics* 80, E49–E61. <https://doi.org/10.1190/GEO2014-0138.1>
- Rojas, R., Feyen, L., Dassargues, A., 2008. Conceptual model uncertainty in groundwater modeling: Combining generalized likelihood uncertainty estimation and Bayesian model averaging. *Water Resour. Res.* 44, 1–16. <https://doi.org/10.1029/2008WR006908>
- Romero-Ruiz, A., Linde, N., Keller, T., Or, D., 2018. A Review of Geophysical Methods for Soil Structure Characterization. *Rev. Geophys.* 56, 672–697. <https://doi.org/10.1029/2018RG000611>
- Ross, M., 2004. Consideration of available geophysical techniques for non-intrusive survey of B291 trenches. Sellafeld, United Kingdom.
- Roubinet, D., Irving, J., 2014. Discrete-dual-porosity model for electric current flow in fractured rock. *J. Geophys. Res. Solid Earth* 119, 767–786. <https://doi.org/10.1002/2013JB010668>
- Routh, P.S., 2009. A practical strategy to interrogate resolution , uncertainty and value of information in geophysical inverse problem. *Geohorizons* 27–37.
- Ruggeri, P., Gloaguen, E., Lefebvre, R., Irving, J., Holliger, K., 2014. Integration of hydrological and geophysical data beyond the local scale: Application of Bayesian sequential simulation to field data from the Saint-Lambert-de-Lauzon site, Québec, Canada. *J. Hydrol.* 514, 271–280. <https://doi.org/10.1016/J.JHYDROL.2014.04.031>
- Ruggeri, P., Irving, J., Gloaguen, E., Holliger, K., 2013. Regional-scale integration of multiresolution hydrological and geophysical data using a two-step Bayesian sequential simulation approach. *Geophys. J. Int.* 194, 289–303. <https://doi.org/10.1093/gji/ggt067>
- Salamon, P., Feyen, L., 2010. Disentangling uncertainties in distributed hydrological modeling using multiplicative error models and sequential data assimilation. *Water Resour. Res.* 46, 1–20. <https://doi.org/10.1029/2009WR009022>
- Scales, J.A., Snieder, R., Treitel, S., 1997. To Bayes or not to Bayes ? *Geophysics* 62, 1045–1046.

References

- Scheidt, C., Li, L., Caers, J., 2018. Quantifying Uncertainty in Subsurface Systems, Geophysical Monograph Series. John Wiley & Sons, Inc., Hoboken, NJ, USA. <https://doi.org/10.1002/9781119325888>
- Schmidt-Hattenberger, C., Bergmann, P., Labitzke, T., Wagner, F., Rippe, D., 2016. Permanent crosshole electrical resistivity tomography (ERT) as an established method for the long-term CO₂ monitoring at the Ketzin pilot site. *Int. J. Greenh. Gas Control* 52, 432–448. <https://doi.org/10.1016/j.ijggc.2016.07.024>
- Schöniger, A., Nowak, W., Hendricks Franssen, H.-J., 2012. Parameter estimation by ensemble Kalman filters with transformed data: Approach and application to hydraulic tomography. *Water Resour. Res.* 48, W04502. <https://doi.org/10.1029/2011WR010462>
- Shi, L., Zeng, L., Tang, Y., Chen, C., Yang, J., 2013. Uncertainty quantification of contaminant transport and risk assessment with conditional stochastic collocation method. *Stoch. Environ. Res. Risk Assess.* 27, 1453–1464. <https://doi.org/10.1007/s00477-012-0682-x>
- Shi, W., 1998. Advanced modeling and inversion techniques for three-dimensional geoelectrical surveys. Massachusetts Institute of Technology.
- Sibbertt, L., Chambers, J.E., Li, B., Wilkinson, P.B., 2017. Total Generalised Variation: An improved regulariser for Electrical Resistivity Tomography inversion., in: *Geophysical Research Abstracts*. pp. EGU2017-14348.
- Singha, K., Day-Lewis, F.D., Johnson, T., Slater, L.D., 2015. Advances in interpretation of subsurface processes with time-lapse electrical imaging. *Hydrol. Process.* 29, 1549–1576. <https://doi.org/10.1002/hyp.10280>
- Singha, K., Gorelick, S.M., 2006. Effects of spatially variable resolution on field-scale estimates of tracer concentration from electrical inversions using Archie's law. *Geophysics* 71, G83. <https://doi.org/10.1190/1.2194900>
- Skyes, J.F., Wilson, J.L., Andrews, R.W., 1985. Sensitivity analysis for steady state groundwater flow using adjoint operators. *Water Resour. Res.* 21, 359–371.
- Slater, L., Binley, A., 2003. Evaluation of permeable reactive barrier (PRB) integrity using electrical imaging methods. *Geophysics* 68, 911–921. <https://doi.org/10.1190/1.1581043>
- Slater, L., Binley, A.M., Daily, W., Johnson, R., 2000. Cross-hole electrical imaging of a controlled saline tracer injection. *J. Appl. Geophys.* 44, 85–102. [https://doi.org/10.1016/S0926-9851\(00\)00002-1](https://doi.org/10.1016/S0926-9851(00)00002-1)

References

- Slater, L.D., Binley, A., Brown, D., 1997. Electrical Imaging of Fractures Using Ground-Water Salinity Change. *Ground Water* 35, 436–442. <https://doi.org/10.1111/j.1745-6584.1997.tb00103.x>
- Sobol', I., 2001. Global sensitivity indices for nonlinear mathematical models and their Monte Carlo estimates. *Math. Comput. Simul.* 55, 271 – 280. [https://doi.org/10.1016/S0378-4754\(00\)00270-6](https://doi.org/10.1016/S0378-4754(00)00270-6)
- Stummer, P., Maurer, H.R., Green, A.G., 2004. Experimental design: Electrical resistivity data sets that provide optimum subsurface information. *Geophysics* 69, 120–139.
- Tarantola, A., 2006. Popper, Bayes and the inverse problem. *Nat. Phys.* 2, 492–494. <https://doi.org/10.1038/nphys375>
- Tarantola, A., 2005. *Inverse Problem Theory and Methods for Model Parameter Estimation*. SIAM.
- Trainor-Guitton, W.J., Ramirez, A., Yang, X., Mansoor, K., Sun, Y., Carroll, S., 2013. Value of information methodology for assessing the ability of electrical resistivity to detect CO₂/brine leakage into a shallow aquifer. *Int. J. Greenh. Gas Control* 18, 101–113. <https://doi.org/10.1016/j.ijggc.2013.06.018>
- Tran, A.P., Dafflon, B., Hubbard, S.S., 2017. Coupled land surface–subsurface hydrogeophysical inverse modeling to estimate soil organic carbon content and explore associated hydrological and thermal dynamics in the Arctic tundra. *Cryosph.* 11, 2089–2109. <https://doi.org/10.5194/tc-11-2089-2017>
- Tran, A.P., Dafflon, B., Hubbard, S.S., Kowalsky, M.B., Long, P., Tokunaga, T.K., Williams, K.H., 2016. Quantifying shallow subsurface water and heat dynamics using coupled hydrological-thermal-geophysical inversion. *Hydrol. Earth Syst. Sci.* 20, 3477–3491. <https://doi.org/10.5194/hess-20-3477-2016>
- Trigo, F.C., Gonzalez-Lima, R., Amato, M.B.P., 2004. Electrical impedance tomography using the extended Kalman filter. *IEEE Trans. Biomed. Eng.* 51, 72–81. <https://doi.org/10.1109/TBME.2003.820389>
- Truex, M.J., Johnson, T.C., Strickland, C.E., Peterson, J.E., Hubbard, S.S., 2013. Monitoring Vadose Zone Desiccation with Geophysical Methods. *Vadose Zo. J.* 12, 0. <https://doi.org/10.2136/vzj2012.0147>
- Tsai, F.T.C., Elshall, A., 2013. Hierarchical Bayesian model averaging for hydrostratigraphic modeling: Uncertainty segregation and comparative evaluation. *Water Resour. Res.* 49, 5520–5536. <https://doi.org/10.1002/wrcr.20428>

References

- Tso, C.-H.M., Kuras, O., Wilkinson, P.B., Uhlemann, S., Chambers, J.E., Meldrum, P.I., Graham, J., Sherlock, E.F., Binley, A., 2017. Improved characterisation and modelling of measurement errors in electrical resistivity tomography (ERT) surveys. *J. Appl. Geophys.* 146, 103–119. <https://doi.org/10.1016/J.JAPPGEO.2017.09.009>
- Tso, C.M., Kuras, O., Binley, A., 2019. On the field estimation of moisture content using electrical geophysics - the impact of petrophysical model uncertainty. *Water Resour. Res.* 2019WR024964. <https://doi.org/10.1029/2019WR024964>
- Uhlemann, S., Wilkinson, P.B., Maurer, H., Wagner, F.M., Johnson, T.C., Chambers, J.E., 2018. Optimized survey design for Electrical Resistivity Tomography: combined optimization of measurement configuration and electrode placement. *Geophys. J. Int.*
- Vauhkonen, M., Karjalainen, P.A., Kaipio, J.P., 1998. A Kalman filter approach to track fast impedance changes in electrical impedance tomography. *IEEE Trans Biomed Eng* 45, 486–493. <https://doi.org/10.1109/10.664204>
- Vrugt, J.A., Robinson, B.A., 2007. Improved evolutionary optimization from genetically adaptive multimethod search. *Proc. Natl. Acad. Sci.* 104, 708–711. <https://doi.org/10.1073/pnas.0610471104>
- Vrugt, J.A., Robinson, B.A., Hyman, J.M., 2009. Self-Adaptive Multimethod Search for Global Optimization in Real-Parameter Spaces. *IEEE Trans. Evol. Comput.* 13, 243–259. <https://doi.org/10.1109/TEVC.2008.924428>
- Wagner, F.M., Bergmann, P., Rücker, C., Wiese, B., Labitzke, T., Schmidt-Hattenberger, C., Maurer, H., 2015a. Impact and mitigation of borehole related effects in permanent crosshole resistivity imaging: An example from the Ketzin CO₂ storage site. *J. Appl. Geophys.* 123, 102–111. <https://doi.org/10.1016/j.jappgeo.2015.10.005>
- Wagner, F.M., Günther, T., Schmidt-Hattenberger, C., Maurer, H., 2015b. Constructive optimization of electrode locations for target-focused resistivity monitoring. *Geophysics* 80, E29–E40. <https://doi.org/10.1190/geo2014-0214.1>
- Wagner, F.M., Wiese, B.U., 2018. Fully coupled inversion on a multi-physical reservoir model – Part II: The Ketzin CO₂ storage reservoir. *Int. J. Greenh. Gas Control* 75, 273–281. <https://doi.org/10.1016/J.IJGGC.2018.04.009>
- Wainwright, H.M., Finsterle, S., Jung, Y., Zhou, Q., Birkholzer, J.T., 2014. Making sense of global sensitivity analyses. *Comput. Geosci.* 65, 84–94. <https://doi.org/10.1016/j.cageo.2013.06.006>

References

- Wainwright, H.M., Flores Orozco, A., Bücken, M., Dafflon, B., Chen, J., Hubbard, S.S., Williams, K.H., 2016. Hierarchical Bayesian method for mapping biogeochemical hot spots using induced polarization imaging. *Water Resour. Res.* 52, 533–551. <https://doi.org/10.1002/2015WR017763>
- Ward, W.O.C., Wilkinson, P.B., Chambers, J.E., Oxby, L.S., Bai, L., 2014. Distribution-based fuzzy clustering of electrical resistivity tomography images for interface detection. *Geophys. J. Int.* 197, 310–321. <https://doi.org/10.1093/gji/ggu006>
- Wehrer, M., Slater, L.D., 2015. Characterization of water content dynamics and tracer breakthrough by 3-D electrical resistivity tomography (ERT) under transient unsaturated conditions. *Water Resour. Res.* 51, 97–124. <https://doi.org/10.1002/2014WR016131>
- Whiteley, J.S., Chambers, J.E., Uhlemann, S., Wilkinson, P.B., Kendall, J.M., 2018. Geophysical monitoring of moisture-induced landslides: a review. *Rev. Geophys.* <https://doi.org/10.1029/2018RG000603>
- Wiese, B., Wagner, F., Norden, B., Maurer, H., Schmidt-Hattenberger, C., 2018. Fully coupled inversion on a multi-physical reservoir model - Part I: Theory and concept. *Int. J. Greenh. Gas Control.*
- Wilkinson, P., Chambers, J., Uhlemann, S., Meldrum, P., Smith, A., Dixon, N., Loke, M.H., 2016. Reconstruction of landslide movements by inversion of 4-D electrical resistivity tomography monitoring data. *Geophys. Res. Lett.* 43, 1166–1174. <https://doi.org/10.1002/2015GL067494>
- Wilkinson, P.B., Chambers, J.E., Lelliott, M., Wealthall, G.P., Ogilvy, R.D., 2008. Extreme sensitivity of crosshole electrical resistivity tomography measurements to geometric errors. *Geophys. J. Int.* 173, 49–62. <https://doi.org/10.1111/j.1365-246X.2008.03725.x>
- Wilkinson, P.B., Chambers, J.E., Meldrum, P.I., Gunn, D.A., Ogilvy, R.D., Kuras, O., 2010a. Predicting the movements of permanently installed electrodes on an active landslide using time-lapse geoelectrical resistivity data only. *Geophys. J. Int.* 183, 543–556. <https://doi.org/10.1111/j.1365-246X.2010.04760.x>
- Wilkinson, P.B., Loke, M.H., Meldrum, P.I., Chambers, J.E., Kuras, O., Gunn, D.A., Ogilvy, R.D., 2012. Practical aspects of applied optimized survey design for electrical resistivity tomography. *Geophys. J. Int.* 189, 428–440. <https://doi.org/10.1111/j.1365-246X.2012.05372.x>
- Wilkinson, P.B., Meldrum, P.I., Chambers, J.E., Kuras, O., Ogilvy, R.D., 2006. Improved strategies for the automatic selection of optimized sets of electrical resistivity

References

- tomography measurement configurations. *Geophys. J. Int.* 167, 1119–1126.
<https://doi.org/10.1111/j.1365-246X.2006.03196.x>
- Wilkinson, P.B., Meldrum, P.I., Kuras, O., Chambers, J.E., Holyoake, S.J., Ogilvy, R.D., 2010b. High-resolution Electrical Resistivity Tomography monitoring of a tracer test in a confined aquifer. *J. Appl. Geophys.* 70, 268–276.
<https://doi.org/10.1016/j.jappgeo.2009.08.001>
- Wilkinson, P.B., Uhlemann, S., Meldrum, P.I., Chambers, J.E., Carrière, S., Oxby, L.S., Loke, M.H.H., 2015. Adaptive time-lapse optimized survey design for electrical resistivity tomography monitoring. *Geophys. J. Int.* 203, 755–766.
<https://doi.org/10.1093/gji/ggv329>
- Xue, L., Zhang, D., 2014. A multimodel data assimilation framework via the ensemble Kalman filter. *Water Resour. Res.* 50, 4197–4219.
<https://doi.org/10.1002/2013WR014525>
- Yang, X., Chen, X., Carrigan, C.R., Ramirez, A.L., 2014. Uncertainty quantification of CO₂ saturation estimated from electrical resistance tomography data at the Cranfield site. *Int. J. Greenh. Gas Control* 27, 59–68.
<https://doi.org/10.1016/j.ijggc.2014.05.006>
- Yang, X., Lassen, R.N., Jensen, K.H., Looms, M.C., 2015. Monitoring CO₂ migration in a shallow sand aquifer using 3D crosshole electrical resistivity tomography. *Int. J. Greenh. Gas Control* 42, 534–544. <https://doi.org/10.1016/J.IJGGC.2015.09.005>
- Yeh, T.-C.J., Liu, S., 2000. Hydraulic tomography : Development of a new aquifer test method. *Water Resour. Res.* 36, 2095–2105.
- Yeh, T.-C.J., Liu, S., Glass, R.J., Baker, K., Brainard, J.R., Alumbaugh, D., LaBrecque, D., 2002. A geostatistically based inverse model for electrical resistivity surveys and its applications to vadose zone hydrology. *Water Resour. Res.* 38, WR001204.
<https://doi.org/10.1029/2001WR001204>
- Zhou, J., Revil, A., Jardani, A., 2016. Stochastic structure-constrained image-guided inversion of geophysical data. *Geophysics* 81, E89–E101.
<https://doi.org/10.1190/geo2014-0569.1>
- Zhou, J., Revil, A., Karaoulis, M., Hale, D., Doetsch, J., Cuttler, S., 2014. Image-guided inversion of electrical resistivity data. *Geophys. J. Int.* 197, 292–309.
<https://doi.org/10.1093/gji/ggu001>

Appendix 1: Derivation of the Gauss-Newton solution to the regularized inverse problem

We begin by writing the objective function $\phi = \phi(\mathbf{m})$ using Taylor expansion and set $\mathbf{m} = \mathbf{m}^k + \Delta\mathbf{m}$

$$\phi(\mathbf{m}^k + \Delta\mathbf{m}) = \phi(\mathbf{m}^k) + \nabla\phi(\mathbf{m}^k)\Delta\mathbf{m} + \frac{1}{2}\Delta\mathbf{m}^T\nabla^2\phi(\mathbf{m}^k)\Delta\mathbf{m} + H.O.T. \quad (11)$$

where \mathbf{m}^k is model estimate at the k -th iteration, $\Delta\mathbf{m}$ is model increment, and *H.O.T.* denotes higher-order terms. At the true solution $\mathbf{m} = \mathbf{m}^*$, ϕ reaches a minimum so the derivative of the above equation is zero. Therefore, we differentiate both sides of the equation above, drop the higher-order terms (third derivatives or above) and set it = 0

$$\nabla\phi(\mathbf{m}^k + \Delta\mathbf{m}) \approx \nabla\phi(\mathbf{m}^k) + \nabla^2\phi(\mathbf{m}^k)\Delta\mathbf{m} = 0 \quad (12)$$

Rearranging the terms give:

$$\boxed{\nabla^2\phi(\mathbf{m}^k)\Delta\mathbf{m} = -\nabla\phi(\mathbf{m}^k)} \quad (13)$$

Now we seek to obtain the first and second derivatives of the objective function. The commonly used objective function takes the form of $\phi = \phi_d + \alpha\phi_m$, where α is a scalar damping factor, ϕ_d and ϕ_m are the data misfit and model roughness objective functions, respectively.

The data misfit function ϕ_d is the sum of data residuals r_i squared (or equivalently in matrix notation):

$$\phi_d = \sum_{i=1}^N r_i^2 = \sum_{i=1}^N \left(\frac{d_i - F_i(\mathbf{m})}{\sigma_i} \right)^2 \quad \text{or} \quad \phi_d = (\mathbf{d} - \mathbf{F}(\mathbf{m}))^T \mathbf{W}_d^T \mathbf{W}_d (\mathbf{d} - \mathbf{F}(\mathbf{m})) \quad (14)$$

where the data weighting matrix \mathbf{W}_d is a diagonal matrix and its (i, i) -th entry is given by $1/\sigma_i$. The model roughness objective function ϕ_m is (or equivalently in matrix notation):

$$\phi_m = \sum_{j=1}^M \sum_{j' \in S_j} (m_j - m_{j'})^2 \quad \text{or} \quad \phi_m = \mathbf{m}^{kT} \mathbf{R}_m \mathbf{m}^k \quad (15)$$

where S_j is a set of parameter indices that are neighbors of j . The roughness matrix \mathbf{R} is a symmetric matrix with integer coefficient. The sum of coefficients in each row and each column should be zero.

Appendix 1: Derivation of the Gauss-Newton solution to the regularized inverse problem

Therefore, the combined objective function is:

$$\phi = \phi_d + \alpha\phi_m = \sum_{i=1}^N \left(\frac{d_i - F_i(\mathbf{m})}{\sigma_i} \right)^2 + \alpha \sum_{j=1}^M \sum_{j'=1}^{M'} (m_j - m_{j'})^2$$

or $\underbrace{\phi}_{1 \times 1} = \phi_d + \alpha\phi_m = (\mathbf{d} - \mathbf{F}(\mathbf{m}))^T \underbrace{\mathbf{W}_d^T}_{N \times N} \underbrace{\mathbf{W}_d}_{N \times 1} (\mathbf{d} - \mathbf{F}(\mathbf{m})) + \alpha \mathbf{m}^k{}^T \underbrace{\mathbf{R}_m}_{M \times M} \underbrace{\mathbf{m}^k}_{M \times 1}$ (16)

Taking derivative with respect to \mathbf{m} gives the first derivative of ϕ ,

$$\frac{\partial \phi}{\partial m_j} = -2 \sum_{i=1}^N \left(\frac{d_i - F_i(\mathbf{m})}{\sigma_i} \right) \left(\frac{1}{\sigma_i} \right) \frac{\partial F_i}{\partial m_j} + 2\alpha \sum_{j=1}^M \sum_{j'=1}^{M'} (m_j - m_{j'})$$

or $\boxed{\nabla \phi(\mathbf{m}^k) = 2[-\mathbf{J}^T \mathbf{W}_d^T \mathbf{W}_d (\mathbf{d} - \mathbf{F}(\mathbf{m})) + \alpha \mathbf{R}_m \mathbf{m}^k]}$ (17)

where $\begin{bmatrix} \partial F_1 / \partial m_1 & \cdots & \partial F_1 / \partial m_M \\ \vdots & \ddots & \vdots \\ \partial F_N / \partial m_1 & \cdots & \partial F_N / \partial m_M \end{bmatrix}$ are the entries of the Jacobian matrix \mathbf{J} of size $N \times M$.

We take derivative with respect to \mathbf{m} again to obtain the second derivative of ϕ ,

$$\frac{\partial^2 \phi}{\partial m_j^2} = -2 \sum_{i=1}^N \left(\frac{d_i - F_i(\mathbf{m})}{\sigma_i} \right) \left(\frac{1}{\sigma_i} \right) \frac{\partial^2 F_i}{\partial m_j^2} + 2 \sum_{i=1}^N \frac{\partial F_i}{\partial m_j} \left(\frac{1}{\sigma_i} \right)^2 \frac{\partial F_i}{\partial m_j} + 2\alpha \sum_{j=1}^M \sum_{j'=1}^{M'} (j - j') \quad \text{for } j = 1, \dots, m$$

or $\boxed{\nabla^2 \phi(\mathbf{m}^k) = 2[-\nabla \mathbf{J}^T \mathbf{W}_d^T \mathbf{W}_d (\mathbf{d} - \mathbf{F}(\mathbf{m})) + \mathbf{J}^T \mathbf{W}_d^T \mathbf{W}_d \mathbf{J} + \alpha \mathbf{R}_m]}$

According to [Oldenburgh and Li \(2005\)](#), the first terms accounts for the change in the sensitivity when the model is perturbed. It is computationally burdensome to compute and also its importance decreases as the optimization proceeds because the difference between the predicted and observed data become smaller. For these reasons this term is generally neglected and we use an approximate Hessian in the computations:

$$\frac{\partial^2 \phi}{\partial m_j^2} \approx 2 \sum_{i=1}^N \frac{\partial F_i}{\partial m_j} \left(\frac{1}{\sigma_i} \right)^2 \frac{\partial F_i}{\partial m_j} + 2\alpha \sum_{j=1}^M \sum_{j'=1}^{M'} (j - j') \quad \text{for } j = 1, \dots, m$$

or $\boxed{\nabla^2 \phi(\mathbf{m}^k) \approx 2[\mathbf{J}^T \mathbf{W}_d^T \mathbf{W}_d \mathbf{J} + \alpha \mathbf{R}_m]}$ (18)

The approximate Hessian is positive semi-definite so its inverse exists. Finally, by combining equations (13), (17) and (18) into:

$$2[\mathbf{J}^T \mathbf{W}_d^T \mathbf{W}_d \mathbf{J} + \alpha \mathbf{R}_m] \Delta \mathbf{m} = -2[-\mathbf{J}^T \mathbf{W}_d^T \mathbf{W}_d (\mathbf{d} - \mathbf{F}(\mathbf{m})) + \alpha \mathbf{R}_m \mathbf{m}^k]$$
 (19)

Cancelling and rearranging terms:

$$\boxed{\underbrace{(\mathbf{J}^T \mathbf{W}_d^T \mathbf{W}_d \mathbf{J} + \alpha \mathbf{R}_m)}_{M \times M} \underbrace{\Delta \mathbf{m}}_{M \times 1} = \underbrace{\mathbf{J}^T \mathbf{W}_d^T \mathbf{W}_d (\mathbf{d} - \mathbf{F}(\mathbf{m})) - \alpha \mathbf{R}_m \mathbf{m}^k}_{M \times 1}}$$
 (20)

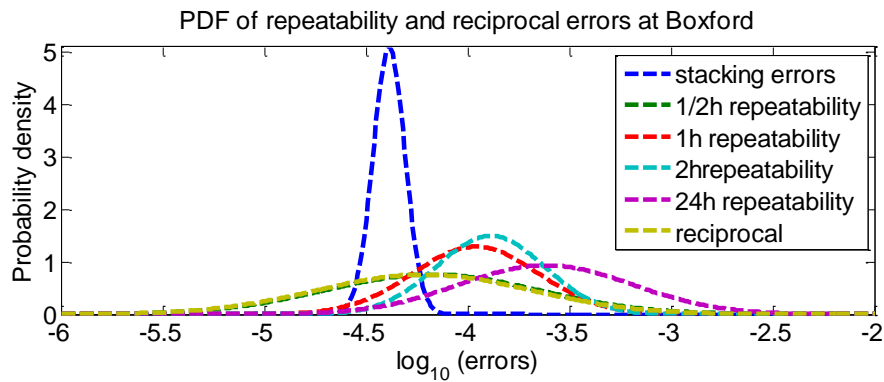
4. Paper 1: Improved characterisation and modelling of measurement errors in electrical resistivity tomography (ERT) surveys

Published as **Tso, C.-H.M.**, Kuras, O., Wilkinson, P., Uhlemann, S., Chambers, J., Meldrum, P., Graham, J., Sherlock, E., Binley, A. (2017): Improved modelling and characterisation of measurement errors in electrical resistivity tomography (ERT) surveys. *Journal of Applied Geophysics*, 145, 103--119, DOI:[10.1016/j.jappgeo.2017.09.009](https://doi.org/10.1016/j.jappgeo.2017.09.009).

Abstract

Measurement errors can play a pivotal role in geophysical inversion. Most inverse models require users to prescribe or assume a statistical model of data errors before inversion. Wrongly prescribed errors can lead to over- or under-fitting of data, however, the derivation of models of data errors is often neglected. With the heightening interest in uncertainty estimation within hydrogeophysics, better characterisation and treatment of measurement errors is needed to provide improved image appraisal. Here we focus on the role of measurement errors in electrical resistivity tomography (ERT). We have analysed two time-lapse ERT datasets: one contains 96 sets of direct and reciprocal data collected from a surface ERT line within a 24h timeframe; the other is a two-year-long cross-borehole survey at a UK nuclear site with 246 sets of over 50,000 measurements. Our study includes the characterisation of the spatial and temporal behaviour of measurement errors using autocorrelation and correlation coefficient analysis. We find that, in addition to well-known proportionality effects, ERT measurements can also be sensitive to the combination of electrodes used, i.e. errors may not be uncorrelated as often assumed. Based on these findings, we develop a new error model that allows grouping based on electrode number in addition to fitting a linear model to transfer resistance. The new model explains the observed measurement errors better and shows superior inversion results and uncertainty estimates in synthetic examples. It is robust, because it groups errors together based on the electrodes used to make the measurements. The new model can be readily applied to the diagonal data weighting matrix widely used in common inversion methods, as well as to the data covariance matrix in a Bayesian inversion framework. We demonstrate its application using extensive ERT monitoring datasets from the two aforementioned sites.

Graphical abstract



Probability density functions (PDF) of different ERT errors for 24h of surface ERT data collected at a wetland site in the UK. The mean repeatability errors generally increase with the period of time considered. Reciprocal errors generally agree with short-term repeatability errors. The PDF of stacking errors shows much lower mean and variance. Using stacking errors as a measure of measurement errors may lead to overfitting of data during inversion and underestimation of uncertainty.

Highlights

- Stacking, reciprocal and repeatability errors are compared using statistical analysis
- Having common electrodes increase correlation between measurements
- A new error model based on grouping the electrodes used is developed
- The new model yields better inversion results and uncertainty estimates

Keywords

ERT, resistivity, measurement errors, uncertainty, linear mixed effects, inversion

1) Introduction

Measurement errors are an integral part of scientific observations. Properly describing such errors is essential to harness the information about the observed behaviour contained in the measurements. Measurement errors may be random or systematic. In commonly used geophysical inverse methods, measurement errors are assumed to be uncorrelated and random. In the context of an inversion, the total data error is given by the square root of the sum of squares of measurement errors and modelling errors. Sources of modelling errors include inaccuracy of the forward model (e.g. due to discretisation of a numerical model) and appropriateness of a forward model (e.g. representing a 3D problem using a 2D model). Numerical modelling errors are relatively well understood because they can be studied by comparing forward modelling data of a homogeneous domain with analytical solutions (see [Binley, 2015](#)). We, therefore, focus here on measurement errors, in particular within the context of electrical resistivity tomography (ERT).

1.1. The role of ERT measurement errors

Measurement error estimates play a critical role in ERT inversion (see more in section 2.3). They affect the amount of damping imposed on the data and also the point at which convergence is attained. Both of the above are achieved by weighting data in the objective function, and thus, measurement error estimates control whether there will be over-fitting or under-fitting of data during inversion. This concept can be illustrated by comparing various inverted images. Figure 1 shows the results of inverting synthetic ERT experiments corrupted by 5% Gaussian noise. In the synthetic domain, a resistive target is placed between $x = 15$ m and $x = 20$ m and the topsoil is relatively conductive (Figure 1a). Inverting the data with 10% assumed Gaussian noise leads to under-fitting and a very smooth resultant image (Figure 1b), while assuming 2% noise leads to over-fitting and a number of artefacts (Figure 1d). This simple example shows that inversion results can be sensitive to the assumed measurement error levels. Failure to prescribe them adequately can significantly change the resultant image.

Attempts have been made to account for data errors in a more sophisticated manner. Robust inversion (Kemna, 2000; Morelli and LaBrecque, 1996) adjusts error weights when there are apparent outliers. It is important, however, to notice that the outliers are linked to a specific error weight derived *a priori* by the error model—they may not be outliers anymore if a different error model is used. Similarly, in Bayesian inversion (e.g. Irving and Singha, 2010; Ramirez et al., 2005), one needs to prescribe the estimated data uncertainty in the likelihood function. While different inversion strategies handle measurement errors differently, a robust and accurate prescription of measurement errors is essential to obtain reliable and realistic inversion results.

The impact of measurement errors is not limited to inversion—it is a natural extension of stochastic inversion where posterior models are estimates of uncertainty, whereas deterministic inversion results (or an ensemble of them) can further be used to estimate uncertainty via Monte Carlo approaches. Therefore, uncertainties in measurements would propagate to uncertainties of model estimates. Similarly, if the inversion results are used to detect or monitor subsurface processes, or to infer hydrological properties, their associated errors can be traced back to measurement errors. It is apparent that measurement errors propagate through the various stages of a hydrogeophysics study workflow. With the heightening interest in uncertainty estimation within hydrogeophysics (Binley et al., 2015; Huisman et al., 2010; Linde et al., 2015b; Rubin and Hubbard, 2005; Vereecken et al., 2006), better characterisation and treatment of measurement errors is necessary to provide better image appraisal.

1.2. Measurement errors in ERT: a review

The handling of measurement errors in ERT surveys, despite its importance as outlined above, is variable. The simplest (but not necessarily the most reliable) method of assessing a measurement error in an ERT measurement is through the use of stacking, i.e. the repeated measurement of transfer resistance through a number of cycles of current injection. Such stacking assessment offers valuable in-field data quality appraisal but, as shown later, may be of limited value in quantifying a data weight for ERT inversion. Alternatively, repeatability errors can be obtained by multiple, separate measurements of transfer resistance over time. Usually this involves

a repetition of the entire ERT measurement sequence sometime after the first attempt. Reciprocity checks are another method of measurement error assessment. Reciprocity is the general physical principle where the switching of source/sink and observation locations would yield the same response (Parasnis, 1988). It is, for example, utilised in groundwater hydrology (Barker, 1991; Bruggeman, 1972; Delay et al., 2011; Falade, 1981). Reciprocity checks for ERT are conducted by swapping the current and potential electrodes. Reciprocity breaks down when the ground response is non-linear (i.e. non-ohmic for ERT) or time-dependent (i.e. something changes between forward and reciprocal measurements).

As LaBrecque et al. (1996a) point out, both repeated and reciprocal measurements are measures of precision not accuracy. Sources of systematic error are not accounted for explicitly in measurements of precision – some procedures may miss them entirely while others lump them as random errors. Reciprocal errors treat the swapping of electrodes as a way to account for some systematic errors while repeatability errors do not consider them at all. Therefore, reciprocal errors may be more useful to eliminate bias caused by using a particular pair of electrodes as transmitter and another as receiver. The most commonly used errors in ERT, however, are stacking errors and they are misreferred as repeatability errors (Day-Lewis et al., 2008). Modern ERT instruments are equipped with stacking capability and they automatically return stacking errors. In other words, stacking errors can be obtained without re-running the measurement procedure, which is very attractive in time-sensitive or time-consuming surveys.

We surveyed a number of published ERT studies and report their description of error analysis in Table 1. From Table 1, we see that reciprocity is a commonly used measure, while a small fraction of field and experimental studies do not report their treatment of errors at all. Studies often attribute their exclusion of reciprocal errors to logistical constraints and argue that reporting stacking errors is sufficient. After errors are obtained, an error model (usually a linear relationship linking error to transfer resistance) is established (Binley et al., 1995). Once obtained, such a relationship may be used to predict the errors of individual measurements and thus contribute to the

data weight in the inverse modelling. Some authors, however, assign observed errors directly in the inverse modelling, although this is potentially flawed unless statistical robustness of the quantified error is established (recognising that for most surveys errors are only computed from two observations). This practice also makes it impossible to identify “disinformative data” (Beven and Westerberg, 2011). From the reported error models, it is observed that error levels are generally higher for cross-borehole surveys, largely due to more challenging electrode contact conditions (compared to most surface ERT array surveys). Prior to fitting the error model and carrying out inversion, measurements with high errors are often eliminated; sometimes more than 20% of the collected data are removed. For time-lapse studies, it is quite common that the entire time series of an individual resistance measurement is removed if any part of the time series is deemed to be an outlier. For recent work on time-lapse cross-borehole ERT, see Schmidt-Hattenberger et al. (2016) and Yang et al. (2014).

Error models are generally a function of average measured transfer resistance (i.e. the error in a transfer resistance increases with the magnitude of transfer resistance) because of the well-known proportionality effects (Aster et al., 2005) in DC resistivity measurement errors (Binley, 2015; Binley et al., 1995). In studies where errors are accounted for, there is generally a preference to use model-predicted errors rather than individually observed errors since error assessment based on two observations is potentially unreliable. Some studies mitigate this potential issue by binning (or grouping) data with similar transfer resistance together before fitting an error model (Koestel et al., 2008; Robinson et al., 2015; Wehrer and Slater, 2015). This practice should give more robust error estimates, although the error model may vary with the number of bins used.

To better characterise measurement errors, more understanding of the factors that contribute to them is needed. Current practice leaves many of the assumptions in ERT measurement errors modelling unchallenged. For example, do measurement errors show temporal or spatial correlations? Can we improve from using linear measurement error models? Are stacking errors and reciprocal errors comparable

indicators of measurement errors? ERT surveys typically use each of the electrodes for multiple measurements. Ramirez et al. (2005) notes that this may increase the probability that measurement errors are correlated, however, there has been no published work addressing this issue.

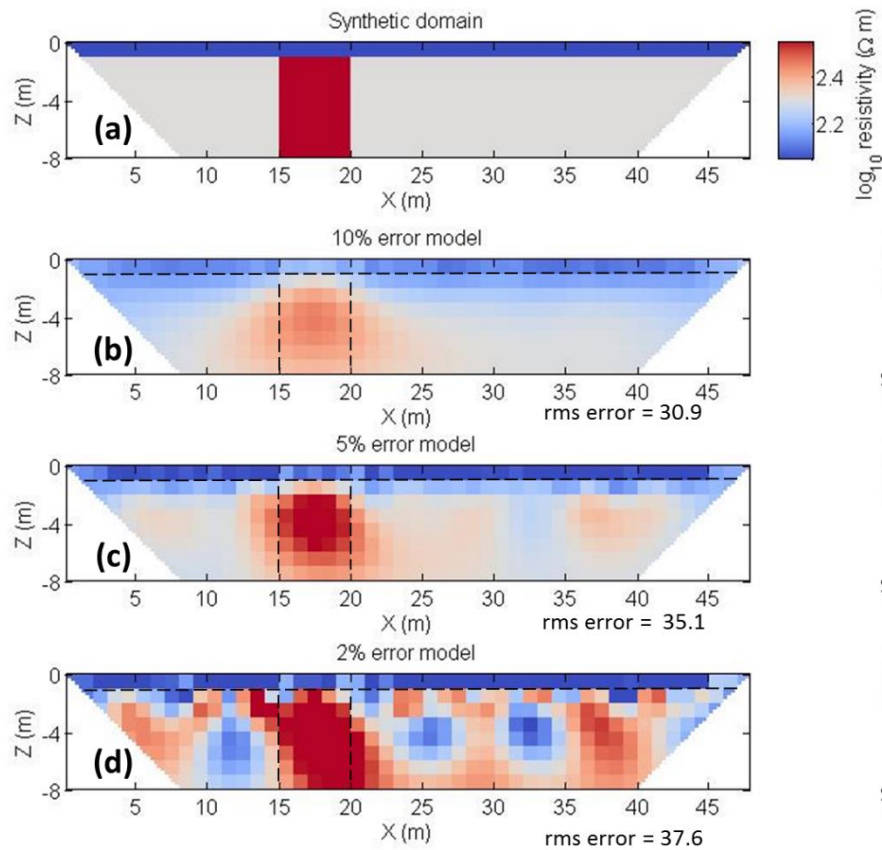


Figure 1 Synthetic problem for demonstration (a) Synthetic domain with a more conductive layer near the surface and a resistive area between $x = 15$ m and $x = 20$ m. The synthetic data from running a forward model in (a) is perturbed with 5% Gaussian noise and then inverted by assuming (b) 10% linear error model (c) 5% linear error model (d) 2% linear error model. Note that rms error is defined as $\sqrt{\sum_{i=1}^n (obs - sim)^2 / n}$, where obs and sim are vectors of observed/true and simulated transferred resistances of length n respectively. Note that the convergence target for all the inversions is a chi-squared statistic of 1.

1.3. Recent work on ERT measurement errors

Attempts have been made to handle potential systematic effects of measurement errors. Zhou and Dahlin (2003) studied the effect of spacing errors for 8 types of common 2D resistivity arrays. They confirm the common observation that ERT error outliers are often correlated with high contact resistances for some of the electrodes used in a measurement. Wilkinson et al. (2008) developed an approach to

filter out configurations that are highly sensitive to geometric error in crosshole ERT surveys. Similarly, [Wilkinson et al. \(2016, 2010a\)](#) developed techniques to recover movements of permanently installed electrodes so that active landslides can be monitored using time-lapse ERT data only. As the popularity of time-lapse surveys increases, specific methods to handle and characterize measurement errors in large time-lapse datasets emerge. [Deceuster et al. \(2013\)](#) developed a method to automate the identification of changes in electrode contact during time-lapse ERT experiments. More recently, [Mitchell and Oldenburg \(2016\)](#) developed a 4-step data quality control methodology for very large ERT datasets.

Recently, [Kim et al. \(2016\)](#) proposed a new measurement protocol in which self-potential (SP) data are obtained immediately prior to measuring DC. It involves swapping the polarities of the two current electrodes in each measurement to obtain a positive and a negative potential (i.e. thus a forward and backward resistance) for each measurement. This protocol claims to account for SP effects in DC measurements and eliminate distortions in the DC resistivity potential field caused by all unknown mechanisms including ambient noise.

1.4. Outline of this work

This paper addresses a number of practical issues related to the treatment of measurement errors in ERT inversion. We compare stacking, repeatability, and reciprocal errors in their utility to describe errors in measurements. We also study whether measurement errors are correlated in time and/or in space. We then hypothesize that measurement errors in ERT are not only linearly dependent on transfer resistances, but that the electrodes used in taking each measurement can be used as a grouping variable to improve error characterisation. We show that using the new error model leads to better inversion results and uncertainty estimates through synthetic and field experiments data. We first describe the datasets and analysis methods in section 2.1 and 2.2. Then we describe the ERT inversion and uncertainty estimation methods used in section 2.3 and 2.4. Section 3) reports results for the error analysis. We introduce a new error model based on linear mixed effects models and grouping of electrodes in section 4), and section 5) shows results of inversion and

uncertainty quantification. We then discuss the implications of the results in section 6), and provide conclusions and recommendations in section 7).

2) Approach

With recent advances made in the development of automated ERT systems, ERT experiments can be conducted remotely, allowing the collection of a large volume of background ERT measurements for quality control purposes. These rich datasets can be exploited to investigate the behaviour of measurement errors through statistical analysis. They provide opportunities to explore errors in ERT datasets, including the assessment of temporal and spatial correlation of errors. We scrutinize two large field datasets through statistical analysis of different types of measurement errors.

First, we examine the probability density functions for each error type, namely stacking, reciprocal and repeatability errors. This allows us to understand the mean and variance of their distributions. Next, we use autocorrelation and correlation coefficient analysis to study the sequential and spatial correlation of errors between measurements. Insights about the potential correlation in measurement errors can help in developing improved error models. We study the validity of repeatability errors by computing the autocorrelation and correlation coefficient of the departure from the mean of repeated measurements instead of using the repeatability errors directly. If repeatability errors are purely random, using any subset of the set of repeats for each given measurement should give the same errors and thus the departure from the mean should exhibit little correlation. We compare inversion of ERT data using different error types and models on identical datasets to illustrate how they manifest in inversion results. Lastly, we obtain uncertainty estimates of inversion results using a Monte Carlo simulation procedure. This allows us to visualize how measurement errors propagate into uncertainty in model estimates (in this study we assume there are no other error sources).

Table 1 Table of error models reported in the literature

Note: outliers are measurements that are not used for inversion. If the error type is reciprocal, reciprocal pairs are counted as one measurement.

Source	Error model	Error type	Survey type	Outliers/measurements	Outlier rule	Other description of errors
(Cassiani et al., 2006)	Linear model	Reciprocal	12 surface lines, tracer	244 of 744 pairs (long) 44 of 744 (high-resolution)	reciprocal error > 5%	
(Chambers et al., 2014)	Not reported	Reciprocal	21 and 15 parallel survey lines	5% of 20,563 0.5% of 23,164	$ e > 0.05 R $	
(Crook et al., 2010)	Not reported	Reciprocal	A line and 2 boreholes 3 surface lines	~25% of 6022 ~10% of 750	$ e > 0.05 R $ $ e > 0.04 R $	
(Flores-Orozco et al., 2011) (French et al., 2002)	Linear model Direct use	Reciprocal Reciprocal	2 surface lines 2 boreholes, snowmelt, tracer	Not reported ? of 1172 pairs	Not reported $ e > 10\% R $ are removed	See also (Flores-Orozco et al., 2012)
(Gélis et al., 2010)	Not reported (probably direct use)	Repeatability and Reciprocal	3 2.5-km long profiles, tunnel	1777 pairs retained	Stacked $ e > 5\%$	Reciprocity of Wenner array was always better than 10%. Reciprocity in dipole-dipole arrays was not reported.
(Haarder et al., 2015) (Hayley et al., 2009)	Direct use Not reported (probably direct use)	Reciprocal Repeatability	5 boreholes, tracer 15 surface lines	Not reported	Not reported Keep only measurements repeatable better than 1%	"It was deemed infeasible to include a reciprocal survey because of the added time and cost."
(Hermans et al., 2012) (Henderson et al., 2010)	$ e = 0.01 + 0.025 R $ Direct use: If $ e > 10\% R $, $ e = 200 e $, else $ e = 2.5 e $.	Reciprocal (200/823) Reciprocal	Surface (W-S) Marine surface	0/823 None	N/A None	Mean ($ e_{repeat} $) < 0.1%. Stacked data error during acquisition did not exist 2%
(Johnson et al., 2012)	$ e = 0.001 + 0.05 R $	Reciprocal	4 parallel surface lines next to river	715 of 8660 (first 20 d) 5021 of 8660 (all)	(i) Injected current <0.01 A (ii) Having reciprocal error > 5% At any timeframe during monitoring	
(Johnson et al., 2015)	$ e = 0.01 + 0.05 R $	Look up error model values from the literature	11 surface lines	200 (-0.5%) of 40,454 nonreciprocal measurements	(i) Apparent resistivities >100 Ωm (ii) Injected current <0.01 A If any of the above is found a measurement in the first five surveys, it is removed in the entire dataset	
(Kuras et al., 2016)	Not reported	Reciprocal and stacked	TL 3D, 4 boreholes	0.79% of ~13,400 each day 9.2% of ~53,100	$ e > 0.01 R $ (log10 scale)	
(Koestel et al., 2008) (Lesparre et al., 2016) (Meyerhoff et al., 2014)	$ e = 0.026 + 0.003 R $ Direct use Not reported	Reciprocal, binned Reciprocal Repeatability	TL 3D soil column Surface and borehole, tunnel 2 surface lines	?/23,130 8022 or 90% retained Not reported	Obvious (i) $ e > 0.05 R $ (ii) Stacked $ e > 0.1\%$ (iii) Active time-constrained inversion: "The first-order operator applied to the sequence of snapshots filters out noisy data that are not correlated in time and is flexible enough to allow relatively abrupt changes to occur on the sequence of inverted tomograms if supported by the data"	
(Nimmer et al., 2007)	Individual difference	Reciprocal	Surface 2D*field	735/2940 557/2830	$ e > 0.05 R $	
(Perri et al., 2012)	Linear	Reciprocal	Surface and borehole tracer test	?/2262 (surface) ?/5179 (borehole)	Not reported	
(Ramirez et al., 1996)	Direct use	Reciprocal	2D*field 3D*field	Not reported	Not reported	Inversions are conducted with both direct and reciprocal measurements are conducted. It was found that change due to using the either of the two is much smaller than changes due to the leak.

Approach

(Revil et al., 2010)	Direct use	Stacked	9 surface lines, volcano	?/9525	Not reported	Each of the resistivity measurements represents the mean of 8 to 16 distinct measurements stacked together with the same set of electrodes. * ...ERT reciprocal errors are approximately 20 times larger than repetition errors*
(Robert et al., 2011)	$N(6.3e-4 - 1.37e-3, 3.2e-4 - 1.1e-3)$ $ e = a + b R $ $a = 0-0.0026$ $b = 0.0031-0.016$	Reciprocal binned	6 surface surveys	?/490-760 per site	$ e_{repeat} > 0.01$ Outside $\pm 2\sigma$	
(Robinson et al., 2015)	Binned log-linear $ e = 0.131 R ^{0.48}$	Reciprocal	8 boreholes, fracture	153 of 4810	$ e > 5\% R $ are removed	
(Singha and Gorelick, 2006)	$ e = 0.01 + 0.05 R $	Reciprocal	TL 3D field	20-50/3150 per day	$ e > 0.05 R $	
(Slater et al., 2000)	$ e = 0.1 + 0.01 R $	Reciprocal	2D* tank, tracer	?/660	$ e > 0.1 R $	
(Slater et al., 2010)	Not reported	Apparent outliers	1-Line continuous waterborne survey	-3.2% out of -65,000	(i) Very small resistivity close to 0 Ωm (ii) Negative apparent chargeability (iii) Further processing	
(Slater and Binley, 2003)	Not reported	Reciprocal	Surface, IP	-25% of 772	$ e > 0.08 R $	
(Slater and Binley, 2006)	$N(5e-4, 8e-3)$ $N(8e-4, 6e-3)$	Reciprocal	2D* field, IP	0/770*6 1521/3744	$ e > 0.03 R $ $ e > 0.05 R $ & $e_{numerical} > 2\%$	
(Uhlemann et al., 2015)	N/A	Reciprocal	TL surface ($// \times 5$)	8-9% of 4285	$ e > 0.05 R $	
(Uhlemann et al., 2016)	$ e = a + b R $ $a = 1e-5 - 5e-4$ $b = 0.001 - 0.01$ $a > 0.001 \Omega$ (system malfunction)	Reciprocal Binned or Individual	TL surface ($\times 2$)	<5%-10% of (1528 + 516) for $ e > 0.05 R $	$ e > 0.10 R $ (Replaced by values derived from their respective time-series, using an inverse distance weighting interpolation)	
(Wagner et al., 2013)	$ e = 0.01 + 0.039 R $	CV from stacked V	TL 3D field	-4% of 258,947	CV > 0.05 $ R > 1700 \Omega$	
(Wallin et al., 2013)	$ e = 0.001 + 0.05 R $	Reciprocal	3 surface lines	851 out of 12,359 pairs	(i) injected current < 0.01A (ii) having reciprocal error > 5% at any timeframe during monitoring	
(Wehrer and Slater, 2014)	Binned quadratic-log10 $ e = -8e-6 R ^2 + 0.062 R + 0.0182$	Reciprocal	36 electrodes on each of the four vertical sides of the lysimeter core	? of 4200 pairs	Not reported	
(Williams et al., 2016)	Direct Use	Stacking	Surface	Not reported	Not reported	Up to three stacks were collected during surveys, with a mean stacking error of 0.2% Over 90% of data has reciprocal errors < 1% 98.7% of the data had errors of < 0.3% and maximum error recorded was only 2.7%
(Wilkinson et al., 2010a)	Not reported	Reciprocal	4 surface lines	516 pairs	Not reported	
(Wilkinson et al., 2010b)	Direct use	Reciprocal	14 boreholes	Not reported	Not reported	
(Wilkinson et al., 2016)	Direct use	Reciprocal	5 surface lines	12% of 2580 pairs	(i) Having negative apparent resistivity (ii) Having reciprocal error > 5% (iii) Having contact resistance > 2000 Ω (iv) Having positive/negative pulse amplitude ratios < 0.75 or > 1.33 (a measure of waveform symmetry)	
(Yeh et al., 2006)	N/A	Compare with homogeneous resistivity field (i.e. only diagnose for possible systematic errors regarding the estimated mean resistivity field)	34 boreholes, leachate injection	? of 2700 for each timeframe	Measurements outside the theoretical voltage variance are removed	N/A

2.1. Dataset description

A synthetic dataset, along with two field datasets collected by the British Geological Survey (BGS) are used for this work.

2.1.1. Synthetic Dataset

A synthetic dataset was created for use as an illustrative example using the synthetic domain and array of Figure 1. The array consists of 25 2-m spaced surface electrodes. As seen in Figure1(a), the resistivity structure of the domain consists of a 1m thick, 100 Ωm top layer. Beneath it is a 200 Ωm formation, in which a 500 Ωm unit protrudes vertically.

We created a forward model of dipole-dipole transfer resistances on the synthetic domain using R2 (<http://www.es.lancs.ac.uk/people/amb/Freeware/R2/R2.htm>) to obtain measurement error-free data. Two sets of synthetic data are generated by adding noise to these data: one with 2% Gaussian noise everywhere, and the other with 10% Gaussian noise on measurements involving three of the electrodes on the left ($x = 6\text{m}, 14\text{m}, 22\text{m}$) and 2% noise everywhere else. The second noisy dataset was created to simulate the effect of a non-uniform error model that may be typical of surveys in areas with variable electrode contact or quality.

2.1.2. Boxford Dataset

The first field dataset is from the Boxford Water Meadows Site of Special Scientific Interest in Berkshire, United Kingdom (Chambers et al., 2014b; Musgrave and Binley, 2011; Uhlemann et al., 2016). The collection of the data was automated using the BGS's PRIME system. The ERT array is next to the Northern Array used in Uhlemann et al. (2016), having 32 electrodes spaced at 0.6 m. A dipole-dipole type measurement configuration was chosen with dipole lengths (a) of 0.6 m to 2.4 m, and dipole separation multipliers (n) of 1 to 8. The measurement sequence includes 516 pairs of reciprocal measurements. Less than 15 minutes was needed to complete the measurement sequence and each of the measurements is obtained by stacking multiple readings from the same cycle of current injection to improve signal-to-noise ratio. The measurement sequence was repeated 96 times within a 24 hour period starting at 5:43 a.m. on 19th November 2015, yielding 96 independent repeats of full reciprocal data.

Each of the repeats has 516 measurements (or pairs of reciprocals). During the 24-hour period, the air temperature in the area varied between 7 and 10 °C and there was no recorded precipitation.

2.1.3. Sellafield Dataset

A full-scale 3-D time lapse cross-borehole ERT trial to monitor simulated subsurface leakage was undertaken at a UK nuclear licensed site in Sellafield, Cumbria, United Kingdom (Kuras et al., 2016). The data collection setup includes four 40m deep boreholes and 160 electrodes. The data collection cycle of each ERT frame is less than a day, and each day's data includes 51,302 dipole-dipole measurements, including 12,481 pairs of reciprocals. The monitoring spanned a 2-year period with 246 days of data collection during that time. The first nine months of monitoring includes three stages of conductive leak simulant injection, while the remainder was designed for long-term background monitoring. The collection of data was automated using BGS's ALERT system. In order to be consistent with the autocorrelation analysis of the Boxford dataset, we divide the data into two subsets of 96 days (one encompasses all three injection periods while the other is during long-term background monitoring) for autocorrelation analysis.

2.2. Analysis methods

2.2.1. Definition of measurement error types

Stacking errors are given by the averaging of 'stacks' obtained by the ERT data collection equipment. Usually they can be output alongside the measured transferred resistance from the data collection console.

For reciprocal errors, if R_f is the forward (normal) transfer resistance for a particular quadrupole and R_r is the reciprocal of that measurement where its current and potential dipoles are swapped with the forward measurement, then the mean absolute transfer resistance ($|R|$) and absolute errors ($|e|$) are simply:

$$|R| = \frac{|R_f| + |R_r|}{2} \quad \text{and} \quad |e| = \frac{|R_f| - |R_r|}{2}. \quad (1)$$

As a proxy for repeatability errors, the departure from the mean of the j -th repeated reading for measurement number i ($d_{i,j}$) is given by:

$$e_{i,j} = d_{i,j} - \bar{d}_i \quad (2)$$

where \bar{d}_i is the mean value for the i -th measurement.

2.2.2. Statistical analysis of measurement errors

The probability density function of an error type for a dataset is obtained by fitting a Gaussian distribution to the population of errors. Autocorrelation is defined as the correlation among a sequence of values at a given lag L :

$$\text{autocorr}(L) = \frac{E[(X_t - \bar{X})(X_{t+L} - \bar{X})]}{\text{var}(X_t)} = \frac{\sum_{t=1}^{q-L} (X_t - \bar{X})(X_{t+L} - \bar{X})}{\text{var}(X_t)} \quad (3)$$

where $E[]$ is the expected value, X_t is a time-series, X_{t+L} is a time-series shifted by lag L , and \bar{X} and $\text{var}(X_t)$ are the mean and variance of the time series respectively. q is the number of repeats for a measurement.

Correlation analysis can be used to study the potential correlation between measurement errors. The correlation coefficient, r , for the correlation between arbitrary variables x and y is defined by the products of standard scores (also known as z-scores or standardized variables) as follows:

$$r = r_{xy} = \frac{1}{q-1} \sum_{i=1}^q \left(\frac{x_i - \bar{x}}{s_x} \right) \left(\frac{y_i - \bar{y}}{s_y} \right) \quad (4)$$

For the purposes of our analysis of measurement error correlations, x and y are series of two measurements that we consider and q is the number of repeats. \bar{x} and \bar{y} are the means of x and y respectively, while s_x and s_y are the standard deviations.

2.3. Inversion methods

To obtain 2D tomograms from electrical measurements from the synthetic study and Boxford site, we use the finite-element based, Occam-type, two-dimensional electrical resistivity inversion program R2 (www.es.lancs.ac.uk/people/amb/Freeware/R2/R2.htm). The three-dimensional inversion (Sellafield dataset) was performed by using the commercial code

Res3DInvx64 (Loke and Barker, 1996). The inverse problem is posed as a minimization problem, where the objective function is defined as

$$\Phi = \Phi_d + \Phi_m = (\mathbf{d} - \mathbf{F}(\mathbf{m}))^T \mathbf{W}_d^T \mathbf{W}_d (\mathbf{d} - \mathbf{F}(\mathbf{m})) + \alpha \mathbf{W}_m^T \mathbf{W}_m \quad (5)$$

where \mathbf{d} are the data vector (e.g. measured apparent resistivities), $\mathbf{F}(\mathbf{m})$ is the set of simulated data using the forward model and estimated parameters \mathbf{m} . \mathbf{W}_d is a data weight matrix, which, if we consider the uncorrelated measurement error case and ignore forward model errors, is a diagonal matrix with entries equal to the reciprocal of the standard deviation of each measurement. Forward modelling errors are also added to the diagonal of \mathbf{W}_d . Usually a forward model is run for the computational grid using a known homogeneous domain. Any discrepancy between the computed and known apparent resistivity values (i.e. data errors) will be added to the reciprocal of \mathbf{W}_d by means of square root of sum of squares. In this study, we assume measurements errors are the only source of data errors while other sources, such as forward modelling errors and field procedural errors, are negligible. To regularize the minimization problem, a model penalty term $\Phi_m = \alpha \mathbf{W}_m^T \mathbf{W}_m$ is added to impose the spatial connectedness of the parameter cell values. α is a scalar that controls the emphasis of smoothing.

We can state a desired level of data misfit as $\Phi_d = N$, where N is the number of measurements (Binley, 2015). In an Occam's solution, we seek to achieve this desired data misfit subject to the largest possible value of α . The process is achieved by utilizing the Gauss–Newton approach, which results in the iterative solution of

$$(\mathbf{J}^T \mathbf{W}_d^T \mathbf{W}_d \mathbf{J} + \alpha \mathbf{W}_m^T \mathbf{W}_m) \Delta \mathbf{m} = \mathbf{J}^T \mathbf{W}_d^T \mathbf{W}_d (\mathbf{d} - \mathbf{F}(\mathbf{m})) - \alpha \mathbf{W}_m^T \mathbf{W}_m \quad (6)$$

$$\mathbf{m}_{k+1} = \mathbf{m}_k + \Delta \mathbf{m}$$

where \mathbf{J} is the Jacobian (or sensitivity) matrix, given by $J_{i,j} = \partial d_i / \partial m_j$; \mathbf{m}_k is the parameter set at iteration k ; and $\Delta \mathbf{m}$ is the parameter update at iteration k . For the DC resistivity case, the inverse problem is typically parameterized using log-transformed resistivities.

The resolution matrix for the inversion is given by:

$$\mathbf{R} = (\mathbf{J}^T \mathbf{W}_d^T \mathbf{W}_d \mathbf{J} + \alpha \mathbf{W}_m^T \mathbf{W}_m)^{-1} \mathbf{J}^T \mathbf{W}_d^T \mathbf{W}_d \mathbf{J} \quad (7)$$

2.4. Error propagation and uncertainty quantification methods

We follow the Monte Carlo uncertainty propagation procedure of [Aster et al. \(2005\)](#) outlined below. The goal is to simulate a collection of noisy data vectors and then examine the statistics of the corresponding models. The advantage of this method is that it can be readily applied to field data where no repeats are available. The procedure is achieved by the following steps:

1. Propagate the inverse solution $\bar{\mathbf{m}}$ into an assumed noise-free baseline $j \times 1$ data vector \mathbf{d} (where j is the size of number of measurements) using the forward model \mathbf{G} :

$$\mathbf{G}\bar{\mathbf{m}} = \mathbf{d} \quad (8)$$

2. Generate q realizations ($i = 1, \dots, q$) of noisy data about $\bar{\mathbf{m}}$ using the error model

$$\mathbf{d}_i = \mathbf{d}_b + \boldsymbol{\varepsilon}.*\mathbf{Z} \quad (9)$$

where $\boldsymbol{\varepsilon}$ is the $j \times 1$ vector of error levels predicted by the error model and \mathbf{Z} is the standard normal distribution variable and $.*$ is element-wise multiplication.

3. Invert the q realizations ($i = 1, \dots, q$) of noisy data using the inverse model

$$\mathbf{G}\mathbf{m}_i = \mathbf{d}_b + \boldsymbol{\varepsilon}_i \quad (10)$$

4. Let \mathbf{A} be a $q \times m$ matrix where the i -th row contains the departure of the i -th model from the baseline inverse solution $\bar{\mathbf{m}}$

$$\mathbf{A}_i = \mathbf{m}_i^T - \bar{\mathbf{m}}^T \quad (11)$$

5. An empirical estimate of the model covariance matrix is given by

$$\text{cov}(\bar{\mathbf{m}}) = \frac{\mathbf{A}^T \mathbf{A}}{q} \quad (12)$$

6. 95% confidence interval about $\bar{\mathbf{m}}$ is given by

$$\bar{\mathbf{m}} \pm 1.96 \cdot \text{diag}(\text{cov}(\bar{\mathbf{m}}))^{1/2} \quad (13)$$

7. Similarly, the coefficient of variation of the estimate is given by

$$\text{diag}(\text{cov}(\bar{\mathbf{m}}))^{1/2} ./ \bar{\mathbf{m}}^T \quad (14)$$

where $\text{diag}()$ is a function that extracts the diagonal elements of a matrix and $./$ is element-wise division.

3) Analysis of Errors in Field Datasets

In this section, we report results from the statistical analysis of different types of errors with the methods outlined in section 2.1 and 2.2. Probability density functions (PDFs) show the ranges of these errors, while autocorrelation and correlation coefficient analysis reveals the potential autocorrelation of errors for successive repeated measurements and correlation of errors between pairs of measurements, respectively.

3.1. Probability density function of reciprocal and repeatability errors

Before detailed statistical analysis of measurement errors is performed, we first examine the probability density function of errors obtained from the Boxford dataset. Since the measurements are repeated 96 times, we can define repeatability errors based on averaging different numbers of repeats. Figure 2 shows the repeatability errors based on measurements obtained with a 30 minute, 1 hour, 2 hour, and 24 hour window. They correspond to averaging 2, 4, 8, and 96 repeats. The mean of the PDF increases with greater time windows while the variance first decreases, then increases for the 24 hour repeatability error. When large windows of averaging are used, changes in the subsurface condition such as diurnal changes in temperature can be mistaken as errors. This is supported by the observed increase in the mean. For the 24 hour sampled PDF, the lower tail overlaps that of the 1 hour and 2 hour PDFs while having a much greater spread. Clearly some measurements do not vary much during the 24 hours monitoring period while others do: measurements sensitive to the shallower subsurface will be more susceptible to external influences (e.g. temperature, evaporation, etc.).

Figure 2 also shows the PDF for stacking errors for each of the measurements as well as the reciprocal errors from individual datasets. The reciprocal errors PDF essentially overlay that of the 30 minute repeatability errors. Their similarities may be explained by the fact that both of them are obtained from averaging pairs of measurements. It is noteworthy, however, that both the mean and variance of the PDF for reciprocal errors (which is collected in a 15 minute timeframe) is slightly higher— which is opposite to our general observation that repeatability errors increase with the size of the averaging window. Reciprocal errors may be sensitive to other error contributions not registered by repeatability errors, or the process of taking a reciprocal measurement introduces an additional source of error.

The stacking errors PDF overlays the low-end of the PDFs of repeatability errors while having a very small variance. In other words, stacking errors do not register any of the high-error measurements that appear in the true assessment of repeatability or in reciprocal errors. For instance, the PDF shows that almost none of the stacking errors are higher than $10^{-4} \Omega$, which covers a majority of the area under the other PDFs. This shows that stacking errors are potentially an inadequate measure for describing the true quality of ERT measurements.

The second portion of Figure 2 shows the PDF of stacking, reciprocal, and 2-week (which correspond to six frames) repeatability errors for the Sellafield dataset. In general, the ranges of magnitude of the errors are greater due to ground conditions and contact resistances. Similar to the Boxford results, we find that the stacking errors are an order of magnitude smaller than reciprocal errors. Since a larger time window (i.e. days) is used to obtain the repeatability errors, they are significantly greater than the reciprocal errors.

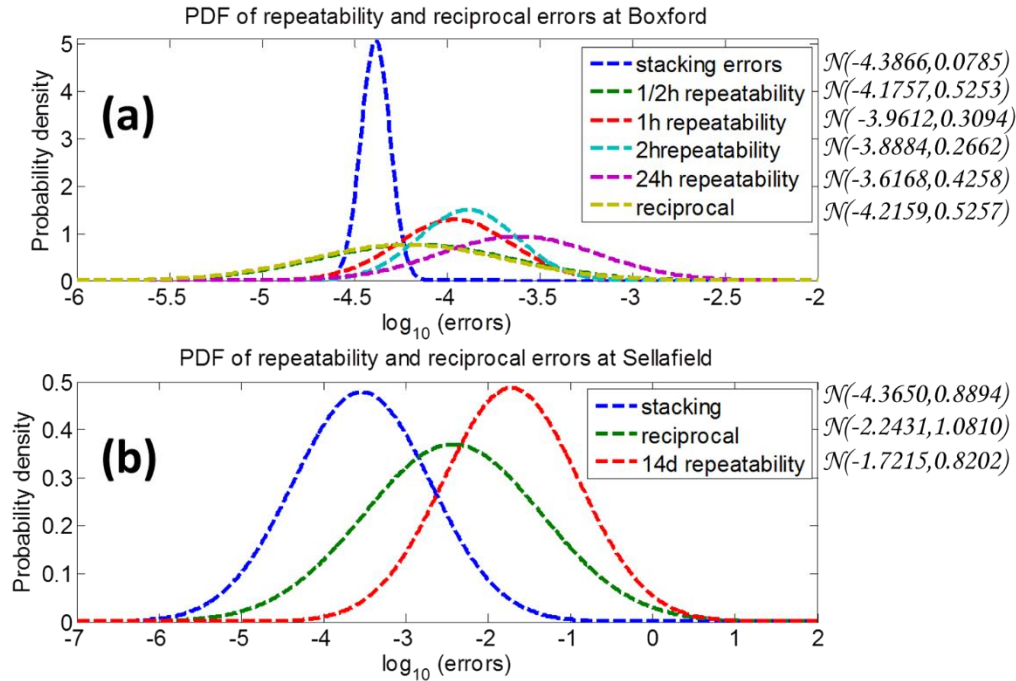


Figure 2 (a) Comparison of stacking errors, repeatability errors, and reciprocal errors for the Boxford dataset by plotting probability density functions. The PDFs of reciprocal errors and repeatability errors are comparable to each other. The stacking errors PDF, however, show very low mean and low variance. Using stacking errors for measurement errors characterisation may lead to significant underestimation of uncertainty and over-fitting of data. (b) Comparison of stacking errors, repeatability errors, and reciprocal errors for the Sellafield dataset. The PDFs for Sellafield show greater variances than those for Boxford. Since a two-week repeatability cycle is used, the repeatability errors are much greater than reciprocal errors. In general, the stacking errors are more than an order-of-magnitude smaller than the reciprocal errors, indicating there may be significant underestimation of errors if they are used as error weights. The mean and standard deviation of each fitted normal distribution is shown next to the legend.

3.2. Autocorrelation analysis

Autocorrelation analysis is used to investigate whether there is “memory” (i.e. correlation in time) in ERT measurement errors. We compare autocorrelation plots between the (i) departure from the mean and (ii) reciprocal errors of individual measurements for the Boxford dataset in Figure 3. Each grey translucent line represents the autocorrelation function of a measurement, while the red line is the mean averaged across all measurements. The red hashed regions highlights the area with an autocorrelation value below the critical Pearson’s correlation coefficient (Pearson and Hartley, 1970), which is around 0.2 for 96 timesteps. For the departure

from the mean, the autocorrelation drops to 0.5 on average at lag 1 and then decreases steadily. This is likely to be due to the presence of diurnal temperature effects within the 24 hour data collection cycle. Individual reciprocal errors, show negligible autocorrelation for all lag numbers (i.e. within the hashed region). Thus, we can conclude the individual reciprocal errors between any two repeated measurements are independent from one another for this survey. From the above, we see that the assumption of uncorrelated errors is appropriate for reciprocal errors but not so much for long-term repeatability errors.

Figure 4 shows the autocorrelation of (a) departure from the mean and (b) reciprocal errors for the 96 datasets collected continuously at the Sellafield site encompassing the three injection periods (22th Jan 2013 – 3rd Nov 2013) and those for another 96 datasets during the long-term background monitoring period (i.e. no injection, 5th Nov 2013 – 31st Mar 2014). We can see much greater autocorrelation of errors at Sellafield than at Boxford. Like in the Boxford dataset, the departure from the mean shows greater autocorrelation than individual reciprocal errors, both for injection and long-term background monitoring. In general, however, the departure from the mean and reciprocal errors during background monitoring reach insignificant autocorrelation sooner than during injections. While the 96 datasets at Boxford were collected in less than 24 hours, the two groups of 96 datasets examined above were collected over a period of months. It is certain that the subsurface condition had changed during the monitoring period due to injection, dilution and dispersal of tracer, as well as regional groundwater and vadose zone changes (see [Kuras et al. \(2016\)](#) for details).

Analysis of Errors in Field Datasets

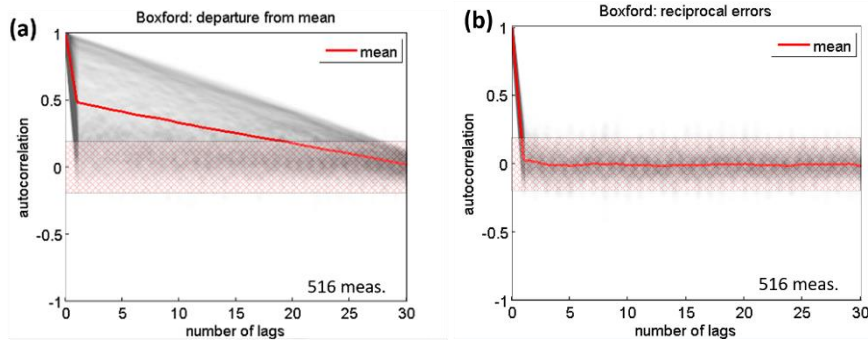


Figure 3 Autocorrelation of (a) departure from the mean (as a measure of repeatability errors) and (b) reciprocal errors for the 96 datasets collected continuously within 24h at the Boxford site. The number of lags is on the horizontal axis (here 1 lag = 15 minutes). Each grey translucent line plots the autocorrelation of one of the 516 ERT measurements as a function of lag. The red line denotes the mean autocorrelation. For each autocorrelation plot, 96 datasets are considered. The hashed region has insignificant correlation according to the critical Pearson's test (around ± 0.2).

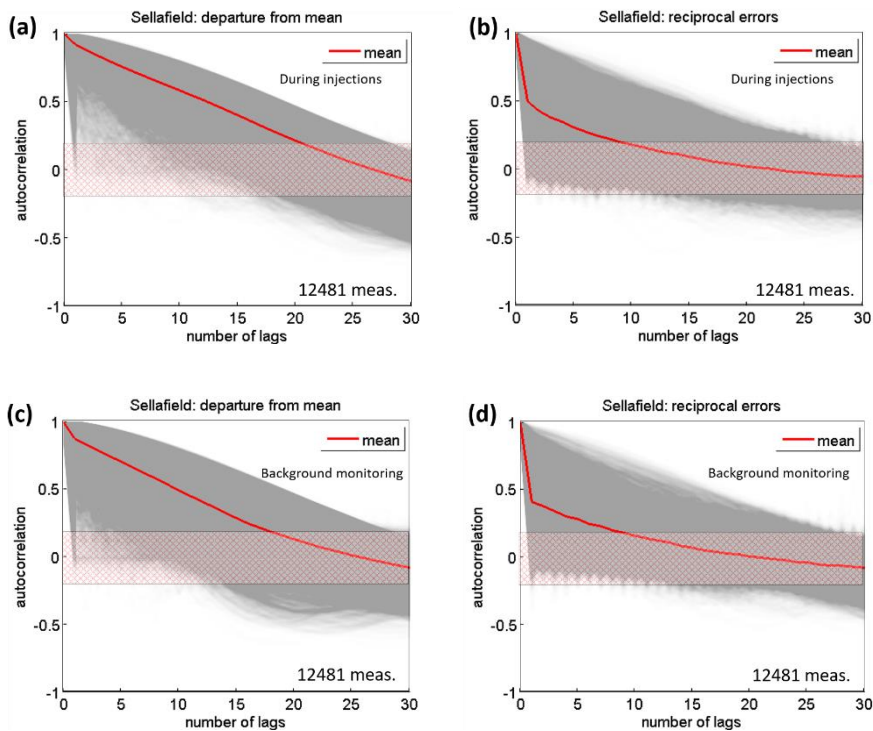


Figure 4 Autocorrelation of (a) departure from the mean (as a measure of repeatability errors) and (b) reciprocal errors for the 96 datasets collected continuously at the Sellafeld site encompassing the three injection periods (22/1/2013 – 3/11/2013). The number of lags is on the horizontal axis (here 1 lag = ~ 2 to 3 days). Each grey translucent line plots the autocorrelation of one of the 12481 ERT measurements as a function of lag. The red line denotes the mean autocorrelation. For each autocorrelation plot, 96 datasets are considered. The hashed region has insignificant correlation according to the critical Pearson's test (around ± 0.2). Similarly, (c) and (d) show the same for the long-term background monitoring period (i.e. no injection, 5/11/2013 – 31/3/2014).

3.3. Correlation coefficient analysis

Although measurement errors are commonly assumed to be uncorrelated in ERT, previous studies have highlighted the potential of correlation in measurement errors because ERT surveys typically use the same electrodes for multiple measurements (Ramirez et al., 2005). We have computed the correlation coefficient matrix for departure from the mean and reciprocal errors for the Boxford dataset. We subdivide all the correlation coefficients into two groups: one group consists of pairs of measurements that share one or more electrodes and the other consists of all measurement pairs. Next, we grouped departure from the mean or reciprocal errors as a function of dipole-dipole separation multiplier n and plot the mean of each group. We show in Figure 5 that for all n used for the Boxford dataset, the mean correlation coefficients for measurement pairs that share one or more electrodes are always higher than the means for all pairs. The mean correlation coefficients for reciprocal errors are orders of magnitude smaller than those of departure from the mean. The effect of electrode sharing is also pronounced for reciprocal errors—the mean correlations of all reciprocal errors pairs are negligible while those for pairs that share one or more electrodes are consistently higher. Note that electrode sharing only occurs in ~10% of all pairs. Figure 5 shows that by taking into account the correlation of the electrodes used to make multiple measurements, ERT measurement errors may be better modelled. With the autocorrelation results, we also show that the departure from the mean exhibits more spatial and temporal correlation than the reciprocal errors.

4) A New Error Model

4.1. Model definition and implementation

Our error analysis reported in section 3) revealed that the combination of electrodes used appears to influence ERT measurement errors. Therefore, we developed a new error model based on linear mixed effects (LME) models to group measurement errors by the electrodes used to obtain them, which allows us to incorporate the effects of electrode combinations.

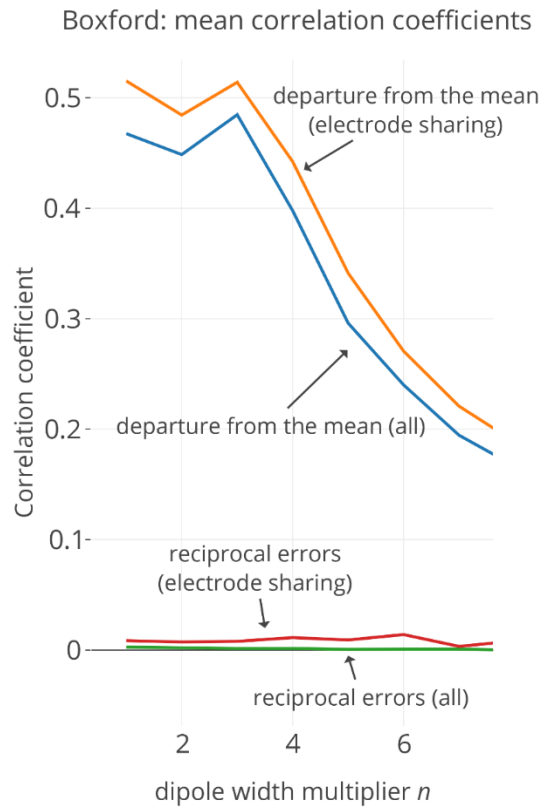


Figure 5 Mean correlation coefficient of departure from the mean (as a measure of measurement errors) and reciprocal errors for measurement pairs from the Boxford dataset as a function of dipole separation multiplier n . For both departure from the mean and reciprocal errors, mean correlation coefficients are distinctively higher for measurements that share electrode(s) in their quadrupoles than the mean correlation coefficients for all measurements, indicating by considering the effect of using each electrode to make multiple measurements may improve error models. Also, note that the reciprocal errors have strikingly lower correlation coefficients than the departure from the mean. Note that electrode sharing only occurs in ~10% of all pairs.

The linear mixed effect model is a powerful statistical tool in settings where repeated measurements are made on the same statistical units (longitudinal study), or where measurements are made on clusters of related statistical units (Bates et al., 2015; Diggle et al., 2015; Pinheiro and Bates, 1988; West et al., 2007). It is especially useful to group qualitative variables that influence the data. In general, a mixed effect model is given by

$$\mathbf{y} = \underbrace{\mathbf{X}\boldsymbol{\beta}}_{\text{fixed}} + \underbrace{\mathbf{Z}\mathbf{b}}_{\text{random}} + \underbrace{\boldsymbol{\varepsilon}}_{\text{error}} \quad (15)$$

where \mathbf{y} is the n -by-1 response vector (i.e. dependent variable), and n is the number of observations; \mathbf{X} is an n -by- p fixed-effects design matrix, and p is the number of fixed effect variables; $\boldsymbol{\beta}$ is a p -by-1 fixed-effects vector and q is the number of random effect variables; \mathbf{Z} is an n -by- q random-effects design matrix; and \mathbf{b} is a q -by-1 random-effects vector. $\boldsymbol{\varepsilon}$ is an n -by-1 unknown vector of random, independent and identically distributed errors. In broad terms, fixed-effects are variables that are expected to have an effect on the dependent variable (i.e. explanatory variables in linear regression), while random effects are categorical grouping factors.

Linear mixed effect models can now be readily fitted using the MATLAB® statistics and machine learning toolbox and the lme4 package for R (Bates et al., 2015). In this paper, we model measurement errors in ERT by treating transfer resistances as fixed effects and each of the electrodes used (A, B, M, N) as grouping variables. The above model was implemented in MATLAB® (see supplementary information for more details).

The linear mixed effect model essentially establishes a hierarchy or grouping when fitting the measurement errors. Fitting is achieved by both optimizing fit within each cluster, while the covariate vectors link the fixed and random effects between clusters. The clustering introduces additional degrees of freedom that allow a better fit of measurement errors than commonly used linear models. An illustrative example of the LME grouping formulation can be found in the supplementary information, along with details for fitting the LME error model to the Boxford and Sellafeld field datasets. The evolution of the error model coefficients with time is also described.

4.2. LME error model behaviour for time-lapse ERT measurements

A longitudinal survey is a correlational research study that involves repeated observations of the same variables over long periods of time. One of the original uses of LME models is to handle longitudinal data in tracking studies to eliminate potential bias of using the same samples. For example, in a drug study the health indicators of the same group of patients are sampled multiple times during a long period. The times

at which they are sampled can be used as an additional grouping variable in the LME model. With the increased popularity of long-term monitoring using ERT and other geophysical methods, it may be beneficial to treat measurement errors as longitudinal data too. In Figure 6, we compare fitting observed measurement errors in the 96 repeat datasets from Boxford individually (i.e. obtaining 96 LME equations) and as longitudinal data (i.e. obtaining one LME equation, with the repeat number as an additional grouping variable). The scatter plots show that a much better fit is obtained by fitting each of the 96 datasets individually. In other words, treating ERT measurement errors as longitudinal data does not better characterise them. Measurement errors should instead be characterised on a frame-by-frame basis for long-term geophysical monitoring. Of course, this comparison does not involve the same degree of freedoms for both methods, which should be repeated using more robust criteria (e.g. Bayesian information criteria).

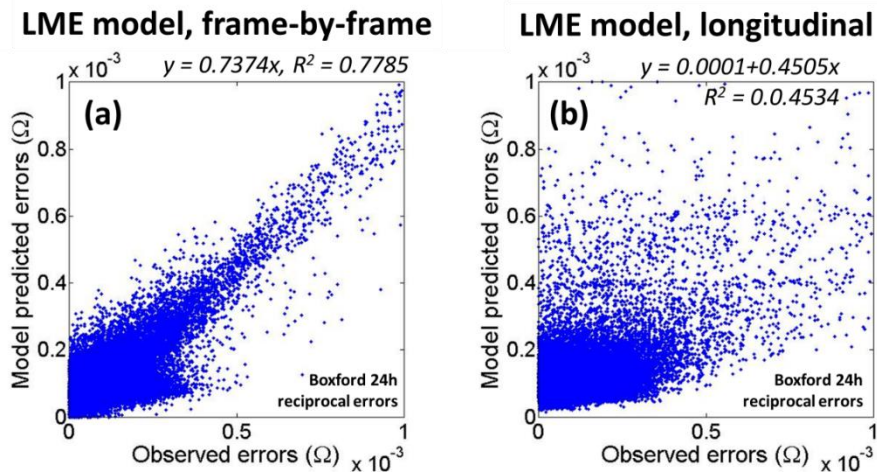


Figure 6 Comparison of fitting reciprocal errors of time-lapse data as (a) individual datasets, fitting each dataset individually with a different LME model and (b) longitudinal data, fitting all data with one LME model. The above shows that it is much better not to treat errors as longitudinal data.

5) Comparison of Error Models using Image Appraisal

Improvements in the measurement error model are only useful if they can lead to better inversion results. We applied the new error model to the synthetic data and field data from the Boxford and Sellafeld sites. Also, we will consider the resolution

matrix and model variance from Monte Carlo simulations to see whether using the new error model can give additional insight to data and reduce uncertainty.

5.1. Synthetic data

Using the synthetic domain introduced in section 2.1, we compared the inversion results and the corresponding resolution matrices and uncertainty estimates using different error models. Note that since Figure 1 and Figure 7 use the same domain and have the same resistivity structure, Figure 1(c) can be seen as a benchmark case where the data is inverted with perfect knowledge of measurement errors.

Figure 7 (a – c) shows inversion results for synthetic data where measurements involving three “bad electrodes” are corrupted by 10% noise and others by 2% noise. We first compare the inversion with two linear error model – one assumes there are no bad electrodes (i.e. the 2% error model), while the other is obtained by fitting the corrupted data with the [Koestel et al. \(2008\)](#) model (i.e. the 4.52% linear model). We see that the resultant resistivity model from assuming the 2% linear error model is very noisy while that from assuming 4.52% linear error model is smoother. With the LME error model, however, the inversion result is the most similar to that of the benchmark case (Figure 1c) (see also rms errors printed on plots). The effect of better characterisation of measurement errors by the LME model is manifested in the inversion results.

Figure 8 (a – c) shows the diagonal terms of the resolution matrices for the inversion using (a) 2% linear, (b) 4.52% linear, and (c) LME error models. In general, the resolution patterns are uniform laterally yet decreases with depth. For the 2% linear error model, we see that some of the artefacts from the inversion results are also shown on the resolution pattern. For the LME error model, the resolution on the right is somewhat higher than on the left for the top layer, where the bad electrodes are located. The resolution values are between that of (a) and (b) in most of the cells, although some of the cells near the surface show very high resolution. The above shows that while the resolution from the linear error model is purely a function of distance away from sources and sensors and therefore cannot distinguish quality between measurements,

the LME error model allows the inversion to resolve areas unaffected by the bad electrodes better.

Subsequently, we ran Monte Carlo experiments using the procedure in section 2.4 to understand how uncertainty in measurement errors propagates to affect uncertainty in the parameter estimates. The Monte Carlo experiment results can be used to form empirical model covariance matrices. This matrix shows how information is shared between parameters (i.e. model estimate of different elements). In the ideal, noise-free and well-defined case, the model covariance matrix should be a zero matrix, meaning the parameter is deterministically known and the parameters are not correlated with one another. Figure 9 (a – b) show that assuming a 2% linear error model yields lower model covariances than the 4.52% model, which is expected because lower percentage error implies less sharing of data. Also, the band of high covariances is also narrower. With the LME model (Figure 9c), however, we notice that the model covariances values are lower than those of the 2% and 4.52% models. More importantly, the spread of the high covariance region is less uniform than the linear models, meaning that only measurements affected by the bad electrodes share information heavily with others. The above agrees with the comparison of resolution matrices—the new error model is able to exploit information in noisy data without increasing the overall noise level.

The diagonal term of the empirical model covariance matrix (i.e. variance) shows the variability among parameter estimates from multiple Monte Carlo simulation realizations. Specifically, the higher a diagonal term, the more uncertain is the estimate. We plot their ranges in Figure 8 (d – f). For all three error models, the variability is always the smallest at depth because deeper regions are less well resolved for surface arrays. As a result, the model estimates at greater depths are closer to the initial guess values and therefore, there is less difference between the realizations of Monte Carlo model estimates. In Figure 8 (g – i), we plot the model-averaged parameter estimates. The transparency of each element is inversely proportional to its model variance, as shown in Figure 8 (d – f). In other words, the elements that have more variable or uncertain estimates have greater transparency. The inversion results

from assuming a 2% error model are more variable than for the 4.52% model. Model averaging also smooths out the noisy artefacts from deterministic inversion (compare Figure 8g and Figure 7a). The LME error model gives the most reliable model estimates among the three error models tested. Also, it is worth noting that the model-averaged parameter estimates are comparable to that obtained from deterministic inversion. This means that with the LME error model, there is no need to run many realizations of the inverse model in order to obtain reliable parameter estimates. Importantly, inversion using the LME error model gives the highest resolution and the least model variance (Figure 8), and reduces uncertainty in inversion results.

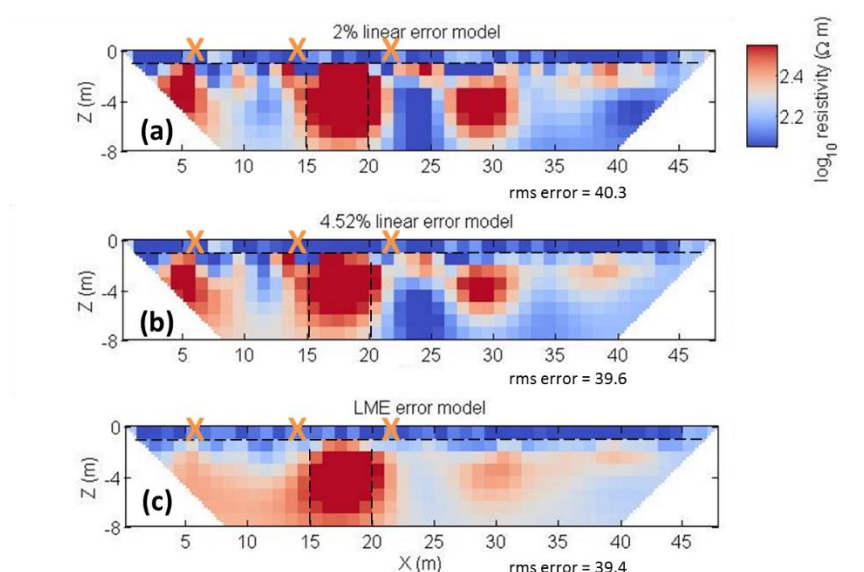


Figure 7 Synthetic surface ERT experiments to demonstrate the performance of the error models. For data involving 3 bad electrodes (marked by “X”), data is corrupted by 10% white noise while for the rest of the data 2% white noise is added. (a) Inverted resistivity distribution using the 2% linear error model (b) Inverted resistivity distribution using a 4.52% (obtained from the Koestel et al. (2008) method) linear error model (c) Inverted resistivity distribution using the LME error model. Note that the convergence target for all the inversions is a chi-squared statistic of 1.

Comparison of Error Models using Image Appraisal

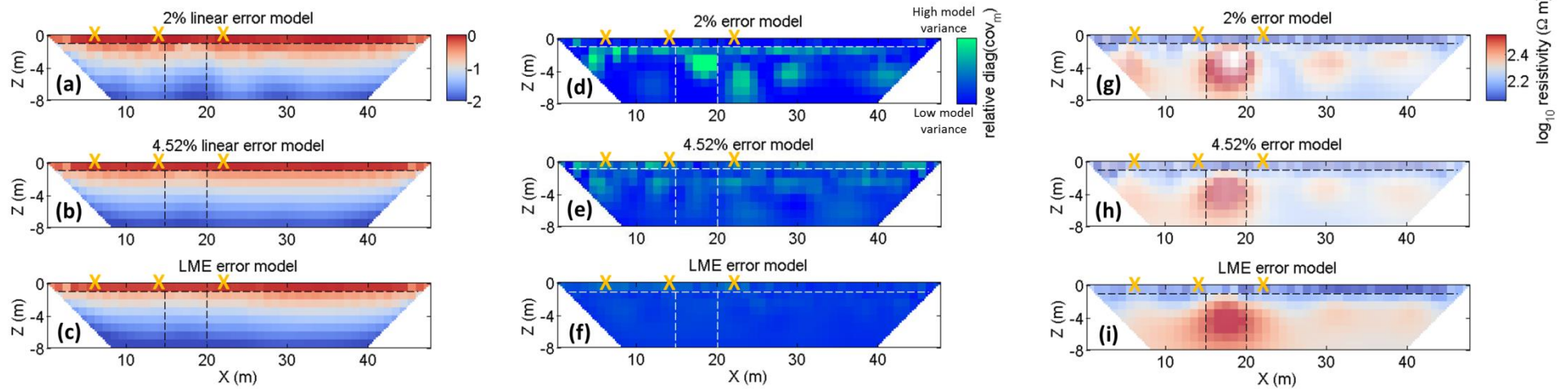


Figure 8 (a – c) Diagonal of resolution matrix for inversion using the following error models for inverting the synthetic data corrupted by “bad electrodes”: (a) 2% linear model (b) 4.52% linear model (c) LME model. (d - f) variance of element-wise log-resistivity estimates using each of the error models obtained from Monte Carlo experiments. The colour scale is the same for all three error models. Darker cells indicate more similar model estimates between Monte Carlo estimates. (g - i) mean model estimates from Monte Carlo experiments. The transparency is controlled linearly by the variance shown in (d – f). With model averaging, the mean estimates of the three error models are similar. It is noted, however, the deterministic results from the LME model agrees the best with its model-averaged results.

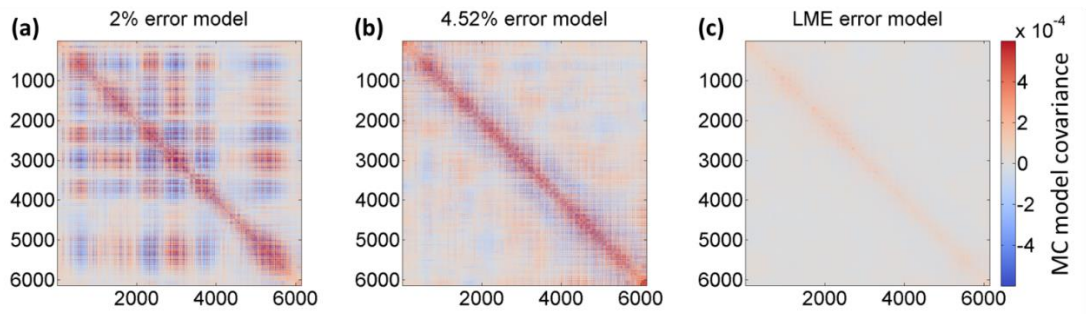


Figure 9 Empirical model covariance matrix using the Monte Carlo uncertainty propagation procedure and the following error models: (a) 2% linear model (b) 4.52% linear model (c) LME model. The size of the matrix is $m \times m$, where m is the number of model parameters. By comparing (a) and (b), it is shown that assuming higher error levels, there is higher covariance between model parameters. With the LME error model, the model covariance is the lowest. While the spread of high covariance entries are quite even throughout the matrix, we can see that the spread for (c) is quite uneven: generally, elements on the left of the domain have higher spread.

5.2. Boxford field data

In Figure 10, we compare the inversion results of field data for the Boxford datasets. When using reciprocal data, we only consider one of the 96 available datasets (i.e. the first of the 96 repeats). The resultant image from using linear or LME error models for reciprocal or 24-h repeatability errors (not shown) for the Boxford dataset are effectively identical. When the linear model is applied to the stacking errors, the resultant image shows a rather sharp feature. Surprisingly, when the LME model is applied to the stacking errors, there is no distinguishable difference between its result and those using reciprocal or 24-h repeatability errors. This shows that although we have shown above and warned against the potential underestimation of measurement errors caused by using the stacking errors, the LME error model is capable of minimizing such effects. We suspect that because of the low mean and low variance of the stacking errors, the linear error model is forced to assign very low errors across the dataset. The LME error model, in contrast, has more degrees of freedom to better fit the observed stacking errors. Note that this does not guarantee physically more realistic results.

This finding has significant implications because all modern ERT equipments output stacking errors and these do not require additional data collection time. For many existing datasets where only stacking errors are available or in applications

where the collection of repeats and reciprocal is prohibitive, we recommend using a LME error model instead of a linear model for the stacking errors.

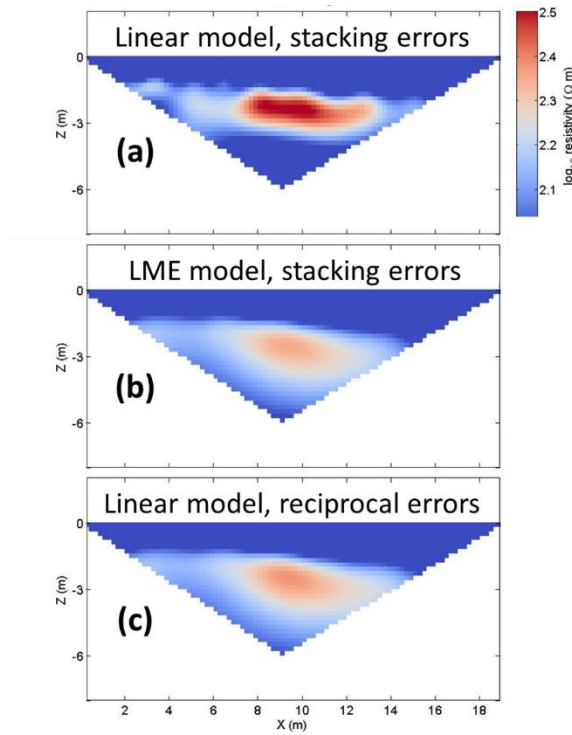


Figure 10 Inversion results from Boxford using (a) linear error model for stacking errors, (b) LME error model for stacking errors, (c) linear error model for reciprocal errors.

5.3. Sellafeld field data

We inverted the Sellafeld data collected on 5th February 2013, which was two days before the first tracer injection (Kuras et al., 2016). Of the 51,302 measurements in the sequence, there are 12,412 pairs of valid reciprocal measurements. We fitted them with the LME error model. Note that we have not removed any high-error outliers. Figure 11 shows the resultant 3-D static inversion image and its associated uncertainty estimates (model standard deviation and model coefficient of variation) derived from Monte Carlo simulations. The resultant model clearly delineates zones of high and low resistivities. In terms of uncertainty, regions next to the borehole and towards the top of the monitoring array have significantly higher model standard deviation. Compared with the absolute images of resistivity reported in Kuras et al. (2016) (note that we use the same mesh and inversion code), Figure 11a shows similar patterns but with a smaller range and variations in resistivities.

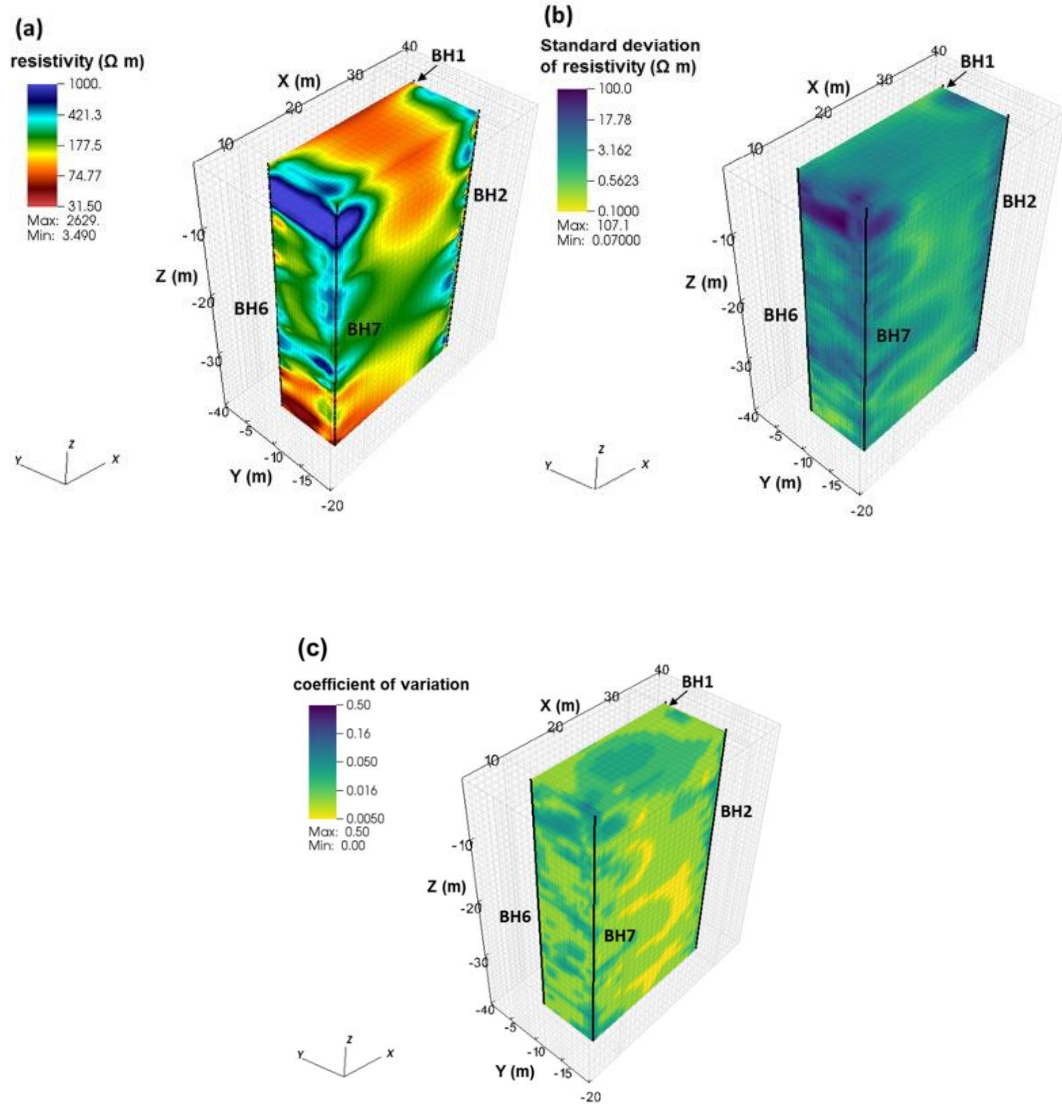


Figure 11 (a) 3-D static deterministic inversion results from Sellafield on 5th February, 2013. Error weights are prescribed by fitting an LME error model. Black lines are boreholes installed with electrodes. (b) The corresponding uncertainty estimates obtained from Monte Carlo simulations, given by model standard deviation from Monte Carlo experiments. (c) The corresponding coefficient of variation of Monte Carlo model estimates.

6) Discussion

In the present study, we have used statistical methods to explore ways to improve the current practice of modelling measurement errors in ERT. Among them, we have found that the correlation coefficients of measurement pairs that share some of the electrodes are consistently higher than average. Therefore, we have developed a

new error model that considers such effects in ERT surveys by adding electrode-specific fitting terms (i.e. the LME error model).

The proposed error model based on the linear mixed effect (LME) model shows superior performance in terms of characterising errors when compared against an unknown linear error model. The LME model assumes that errors are linearly dependent on transfer resistances and employs the electrodes used to make each measurement as grouping variables. The LME error model can more accurately predict observed measurement errors. However, as we have already argued in section 4.2, individual errors should not be used directly for inversion because in most practical situations they are only averages between two points. To improve the robustness of the linear error models, errors can be grouped by the magnitude of transfer resistances (Koestel et al., 2008). Such binning, however, is arbitrary and the resultant error models can be sensitive to the number of bins used. The LME error model is based on the same idea of grouping, yet it considers all of the four electrodes that are used to make each dipole-dipole quadrupole measurement and uses them as the grouping variable. Electrode number is a qualitative variable and it is a reasonable assumption that each electrode has slightly different quality.

The patterns of resolution matrix and model covariance matrix associated with using the LME error model are different from those using the linear model. This has important implications for inversion and uncertainty estimation because it shows that the LME model is capable of detecting poorer measurements and downweighting them in an inversion. Most inversion schemes are capable of weighting data according to their quality. Yet in common ERT practice, either uniform percentage errors (i.e. a linear model) are assumed or the errors are not characterised at all. The LME error model is one of the first statistical tools to characterise the variable quality of ERT measurements (while not using individual errors directly) so that the data weighting schemes in inverse models can be fully utilized.

While fitting a LME model for each set of reciprocal errors gives promising estimates, fitting time series of reciprocal errors with a single LME model and using the sequence of data collection as an additional grouping variable (i.e. as longitudinal

data) can yield inferior results. Evaluation of the individual resultant LME error models reveals that, for the dataset considered here, the fixed and random effects coefficients vary over the 24-hour period. Such results challenge our common assumption that electrode quality is extremely stable. The laboratory study by LaBrecque and Daily (2008) on the measurement errors of 15 electrode materials showed many possibilities for electrode quality to evolve during the course of a ERT experiment, some even in the timescale of minutes. Therefore, taking many repeats for measurements probably will not provide better error estimates because electrode quality may evolve during the process. In summary, we recommend the collection of reciprocal measurements at each timeframe and fit a LME model based on the measured transfer resistance and electrodes used to capture the minor variations in electrode quality during ERT experiments.

We have found in the Boxford inversion results that there is no distinguishable difference between using repeatability and reciprocal errors in inversions (figures not shown). From the PDFs, the stacking errors are much smaller and much less variable than the repeatability or reciprocal errors at Boxford. With the linear error model, the resultant image for using stacking errors is noisy. With the LME error model, however, the inversion image is comparable to that obtained from using repeatability or reciprocal errors. We attributed its better results to the better handling of spurious and overly optimistic estimates of errors by the LME error model.

For the Sellafeld dataset, we demonstrated the application of the new LME error model to model reciprocal errors and used its predicted errors for 3-D inversion and uncertainty quantification (i.e. model variance). Such uncertainty estimates are useful as they visualize how uncertainties in measurements propagate to uncertainties in the inverse model estimate.

We have highlighted in the previous section that the new LME error model can be widely applied to essentially any ERT inversion algorithms. It better predicts errors that are used to prescribe weights of the data weighting or covariance matrix. The resultant matrix remains diagonal so that it does not increase computation costs during inversion. Unlike the data quality control strategies recently proposed by [Deceuster et](#)

al. (2013) and Mitchell and Oldenburg (2016), the new LME error model can be applied to any static and time-lapse ERT problems regardless of their size. Since the model considers the effect of the variable quality of electrodes, it requires minimum culling of data or re-inversion. Alternatively, the new LME error model can be used alongside with other data quality control strategies.

The flexibility of the LME model allows it to be applied to characterisation of errors in other geophysical measurements. For example, geophones used in seismic tomography can be used as grouping variables for their errors. A straightforward next step for future study would be to extend the LME error model to induced polarisation (IP) studies. It has been reported in the literature that IP surveys are even more sensitive to electrode configuration than ERT. Much recent work has been done to improve quality of IP measurements. For example, Dahlin et al. (2013) conducted a duplicate IP survey for a planned tunnel using two types of cable spreads: one with standard multi-core cables and the other with separate cable spreads for transmitting current and measuring potentials. They suggest that the single cable spread is sufficient to give good IP data but suggest the use of separate cable spread for spectral IP inversion and recovery of Cole-Cole parameters. Flores-Orozco et al. (2012) quantified the measurement errors in spectral IP imaging and established a new phase error model. It is an extension of previous models where the discrepancy between normal and reciprocal measurements is analysed (Binley et al., 1995; LaBrecque et al., 1996a; Slater and Binley, 2006). They also conducted a bin analysis to ensure the assumption of a normal distribution of errors is valid and showed that, for spectral IP measurements, phase error discrepancies show a consistent behaviour for all frequencies. They proposed an inverse power-law relationship between the error on phase and the corresponding resistance. This brief review highlights the similarities between ERT and IP measurement error models and we believe that the proposed LME model can improve IP measurement errors characterisation, too. Future studies should consider applying the LME error model.

Finally, the proposed LME models can be used readily in Bayesian formulations for ERT inversion. The LME error model can be used to prescribe entries

of the data covariance matrix in their likelihood functions, which are usually assumed to be diagonal for computational convenience. Note that the LME method considers errors due to electrodes used as a grouping variable rather than enforcing a correlation function, which would lead to a full data covariance that is computationally difficult to invert. By treating the potential correlation of electrode effects as grouping variables instead, the data weighting or covariance matrix remains diagonal; furthermore, strict and unnecessary assumptions on the correlation between measurements are avoided.

7) Conclusion and recommendations

Our analysis of field datasets shows that short-term repeatability and reciprocal errors are very comparable, while stacking errors are significantly lower. Repeatability errors, however, may increase over time because of subsurface changes between repeats. Repeatability errors also tend to show greater autocorrelation in time for the same measurements, as well as correlation between measurements, than reciprocal errors. Stacking errors are found to have significantly lower magnitude and variability, indicating it may be an overly optimistic measure of measurement error. Correlation coefficients between pairs of measurements that share some of the electrodes used are higher than pairs that use completely different electrodes. This confirms speculations from previous studies that the common use of electrodes may contribute to some correlation in errors ([Ramirez et al., 2005](#)).

Based on our error analysis, we confirm the value of collecting reciprocal data in ERT studies, although when making reciprocal measurements, care should be taken to avoid electrode charge-up effects ([Dahlin, 2000](#); [Wilkinson et al., 2012](#)). If it is too difficult to set up reciprocal measurements, we recommend running a duplicate survey immediately after the completion of the original survey. Long-term repeatability data does not bring extra benefits for fitting error models because subsurface conditions may change over time. But they may be very useful for long-term quality assurance, for example, detecting instrument drift or abnormal system behaviour. Stacking errors should be avoided when assigning error weights because of their low magnitude and low variability. For modelling the measurement errors, we recommend fitting a linear

mixed effect (LME) model over the commonly used linear model. The new LME error model uses both the combination of electrodes used for making ERT measurements and the proportional relationship between errors and transferred resistance in order to better characterize measurement errors. Our synthetic example shows that the LME error model is capable of picking up errors due to the varying quality of electrodes and adjusts resolutions in the inverse model accordingly. This is different from the traditional linear model approach where the resolution everywhere in the entire inverse model domain has to reduce. The new LME model not only improves the inversion results, but also reduces the uncertainty (i.e. variance) in the model estimates. For time-lapse data, we recommend fitting a LME model for each time step because its coefficients change over time and fitting all the data from the different time steps with a single LME model (i.e. as longitudinal data) yields inferior results. We have demonstrated the applicability of the above-recommended procedure by fitting the LME model to errors observed in two field datasets and inverting the data. This procedure is easy to implement and requires minimal changes to the current practice. Widely implementing this procedure in future geophysical studies can greatly improve their overall reliability—a necessary step towards obtaining more quantitative information from geophysical methods across a range of disciplines and applications.

8) Acknowledgements

This work is supported by a Nuclear Decommissioning Authority PhD Bursary awarded to the first author and an accompanying PhD studentship provided by Lancaster University. This paper is published with the permission of the Nuclear Decommissioning Authority, Sellafield Ltd., and the Executive Director of the British Geological Survey (NERC). We thank Paul Mclachlan (Lancaster University) for assistance on using R. We are grateful to two anonymous reviewers for the constructive reviews of the manuscript.

9) References

- Aster, R., Borchers, B., Thurber, C.H., 2005. Parameter estimation and inverse problems. Elsevier, Burlington, Massachusetts, USA.
- Barker, J.A., 1991. The reciprocity principle and an analytical solution for Darcian flow in a network. *Water Resour. Res.* 27, 743–746. <https://doi.org/10.1029/91WR00258>
- Bates, D., Maechler, M., Bolker, B.M., Walker, S., 2015. Fitting Linear Mixed-Effects Models using {lme4}. *J. Stat. Softw.* 67, 1–48. <https://doi.org/10.18637/jss.v067.i01>
- Beven, K., Westerberg, I., 2011. On red herrings and real herrings: disinformation and information in hydrological inference. *Hydrol. Process.* 25, 1676–1680. <https://doi.org/10.1002/hyp.7963>
- Binley, A., 2015. Tools and techniques: Electrical methods. *Treatise Geophys.* <https://doi.org/10.1016/B978-0-444-53802-4.00192-5>
- Binley, A., Hubbard, S.S., Huisman, J.A., Revil, A., Robinson, D.A., Singha, K., Slater, L.D., 2015. The emergence of hydrogeophysics for improved understanding of subsurface processes over multiple scales. *Water Resour. Res.* 51, 3837–3866. <https://doi.org/10.1002/2015WR017016>
- Binley, A., Ramirez, A.L., Daily, W., 1995. Regularised image reconstruction of noisy electrical resistance data, in: *Proceedings of the 4th Workshop of the European Concerted Action on Process Tomography*,. Bergen, pp. 401–410.
- Bruggeman, G.A., 1972. The reciprocity principle in flow through heterogeneous porous media, in: *Fundamentals of Transport Phenomena in Porous Media*,. Elsevier, New York, p. 136.
- Cassiani, G., Bruno, V., Villa, A., Fusi, N., Binley, A.M., 2006. A saline tracer test monitored via time-lapse surface electrical resistivity tomography. *J. Appl. Geophys.* 59, 244–259. <https://doi.org/10.1016/j.jappgeo.2005.10.007>
- Chambers, J.E., Wilkinson, P.B., Uhlemann, S., Sorensen, J.P.R., Roberts, C., Newell, A.J., Ward, W.O.C., Binley, A., Williams, P.J., Goody, D.C., Old, G., Bai, L., 2014. Derivation of lowland riparian wetland deposit architecture using geophysical image analysis and interface detection. *Water Resour. Res.* 50, 5886–5905. <https://doi.org/10.1002/2014WR015643>
- Crook, N., Binley, A., Knight, R., Robinson, D.A., Zarnetske, J., Haggerty, R., 2010. Electrical resistivity imaging of the architecture of substream sediments. *Water Resour. Res.* 46, W00D13. <https://doi.org/10.1029/2008WR006968>

References

- Dahlin, T., 2000. Short note on electrode charge-up effects in DC resistivity data acquisition using multi-electrode arrays. *Geophys. Prospect.* 48, 181–187. <https://doi.org/10.1046/j.1365-2478.2000.00172.x>
- Dahlin, T., Dalsegg, E., Sandstrom, T., 2013. Data quality quantification for time domain IP data acquired along a planned tunnel near Oslo, Norway, in: *Near Surface Geoscience 2013--19th European Meeting of Environmental and Engineering Geophysics*. Bochum, Germany.
- Day-Lewis, F.D., Johnson, C.D., Singha, K., Lane Jr, J.W., 2008. Best practices in electrical resistivity imaging: Data collection and processing, and application to data from Corinna, Maine. EPA report, Boston, MA.
- Deceuster, J., Kaufmann, O., Camp, M. Van, 2013. Automated identification of changes in electrode contact properties for long-term permanent ERT monitoring experiments. *Geophysics* 78, E79–E94. <https://doi.org/10.1190/GEO2012-0088.1>
- Delay, F., Ackerer, P., Guadagnini, A., 2011. Theoretical analysis and field evidence of reciprocity gaps during interference pumping tests. *Adv. Water Resour.* 34, 592–606. <https://doi.org/10.1016/j.advwatres.2011.02.006>
- Diggle, P.J., Heagerty, P., Liang, K.-Y., Zeger, S., 2015. *Analysis of Longitudinal Data*, 2nd ed. Oxford University Press.
- Falade, G.K., 1981. Analysis of the reciprocity concept in a porous medium. *Water Resour. Res.* 17, 918–920. <https://doi.org/10.1029/WR017i004p00918>
- Flores-Orozco, A., Kemna, A., Zimmermann, E., 2012. Data error quantification in spectral induced polarization imaging. *Geophysics* 77, E227. <https://doi.org/10.1190/geo2010-0194.1>
- Flores-Orozco, A., Williams, K.H., Long, P.E., Hubbard, S.S., Kemna, A., 2011. Using complex resistivity imaging to infer biogeochemical processes associated with bioremediation of an uranium-contaminated aquifer. *J. Geophys. Res. Biogeosciences* 116, 1–17. <https://doi.org/10.1029/2010JG001591>
- French, H.K., Hardbattle, C., Binley, A., Winship, P., Jakobsen, L., 2002. Monitoring snowmelt induced unsaturated flow and transport using electrical resistivity tomography. *J. Hydrol.* 267, 273–284. [https://doi.org/10.1016/S0022-1694\(02\)00156-7](https://doi.org/10.1016/S0022-1694(02)00156-7)
- Gélis, C., Revil, A., Cushing, M.E., Jougnot, D., Lemeille, F., Cabrera, J., de Hoyos, A., Rocher, M., 2010. Potential of electrical resistivity tomography to detect fault zones in limestone and argillaceous formations in the experimental platform of

References

- Tournemire, France. *Pure Appl. Geophys.* 167, 1405–1418.
<https://doi.org/10.1007/s00024-010-0097-x>
- Haarder, E.B., Jensen, K.H., Binley, A.M., Nielsen, L., Uglebjerg, T.B., Looms, M.C., 2015. Estimation of recharge from long-term monitoring of saline tracer transport using electrical resistivity tomography. *Vadose Zo. J.*
<https://doi.org/10.2136/vzj2014.08.0110>
- Hayley, K., Bentley, L.R., Gharibi, M., 2009. Time-lapse electrical resistivity monitoring of salt-affected soil and groundwater. *Water Resour. Res.* 45, 1–14.
<https://doi.org/10.1029/2008WR007616>
- Henderson, R.D., Day-Lewis, F.D., Abarca, E., Harvey, C.F., Karam, H.N., Liu, L., Lane, J.W.J., 2010. Marine electrical resistivity imaging of submarine groundwater discharge: sensitivity analysis and application in Waquoit Bay, Massachusetts, USA. *Hydrogeol. J.* 18, 173–185. <https://doi.org/10.1007/s10040-009-0498-z>
- Hermans, T., Vandenbohede, A., Lebbe, L., Nguyen, F., 2012. A shallow geothermal experiment in a sandy aquifer monitored using electric resistivity tomography. *Geophysics* 77, B11. <https://doi.org/10.1190/geo2011-0199.1>
- Huisman, J.A., Rings, J., Vrugt, J.A., Sorg, J., Vereecken, H., 2010. Hydraulic properties of a model dike from coupled Bayesian and multi-criteria hydrogeophysical inversion. *J. Hydrol.* 380, 62–73. <https://doi.org/10.1016/j.jhydrol.2009.10.023>
- Irving, J., Singha, K., 2010. Stochastic inversion of tracer test and electrical geophysical data to estimate hydraulic conductivities. *Water Resour. Res.* 46, W11514.
<https://doi.org/10.1029/2009WR008340>
- Johnson, T.C., Slater, L.D., Ntarlagiannis, D., Day-Lewis, F.D., Elwaseif, M., 2012. Monitoring groundwater-surface water interaction using time-series and time-frequency analysis of transient three-dimensional electrical resistivity changes. *Water Resour. Res.* 48, 1–13. <https://doi.org/10.1029/2012WR011893>
- Johnson, T.C., Versteeg, R., Thomle, J., Hammond, G., Chen, X., Zachara, J., 2015. Four-dimensional electrical conductivity monitoring of stage-driven river water intrusion: Accounting for water table effects using a transient mesh boundary and conditional inversion constraints. *Water Resour. Res.* 51, 6177–6196.
<https://doi.org/10.1002/2014WR016129>
- Kemna, A., 2000. Tomographic inversion of complex resistivity. Ruhr-Universität Bochum.

References

- Kim, J., Supper, R., Ottowitz, D., Jochum, B., Yi, M., 2016. A new measurement protocol of direct current resistivity data. *Geophysics* 81.
- Koestel, J., Kemna, A., Javaux, M., Binley, A., Vereecken, H., 2008. Quantitative imaging of solute transport in an unsaturated and undisturbed soil monolith with 3-D ERT and TDR. *Water Resour. Res.* 44, 1–17. <https://doi.org/10.1029/2007WR006755>
- Kuras, O., Wilkinson, P.B., Meldrum, P.I., Oxby, L.S., Uhlemann, S., Chambers, J.E., Binley, A., Graham, J., Smith, N.T., Atherton, N., 2016. Geoelectrical monitoring of simulated subsurface leakage to support high-hazard nuclear decommissioning at the Sellafield Site, UK. *Sci. Total Environ.* 566–567, 350–359. <https://doi.org/10.1016/j.scitotenv.2016.04.212>
- LaBrecque, D.J., Mletto, M., Daily, W., Ramirez, A.L., Owen, E., 1996. The effects of noise on Occam's inversion of resistivity tomography data. *Geophysics* 61, 538. <https://doi.org/10.1190/1.1443980>
- Lesparre, N., Boyle, A., Grychtol, B., Cabrera, J., Marteau, J., Adler, A., 2016. Electrical resistivity imaging in transmission between surface and underground tunnel for fault characterization. *J. Appl. Geophys.* <https://doi.org/10.1016/j.jappgeo.2016.03.004>
- Linde, N., Renard, P., Mukerji, T., Caers, J., 2015. Geological Realism in Hydrogeological and Geophysical Inverse Modeling: a Review. *Adv. Water Resour.* 86, 86–101. <https://doi.org/10.1016/j.advwatres.2015.09.019>
- Loke, M.H., Barker, R.D., 1996. Practical techniques for 3D resistivity surveys and data inversion. *Geophys. Prospect.* 44, 499–523. <https://doi.org/10.1111/j.1365-2478.1996.tb00162.x>
- Meyerhoff, S.B., Maxwell, R.M., Revil, A., Martin, J.B., Karaoulis, M., Graham, W.D., 2014. Characterization of groundwater and surface water mixing in a semiconfined karst aquifer using time-lapse electrical resistivity tomography. *Water Resour. Res.* 50, 2566–2585. <https://doi.org/10.1002/2013WR013991>
- Mitchell, M.A., Oldenburg, D.W., 2016. Data quality control methodology for large , non-conventional DC resistivity datasets. *J. Appl. Geophys.* 3, 948–953. <https://doi.org/10.1016/j.jappgeo.2016.09.018>
- Morelli, G., LaBrecque, D.J., 1996. Advances in ERT inverse modeling. *Eur. J. Environ. Eng. Geophys.* 1, 171–186.

References

- Musgrave, H., Binley, A., 2011. Revealing the temporal dynamics of subsurface temperature in a wetland using time-lapse geophysics. *J. Hydrol.* 396, 258–266. <https://doi.org/10.1016/j.jhydrol.2010.11.008>
- Nimmer, R.E., Osiensky, J.L., Binley, A.M., Sprenke, K.F., Williams, B.C., 2007. Electrical resistivity imaging of conductive plume dilution in fractured rock. *Hydrogeol. J.* 15, 877–890. <https://doi.org/10.1007/s10040-007-0159-z>
- Parasnis, D.S., 1988. Reciprocity theorems in geoelectric and geoelectromagnetic work. *Geoexploration* 25, 177–198. [https://doi.org/10.1016/0016-7142\(88\)90014-2](https://doi.org/10.1016/0016-7142(88)90014-2)
- Pearson, E.S., Hartley, H.O. (Eds.), 1970. *Biometrika tables for statisticians*. Cambridge University Press.
- Perri, M.T., Cassiani, G., Gervasio, I., Deiana, R., Binley, A., 2012. A saline tracer test monitored via both surface and cross-borehole electrical resistivity tomography: Comparison of time-lapse results. *J. Appl. Geophys.* 79, 6–16. <https://doi.org/10.1016/j.jappgeo.2011.12.011>
- Pinheiro, J., Bates, D., 1988. Unconstrained parameterizations for variance-covariance matrices. *Stat. Comput.* 6, 289–296.
- Ramirez, A., Daily, W., Binley, A., Labrecque, D., Roelant, D., 1996. Detection of leaks in underground storage tanks using electrical resistance methods. *J. Environ. Eng. Geophys.* 1, 189–203. <https://doi.org/10.4133/JEEG1.3.189>
- Ramirez, A.L., Nitao, J.J., Hanley, W.G., Aines, R., Glaser, R.E., Sengupta, S.K., Dyer, K.M., Hickling, T.L., Daily, W.D., 2005. Stochastic inversion of electrical resistivity changes using a Markov Chain Monte Carlo approach. *J. Geophys. Res.* 110, B02101. <https://doi.org/10.1029/2004JB003449>
- Revil, A., Johnson, T.C., Finizola, A., 2010. Three-dimensional resistivity tomography of Vulcan's forge, Vulcano Island, southern Italy. *Geophys. Res. Lett.* 37, 1–5. <https://doi.org/10.1029/2010GL043983>
- Robert, T., Dassargues, A., Brouyère, S., Kaufmann, O., Hallet, V., Nguyen, F., 2011. Assessing the contribution of electrical resistivity tomography (ERT) and self-potential (SP) methods for a water well drilling program in fractured/karstified limestones. *J. Appl. Geophys.* 75, 42–53. <https://doi.org/10.1016/j.jappgeo.2011.06.008>
- Robinson, J., Johnson, T., Slater, L., 2015. Challenges and opportunities for fractured rock imaging using 3D cross borehole electrical resistivity. *Geophysics* 80, E49–E61. <https://doi.org/10.1190/GEO2014-0138.1>

References

- Rubin, Y., Hubbard, S.S. (Eds.), 2005. *Hydrogeophysics*. Springer.
- Schmidt-Hattenberger, C., Bergmann, P., Labitzke, T., Wagner, F., Rippe, D., 2016. Permanent crosshole electrical resistivity tomography (ERT) as an established method for the long-term CO₂ monitoring at the Ketzin pilot site. *Int. J. Greenh. Gas Control* 52, 432–448. <https://doi.org/10.1016/j.ijggc.2016.07.024>
- Singha, K., Gorelick, S.M., 2006. Effects of spatially variable resolution on field-scale estimates of tracer concentration from electrical inversions using Archie's law. *Geophysics* 71, G83. <https://doi.org/10.1190/1.2194900>
- Slater, L., Binley, A., 2006. Synthetic and field-based electrical imaging of a zerovalent iron barrier: Implications for monitoring long-term barrier performance. *Geophysics* 71, B129–B137. <https://doi.org/10.1190/1.2235931>
- Slater, L., Binley, A., 2003. Evaluation of permeable reactive barrier (PRB) integrity using electrical imaging methods. *Geophysics* 68, 911–921. <https://doi.org/10.1190/1.1581043>
- Slater, L., Binley, A.M., Daily, W., Johnson, R., 2000. Cross-hole electrical imaging of a controlled saline tracer injection. *J. Appl. Geophys.* 44, 85–102. [https://doi.org/10.1016/S0926-9851\(00\)00002-1](https://doi.org/10.1016/S0926-9851(00)00002-1)
- Slater, L.D., Ntarlagiannis, D., Day-Lewis, F.D., Mwakanyamale, K., Versteeg, R.J., Ward, A., Strickland, C., Johnson, C.D., Lane, J.W., 2010. Use of electrical imaging and distributed temperature sensing methods to characterize surface water-groundwater exchange regulating uranium transport at the Hanford 300 Area, Washington. *Water Resour. Res.* 46, 1–13. <https://doi.org/10.1029/2010WR009110>
- Uhlemann, S., Sorensen, J.P.R., House, A.R., Wilkinson, P.B., Roberts, C., Goody, D.C., 2016. Integrated time-lapse geoelectrical imaging of wetland hydrological processes. *Water Resour. Res.* 52, 1607–1625. <https://doi.org/10.1002/2015WR017932>
- Uhlemann, S., Wilkinson, P., Chambers, J., Maurer, H., Merritt, A., Gunn, D., Meldrum, P., 2015. Interpolation of landslide movements to improve the accuracy of 4D geoelectrical monitoring. *J. Appl. Geophys.* 121, 93–105. <https://doi.org/10.1016/j.jappgeo.2015.07.003>
- Vereecken, H., Binley, A., Cassiani, G., Revil, A., Titov, K. (Eds.), 2006. *Applied Hydrogeophysics*, NATO Science Series. Springer Netherlands, Dordrecht. <https://doi.org/10.1007/978-1-4020-4912-5>

References

- Wagner, F.M., Möller, M., Schmidt-Hattenberger, C., Kempka, T., Maurer, H., 2013. Monitoring freshwater salinization in analog transport models by time-lapse electrical resistivity tomography. *J. Appl. Geophys.* 89, 84–95. <https://doi.org/10.1016/j.jappgeo.2012.11.013>
- Wallin, E.L., Johnson, T.C., Greenwood, W.J., Zachara, J.M., 2013. Imaging high stage river-water intrusion into a contaminated aquifer along a major river corridor using 2-D time-lapse surface electrical resistivity tomography. *Water Resour. Res.* 49, 1693–1708. <https://doi.org/10.1002/wrcr.20119>
- Wehrer, M., Slater, L.D., 2015. Characterization of water content dynamics and tracer breakthrough by 3-D electrical resistivity tomography (ERT) under transient unsaturated conditions. *Water Resour. Res.* 51, 97–124. <https://doi.org/10.1002/2014WR016131>
- West, B., Welch, K.E., Galecki, A.T., 2007. *Linear Mixed Models: a practical guide using statistical software*, 2nd ed. Chapman and Hall/CRC.
- Wilkinson, P., Chambers, J., Uhlemann, S., Meldrum, P., Smith, A., Dixon, N., Loke, M.H., 2016. Reconstruction of landslide movements by inversion of 4-D electrical resistivity tomography monitoring data. *Geophys. Res. Lett.* 43, 1166–1174. <https://doi.org/10.1002/2015GL067494>
- Wilkinson, P.B., Chambers, J.E., Lelliott, M., Wealthall, G.P., Ogilvy, R.D., 2008. Extreme sensitivity of crosshole electrical resistivity tomography measurements to geometric errors. *Geophys. J. Int.* 173, 49–62. <https://doi.org/10.1111/j.1365-246X.2008.03725.x>
- Wilkinson, P.B., Chambers, J.E., Meldrum, P.I., Gunn, D.A., Ogilvy, R.D., Kuras, O., 2010a. Predicting the movements of permanently installed electrodes on an active landslide using time-lapse geoelectrical resistivity data only. *Geophys. J. Int.* 183, 543–556. <https://doi.org/10.1111/j.1365-246X.2010.04760.x>
- Wilkinson, P.B., Loke, M.H., Meldrum, P.I., Chambers, J.E., Kuras, O., Gunn, D.A., Ogilvy, R.D., 2012. Practical aspects of applied optimized survey design for electrical resistivity tomography. *Geophys. J. Int.* 189, 428–440. <https://doi.org/10.1111/j.1365-246X.2012.05372.x>
- Wilkinson, P.B., Meldrum, P.I., Kuras, O., Chambers, J.E., Holyoake, S.J., Ogilvy, R.D., 2010b. High-resolution Electrical Resistivity Tomography monitoring of a tracer test in a confined aquifer. *J. Appl. Geophys.* 70, 268–276. <https://doi.org/10.1016/j.jappgeo.2009.08.001>

- Williams, M.R., Buda, A.R., Singha, K., Folmar, G.J., Elliott, H.A., Schmidt, J.P., 2016. Imaging Hydrological Processes in Headwater Riparian Seeps with Time-Lapse Electrical Resistivity. *Groundwater* 1–13. <https://doi.org/10.1111/gwat.12461>
- Yang, X., Chen, X., Carrigan, C.R., Ramirez, A.L., 2014. Uncertainty quantification of CO₂ saturation estimated from electrical resistance tomography data at the Cranfield site. *Int. J. Greenh. Gas Control* 27, 59–68. <https://doi.org/10.1016/j.ijggc.2014.05.006>
- Yeh, T.-C.J., Zhu, J., Englert, A., Guzman, A., Flaherty, S., 2006. A successive linear estimator for electrical resistivity tomography, in: Vereecken, H., Binley, A.M., Cassini, G., Revil, A., Titov, K. (Eds.), *Applied Hydrogeophysics*. Springer Netherlands, pp. 45–74. https://doi.org/10.1007/978-1-4020-4912-5_3
- Zhou, B., Dahlin, T., 2003. Properties and effects of measurement errors on 2D resistivity imaging surveying. *Near Surf. Geophys.* 1, 105–117. <https://doi.org/10.3997/1873-0604.2003001>

10) Supplementary information

LME electrode grouping formulation

To demonstrate the formulation of the new error model, we use a small subset of the Boxford data to create different formulations of the linear mixed effects (LME) error model. The first 25 measurements from the first set of Boxford are selected to fit different models. We show that in Figure SI 1 that the linear or the binned linear models perform poorly when fitting the reciprocal errors. By using LME models that use average transfer resistance as the fixed effect, we see that much better fit of errors is achieved by selecting any one of the four electrodes as a grouping variable. The LME model essentially matches all the observed errors if all four electrodes are used as grouping variables. It can be further improved by using dipole separation a and dipole-dipole separation multiplier n as additional grouping variables.

We recommend fitting the LME error model in log-log scale to avoid negative error estimates. Also, one should recognize if reciprocal errors are used, either the configuration for “direct” and “reciprocal” set can be used to fit the model. Finally, when there are incomplete reciprocal measurements, the LME model can be used in “prediction mode” to estimate their errors.

Fitting LME models to field data

We fit each of the 96 sets of Boxford reciprocal errors data individually with a LME model, where average transfer resistance is the fixed effect variable and the 4 dipole-dipole electrodes (i.e. c_1 , c_2 , p_1 , p_2) are the grouping variables. Figure SI 2 shows the evolution of the fixed-effect coefficients with time. The resultant coefficients vary within a range but we can see they fluctuate significantly over time. The $\pm 95\%$ confidence interval is also plotted as shaded regions. Figure SI 3 shows the random effects coefficients of the resultant LME model for the first set of Boxford data as a function of electrode number. We can see that the random effects coefficients span a smaller range than the fixed effect ones. We can also see that the coefficients for the four grouping variables (i.e. c_1 , c_2 , p_1 , p_2) are somewhat correlated. It is important, however, to note that random effect coefficients change discernibly with time.

We find that the binned linear model is quite stable at Sellafield regardless of whether tracer was injected or not (Figure SI 4). It is therefore important to study whether an LME model is stable too. Again, we fit each of the 246 sets of Sellafield data individually with an LME model. Figure SI 5 shows the evolution of the fixed-effect coefficients with time. Figure SI 6 shows the random effects coefficients of the resultant LME model for the 5th February 2013 Sellafield data as a function of electrode number. We can see that the coefficients are an order-of-magnitude higher than in the Boxford data. We can also see that for certain electrode numbers the random effect coefficients have much higher magnitudes, which indicates that some electrodes have a greater impact on the observed errors from the fixed effect (i.e. transferred resistance). Finally, the coefficients estimates do not show significant trends during the 2-year monitoring periods, both during and outside the injection periods.

A guide to implement the LME error model in MATLAB®

To fit a LME model in MATLAB®, the statistics and machine learning toolbox is required. Assume you have vectors of electrode configurations c_1, c_2, p_1, p_2 , average transferred resistances R , and observed measurement errors err , they first need to be put into a MATLAB® table by using the command:

Supplementary information

```
tbl=table(log10(R),log10(err),c1,c2
p1,p2,'VariableNames',{'R','err','c1','c2','p1','p2'});
```

Then fit the LME model with the following command:

```
lme = fitlme(tbl,'err ~ R+(R|c1)+(R|c2)+(R|p1)+(R|p2)');
```

This formulation assumes potential correlated random effects among grouping variables $c1$, $c2$, $p1$, $p2$. To get the LME model-predicted measurement errors, use the command:

```
fitted(lme)
```

If prediction of measurement errors is needed (i.e. the dataset contains measurements with no error observations available), use the command:

```
predict(lme,tblnew)
```

where `tblnew` is a table of vectors of electrode configurations where predictions are made.

A guide to implement the LME error model in R

To fit a LME model in R, the `lme4` package is required. Fit the LME error model using the command:

```
lme <- lmer(Res_Err ~
Res_Ave+(Res_Err|C1)+(Res_Err|C2)+(Res_Err|P1)+(Res_Err|P2))
```

If you would like to run the above R script in Python, the `rpy2` (<https://rpy2.bitbucket.io/>) interface may be used.

Supplementary information

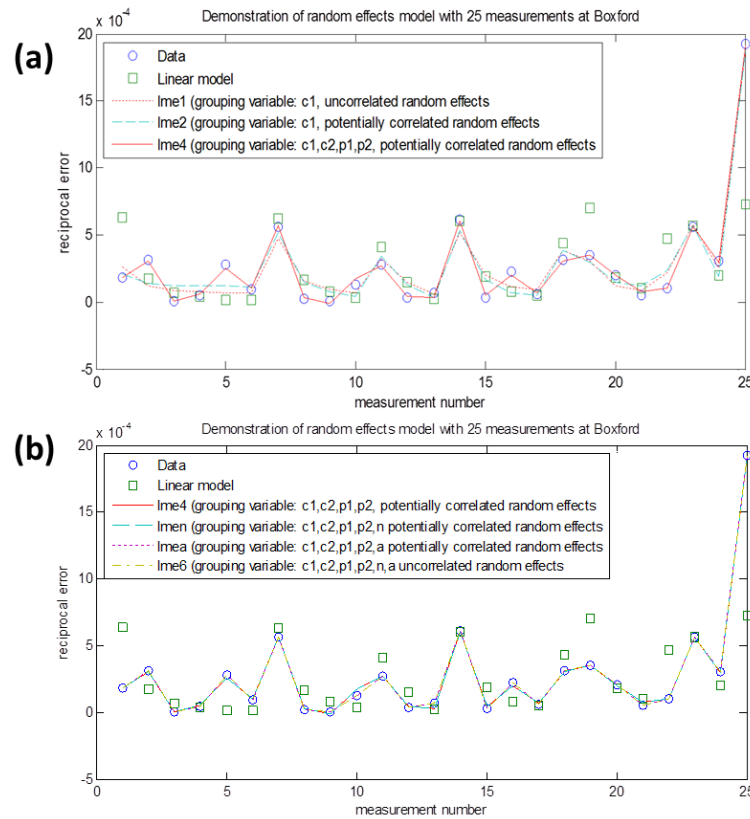


Figure SI 1 Illustration plot to compare fitting linear and LME model for ERT measurement errors. The LME error model provides a much better fit to measurement errors, especially the high measurement errors.

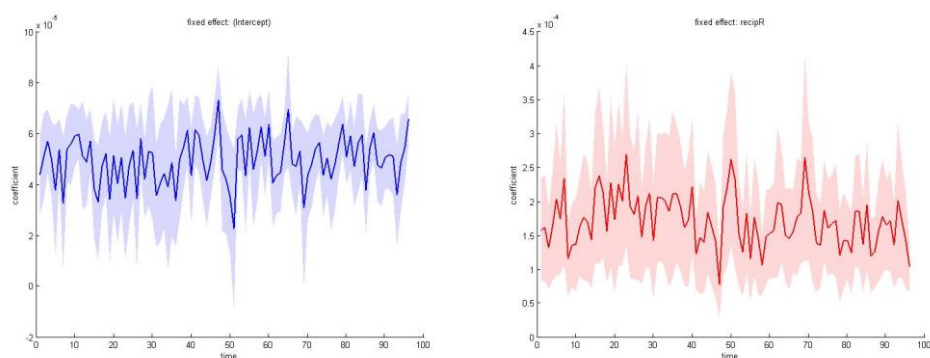


Figure SI 2 Fixed effects coefficients for the LME error models for each of the Boxford datasets. The x-axis is the dataset number in ascending order of collection (the time required to collect the 96 datasets is around 24 hours). The left panel is when 'intercept' is used as the random-effect coefficient and the right panel is for transfer resistance. The solid line is the maximum-likelihood estimate, while the shaded area is enclosed by $\pm 95\%$ confidence intervals.

Supplementary information

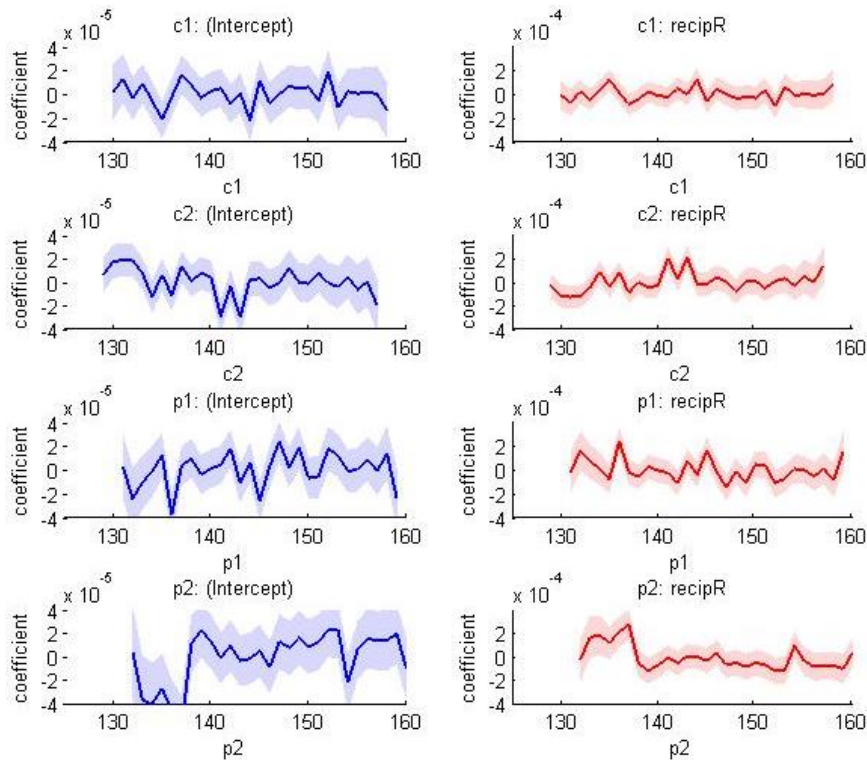


Figure SI 3 Random effects coefficients for the LME error model for a frame of the Bofford dataset. The x-axis is the electrode number, where c1 and c2 are when the measurements are used as current electrodes and p1 and p2 are when they are used as potential electrodes. The left panel is when 'intercept' is used as the random-effect coefficient and the right panel is for transfer resistance. The solid line is the maximum-likelihood estimate, while the shaded area is enclosed by +/-95% confidence intervals. Note the fixed effects for this linear mixed effect error model is $4.3708e-05 \pm 1.5628e-05$ for 'intercept' and $1.5742e-04 \pm 7.527e-05$ for transfer resistance.

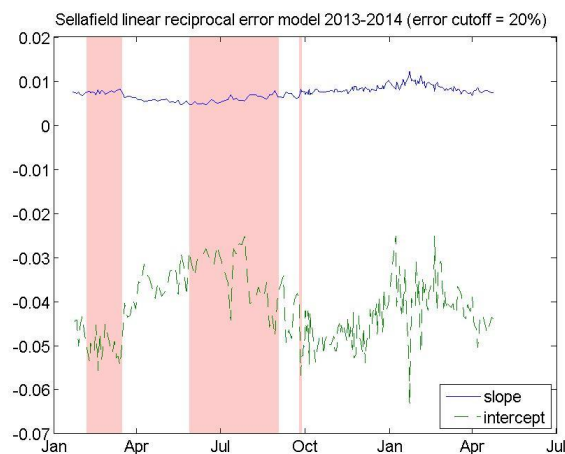


Figure SI 4 Time series of linear error model for reciprocal errors at Sellafield. Errors higher than 20% are not fitted. The blue line is the intercept of the linear model estimate, while the green and red lines are the estimates for the slope. The three shaded regions are stimulant injection periods. It is shown that the slope of the linear error models (i.e. percentage errors) did not vary significantly during the monitoring period and the stimulant injection has little impact on error levels.

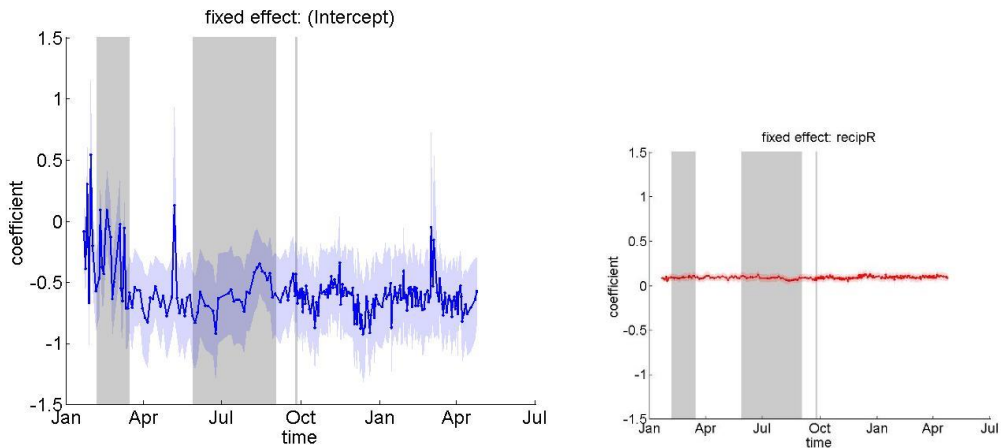


Figure SI 5 Time series of the fixed effect coefficients estimates for the LME error model for Sellfield. The three shaded regions are stimulant injection periods.

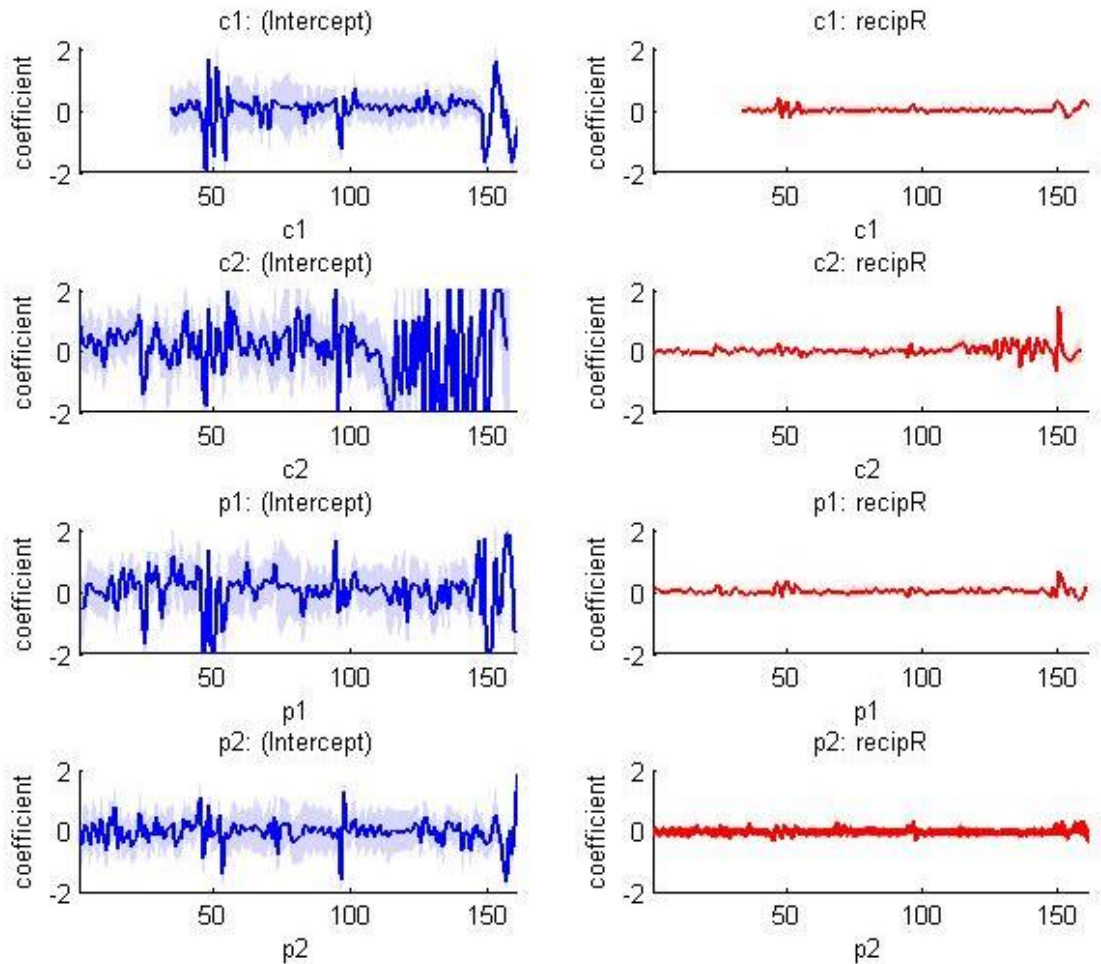


Figure SI 6 Random effect coefficients for LME error model at Sellfield on 5th February, 2014. The x-axis is the electrode number, where c1 and c2 are when the measurements are used as current electrodes and p1 and p2 are when they are used as potential electrodes. The left panel is when 'intercept' is used as the random-effect coefficient and the right panel is for transfer resistance. The solid line is the maximum-likelihood estimate, while the shaded area is enclosed by +/-95% confidence intervals. Note the fixed effects for this linear mixed effect error model is 0.47852 +/- 0.4865 for 'intercept' and 0.01428 +/- 0.027414 for transfer resistance.

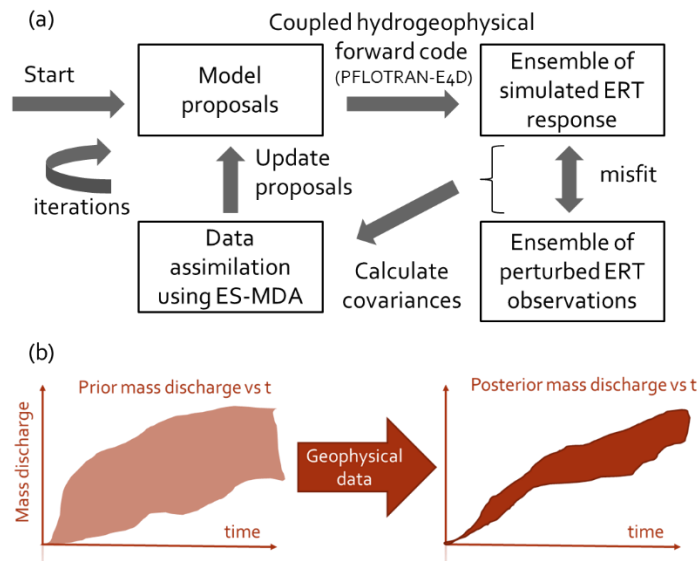
5. Paper 2: Integrated hydrogeophysical modelling and data assimilation for geoelectrical leak detection

Submitted for peer review to *Journal of Contaminant Hydrology* as **Tso, C.-H.M.**,
Johnson, T., Song, X., Chen, X., Kuras, O., Wilkinson, P., Uhlemann, S., Chambers, J.,
Binley, A. (201x) Integrated hydrogeophysical modelling and data assimilation for
geoelectrical leak detection

Abstract

Time-lapse electrical resistivity tomography (ERT) measurements provide indirect observations of hydrological processes in the Earth's shallow subsurface at high spatial and temporal resolution. ERT has been used in the past decades to detect leaks and monitor the evolution of associated contaminant plumes. Specifically, inverted resistivity images allow visualization of the dynamic changes in the structure of the plume. However, existing methods do not allow the direct estimation of leak parameters (e.g. leak rate, location, etc.) and their uncertainties. We propose an ensemble-based data assimilation framework that evaluates proposed hydrological models against observed time-lapse ERT measurements without directly inverting for the resistivities. Each proposed hydrological model is run through the parallel coupled hydro-geophysical simulation code PFLOTRAN-E4D to obtain simulated ERT measurements. The ensemble of model proposals is then updated using an iterative ensemble smoother. We demonstrate the proposed framework on synthetic and field ERT data from controlled tracer injection experiments. Our results show that the approach allows joint identification of contaminant source location, initial release time, and solute loading from the cross-borehole time-lapse ERT data, alongside with an assessment of uncertainties in these estimates. We demonstrate a reduction in site-wide uncertainty by comparing the prior and posterior plume mass discharges at a selected image plane. This framework is particularly attractive to sites that have previously undergone extensive geological investigation (e.g., nuclear sites). It is well suited to complement ERT imaging and we discuss practical issues in its application to field problems.

Graphical abstract



Estimation of leak parameters and their uncertainties using raw geophysical data and data assimilation.

1) Introduction

Identification of solute loadings from an unknown source is a complex yet critical problem. For example, understanding the whereabouts of the source(s) of contamination is often the first question that needs to be addressed in a remediation project. This identification, however, is not straightforward and it is often complicated by factors such as unknown forcing (e.g., boundary and flow conditions), aquifer and vadose zone heterogeneity, and limited data (in terms of number, types, temporal and spatial coverage). Because of these complications, attempts to assess source identification should also address the uncertainties in the estimates, and provide realistic and actionable uncertainty bounds.

Traditional point-based sampling methods suffer from limited coverage and resolution. As prompted, in part, by the wealth of studies in stochastic subsurface hydrology that argued for better field techniques, geophysical methods have emerged as valuable tools for investigating shallow subsurface processes over the past two decades (Binley et al., 2015). Geophysical methods can provide much larger spatial and temporal resolution. Once installed, autonomous long-term monitoring systems, such

as ALERT (Kuras et al., 2009), can repeatedly collect geophysical data and transmit it back to the office using telemetry. Among them, electrical resistivity tomography (ERT) is particularly suitable for leak detection due to its sensitivity to fluid conductivity. Note that leak detection is not limited to the detection of the breakthrough of saline fluids (as proxies of contaminants), but it also includes monitoring the integrity of water-retaining structures (e.g. embankments or levees) (Abdulsamad et al., 2019) and landfills (Audebert et al., 2014; Chambers et al., 2006; Maurya et al., 2017).

Many previous ERT studies have focused on inferring plume characteristics by delineating the plume geometry (Aghasi et al., 2013), obtaining summary statistics of the plume structure (e.g. spatial and temporal movements) (Crestani et al., 2015; Pidlisecky et al., 2011; Singha and Gorelick, 2006), or developing methods for automatic tracking of plumes (Ward et al., 2016). There is also a substantial amount of work dedicated to delineating local hydraulic properties using ERT (e.g. Camporese et al., 2011). As an effort to better use geophysical data for hydrogeological studies, comparisons between coupled and uncoupled hydrogeophysical inversions of ERT-monitored tracer tests have been made (Camporese et al., 2015; Hinnell et al., 2010). Others have tried to address the uncertain link between hydrological systems and geophysical data using data-driven or machine learning approaches (Hermans et al., 2016b, 2015; Oware et al., 2013). There is also increased use of geophysics to estimate remediation efficiency (LaBrecque et al., 1996b). For example, Power et al. (2014) applied 4D active time-constrained inversion to time-lapse ERT data to estimate the volume of solute plume remediated in a laboratory experiment.

The various electrical methods applied to the mapping and monitoring at the U.S. Department of Energy Hanford nuclear site has greatly improved the readiness of these methods (Johnson et al., 2015a). For example, the work on the monitoring of the groundwater/river water interaction beneath the Hanford 300 Area infiltration bonds (Johnson et al., 2012; Johnson et al., 2015b; Slater et al., 2010; Wallin et al., 2013) shows ERT is well suited for monitoring such complex and dynamic processes, while the successful monitoring of vadose zone desiccation (Truex et al., 2013b, 2012) at the BC Cribs Area demonstrates its capability to monitor 3-D changes in moisture content

caused by gas injection. The leak tank experiments in the 1990s and 2000s have contributed some important work in geoelectrical leak detection. The first two mock tank experiments set up a 15 m diameter steel tank at the Hanford site and ERT tomograms clearly shows area of resistivity decrease of the leak plume (Ramirez et al., 1996). A subsequent series of mock tank experiments evaluated a number of electrical methods for leak detection (Barnett et al., 2003). Among them, a “blind test” was carried out for 110 days where the release episodes were not known to the modeller (Daily et al., 2004). The modeller achieved a 57% success rate in defining a leak or no leak declaration during the test, although further analysis have greatly improved the success rate. A follow-up study on the dataset used Markov chain Monte Carlo inversion to estimate the probability distribution of the plume of being in different sizes and shapes (Ramirez et al., 2005).

In groundwater hydrology or hydrogeophysical problems, models are often too complex (in terms of parameterisation) such that fully Bayesian methods such as Markov chain Monte Carlo (McMC) methods are rarely applied (Irving and Singha, 2010). Data assimilation has played an increasingly important role in subsurface characterization (Zhou et al., 2014). For example, Chen et al. (2013) used p-space ensemble Kalman filter (EnKF) (Nowak, 2009; Schöniger et al., 2012) and ensemble smoother (ES) to assimilate head, flowmeter, and conservative tracer test data to characterize the permeability field of the Hanford 300 area. Zovi et al. (2017) used surface ERT results to generate facies model that honour the geophysical data, then used restart normal-score EnKF to estimate the hydraulic conductivity (K) field. In a recent review, it was concluded that the iterative ES (IES) could achieve results comparable with those of the EnKF, at a fraction of EnKF’s computational cost (Li et al., 2018). This computational saving stems from the difference in their formulation— in the EnKF, the data are sequentially integrated into the model at simulation time steps while in ES all the data are combined together and assimilated only once (note in IES the amount of data between updating steps are the same). Since EnKF assimilates data in a sequential fashion (i.e. one time step after another), the number of

assimilation steps equals the number of time steps present in the data. Therefore, EnKF is more computationally expensive than IES when data from many time steps are used.

The Hanford leak tank studies and other earlier work on geoelectrical leak monitoring have focused on obtaining time-lapse ERT images during the suspected leak, and making “leak/ no leak” decisions based on the images. It is difficult, however, to use geophysical images to infer leak parameters such as leak location, solute loading, and onset time. Recent hydrogeophysical studies have attempted to estimate parameters of interest from geophysical data without inverting for geophysical images. Different hydrological model proposals are evaluated and compared to observed geophysical data. For example, [Manoli et al. \(2015\)](#) used an iterative particle filter approach and a coupled hydrogeophysical forward model to estimate hydraulic conductivity, K , of up to four zones from ERT data obtained during a controlled infiltration experiment. This approach is then extended to a field study which considers both ERT and ground penetrating radar (GPR) data in K estimation ([Rossi et al., 2015](#)). [Scholer et al. \(2012\)](#) used time-lapse crosshole ground GPR data collected under different infiltration conditions to estimate unsaturated soil hydraulic properties using a MCMC inversion. [Kowalsky et al. \(2005\)](#) jointly estimated the dielectric and unsaturated zone parameters using both GPR and hydrological data. [Johnson et al. \(2009\)](#) developed a data-domain correlation approach for joint hydrogeological inversion of time-lapse hydrogeological and ERT data to jointly estimate fluid solute concentration and resistivity without explicitly specifying a petrophysical transform.

Though contaminant source identification has been a persistent problem in hydrogeology ([Michalak and Shlomi, 2007](#); [Shlomi and Michalak, 2007](#); [Sun, 2007](#); [Sun et al., 2006](#); [Sun and Sun, 2015](#)), advances in data assimilation methods have opened a new avenue in addressing this problem. Only a few studies have jointly estimated leak parameters and hydraulic parameters ([Datta et al., 2009](#); [Koch and Nowak, 2016](#); [Wagner, 1992](#)). [Zeng et al. \(2012\)](#) developed a sparse grid Bayesian method for contaminant source identification, which greatly reduced the computational burden in MCMC sampling and accurately identifies both leak parameters and time-varying source strengths in case studies. [Xu et al. \(2016\)](#) simultaneously identified the above

contaminant source parameters using the restart normal-score ensemble Kalman filter, while subsequently [Xu et al. \(2018\)](#) extended the method to also identify the heterogeneous hydraulic conductivity field. The method has recently been applied to a sandbox study ([Chen et al., 2018](#)), where six leak parameters and 2 parameters for the location of an impermeable plate are estimated. Assuming known source location, [Kang et al. \(2018\)](#) estimated K and Dense Non-Aqueous Phase Liquid (DNAPL) saturation (and thus total DNAPL volume) from ERT data using restart EnKF.

In contaminated land studies, there has been a paradigm shift to focus more on site-wide metrics. Instead of focusing on thresholds from point-based measurements, mass discharge and mass flux has been used increasingly ([Brusseu and Guo, 2014](#); [Christ et al., 2010, 2006](#); [Hadley and Newell, 2012](#)). Several studies are dedicated to studying their estimation and uncertainty bounds from point measurements ([Cai et al., 2011](#); [Troldborg et al., 2012, 2010](#)), while [Balbarini et al. \(2018\)](#) used regression kriging of collocated concentration and geoelectrical data to improve mass discharge estimates.

In this paper, we introduce an ensemble-based data assimilation framework to jointly identify various leak parameters with their associated uncertainty bounds from ERT data. The method evaluates proposed hydrological models (i.e. different hydrogeological units, different leak locations and loads) against observed time-lapse ERT measurements. To the best of our knowledge, this work is the first attempt to estimate solute source parameters using raw ERT data, as most previous work focuses on estimating hydraulic parameters or reconstructing solute distribution. A key feature of our method is that it allows visualization of uncertainty reduction by comparing the envelopes of prior and posterior mass discharge curves. The methods and data used in this work are detailed in [section 2](#). Results of the various synthetic and field test cases are reported in [section 3](#) and [4](#) respectively. Finally, we discuss and summarize our findings in [section 5](#) and [6](#) respectively.

2) Methodology

We begin by outlining the different steps in the framework, followed by details of the different framework components. Finally, we introduce the datasets used in test cases.

2.1. Overview of framework

The data assimilation framework (summarized by Figure (a)) begins by proposing a range of hydrological models (i.e. model parameters such as leak locations). All parameters for variably saturated flow and transport simulation need to be prescribed, either as a fixed constant or a distribution (which will be updated by the DA framework). Also, the setup for the ERT experiment (e.g. mesh, electrode locations, measurement protocols, petrophysical transforms) need to be included. Once we have an ensemble of model proposals, they are fed to simulate the ERT response using PFLOTRAN-E4D (Johnson et al., 2017). The misfits between observed and simulated ERT responses are used to form data error covariance matrices, which in turn are used to update the model proposals. The entire process repeats until the misfit criterion is met or the algorithm reaches the user-specified maximum number of iterations.

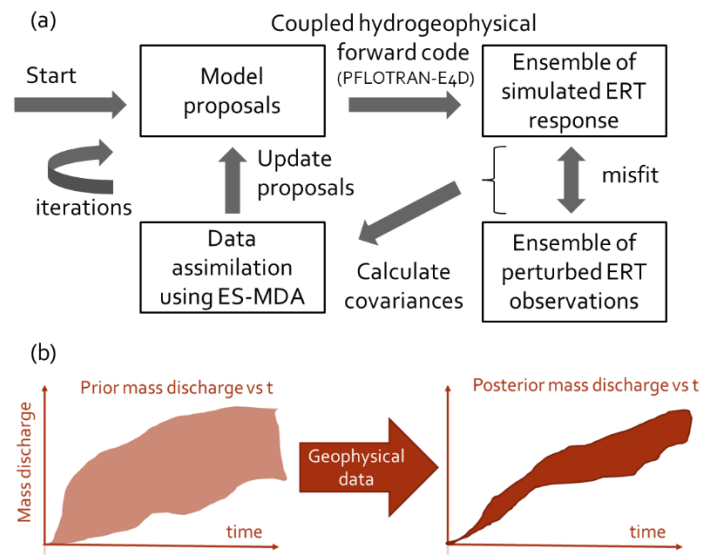


Figure 1 (a) Flowchart of the overall data assimilation framework used in this work. More details are found in the subsections. (b) The goal of this framework is that upon conditioning of geophysical data, the envelope of possible mass discharge time series will become less uncertain.

2.2. Coupled hydrogeophysical forward modelling

We use the massively parallel code PFLOTTRAN-E4D (Johnson et al., 2017) for coupled hydrogeophysical forward modelling. E4D (Johnson et al., 2010) is an ERT code which has state-of-the-art capability for parallelization and for accurate modelling of metallic infrastructure (e.g. tanks and pipes that are common at contaminated sites) (Johnson and Wellman, 2015) and near-real-time inversion to monitoring bioremediation (Johnson et al., 2015c). E4D has been used for ERT modelling on a number of complex problems such as those at the Hanford Site. PFLOTTRAN (Hammond and Lichtner, 2010, also see pflotran.org) is a state-of-the-art massively parallel subsurface flow and reactive transport code. PFLTORAN-E4D (implemented as “hydrogeophysics” mode in the 2018 PFLOTTRAN distributions used in this work) translates states of the PFLTORAN model to bulk electrical conductivity σ_b distribution using an interpolation matrix that maps between the meshes of the two codes given a petrophysical transform. To do so, users need to provide elementwise petrophysical parameters (e.g. Archie parameters), times when the simulated ERT measurements are needed, and the fluid conductivities of the groundwater and the injected tracer. In this work, we assume surface electrical conductivity is negligible and use Archie’s law as the petrophysical relationship:

$$\sigma_b = \sigma_w \Phi^m S_w^n \quad (1)$$

where m , is the cementation exponent, and n is the saturation exponent. Specifically, fluid conductivity σ_w , porosity Φ , and fluid saturation S_w are passed from the PFLOTTRAN output to E4D through the mapping routine. After the petrophysical mapping, E4D will run a forward simulation with the given ERT survey configuration and σ_b distribution to produce the simulated ERT data. Note that PFLOTTRAN-E4D is no longer supported in newer PFLOTTRAN releases. The mapping routine is available through the corresponding author.

2.3. Prior parameter generation: Latin hypercube sampling

For multi-parameter data assimilation problems, we need to use an efficient scheme to generate $nreaz$ model proposals. We use Latin hypercube sampling (LHS) to obtain multi-parameter model proposals that efficiently span the parameter space. The LHS

approach is implemented using the R package *Envstats* (Millard, 2013). For the synthetic and field examples, we assume multivariate Gaussian distribution ($n_{reaz} = 32$) and multivariate uniform distribution ($n_{reaz} = 64$) for the prior distribution of parameter values respectively. The use of more realizations and a non-informative prior in the field example is due to greater parameter uncertainty.

2.4. Data assimilation: ensemble smoother with multiple data assimilation (ES-MDA)

In this work, we use the ensemble smoother with multiple data assimilation (ES-MDA) (Emerick and Reynolds, 2013) to update hydrological models. ES-MDA is also known as an iterative variant of ensemble smoother (ES). The ES-MDA has been used heavily in hydrocarbon reservoir history matching of production and seismic data, but there are growing applications in hydrology. For example, Ju et al. (2018) combined ES-MDA with Gaussian process surrogate modelling and tested the new method on synthetic 2-D transient groundwater flow problems. Lan et al. (2018) combined sequential ensemble-based optimal design and ES-MDA to accurately and efficiently estimate the heterogeneous distribution of physical and geochemical parameters in groundwater models. Aalstad et al. (2018) used ES-MDA and fractional snow-covered area retrieved from satellites to estimate the snow distribution at Arctic sites. Song et al. (2019) used ES-MDA with level set parameterization to estimate the three-facies heterogeneous permeability field at the Hanford IFRC site, while Kang et al. (2019) jointly assimilated ERT and concentration data using ES-MDA alongside with direct sampling (Mariethoz et al., 2010) to estimate the non-Gaussian hydraulic conductivity field from a synthetic salt injection experiment. More recently, a modified version of ES-MDA has been used for crosshole GPR travel-time tomography in conjunction with approximate forward solvers and model error correction (Köpke et al., 2019).

An ensemble smoother (ES) considers all available time-lapse data simultaneously for updating the model parameters. The ES-MDA method essentially allows iterative updating of the nonlinear ES problem by inflating the observational errors by a factor α and solve the updating equation α times iteratively. It has been

shown that iterative updating better handles nonlinearity in the data assimilation problem than the classic ES formulation. Our implementation of the ES-MDA procedure is summarized below:

1. Prepare observational data (and their error levels) to be used for data assimilation (DA)
2. Set up a base PFLOTTRAN-E4D model
3. Decide on which parameter(s) to update, either based on expert judgement or some preliminary global sensitivity analysis. The parameter estimation may be affected if important parameters are neither assumed correctly nor updated. Sample N_e realizations from the prior distribution of parameter(s) values (e.g. assume normal or uniform distribution) to obtain parameter array \mathbf{m} at $l = 0$ (\mathbf{m}_0). Parameters that are not being updated are assumed known and base model values are used throughout the DA process for all realizations.
4. Run PFLOTTRAN-E4D using \mathbf{m}_0 to obtain an ensemble of simulated ERT data
5. Updating. For $l = 1$ to N_a (where N_a is the number of data assimilation steps),
 - (i) The data misfit from the $(l - 1)$ -th iteration is given by

$$misfit = \frac{\sum_{i=1}^{N_d} \sum_{j=1}^{N_e} (d_{i,obs} - d_{i,j})}{N_e \times N_d} \quad (2)$$

where N_d is the number of measurements and $d_{i,j}$ is the i -th data of the j -th realization.

- (ii.) Obtain the auto covariance matrix of model predictions \mathbf{C}_{DD} and the cross-covariance matrix between the parameter vector and model predictions \mathbf{C}_{MD} by

$$\mathbf{C}_{DD} = \text{cov}(\mathbf{d}^j, \mathbf{d}^j) \approx \frac{1}{N_e - 1} \sum_{j=1}^{N_e} (\mathbf{d}_j - \bar{\mathbf{d}})(\mathbf{d}_j - \bar{\mathbf{d}})^T \quad (3)$$

$$\mathbf{C}_{MD} = \text{cov}(\mathbf{m}^j, \mathbf{d}^j) \approx \frac{1}{N_e - 1} \sum_{j=1}^{N_e} (\mathbf{m}_j - \bar{\mathbf{m}})(\mathbf{d}_j - \bar{\mathbf{d}})^T \quad (4)$$

where \mathbf{d}_j and \mathbf{m}_j are vectors of simulated data and model parameter estimates of the j -th realization, respectively. The overbar denotes the mean across realizations of a matrix.

- (iii.) For each ensemble member, perturb the observation vector using

$$\mathbf{d}_{uc} = \mathbf{d}_{obs} + \sqrt{\alpha_l} \mathbf{C}_D^{1/2} \mathbf{z}_d \quad (5)$$

where α_l is an inflation coefficient, $\mathbf{z}_d \sim N(0, \mathbf{I}_{N_d})$, \mathbf{I}_{N_d} is an identity matrix of size N_d , \mathbf{C}_D is the covariance matrix of the measurements error, \mathbf{d}_{obs} is a vector of the observed field data. Because of the linear approximation in the update step and the use of a limited number of realizations in an ensemble, the ensemble Kalman filter-like methods have a tendency to systematically underestimate the variance of the model variables (Zhang et al., 2010). Resampling the vector of perturbed observations at each iteration tends to reduce sampling problems caused by matching outliers that may be generated when perturbing the observations (Emerick and Reynolds, 2013).

- (iv.) Update the parameter ensemble using:

$$\mathbf{m}_l = \mathbf{m}_{l-1} + \underbrace{\mathbf{C}_{MD}(\mathbf{C}_{DD} + \alpha_l \mathbf{C}_D)^{-1}}_{\text{Kalman gain}} \underbrace{(\mathbf{d}_{uc} - \mathbf{d}_{l-1})^T}_{\text{misfit}} \quad (6)$$

Note that in order to preserve the equivalence between single and multiple data assimilation, it is necessary that $\sum_l^N 1/\alpha_l = 1$ (Emerick and Reynolds, 2013). This effectively serves to update the average sensitivity matrix.

- (v.) Run PFLOTTRAN-E4D N_e times using \mathbf{m}_l to obtain the updated simulated data ensemble

7. If solution does not converge, repeat steps 3-7 with a higher α and/or $nreaz$. Convergence is achieved when the ensemble root-mean-square-error of the ERT data misfit equilibrates:

$$RMSE = \sqrt{\frac{1}{N_d} \frac{1}{N_e} \sum_{i=1}^{N_d} \sum_{j=1}^{N_e} (d_i^{obs} - d_{i,j}^{sim})^2} \quad (7)$$

ES-MDA outperforms ES in non-linear problems because the smoother effectively represents a single Gauss-Newton iteration with a full step and an average sensitivity matrix (Reynolds et al., 2006) that is approximated by the covariance matrices of the prior ensemble. Instead of a single and potentially large Gauss-Newton correction, ES-MDA allows multiple smaller corrections through the use of multiple

iterations. To damp the parameter updating and to correctly sample from the posterior distribution of model parameters, the covariance matrices must be inflated ([Emerick and Reynolds, 2013](#)). The above issue is sometimes referred to as residual sampling error in data assimilation literature, with inflation being a common technique to account for it ([Carrassi et al., 2018](#)). The ES-MDA scheme is more flexible and easier to implement than conventional Gauss-Newton methods because it does not require derivation of sensitivity matrices. Previous work have shown that good results can be obtained in a few iterations (e.g. 4-10), while using a decreasing order of α_l 's only resulted in small improvements compared to using constant α_l 's. It can be shown that ES-MDA has links to annealed importance sampling ([Stordal and Elsheikh, 2015](#)). A comparison between ES-MDA and ES is provided by [Evensen \(2018\)](#).

In this work, the above steps (except forward modelling) were implemented in R. For the synthetic studies presented, we set N_a to 7 and use a constant α_l of 7, which appears to obtain convergence in all cases and also satisfies the criterion $\sum_l^{N_a} 1/\alpha_l = 1$. Because the initial misfit for the field data is much larger than that for the synthetic data, the algorithm was unstable and more difficult to converge. Thus, for our field study we set a constant α_l to 200 and iterate until the RMSE is stabilized, which is achieved within ten iterations. Although this violates the $\sum_l^{N_a} 1/\alpha_l = 1$ criterion, we remark that its choice is determined based on data noise levels and discrepancy between observed and simulated data, which can be high in field data. A higher α_l can be seen as adding regularization to the ensemble Kalman scheme ([Iglesias, 2016](#)). An alternative approach is to adaptively decide α_l at each iteration automatically (e.g. [Iglesias and Yang, n.d.](#); [Le et al., 2016](#)) based on the mean of RMSE of data misfit across all realizations.

In previous hydrogeology applications using ensemble Kalman methods, the hydraulic heads or solute concentrations are often transformed using normal-score transformation (e.g. [Schöniger et al., 2012](#)). We consider ERT data to be more Gaussian than hydrogeological data so we use raw ERT data (transfer resistances) directly in this study but such scaling may improve results.

2.5. Plume mass discharge

Mass discharge is the integral of solute fluxes across a control plane (ITRC, 2010). The control plane can be a model or site boundary, the water table, or any arbitrary planes. Mass flux is defined as $J = q_0 C$, where q_0 is groundwater flux and C is solute concentration. It follows that the solute mass discharge (or equivalently solute integral flux) across a control plane is defined as $M_d = \int_A J dA$, where A is area of the control plane and J is the spatially variable solute mass flux. Note that since the solute fluxes are vectors, it is possible for solute mass discharge to be negative. As shown in Figure 1(b), one way to visualize reduction in site-wide uncertainty is by observing a reduction of spread of the mass discharge time series.

3) Synthetic experiments based on the Sellafield ERT field trial

Between 2013-2014, a field ERT trial was conducted at the Sellafield Nuclear Site in Cumbria, U.K. (Kuras et al., 2016; Tso et al., 2017) by the British Geological Survey to demonstrate the utility of a permanent ERT monitoring system to support critical decommissioning activities at nuclear sites. Four vertical boreholes and two inclined boreholes with forty electrodes each were installed in front of the Sellafield MSSS building. The field trial included three controlled injections of an electrically conductive tracer (as simulant of the silo liquor) into the vadose zone. Time-lapse ERT data were collected during the experiment.

We built a PFLOTRAN model based on the hydrogeological model developed for Sellafield (Kwong and Fowler, 2014) and an E4D model based on the electrode locations and design of the field trial. Details of the PFLOTRAN and E4D models are found in Table 2. Note that there are multiple units in the domain, but only the hydraulic parameters in the main unit (i.e. sandy drift) is listed in Table 2. The parameters not being estimated are kept constant during parameter estimation.

To test our method, we obtained synthetic ERT data based on the experimental setup of the field trial and consider a series of parameter estimation cases. They are summarized in

Table 3. Unless otherwise stated, the parameters not being estimated are assumed to be known exactly. We began by considering the estimation of leak location ($xloc, yloc$), both for a leak inside and outside the ERT monitoring cell. Then we proceed by also estimating the solute loading (q), release onset time (t_0). Subsequently, we estimate both leak parameters and uniform Archie parameters (m, n) jointly, which is important in field applications as fixing the parameters imposes too much confidence on uncertain petrophysical relationships. Finally, we consider a few cases with uncertainty and heterogeneity in hydraulic conductivity (K). In the first case, the K field has a log variance of 1.0 but its mean value is unknown; while in the second case, the K field is heterogeneous but its mean value is known. In the last case, the mean K value is being estimated for a heterogeneous field. Other potential parameters to consider includes water table depths, permeability [$\log_{10} (m^2)$], porosity, unsaturated zone van Genuchten parameters, recharge rates, depth of the leak ($zloc$), and duration of the leak (dt). Each iteration takes 40 minutes on average to run on 192 cores on PNNL's institutional computing facility. Note that only the forward modelling is parallelized, not the parameter updating.

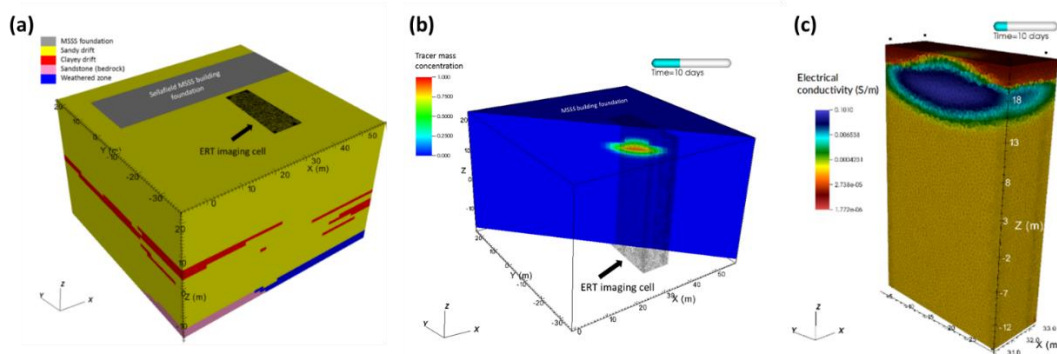


Figure 2. (a) PFLOTRAN model domain for the Sellafield MSSS. The grey area is the MSSS building, which is modelled as impermeable. The hashed area is the ERT imaging cell consisting of four ERT boreholes. (b) A snapshot of the simulated tracer concentration due to injection. (c) The corresponding distribution of electrical conductivity within the ERT imaging cell obtained via petrophysical transform.

Table 2 “True” coupled hydrogeophysical model parameters used for synthetic experiments. It is developed based on the Sellafield field trial. *Only parameters for the main zone are listed below. #Leak location for some cases is (33.4534, -14.4303) instead. Note that for all cases the leak location is at the water table.

PFLOTRAN simulation	Value
Total simulation time (days)	30
Model dimensions (m)	40 x 40 x 20
Grid spacing (m)	1 x 1 x 1
Horizontal permeability (m ²) *	8.8854 x 10 ⁻¹⁰
Vertical permeability (m ²) *	4.4427 x 10 ⁻¹¹
Porosity *	0.2
Water table depth (m)	6.0
van Genuchten <i>m</i>	0.5
van Genuchten α	1 x 10 ⁻⁴
Residual water saturation	0.1
Leak location (m) #	(20,-10,18.1)
Leak period (day)	12-30
Leak rate (m ³ /d)	8.0
Background fluid conductivity (S/m)	1 x 10 ⁻⁴
Leak fluid conductivity (S/m)	0.1
Mass discharge plane	Vertical plane at y=-25.03m
E4D simulation	Value
Full Model dimensions (m)	100 x 100 x 100
Imaging cell dimensions (m)	9.5 x 22.8 x 41.5
Grid spacing	Unstructured
Number of elements	380457
ERT imaging times (day)	Every 5 days between day 5 to day 30
Archie’s cementation exponent	1.3
Archie’s saturation exponent	2.0

Table 3 Summary of synthetic cases. All cases converge in seven iterations.

Figure	Size of ensemble (N_e)	Parameter(s) to estimate	Prior distribution	Comments	Initial and final RMSE
Figure 3a	32	$xloc, yloc$	6x6 grid (exclude corners) Uniform spacing X range: -5 - 55m Y range: -33 - -3m	Estimation of the leak location on the x,y plane ; leak is located within the ERT cell	3.63 → 1.01
Figure 3b	32	$xloc, yloc$	6x6 grid (exclude corners) Uniform spacing X range: -5 - 55m Y range: -33 - -3m	Estimation of the leak location on the x,y plane; leak location is outside the ERT cell	7.66 → 1.01
Figure 4	32	$xloc, yloc, q, t0$	Multivariate uncorrelated truncated Gaussian: $xloc = list(mean=25.0, sd=20.0, min=-5.0, max=55.0)$, $yloc = list(mean=-18.0, sd=10.0, min=-33.0, max=-3.0)$, $q = list(mean=15.0, sd=10.0, min=0.0, max=30.0)$, $t0 = list(mean=15.0, sd=10.0, min=0.0, max=30.0)$	Estimation of the 4 leak parameters	7.01 → 1.01
Figure 5	32	$xloc, yloc, q, t0, m, n$	Multivariate uncorrelated truncated Gaussian: $xloc = list(mean=25.0, sd=20.0, min=-5.0, max=55.0)$, $yloc = list(mean=-18.0, sd=10.0, min=-33.0, max=-3.0)$, $q = list(mean=15.0, sd=10.0, min=0.0, max=30.0)$, $t0 = list(mean=15.0, sd=10.0, min=0.0, max=30.0)$, $c = list(mean=1.6, sd=0.5, min=0.0, max=2.0)$, $m = list(mean=2.5, sd=0.8, min=0.0, max=3.0)$	Joint estimation of leak parameters and uncertain (homogeneous) petrophysical parameters (Archie's cementation factor and saturation exponent)	22.65 → 1.65
Figure 6a	32	$xloc, yloc, q, t0$	Multivariate uncorrelated truncated Gaussian: $xloc = list(mean=25.0, sd=20.0, min=-5.0, max=55.0)$, $yloc = list(mean=-18.0, sd=10.0, min=-33.0, max=-3.0)$, $q = list(mean=15.0, sd=10.0, min=0.0, max=30.0)$, $t0 = list(mean=15.0, sd=10.0, min=0.0, max=30.0)$	Leak estimation under the influence of permeability heterogeneity	3.30 → 1.10
Figure 6b	32	$xloc, yloc, q, t0$	Multivariate uncorrelated truncated Gaussian: $xloc = list(mean=25.0, sd=20.0, min=-5.0, max=55.0)$, $yloc = list(mean=-18.0, sd=10.0, min=-33.0, max=-3.0)$, $q = list(mean=15.0, sd=10.0, min=0.0, max=30.0)$, $t0 = list(mean=15.0, sd=10.0, min=0.0, max=30.0)$	Leak estimation under the influence of and uncertain (homogeneous) permeability	6.47 → 1.31 6.66 → 1.70 6.50 → 1.22 6.53 → 1.41 6.54 → 1.27
Figure 7	32	$xloc, yloc, q, t0, K$	Multivariate uncorrelated truncated Gaussian: $xloc = list(mean=25.0, sd=20.0, min=-5.0, max=55.0)$, $yloc = list(mean=-18.0, sd=10.0, min=-33.0, max=-3.0)$, $q = list(mean=15.0, sd=10.0, min=0.0, max=30.0)$, $t0 = list(mean=15.0, sd=10.0, min=0.0, max=30.0)$, $K = list(mean=-9.0, sd=sqrt(1.0), min=-11.0, max=-7.0)$	Joint estimation of leak parameters and uncertain (homogeneous) permeability values	3.30 → 1.03

3.1. Base cases

Our initial example considers the estimation of the leak location (Figure 3). The prior realizations are laid in a rectangular grid. We consider both the cases where the leak is within and outside the ERT imaging cell. Although the estimate at the first iteration is superior when the leak is within the imaging cell, the leak location is accurately estimated after seven iterations in both cases. Figure 4 shows the results from the joint estimation of four leak parameters: the (x, y) coordinates of the leak location, leak rate, and onset time, assuming a wide multivariate Gaussian prior distribution. After conditioning the parameter values with ERT data, all four leak parameters are accurately estimated. Figure 4b shows the mass discharge curves across a pre-defined plane. The mass discharge curves for the prior distribution are highly variable, while those for posterior distribution collapse to the true curve.

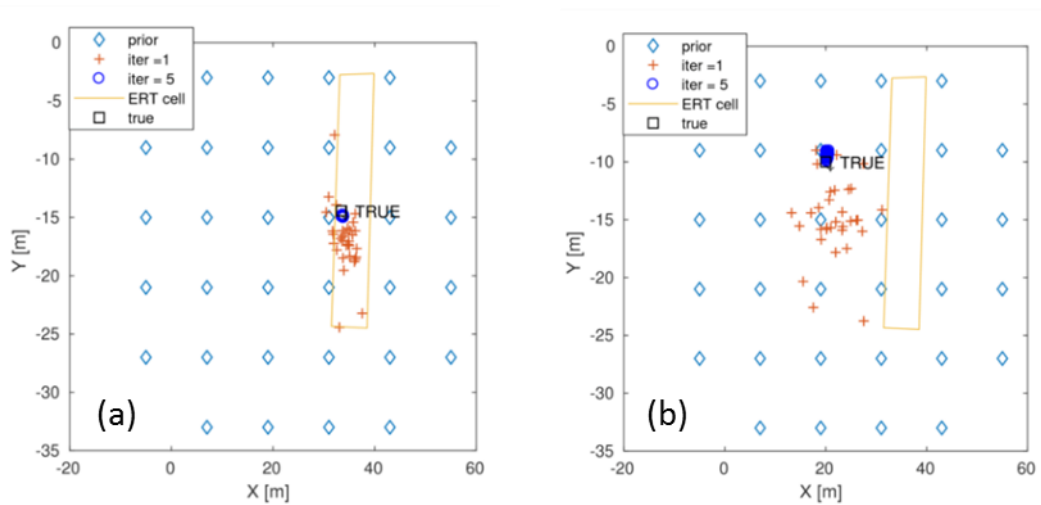


Figure 3 Estimation of leak location. (a) The true leak location is within the ERT array (33.4534, -14.4303). (b) The true leak location is outside the ERT array (20, -10). In both cases, the data assimilation framework successfully identified the true leak location within a few iterations.

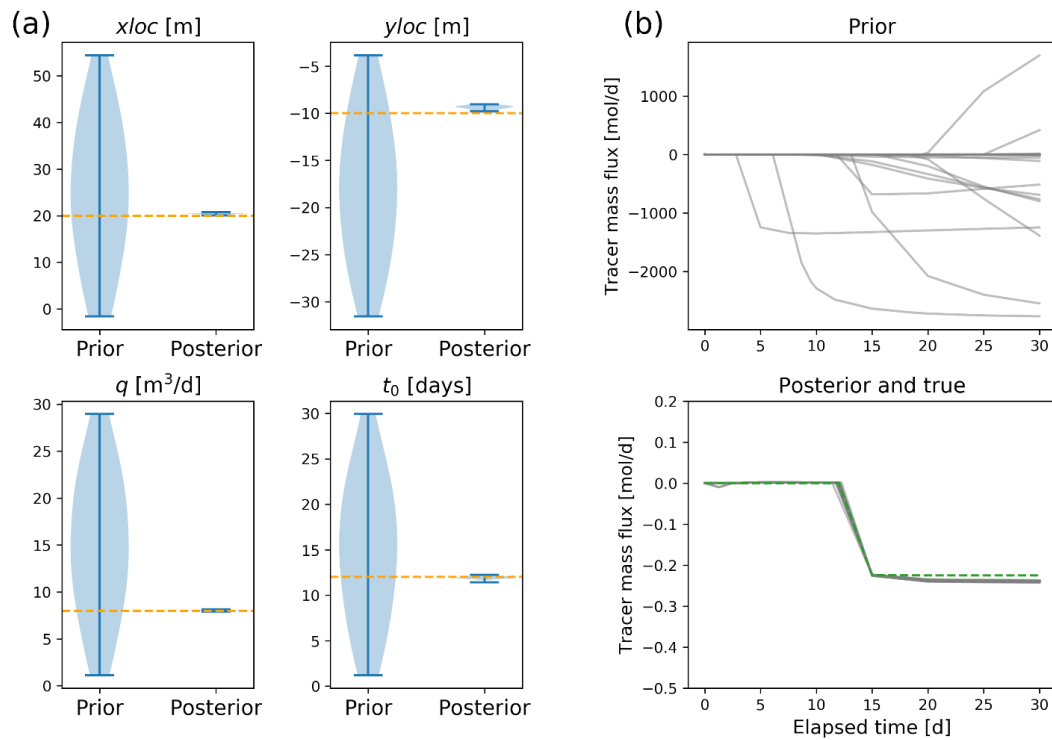


Figure 4 Joint estimation of leak parameters: (x, y) location, leak rate, and onset time. (a) Violin plots showing the prior and posterior parameter distributions. The true values are marked with an orange lines. The posterior parameter values collapse around the true values (b) Prior and posterior tracer mass flux across the pre-defined plane. All the posterior curves collapse to nearly the true curve (green). Note that the sign of mass discharge denotes its direction across the plane.

3.2. Effects of petrophysical parameters

Figure 5 shows the joint estimation of leak parameters and Archie petrophysical parameters. The prior estimates are generated as multivariate Gaussian distributions using Latin hypercube sampling. The posterior estimates are in very good agreement with the true values, with the exception that the onset time is slightly underestimated. It is noteworthy that including the Archie parameters as a covariate has caused the RMSE of the prior ensemble to be much higher than those in other synthetic test cases (see

Table 3), highlighting that it causes a larger range of transfer resistance values.

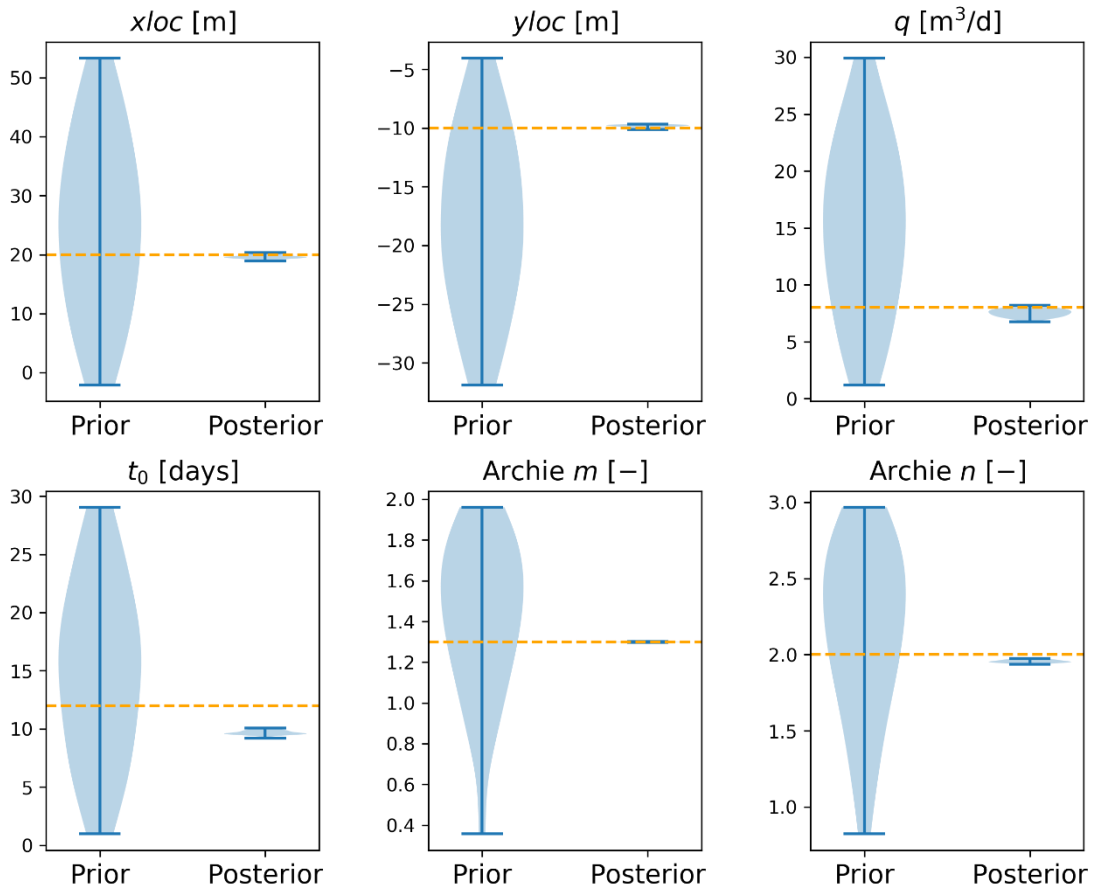


Figure 5 Joint estimation of leak and petrophysical parameters: the prior and posterior parameter distributions are shown as violin plots. The true values are marked with orange lines.

3.3. Influence and joint estimation of uncertain (homogeneous) hydraulic conductivity

Figure 6a shows the estimation of leak parameters under uncertain K values. Estimating leak parameters under K uncertainty leads to highly uncertain and inaccurate leak parameter estimates. Figure 6b shows the estimation of leak parameters with variance of $\log K$ equal to 2, 3, 5, 7, 10, while assuming the mean K values are known exactly and unit correlation lengths. Although some variations in the estimates are seen, they generally lie close to the true values. There is no apparent correlation between the leak parameter estimation performance and the variance of the field. Figure 7 shows the estimates of leak parameters and effective hydraulic conductivity. The results show good estimates

of the leak locations, while that for q and t_0 is manifested as a narrow envelope. The posterior uncertainty for K remains high and the algorithm underestimates the effective K value. Again, the envelope of mass discharge curves is greatly reduced, demonstrating a reduction in uncertainty. However, the posterior curves do not collapse to the true curve, indicating significant uncertainty in the estimates.

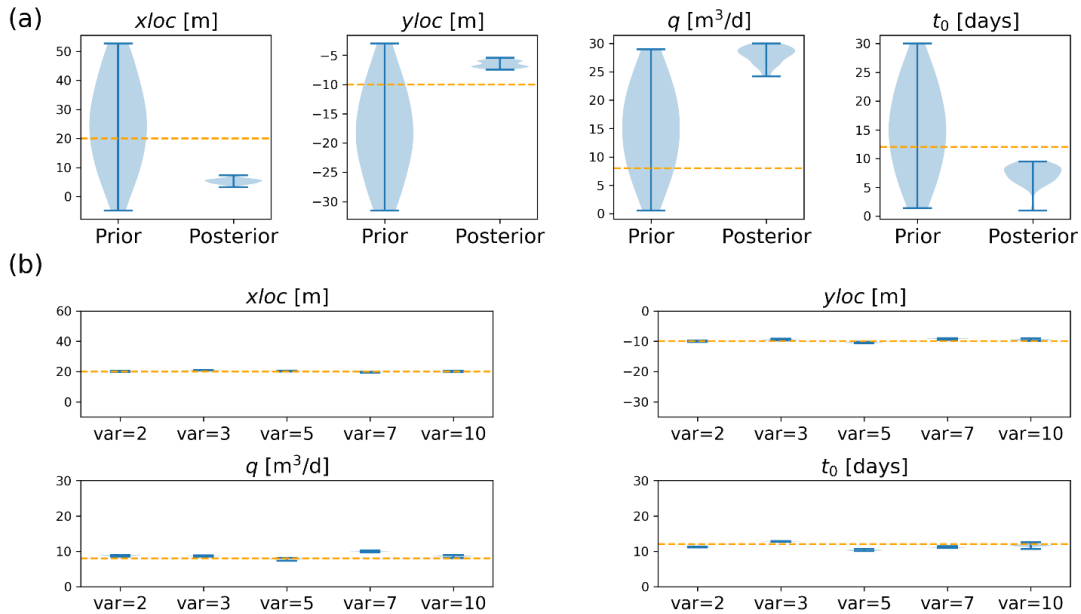


Figure 6 (a) The estimation leak parameters under uncertain K values and $\log K$ variance = 1.0. The violin plots show the prior and posterior parameter distributions. The true value is marked with an orange line. (b) The estimation of leak parameters at variance of $\log_{10}(K)$ equal to 2, 3, 5, 7, 10, while assuming the mean K values are known exactly and the K field is isotropic and is of unit correlation length. The violin plots show the posterior parameter distribution, while the true value is marked with an orange line.

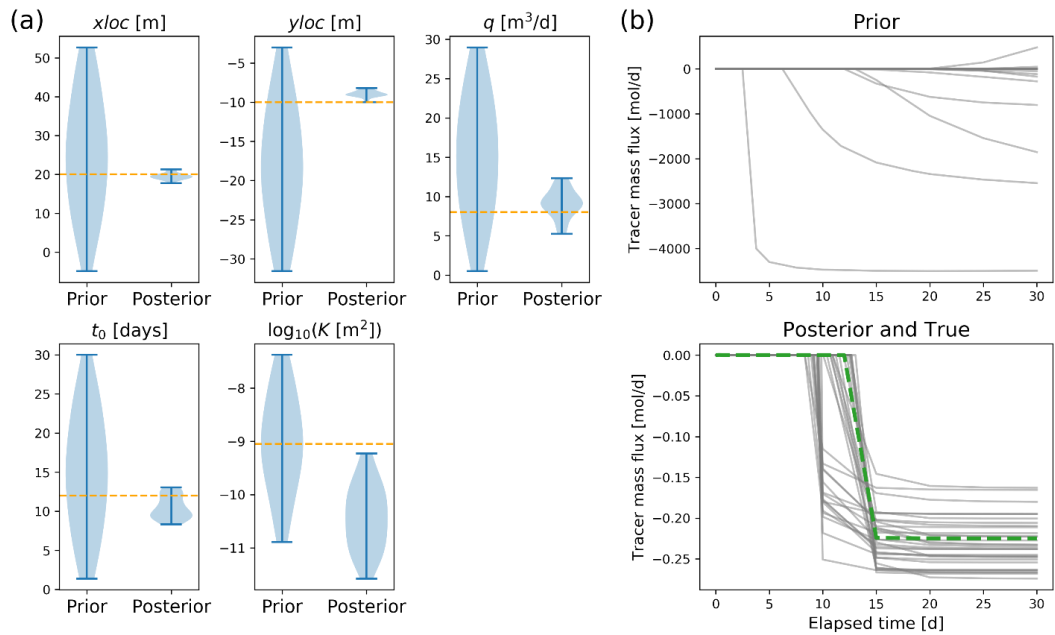


Figure 7 (a) Joint estimation of leak parameters and effective hydraulic conductivity. The violin plots show the prior and posterior parameter distributions. The true value is marked with an orange line. (b) Prior and posterior tracer mass flux across the pre-defined plane. The true curve is marked in green in the posterior plot.

4) Field application at the Hatfield site

4.1. Data description

To illustrate the approach in a field setting we use data from a solute injection experiment at the Hatfield (Yorkshire) site in the UK. At the site, six boreholes were drilled in 1998 in order to monitor tracer injection, two of which were for transmission GPR measurements (H-R1 and H-R2), while four were for ERT measurements (H-E1, H-E2, H-E3, and H-E4). These four ERT boreholes consist of sixteen stainless steel mesh electrodes equally spaced between 2 and 13 m depth. These boreholes were drilled to a depth of 12 m and completed with 75 mm PVC casing. Both the ERT and radar boreholes have a weak sand/cement grout backfilling the annulus. A tracer injection borehole was also installed (H-I2), located within the centre of the borehole array. The injection borehole is 3.5 m deep, with a 100 mm diameter slotted section and gravel pack between 3 and 3.5 m depth.

We focus our discussion using the ERT results from the March 2003 tracer infiltration experiment at Hatfield (Winship et al., 2006). The tracer consisted of 1,200 litres of water, dosed with NaCl to give an electrical conductivity value of $2200 \mu\text{S cm}^{-1}$ (groundwater electrical conductivity at the site was measured as $650 \mu\text{S cm}^{-1}$). The tracer was injected over a period of three days, from 14th March 2003 to 17th March 2003 at a steady rate of approximately 17 litres per hour. A float valve in the injection borehole was used to control the head in the injection borehole, and hence the flow rate. Duplicate sets of background measurements of ERT were made on 6th March and 13th March. Tracer flow was monitored by means of a pressure transducer in a storage tank, which gave a way of calculating the cumulative injection volume over time. The tracer injection port H-I2 was screened between 3m and 3.5m below ground surface. The tracer injection was monitored by ERT measurements from four boreholes and inverted images clearly show the plume migration, as shown in Figure 8 (Winship et al., 2006). During the tracer test no rainfall was observed at the site. The water table was observed at approximately 10 m depth.

After removal of outliers, 3108 of the 3172 measurements are kept and 5% Gaussian data error is assumed in the inversions. Let $t = 8$ be the day where injection commenced, ERT snapshots for $t = 7, 10, 15, 21$ days are used in the inversion. Table 4 lists the baseline parameters for our simulation, which are largely adopted from Binley et al. (2002a). The parameters not being estimated are kept constant during parameter estimation.

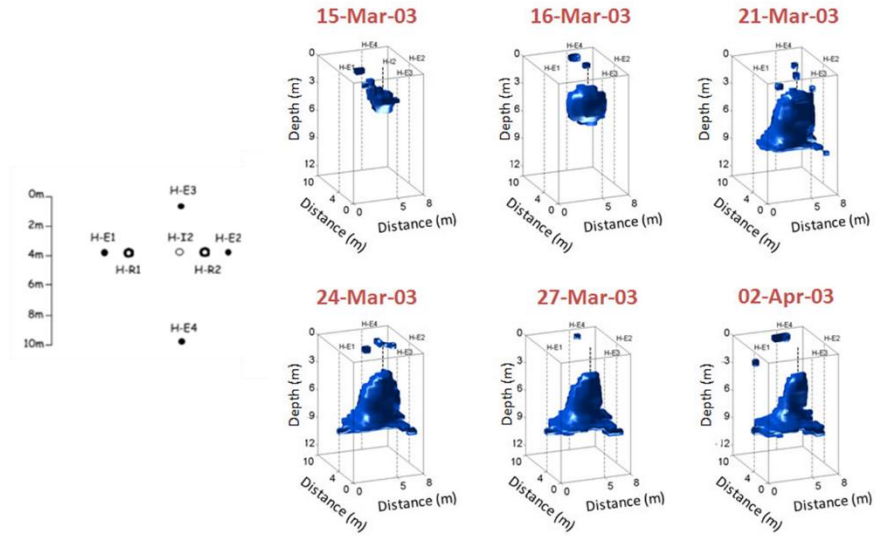


Figure 8 Setup of the tracer injection test at Hatfield (H-I2 is the injection borehole and H-E1 to H-E4 are ERT boreholes) and the time-lapse resistivity images (iso-surfaces are plotted for 7.5% reduction of resistivity relative to baseline) obtained from a difference inversion of the ERT data (reproduced from Winship et al., 2006)

Table 4 Baseline coupled hydrogeophysical model parameters used for the parameter estimation from the Hatfield field ERT data. *The domain consists of 3 meters of top soil and a uniform main zone. Only parameters of the main zone are listed below.

PFLOTRAN simulation	Value
Total simulation time (days)	41
Model dimensions (m)	30 x 33 x 16
Grid spacing (m)	1 x 1 x 0.5
Permeability (m ²) *	4.8225 x 10 ⁻¹³
Porosity *	0.32
Water table depth (m)	-12.0
van Genuchten <i>m</i> *	0.6
van Genuchten α *	3.5 x 10 ⁻³
Residual water saturation *	0.04
Recharge (m/day)	1 x 10 ⁻⁴
Leak location (m)	(3.0, 4.0, -3.0)
Leak period (day)	8-11
Leak rate (m ³ /d)	0.408
Background fluid conductivity (S/m)	0.22
Leak fluid conductivity (S/m)	0.065
Mass discharge plane	Vertical plane at y = -3 m
E4D simulation	Value
Full Model dimensions (m)	500 x 500 x 50
Imaging cell dimensions (m)	10 x 13 x 15
Grid spacing	Unstructured
Number of elements	46482
ERT imaging times (day) for inversion	7, 10, 15, 21
Archie's cementation exponent	1.35
Archie's saturation exponent	1.35

4.2. Parameter estimation

We applied the proposed leak detection framework to the Hatfield field data and consider two cases (details are listed in Table 5). The first case estimates four leak parameters and two Archie parameters ($xloc, yloc, \log q, t_0, m, n$). The second case considers the estimation of a few additional parameters, namely the duration of the leak event (dt) and the uniform horizontal and vertical hydraulic conductivity (K and Kz). We consider K anisotropy may exist at the site because well logs suggest the presence of fine layers (Binley et al., 2001). Compared to the earlier synthetic examples, convergence was much more difficult to achieve. We have used the following modification to our methods to circumvent this issue: we estimated $\log q$ instead of q , used more realizations, and used a uniform prior instead of a Gaussian one. We transformed the leak location priors to a uniform grid to aid the interpretation of the results. We have not considered the estimation of depth of the leak source in any of our examples because for most leak detection problems, the leak depth is usually precisely known: for example, base of storage tanks/silos, depth of buried pipelines, and bottom of landfill lining. Each iteration takes 2.5 hours on average to run on 192 cores. Note that only the forward modelling is parallelized, not the parameter updating.

Results from the base case is reported in Figure 9. Figure 9(a) shows that the posterior estimates of most parameter pairs form a small cluster. The estimates of $xloc$ and $\log q$ are close to the true values, while those for $yloc$ and t_0 are slightly above the true (known) values. The inversion appears to have no sensitivity to m , while the estimation of n converges to a very small value of about 0.53. Note that in this field test the true values of m and n are not known. In the inversion of field data, we would not necessarily consider the estimates of m and n representative of actual petrophysical parameters, but rather they act as hyperparameters to adjust any discrepancy in model structure. Figure 9(b) shows that the variability of mass discharge curves between realizations is greatly reduced upon conditioning of ERT data. Specifically, its spread

is reduced by two orders of magnitude, highlighting a reduction in site-wide uncertainty of the plume migration.

Results from the second case are reported in Figure 10. We observe a larger spread in the parameter space but similar results for the estimation of m and n . $xloc$, $yloc$, and t_0 are slightly overestimated. The inversion appears to have no sensitivity to K and Kz . The estimates of $\log q$ and dt centres around the true value, indicating the inversion algorithm also correctly estimates the total solute loading ($q \times dt$) that enters the flow and transport modelling domain. This underscores that the proposed data assimilation framework does not suffer from mass balance issues that are common in inverted resistivity-based approaches.

Table 5 Summary of cases for the Hatfield field example

Figure	Size of ensemble (N_e)	Parameter(s) to estimate	Prior distribution	Comments	Final RMSE
Figure 9	64	$xloc, yloc, \log q, t_0, m, n$	Multivariate uncorrelated uniform: Adjusted uniform grid from $xloc$ 0-8m and $yloc$ =0-10m $\log q = \text{list}(\text{min}=-2.0, \text{max}=1.0)$, $t_0 = \text{list}(\text{min}=0.0, \text{max}=20.0)$, $m = \text{list}(\text{min}=0.5, \text{max}=2.5)$, $n = \text{list}(\text{min}=0.5, \text{max}=2.5)$	Base case	223.16 \rightarrow 15.3 (iter=8, stabilized afterwards)
Figure 10	64	$xloc, yloc, \log q, t_0, dt, m, n, K, Kz$	Multivariate uncorrelated uniform: Adjusted uniform grid from $xloc$ 0-8m and $yloc$ =0-10m $\log q = \text{list}(\text{min}=-2.0, \text{max}=1.0)$, $t_0 = \text{list}(\text{min}=0.0, \text{max}=20.0)$, $dt = \text{list}(\text{min}=1.0, \text{max}=5.0)$, $m = \text{list}(\text{min}=0.5, \text{max}=2.5)$, $n = \text{list}(\text{min}=0.5, \text{max}=2.5)$, $K = \text{list}(\text{min}=-13.0, \text{max}=-9.0)$, $Kz = \text{list}(\text{min}=-13.0, \text{max}=-9.0)$	K, Kz , and dt are also estimated.	310.66 \rightarrow 13.95 (iter = 2, stabilized afterwards)

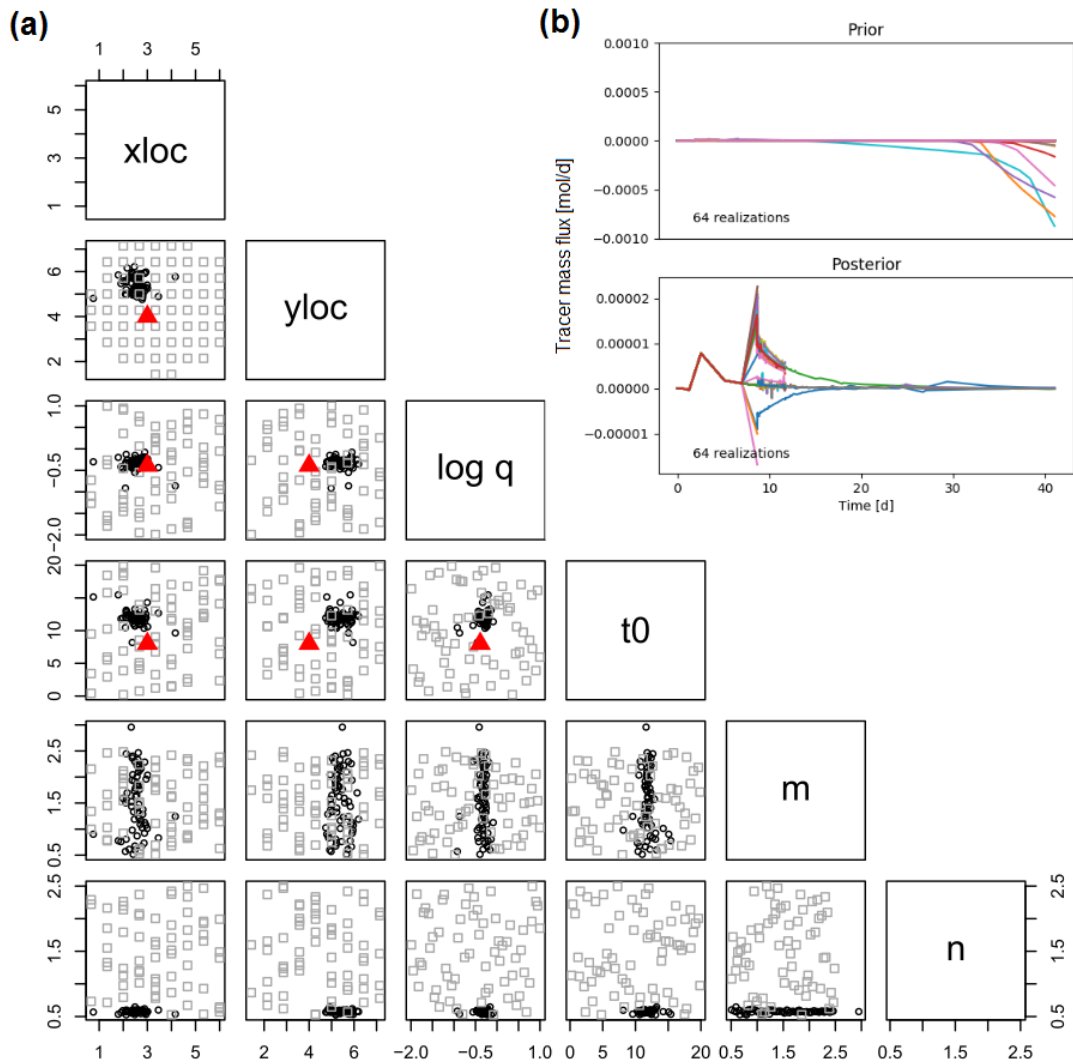


Figure 9 (a) Parameter scatterplots showing pairs of parameter values for the Hatfield example estimating leak and Archie parameters. The parameter symbols and units are defined in section 3. Grey squares indicate prior parameter values while black circles indicate posterior values. The true leak parameters used in the field injection experiment is indicated by red triangles. (b) The prior and posterior mass discharge time series. The sign of mass discharge indicates the direction across the defined plane.

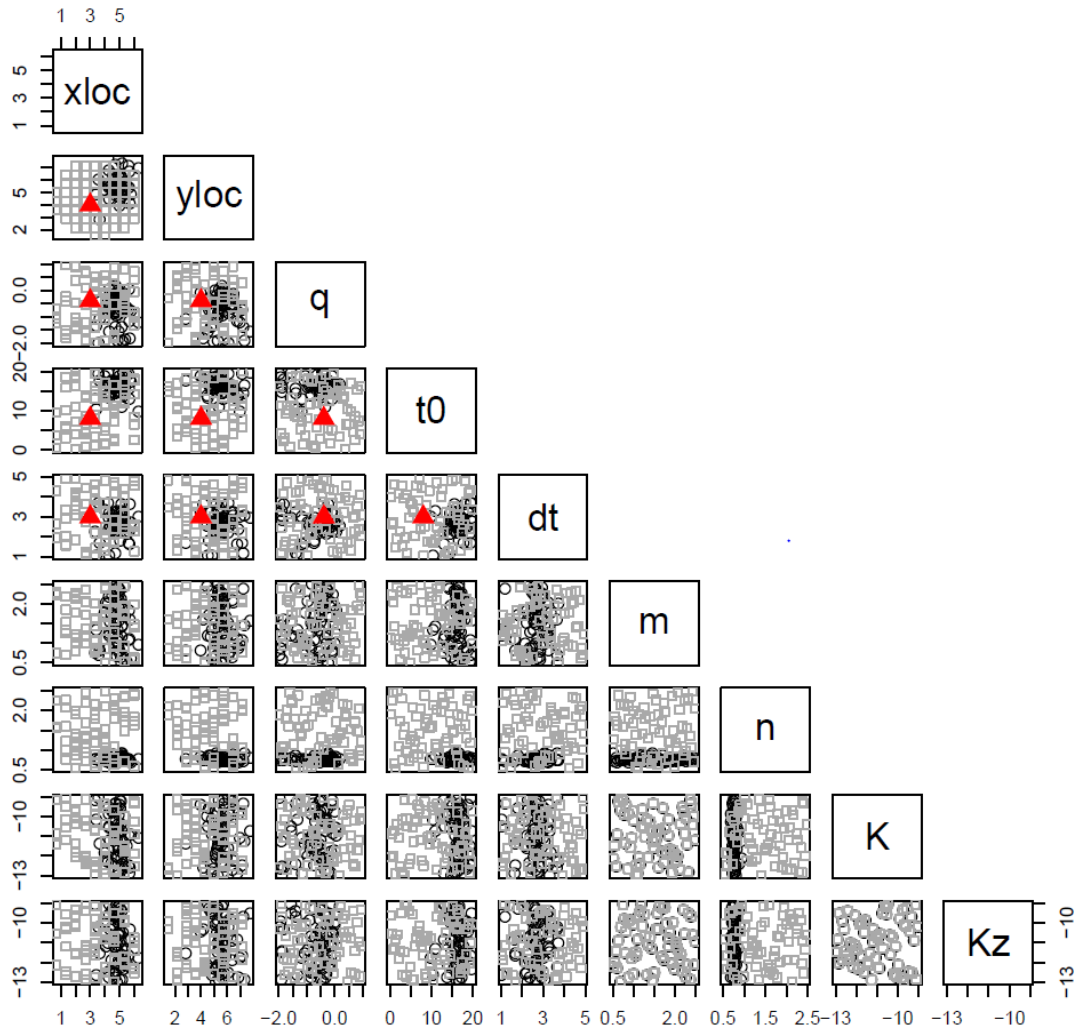


Figure 10 Parameter scatterplots showing pairs of parameter values for the Hatfield example estimating leak and Archie parameters and hydraulic conductivities. The parameter symbols and units are defined in Table 4 and section 3. Grey squares indicate prior parameter values while black circles indicate posterior values. The true leak parameters used in the field injection experiment is indicated by red triangles.

4.3. Global sensitivity analysis using the Morris method

To better understand the sensitivity of ERT data to various parameters in the coupled hydrogeophysical problem used to analyse the Hatfield dataset, we performed a global sensitivity analysis using the Morris method (Morris, 1991; Tran et al., 2016; Wainwright et al., 2014b) that is implemented in the R package *sensitivity* (Iooss, 2019). The Morris method returns the elementary effect (EE) of the parameters, which can be considered as an extension of the local sensitivity method. Since the mean EE represents the average effect of each parameter over the parameter space, the mean

EE can be regarded as a global sensitivity measure. To ignore the effects of the sign, the mean of absolute EE is usually reported (mean $|EE|$). In general, for the parameter ranges considered, parameters with high mean $|EE|$ have a large impact on the data. Unconditional realizations are generated using the Morris algorithm based on the parameter ranges specified in Table 6 and the parameter space is sampled uniformly. We used 25 chains, so for a 13 parameter problem $25 \times (13 + 1) = 350$ realizations are generated. We run the forward models using PFLOTRAN-E4D to obtain simulated ERT response (the settings are the same as those in Table 4, unless otherwise stated). We set the objective function for calculating the mean $|EE|$ to be the weighted misfit between the simulated and observed ERT data at Hatfield. The same dataset as in the previous section is used.

Results from the global sensitivity analysis of the Hatfield experiment shows that some parameters, especially water table depths and two of the van Genuchten parameters have the largest effects on the data misfit (Table 6), followed by uniform permeability, porosity and Archie parameter values. Leak parameters has low mean $|EE|$, indicating the difficulty for ERT data to inform their estimation if the others are not known with confidence. Among them, $xloc$ and $yloc$ have the highest and the lowest mean $|EE|$, respectively. Recharge has virtually no effect on the data misfit. The results show that using ERT data and coupled hydrogeophysical modelling is a challenging problem. Future work can benefit from better constraining the problem incorporating additional data sources (e.g. pressure head, concentration, temperature, saturated and unsaturated hydraulic parameters). Our results agree with that of [Tran et al. \(2016\)](#), who showed Archie parameters have a higher mean $|EE|$ than van Genuchten α . However, they found the mean $|EE|$ of van Genuchten m is negligible, while the largest mean $|EE|$ they found is around 8.0. This highlights the Morris sensitivity analysis is best considered in a case-to-case basis, as it is affected by the observed data and the selected parameter ranges. We also report a list of realizations with low data misfit in Table 6. We observe that none of the realizations have an RMSE lower than 7.4 and their parameter values vary greatly. It is noteworthy that a “true” deterministic run (using parameters in Table 4) would give an RMSE of 4.82 (Figure

11). The above shows that some solutions to the ERT leak detection problem can be considered equifinal.

Table 6 Global sensitivity analysis results using the Morris (1991) method on selected parameters on the Hatfield coupled hydrogeophysical model. The parameter ranges considered and the mean absolute elementary effect (|EE|) are reported. Parameter value combinations from ten realizations with the lowest RMSE are also reported.

Parameters [units]	Range	Mean EE	#24	#59	#61	#62	#63	#133	#150	#152	#153	#154
xloc [m]	0.0 – 8.0	7.65	0.0	8.0	2.0	2.0	2.0	6.0	2.0	2.0	2.0	2.0
yloc [m]	0.0 – 10.0	0.18	0.0	10.0	2.5	2.5	2.5	10.0	7.5	7.5	7.5	7.5
q [log10 (m ³ /d)]	-2.0 – 1.0	1.82	-2.00	-1.25	-1.25	-1.25	-1.25	1.00	-1.25	-1.25	-1.25	-1.25
t0 [d]	0.0 – 20.0	1.53	15.00	5.00	5.00	5.00	5.00	15.00	20.00	20.00	20.00	20.00
Archie m [-]	1.0 – 1.5	26.52	1.38	1.00	1.00	1.00	1.00	1.50	1.50	1.50	1.50	1.50
Archie n [-]	0.5 – 2.0	11.68	1.63	0.88	0.88	0.88	0.88	2.00	1.63	1.63	1.63	1.63
water table [m]	-14.0 – -9.0	49.39	-14.00	-14.00	-14.00	-14.00	-14.00	-14.00	-12.75	-12.75	-12.75	-12.75
permeability [log10 (m ²)]	-15.0 – -12.0	6.85	-15.00	-12.00	-12.00	-14.25	-14.25	-12.00	-12.00	-12.00	-12.00	-12.00
porosity [-]	0.25 – 0.35	12.34	0.25	0.35	0.35	0.35	0.35	0.28	0.35	0.35	0.28	0.28
VG α [Pa ⁻¹]	2e-4 – 2e-3	7.50	2.0e-3	2.0e-4	2.0e-4	2.0e-4	1.55e-3	2.0e-4	6.5e-4	6.5e-4	6.5e-4	6.5e-4
VG m [-]	0.4 – 0.8	115.16	0.7	0.7	0.7	0.7	0.7	0.5	0.4	0.7	0.7	0.7
VG Sr [-]	0.01 – 0.2	69.30	0.2	0.01	0.01	0.01	0.01	0.1525	0.01	0.1525	0.1525	0.1525
recharge [mm/d]	0.0 – 0.001	0.03	0.00	7.5e-4	7.5e-4	7.5e-4	7.5e-4	0.00	1.0e-3	1.0e-3	1.0e-3	2.5e-4
RMSE	--	--	7.54	11.10	11.22	11.15	10.57	9.30	8.25	9.40	7.44	7.42

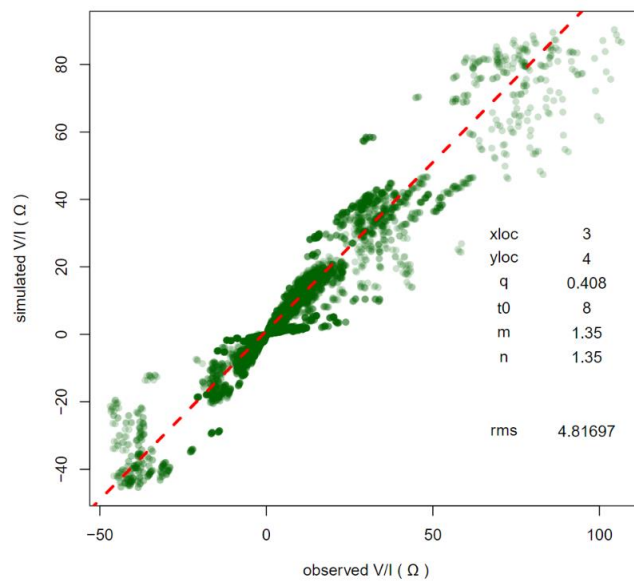


Figure 11 Transfer resistance scatter plot between the observed and simulated data at Hatfield. The simulated data uses parameter values listed in Table 4.

5) Discussion

ERT has been used to detect leaks from nuclear sites for more than two decades. The conventional approach is to use inversion to obtain smoothed images of resistivity at different times and to assess whether there is a leak. This approach does not allow estimation of leak parameters and inversion of large time-lapse ERT datasets can be computationally demanding. We have presented a data assimilation framework to estimate leak parameters from ERT data. It evaluates hydrological model proposals based on the misfits between simulated and observed ERT data and update the model proposals. The estimated leak parameters are presented as a posterior distribution. It also outputs plume mass discharge across a plane, which can be used as a metric to evaluate site-wide uncertainty reduction. These features are not available in existing methods. Since current methods to estimate mass discharge are based on interpolation of point measurements, our coupled modelling approach provides an alternative to quantify mass discharge estimates. Together with point measurements and ERT imaging, other methods can help establish multiple lines of evidence to better inform decision making in nuclear site characterisation.

Our synthetic results show that the method allows very good estimation of leak parameters (e.g. leak rate, loading size, and location). They also show that this framework can work reasonably well under the influence of uncertain petrophysical parameters and mean K values, as well as under K heterogeneity with small correlation lengths. With the rapid growth of autonomous ERT systems to monitor infrastructure, such as British Geological Survey's ALERT and PRIME (Huntley et al., 2019) systems, our approach can provide additional value to ERT data and supplement inverted resistivity images. Our work also has potential to be applied to other non-point source leak detection problems such as seepage through embankments, or using a different geophysical method such as self potential (SP).

We have only examined problems with a few parameters (e.g. leak parameters and homogeneous Archie and permeability values). All hydrological and petrophysical parameters that are not being updated are treated as known constants, which can be strong assumptions on uncertain subsurface properties. Future work

should strive to relax such assumption and jointly estimate more parameters. The prior distribution of the uncertain parameters may have an effect on the performance of our data assimilation approach. Nonetheless, we emphasize that they should be chosen based on site-specific prior knowledge. In this work, we have considered a relatively simple problem: a single conservative source with known concentration (thus fluid conductivity) with a single release episode. With the aid of relevant auxiliary information, our framework has the potential to be extended to more complex problems.

The challenges we have encountered when dealing with field data highlights the need of unbiased and reliable prior information for the proposed method to work in practice. Equifinality (Beven, 2006; Binley and Beven, 2003) obviously exist in the leak detection problem since multiple combinations of leak, petrophysical, and hydraulic parameters can give similar data misfits. Different parameterization, scaling of parameters, and additional data sources may alleviate the problem. But ultimately, methods that allow rejection of model proposals may be desirable. Nevertheless, our method can be considered both a quick and approximate method for quantifying posterior uncertainty of parameters of interest, as well as a flexible method to perform regularized inversion without forming the Jacobian (Iglesias, 2016), which can be advantageous for coupled problems. Our proposed method is best used in well characterized sites where an abundance of historical data can be used to build prior models. Alternatively, our method can also be used in controlled tracer injection experiments to estimate hydraulic, petrophysical and transport parameters.

There exists unique challenges for using raw ERT data in data assimilation. ERT datasets are usually quite large, with each timeframe containing hundreds to tens of thousands of data points. The fast collection of ERT data mean that multiple datasets can be collected daily. However, due to computation constraints, we have only used data from a few selected days. Also, each ERT quadrupole measurement neither represent the state response at a point (as in head or concentration data) or the overall system response (as in hydrocarbon production rates). These challenges do not appear to impact leak estimation from synthetic results. But their implications warrant further

investigation—for example, can we compress raw ERT data for data assimilation since they may contain significant redundant information?

Frameworks for efficient high-dimensional data assimilation (Ghorbanidehno et al., 2015; Li et al., 2015, 2016) can be used to jointly estimate a heterogeneous permeability field. Methods such as level set methods, discrete cosine transform (DCT) and principal component analysis (PCA) can reduce the number of parameters to describe a highly heterogeneous field. A recent study has applied ES-MDA in combination with level set methods (Iglesias and McLaughlin, 2011; Tai and Chan, 2004) to estimate the three-facies heterogeneous permeability field from conservative tracer test data at the Hanford IFRC site (Song et al., 2019). Future work should explore their utility in hydrogeophysical data assimilation. Likewise, we have assumed relatively simple petrophysical relationships in our coupled hydrogeophysical models. Whether more complex petrophysical models will improve data assimilation results remains an open question. We also have not examined joint assimilation of ERT data with head or concentration data, which can be promising for further constraining our results. In this paper, we have used a relatively small ensemble of highly detailed, fully coupled hydrogeophysical simulations as the forward model. Our work can benefit from a recently developed, adaptive multi-fidelity version of ES-MDA (Zheng et al., 2018), which leverages both the accuracy of highly detailed models and the efficiency of simplified models within the ES-MDA framework.

6) Conclusions

We propose a data assimilation framework that allows the use of time-lapse ERT data for solving hydrological parameters in a leak detection problem. It does not produce any ERT images during inversion; rather, it updates parameters in the hydrological model to minimize ERT data misfit. The use of an ensemble-based framework allows straightforward computation of uncertainty estimates. Site-wide uncertainty reduction can be visualized by comparison of prior and posterior mass discharge curves. Synthetic and field results demonstrate its utility under a variety of settings, e.g. when uniform hydrological and Archie parameters are estimated jointly.

This new framework can be readily extended to solving other complex problems (e.g. multiple modalities) of interest that is monitored by geophysical data. We have only used ERT data in our analysis but the framework is highly flexible that it is straightforward to incorporate multiple data types. Our method complements electrical resistivity imaging and is particularly applicable to sites where some prior characterization is performed and uncertainty estimates for the parameters that drive the underlying processes observed are desired.

7) Acknowledgement

This paper is published with the permission of the Executive Director of the British Geological Survey (NERC) and Sellafield Ltd. (on behalf of the Nuclear Decommissioning Authority). James Graham and Nick Atherton provided comments that helped improve an earlier version of the manuscript. This work is supported by a Lancaster Environmental Centre PhD studentship and a NDA PhD Bursary; the latter enabled the first author's visits to the PNNL to conduct this work. We thank the PNNL Institutional Computing (PIC) for computing resources. Additional computing resources was provided by the National Energy Research Scientific Computing Center (NERSC), a DOE Office of Science User Facility supported by the Office of Science of the U.S. Department of Energy under Contract No. DE-AC02-05CH11231.

References

- Aalstad, K., Westermann, S., Schuler, T.V., Boike, J., Bertino, L., 2018. Ensemble-based assimilation of fractional snow-covered area satellite retrievals to estimate the snow distribution at Arctic sites. *Cryosphere* 12, 247–270. <https://doi.org/10.5194/tc-12-247-2018>
- Abdulsamad, F., Revil, A., Soueid Ahmed, A., Coperey, A., Karaoulis, M., Nicaise, S., Peyras, L., 2019. Induced polarization tomography applied to the detection and the monitoring of leaks in embankments. *Eng. Geol.* 254, 89–101. <https://doi.org/10.1016/J.ENGGEOL.2019.04.001>
- Aghasi, A., Mendoza-Sanchez, I., Miller, E.L., Ramsburg, C.A., Abriola, L.M., 2013. A geometric approach to joint inversion with applications to contaminant source

References

- zone characterization. *Inverse Probl.* 29, 115014. <https://doi.org/10.1088/0266-5611/29/11/115014>
- Audebert, M., Clément, R., Touze-Foltz, N., Günther, T., Moreau, S., Duquennoi, C., 2014. Time-lapse ERT interpretation methodology for leachate injection monitoring based on multiple inversions and a clustering strategy (MICS). *J. Appl. Geophys.* 111, 320–333. <https://doi.org/10.1016/j.jappgeo.2014.09.024>
- Balbarini, N., Rønde, V., Maurya, P., Fiandaca, G., Møller, I., Erik Klint, K., Christiansen, A. V., Binning, P.J., Bjerg, P.L., 2018. Geophysics Based Contaminant Mass Discharge Quantification Downgradient of a Landfill and a Former Pharmaceutical Factory. *Water Resour. Res.* <https://doi.org/10.1029/2017WR021855>
- Barnett, D.B., Gee, G.W., Sweeney, M.D., Johnson, M.D., Medina, V.F., Khan, F., 2003. Results of Performance Evaluation Testing of Electrical Leak-Detection Methods at the Hanford Site Mock Tank – FY 2002-2003. Richland, Washington.
- Beven, K., 2006. A manifesto for the equifinality thesis. *J. Hydrol.* 320, 18–36. <https://doi.org/10.1016/j.jhydrol.2005.07.007>
- Binley, A., Beven, K., 2003. Vadose zone flow model uncertainty as conditioned on geophysical data. *Groundwater* 41, 119–127.
- Binley, A., Cassiani, G., Middleton, R., Winship, P., 2002. Vadose zone flow model parameterisation using cross-borehole radar and resistivity imaging. *J. Hydrol.* 267, 147–159. [https://doi.org/10.1016/S0022-1694\(02\)00146-4](https://doi.org/10.1016/S0022-1694(02)00146-4)
- Binley, A., Hubbard, S.S., Huisman, J.A., Revil, A., Robinson, D.A., Singha, K., Slater, L.D., 2015. The emergence of hydrogeophysics for improved understanding of subsurface processes over multiple scales. *Water Resour. Res.* 51, 3837–3866. <https://doi.org/10.1002/2015WR017016>
- Binley, A., Winship, P., Middleton, R., Pokar, M., West, J., 2001. High-resolution characterization of vadose zone dynamics using cross-borehole radar. *Water Resour. Res.* 37, 2639–2652. <https://doi.org/10.1029/2000WR000089>
- Brusseau, M.L., Guo, Z., 2014. Assessing contaminant-removal conditions and plume persistence through analysis of data from long-term pump-and-treat operations. *J. Contam. Hydrol.* 164, 16–24. <https://doi.org/10.1016/j.jconhyd.2014.05.004>
- Cai, Z., Wilson, R.D., Cardiff, M.A., Kitanidis, P.K., 2011. Increasing Confidence in Mass Discharge Estimates Using Geostatistical Methods. *Ground Water* 49, 197–208. <https://doi.org/10.1111/j.1745-6584.2010.00709.x>

References

- Camporese, M., Cassiani, G., Deiana, R., Salandin, P., 2011. Assessment of local hydraulic properties from electrical resistivity tomography monitoring of a three-dimensional synthetic tracer test experiment. *Water Resour. Res.* 47, 1–15. <https://doi.org/10.1029/2011WR010528>
- Camporese, M., Cassiani, G., Deiana, R., Salandin, P., Binley, A., 2015. Coupled and uncoupled hydrogeophysical inversions using ensemble Kalman filter assimilation of ERT-monitored tracer test data. *Water Resour. Res.* 51, 3277–3291. <https://doi.org/10.1002/2014WR016017>
- Chambers, J.E., Kuras, O., Meldrum, P.I., Ogilvy, R.D., Hollands, J., 2006. Electrical resistivity tomography applied to geologic, hydrogeologic, and engineering investigations at a former waste-disposal site. *Geophysics* 71, B231–B239. <https://doi.org/10.1190/1.2360184>
- Chen, X., Hammond, G.E., Murray, C.J., Rockhold, M.L., Vermeul, V.R., Zachara, J.M., 2013. Application of ensemble-based data assimilation techniques for aquifer characterization using tracer data at Hanford 300 area. *Water Resour. Res.* 49, 7064–7076. <https://doi.org/10.1002/2012WR013285>
- Chen, Z., Gómez-Hernández, J.J., Xu, T., Zanini, A., 2018. Joint identification of contaminant source and aquifer geometry in a sandbox experiment with the restart ensemble Kalman filter. *J. Hydrol.* 564, 1074–1084. <https://doi.org/10.1016/J.JHYDROL.2018.07.073>
- Christ, J.A., Ramsburg, C.A., Pennell, K.D., Abriola, L.M., 2010. Predicting DNAPL mass discharge from pool-dominated source zones. *J. Contam. Hydrol.* <https://doi.org/10.1016/j.jconhyd.2010.02.005>
- Christ, J.A., Ramsburg, C.A., Pennell, K.D., Abriola, L.M., 2006. Estimating mass discharge from dense nonaqueous phase liquid source zones using upscaled mass transfer coefficients: An evaluation using multiphase numerical simulations. *Water Resour. Res.* 42, 1–13. <https://doi.org/10.1029/2006WR004886>
- Crestani, E., Camporese, M., Salandin, P., 2015. Assessment of hydraulic conductivity distributions through assimilation of travel time data from ERT-monitored tracer tests. *Adv. Water Resour.* 84, 23–36. <https://doi.org/10.1016/j.advwatres.2015.07.022>
- Daily, W., Ramirez, A., Binley, A., 2004. Remote monitoring of leaks in storage tanks using electrical resistance tomography: Application at the Hanford Site. *J. Environ. Eng. Geophys.* 9, 11–24. <https://doi.org/10.4133/jee9.1.11>

References

- Datta, B., Chakrabarty, D., Dhar, A., 2009. Simultaneous identification of unknown groundwater pollution sources and estimation of aquifer parameters. *J. Hydrol.* 376, 48–57. <https://doi.org/10.1016/J.JHYDROL.2009.07.014>
- Emerick, A.A., Reynolds, A.C., 2013. Ensemble smoother with multiple data assimilation. *Comput. Geosci.* 55, 3–15. <https://doi.org/10.1016/j.cageo.2012.03.011>
- Ghorbanidehno, H., Kokkinaki, A., Li, J.Y., Darve, E., Kitanidis, P.K., 2015. Real-time data assimilation for large-scale systems: The spectral Kalman filter. *Adv. Water Resour.* 86, 260–272. <https://doi.org/10.1016/j.advwatres.2015.07.017>
- Hadley, P.W., Newell, C.J., 2012. Groundwater Remediation: The Next 30 Years. *Ground Water* 50, 669–678. <https://doi.org/10.1111/j.1745-6584.2012.00942.x>
- Hammond, G.E., Lichtner, P.C., 2010. Field-scale model for the natural attenuation of uranium at the Hanford 300 Area using high-performance computing. *Water Resour. Res.* 46, 1–31. <https://doi.org/10.1029/2009WR008819>
- Hermans, T., Nguyen, F., Caers, J., 2015. Uncertainty in training image-based inversion of hydraulic head data constrained to ERT data: Workflow and case study. *Water Resour. Res.* 51, 5332–5352. <https://doi.org/10.1002/2014WR016259>
- Hermans, T., Oware, E., Caers, J., 2016. Direct prediction of spatially and temporally varying physical properties from time-lapse electrical resistance data. *Water Resour. Res.* 52, 7262–7283. <https://doi.org/10.1002/2016WR019126>
- Hinnell, A.C., Ferr, T.P.A., Vrugt, J.A., Huisman, J.A., Moysey, S., Rings, J., Kowalsky, M.B., 2010. Improved extraction of hydrologic information from geophysical data through coupled hydrogeophysical inversion. *Water Resour. Res.* 46, 1–14. <https://doi.org/10.1029/2008WR007060>
- Huntley, D., Bobrowsky, P., Hendry, M., Macciotta, R., Elwood, D., Sattler, K., Best, M., Chambers, J., Meldrum, P., 2019. Application of multi-dimensional electrical resistivity tomography datasets to investigate a very slow-moving landslide near Ashcroft, British Columbia, Canada. *Landslides* 16, 1033–1042. <https://doi.org/10.1007/s10346-019-01147-1>
- Iglesias, M., Yang, Y., n.d. A Computational efficient framework for ensemble Kalman inversion with applications to non-destructive testing and imaging. Prep.
- Iglesias, M.A., 2016. A regularizing iterative ensemble Kalman method for PDE-constrained inverse problems. *Inverse Probl.* 32, 025002. <https://doi.org/10.1088/0266-5611/32/2/025002>

References

- Iglesias, M.A., McLaughlin, D., 2011. Level-set techniques for facies identification in reservoir modeling. *Inverse Probl.* 27, 36. <https://doi.org/10.1088/0266-5611/27/3/035008>
- Iooss, B., 2019. Package 'sensitivity.'
- Irving, J., Singha, K., 2010. Stochastic inversion of tracer test and electrical geophysical data to estimate hydraulic conductivities. *Water Resour. Res.* 46, W11514. <https://doi.org/10.1029/2009WR008340>
- ITRC, 2010. Use and Measurement of Mass Flux and Mass Discharge, Use and Measurement of Mass Flux and Mass Discharge. Washington DC.
- Johnson, T.C., Hammond, G.E., Chen, X., 2017. PFLOTRAN-E4D: A parallel open source PFLOTRAN module for simulating time-lapse electrical resistivity data. *Comput. Geosci.* 99, 72–80. <https://doi.org/10.1016/j.cageo.2016.09.006>
- Johnson, T.C., Rucker, D.F., Glaser, D.R., 2015a. Near-Surface Geophysics at the Hanford Nuclear Site, the United States, in: *Treatise on Geophysics*. Elsevier, pp. 571–595. <https://doi.org/10.1016/B978-0-444-53802-4.00205-0>
- Johnson, T.C., Slater, L.D., Ntarlagiannis, D., Day-Lewis, F.D., Elwaseif, M., 2012. Monitoring groundwater-surface water interaction using time-series and time-frequency analysis of transient three-dimensional electrical resistivity changes. *Water Resour. Res.* 48, 1–13. <https://doi.org/10.1029/2012WR011893>
- Johnson, T.C., Versteeg, R., Thomle, J., Hammond, G., Chen, X., Zachara, J., 2015b. Four-dimensional electrical conductivity monitoring of stage-driven river water intrusion: Accounting for water table effects using a transient mesh boundary and conditional inversion constraints. *Water Resour. Res.* 51, 6177–6196. <https://doi.org/10.1002/2014WR016129>
- Johnson, T.C., Versteeg, R.J., Day-Lewis, F.D., Major, W., Lane, J.W., 2015c. Time-Lapse Electrical Geophysical Monitoring of Amendment-Based Biostimulation. *Groundwater* 53, 920–932. <https://doi.org/10.1111/gwat.12291>
- Johnson, T.C., Versteeg, R.J., Huang, H., Routh, P.S., 2009. Data-domain correlation approach for joint hydrogeologic inversion of time-lapse hydrogeologic and geophysical data. *Geophysics* 74, F127. <https://doi.org/10.1190/1.3237087>
- Johnson, T.C., Versteeg, R.J., Ward, A., Day-Lewis, F.D., Revil, A., 2010. Improved hydrogeophysical characterization and monitoring through parallel modeling and inversion of time-domain resistivity and induced-polarization data. *Geophysics* 75, WA27. <https://doi.org/10.1190/1.3475513>

References

- Johnson, T.C., Wellman, D., 2015. Accurate modelling and inversion of electrical resistivity data in the presence of metallic infrastructure with known location and dimension. *Geophys. J. Int.* 202, 1096–1108. <https://doi.org/10.1093/gji/ggv206>
- Ju, L., Zhang, J., Meng, L., Wu, L., Zeng, L., 2018. An adaptive Gaussian process-based iterative ensemble smoother for data assimilation. *Adv. Water Resour.* <https://doi.org/10.1016/j.advwatres.2018.03.010>
- Kang, X., Shi, X., Deng, Y., Revil, A., Xu, H., Wu, J., 2018. Coupled hydrogeophysical inversion of DNAPL source zone architecture and permeability field in a 3D heterogeneous sandbox by assimilation time-lapse cross-borehole electrical resistivity data via ensemble Kalman filtering. *J. Hydrol.* 567, 149–164. <https://doi.org/10.1016/J.JHYDROL.2018.10.019>
- Kang, X., Shi, X., Revil, A., Cao, Z., Li, L., Lan, T., Wu, J., 2019. Coupled hydrogeophysical inversion to identify non-Gaussian hydraulic conductivity field by jointly assimilating geochemical and time-lapse geophysical data. *J. Hydrol.* <https://doi.org/10.1016/j.jhydrol.2019.124092>
- Koch, J., Nowak, W., 2016. Identification of contaminant source architectures—A statistical inversion that emulates multiphase physics in a computationally practicable manner. *Water Resour. Res.* 52. <https://doi.org/10.1002/2014WR015716>
- Köpke, C., Elsheikh, A.H., Irving, J., 2019. Hydrogeophysical Parameter Estimation Using Iterative Ensemble Smoothing and Approximate Forward Solvers. *Front. Environ. Sci.* 7, 34. <https://doi.org/10.3389/fenvs.2019.00034>
- Kowalsky, M.B., Finsterle, S., Peterson, J., Hubbard, S., Rubin, Y., Majer, E., Ward, A., Gee, G., 2005. Estimation of field-scale soil hydraulic and dielectric parameters through joint inversion of GPR and hydrological data. *Water Resour. Res.* 41, n/a-n/a. <https://doi.org/10.1029/2005WR004237>
- Kuras, O., Pritchard, J.D., Meldrum, P.I., Chambers, J.E., Wilkinson, P.B., Ogilvy, R.D., 2009. Monitoring hydraulic processes with Automated time-Lapse Electrical Resistivity Tomography (ALERT). *Comptes Rendus Geosci.* 351, 868–885.
- Kuras, O., Wilkinson, P.B., Meldrum, P.I., Oxby, L.S., Uhlemann, S., Chambers, J.E., Binley, A., Graham, J., Smith, N.T., Atherton, N., 2016. Geoelectrical monitoring of simulated subsurface leakage to support high-hazard nuclear decommissioning at the Sellafield Site, UK. *Sci. Total Environ.* 566–567, 350–359. <https://doi.org/10.1016/j.scitotenv.2016.04.212>

References

- Kwong, S., Fowler, L., 2014. Technical Memorandum: MSSS Electrical Resistivity Tomography (ERT): TRAFFIC modelling of the ERT trial.
- LaBrecque, D.J., Ramirez, A.L., Daily, W.D., Binley, A.M., Schima, S.A., 1996. ERT monitoring on environmental remediation processes. *Meas. Sci. Technol.* 7, 375–383. <https://doi.org/10.1088/0957-0233/7/3/019>
- Lan, T., Shi, X., Jiang, B., Sun, Y., Wu, J., 2018. Joint inversion of physical and geochemical parameters in groundwater models by sequential ensemble-based optimal design. *Stoch. Environ. Res. Risk Assess.* 5. <https://doi.org/10.1007/s00477-018-1521-5>
- Le, D.H., Emerick, A. A., Reynolds, A.C., 2016. An Adaptive Ensemble Smoother With Multiple Data Assimilation for Assisted History Matching. *SPE J.* 21, 2195–2207. <https://doi.org/10.2118/173214-PA>
- Li, J.Y., Kokkinaki, A., Ghorbanidehno, H., Darve, E.F., Kitanidis, P.K., 2015. The compressed state Kalman filter for nonlinear state estimation: Application to large-scale reservoir monitoring. *Water Resour. Res.* 51, 9942–9963. <https://doi.org/10.1002/2015WR017203>
- Li, L., Puzel, R., Davis, A., 2018. Data assimilation in groundwater modelling: ensemble Kalman filter versus ensemble smoothers. *Hydrol. Process.* 32, 2020–2029. <https://doi.org/10.1002/hyp.13127>
- Li, Y.J., Kokkinaki, A., Darve, E.F., 2016. Smoothing-based compressed state Kalman filter for joint state-parameter estimation: applications in reservoir characterization and CO₂ storage monitoring. *Water Resour. Res.* 53, 7190–7207. <https://doi.org/10.1002/2016WR020168>
- Manoli, G., Rossi, M., Pasetto, D., Deiana, R., Ferraris, S., Cassiani, G., Putti, M., 2015. An iterative particle filter approach for coupled hydro-geophysical inversion of a controlled infiltration experiment. *J. Comput. Phys.* 283, 37–51. <https://doi.org/10.1016/J.JCP.2014.11.035>
- Mariethoz, G., Renard, P., Straubhaar, J., 2010. The direct sampling method to perform multiple-point geostatistical simulations. *Water Resour. Res.* 46, 1–14. <https://doi.org/10.1029/2008WR007621>
- Maurya, P.K., Rønde, V.K., Fiandaca, G., Balbarini, N., Auken, E., Bjerg, P.L., Christiansen, A.V., 2017. Detailed landfill leachate plume mapping using 2D and 3D electrical resistivity tomography - with correlation to ionic strength measured in screens. *J. Appl. Geophys.* 138, 1–8. <https://doi.org/10.1016/j.jappgeo.2017.01.019>

References

- Michalak, A.M., Shlomi, S., 2007. A geostatistical data assimilation approach for estimating groundwater plume distributions from multiple monitoring events. pp. 73–88. <https://doi.org/10.1029/171GM08>
- Millard, S.P., 2013. Designing a Sampling Program. *EnvStats An R Packag. Environ. Stat.* 25–61. <https://doi.org/10.1007/978-1-4614-8456-1>
- Morris, M.D., 1991. Factorial Sampling Plans for Preliminary Computational Experiments, *Technometrics*.
- Nowak, W., 2009. Best unbiased ensemble linearization and the quasi-linear Kalman ensemble generator. *Water Resour. Res.* 45. <https://doi.org/10.1029/2008WR007328>
- Oware, E.K., Moysey, S.M.J., Khan, T., 2013. Physically based regularization of hydrogeophysical inverse problems for improved imaging of process-driven systems. *Water Resour. Res.* 49, 6238–6247. <https://doi.org/10.1002/wrcr.20462>
- Pidlisecky, A., Singha, K., Day-Lewis, F.D., 2011. A distribution-based parametrization for improved tomographic imaging of solute plumes. *Geophys. J. Int.* 187, 214–224. <https://doi.org/10.1111/j.1365-246X.2011.05131.x>
- Power, C., Gerhard, J.I., Karaoulis, M., Tsourlos, P., Giannopoulos, A., 2014. Evaluating four-dimensional time-lapse electrical resistivity tomography for monitoring DNAPL source zone remediation. *J. Contam. Hydrol.* 162–163, 27–46. <https://doi.org/10.1016/j.jconhyd.2014.04.004>
- Ramirez, A., Daily, W., Binley, A., Labrecque, D., Roelant, D., 1996. Detection of leaks in underground storage tanks using electrical resistance methods. *J. Environ. Eng. Geophys.* 1, 189–203. <https://doi.org/10.4133/JEEG1.3.189>
- Ramirez, A.L., Nitao, J.J., Hanley, W.G., Aines, R., Glaser, R.E., Sengupta, S.K., Dyer, K.M., Hickling, T.L., Daily, W.D., 2005. Stochastic inversion of electrical resistivity changes using a Markov Chain Monte Carlo approach. *J. Geophys. Res.* 110, B02101. <https://doi.org/10.1029/2004JB003449>
- Reynolds, A.C., Zafari, M., Li, G., 2006. Iterative forms of the ensemble Kalman filter, in: *Proceedings of 10th European Conference on the Mathematics of Oil Recovery*. Amsterdam, The Netherlands.
- Rossi, M., Manoli, G., Pasetto, D., Deiana, R., Ferraris, S., Strobbia, C., Putti, M., Cassiani, G., 2015. Coupled inverse modeling of a controlled irrigation experiment using multiple hydro-geophysical data. *Adv. Water Resour.* 82, 150–165. <https://doi.org/10.1016/J.ADVWATRES.2015.03.008>

References

- Scholer, M., Irving, J., Looms, M.C., Nielsen, L., Holliger, K., 2012. Bayesian Markov-chain-Monte-Carlo inversion of time-lapse crosshole GPR data to characterize the vadose zone at the Arrenaes site, Denmark. (Special Section: Model-data fusion in the vadose zone.). *Vadose Zo. J.* 11, 153. <https://doi.org/10.2136/vzj2011.0153>
- Schöniger, A., Nowak, W., Hendricks Franssen, H.-J., 2012. Parameter estimation by ensemble Kalman filters with transformed data: Approach and application to hydraulic tomography. *Water Resour. Res.* 48, W04502. <https://doi.org/10.1029/2011WR010462>
- Shlomi, S., Michalak, A.M., 2007. A geostatistical framework for incorporating transport information in estimating the distribution of a groundwater contaminant plume. *Water Resour. Res.* 43. <https://doi.org/10.1029/2006WR005121>
- Singha, K., Gorelick, S.M., 2006. Effects of spatially variable resolution on field-scale estimates of tracer concentration from electrical inversions using Archie's law. *Geophysics* 71, G83. <https://doi.org/10.1190/1.2194900>
- Slater, L.D., Ntarlagiannis, D., Day-Lewis, F.D., Mwakanyamale, K., Versteeg, R.J., Ward, A., Strickland, C., Johnson, C.D., Lane, J.W., 2010. Use of electrical imaging and distributed temperature sensing methods to characterize surface water-groundwater exchange regulating uranium transport at the Hanford 300 Area, Washington. *Water Resour. Res.* 46, 1–13. <https://doi.org/10.1029/2010WR009110>
- Song, X., Chen, X., Ye, M., Dai, Z., Hammond, G., Zachara, J.M., 2019. Delineating Facies Spatial Distribution by Integrating Ensemble Data Assimilation and Indicator Geostatistics With Level-Set Transformation. *Water Resour. Res.* 2018WR023262. <https://doi.org/10.1029/2018WR023262>
- Stordal, A.S., Elsheikh, A.H., 2015. Iterative ensemble smoothers in the annealed importance sampling framework. *Adv. Water Resour.* 86, 231–239. <https://doi.org/10.1016/j.advwatres.2015.09.030>
- Sun, A.Y., 2007. A robust geostatistical approach to contaminant source identification. *Water Resour. Res.* <https://doi.org/10.1029/2006WR005106>
- Sun, A.Y., Painter, S.L., Wittmeyer, G.W., 2006. A constrained robust least squares approach for contaminant release history identification. *Water Resour. Res.* 42. <https://doi.org/10.1029/2005WR004312>
- Sun, N.-Z., Sun, A., 2015. *Model Calibration and Parameter Estimation*. Springer New York, New York, NY. <https://doi.org/10.1007/978-1-4939-2323-6>

References

- Tai, X., Chan, T.F., 2004. A survey on multiple level set methods with applications for identifying piecewise constant functions. *Int. J. Numer. Anal. Model* 1, 25–48.
- Tran, A.P., Dafflon, B., Hubbard, S.S., Kowalsky, M.B., Long, P., Tokunaga, T.K., Williams, K.H., 2016. Quantifying shallow subsurface water and heat dynamics using coupled hydrological-thermal-geophysical inversion. *Hydrol. Earth Syst. Sci.* 20, 3477–3491. <https://doi.org/10.5194/hess-20-3477-2016>
- Troldborg, M., Nowak, W., Lange, I. V., Santos, M.C., Binning, P.J., Bjerg, P.L., 2012. Application of Bayesian geostatistics for evaluation of mass discharge uncertainty at contaminated sites. *Water Resour. Res.* 48, 1–19. <https://doi.org/10.1029/2011WR011785>
- Troldborg, M., Nowak, W., Tuxen, N., Bjerg, P.L., Helmig, R., Binning, P.J., 2010. Uncertainty evaluation of mass discharge estimates from a contaminated site using a fully Bayesian framework. *Water Resour. Res.* 46, 1–19. <https://doi.org/10.1029/2010WR009227>
- Truex, M.J., Johnson, T.C., Strickland, C.E., Peterson, J.E., Hubbard, S.S., 2013. Monitoring Vadose Zone Desiccation with Geophysical Methods. *Vadose Zo. J.* 12. <https://doi.org/10.2136/vzj2012.0147>
- Truex, M.J., Oostrom, M., Strickland, C.E., Chronister, G.B., Benecke, M.W., Johnson, C.D., 2012. Field-Scale Assessment of Desiccation Implementation for Deep Vadose Zone Contaminants. *Vadose Zo. J.* 11, 0. <https://doi.org/10.2136/vzj2011.0144>
- Tso, C.-H.M., Kuras, O., Wilkinson, P.B., Uhlemann, S., Chambers, J.E., Meldrum, P.I., Graham, J., Sherlock, E.F., Binley, A., 2017. Improved characterisation and modelling of measurement errors in electrical resistivity tomography (ERT) surveys. *J. Appl. Geophys.* 146, 103–119. <https://doi.org/10.1016/J.JAPPGEO.2017.09.009>
- Wagner, B.J., 1992. Simultaneous parameter estimation and contaminant source characterization for coupled groundwater flow and contaminant transport modelling. *J. Hydrol.* 135, 275–303. [https://doi.org/10.1016/0022-1694\(92\)90092-A](https://doi.org/10.1016/0022-1694(92)90092-A)
- Wainwright, H.M., Finsterle, S., Jung, Y., Zhou, Q., Birkholzer, J.T., 2014. Making sense of global sensitivity analyses. *Comput. Geosci.* 65, 84–94. <https://doi.org/10.1016/j.cageo.2013.06.006>
- Wallin, E.L., Johnson, T.C., Greenwood, W.J., Zachara, J.M., 2013. Imaging high stage river-water intrusion into a contaminated aquifer along a major river corridor

References

- using 2-D time-lapse surface electrical resistivity tomography. *Water Resour. Res.* 49, 1693–1708. <https://doi.org/10.1002/wrcr.20119>
- Ward, W.O.C., Wilkinson, P.B., Chambers, J.E., Nilsson, H., Kuras, O., Bai, L., 2016. Tracking tracer motion in a 4-D electrical resistivity tomography experiment. *Water Resour. Res.* 52, 4078–4094. <https://doi.org/10.1002/2015WR017958>
- Winship, P., Binley, A., Gomez, D., 2006. Flow and transport in the unsaturated Sherwood Sandstone: characterization using cross-borehole geophysical methods. *Geol. Soc. London, Spec. Publ.* 263, 219–231. <https://doi.org/10.1144/GSL.SP.2006.263.01.12>
- Xu, T., Gómez-Hernández, J.J., 2018. Simultaneous identification of a contaminant source and hydraulic conductivity via the restart normal-score ensemble Kalman filter. *Adv. Water Resour.* 112, 106–123. <https://doi.org/10.1016/j.advwatres.2017.12.011>
- Xu, T., Gómez-Hernández, J.J., 2016. Joint identification of contaminant source location, initial release time, and initial solute concentration in an aquifer via ensemble Kalman filtering. *Water Resour. Res.* 52, 6587–6595. <https://doi.org/10.1002/2016WR019111>
- Zeng, L., Shi, L., Zhang, D., Wu, L., 2012. A sparse grid based Bayesian method for contaminant source identification. *Adv. Water Resour.* 37, 1–9. <https://doi.org/10.1016/J.ADVWATRES.2011.09.011>
- Zhang, Y., Liu, N., Oliver, D.S., 2010. Ensemble filter methods with perturbed observations applied to nonlinear problems. *Comput. Geosci.* 14, 249–261. <https://doi.org/10.1007/s10596-009-9149-7>
- Zheng, Q., Zhang, J., Xu, W., Wu, L., Zeng, L., 2018. Adaptive Multi-Fidelity Data Assimilation for Nonlinear Subsurface Flow Problems. *Water Resour. Res.* 2018WR023615. <https://doi.org/10.1029/2018WR023615>
- Zhou, H., Gómez-Hernández, J.J., Li, L., 2014. Inverse methods in hydrogeology: Evolution and recent trends. *Adv. Water Resour.* 63, 22–37. <https://doi.org/10.1016/j.advwatres.2013.10.014>
- Zovi, F., Camporese, M., Hendricks Franssen, H.J., Huisman, J.A., Salandin, P., 2017. Identification of high-permeability subsurface structures with multiple point geostatistics and normal score ensemble Kalman filter. *J. Hydrol.* 548, 208–224. <https://doi.org/10.1016/j.jhydrol.2017.02.056>

6. Paper 3: On the field estimation of moisture content using electrical geophysics—the impact of petrophysical model uncertainty

Published as **Tso, C.-H.M., Kuras, O., Binley, A.** (2019): On the field estimation of moisture content using electrical geophysics-the impact of petrophysical model uncertainty. *Water Resources Research*, 55, 2019, DOI:[10.1029/2019WR024964](https://doi.org/10.1029/2019WR024964).

Abstract

The spatiotemporal distribution of pore water in the vadose zone can have a critical control on many processes in the near-surface Earth, such as the onset of landslides, crop yield, groundwater recharge, and runoff generation. Electrical geophysics has been widely used to monitor the moisture content (θ) distribution in the vadose zone at field sites, and often resistivity (ρ) or conductivity (σ) is converted to moisture contents through petrophysical relationships (e.g. Archie's law). Though both the petrophysical relationships (i.e. choices of appropriate model and parameterisation) and the derived moisture content are known to be subject to uncertainty, they are commonly treated as exact and error-free. This study examines the impact of uncertain petrophysical relationships on the moisture content estimates derived from electrical geophysics. We show from a collection of data from multiple core samples that significant variability in the $\theta(\rho)$ relationship can exist. Using rules of error propagation, we demonstrate the combined effect of inversion and uncertain petrophysical parameterization on moisture content estimates and derive their uncertainty bounds. Through investigation of a water injection experiment, we observe that the petrophysical uncertainty yields a large range of estimated total moisture volume within the water plume. The estimates of changes in water volume, however, generally agree within (large) uncertainty bounds. Our results caution against solely relying on electrical geophysics to estimate moisture content in the field. The uncertainty propagation approach is transferrable to other field studies of moisture content estimation.

Key points:

- Field evidence demonstrating strong variability of $\theta(\rho)$ relationships at the site is provided
- The proposed methods show the impact of different uncertain $\theta(\rho)$ models on θ estimates from ERT and their associated uncertainty bounds
- Nevertheless, different Archie models give consistent difference in θ estimates, though their uncertainty bounds are large

Plain language summary

Maps and images of electrical resistivity have been widely applied to effectively monitor the wetting or drying of the Earth's near-surface. But how well can they quantify such change? How variable are the petrophysical model parameters that relate resistivity and moisture content? Does uncertainty in such relationships impact our confidence in moisture content estimates from resistivity imaging? Our analysis of field samples collected at a UK field site reveals great variability in petrophysical parameters. Using an uncertainty propagation method, which combines the uncertainty contributions from both petrophysical parameters and resistivity data errors, we find that the variable petrophysical parameters can lead to high uncertainty in moisture content estimates and they appear to be the dominating factor in many cases. These effects on uncertainty are greater than previously appreciated. The implication is that realistic uncertainty bounds are needed whenever electrical geophysical methods are used to quantify the amount of water present underground or its changes over time. The findings highlight the importance of better characterization of petrophysical parameters and the need to supplement the interpretation of resistivity-based moisture content estimates with other data sources.

1) Introduction

Monitoring the amount of moisture in the Earth's near-surface is critical in many applications. For example, the distribution of soil moisture is an important trigger for landslides (Ray and Jacobs, 2007). The amount of water available for root water uptake is the most important factor for crop yield (Ahmed et al., 2018). Similarly, the saturation of the vadose zone governs the rate of groundwater recharge and travel times of surface contaminants (e.g., nitrate) to an aquifer (Green et al., 2018; Turkeltaub et al., 2018).

The measurement of moisture content (θ) in the subsurface is not straightforward. Point sampling can only cover a small number of discrete points in an investigation area and can be labor-intensive. These point data may not be representative of site-scale variability. In addition, intrusive sampling may disrupt the

critical processes occurring in the soil (e.g., root growth). Alternative field methods are needed to improve our ability to measure and monitor moisture content. A comprehensive review of the different ground-based methods to determine soil moisture is given by [Jonard et al. \(2018\)](#).

The well-established correlation between moisture content and the bulk resistivity (ρ) in porous media ([Glover, 2015](#); [Lesmes and Friedman, 2005](#)) allows the use of electrical methods (e.g., electrical resistivity tomography [ERT] and electromagnetic induction [EMI]) to be applied to study vadose zone processes. They can be used to derive 2-D or 3-D distributed resistivity models over a relatively large area, and these resistivity models can, in turn, be used for translation to moisture content via petrophysical relationships. ERT or EMI offers much larger spatial coverage than point-based methods without disrupting the Earth materials. Specifically, ERT is typically performed in transects or between boreholes, while EMI tends to provide even greater spatial coverage since it is commonly used for mapping. When applied in time-lapse mode, they can be a powerful tool to reveal temporal variations in soil moisture ([Robinson et al., 2009](#)).

Over the past two decades, electrical geophysics has been widely used in many applications in the vadose zone, and increasingly the resistivity images are translated to obtain quantitative estimates of moisture content. Examples of these applications include monitoring the onset of landslides ([Lehmann et al., 2013](#); [Uhlemann et al., 2017](#)), hillslope moisture dynamics ([Bass et al., 2017](#); [Cassiani et al., 2009](#); [Hübner et al., 2015](#); [Yamakawa et al., 2012](#)), seasonal changes in soil moisture dynamics ([Amidu and Dunbar, 2007](#); [Binley et al., 2002b](#)), root zone water uptake ([Beff et al., 2013](#); [Brillante et al., 2015](#); [Garré et al., 2011](#)), unfrozen moisture in permafrost ([Oldenborger and LeBlanc, 2015](#)), soil moisture profiles beneath different wheat genotypes ([Shanahan et al., 2015](#)), watershed characterization ([Miller et al., 2008](#)), and wetland dynamics ([Chambers et al., 2014b](#); [Scaini et al., 2017](#); [Uhlemann et al., 2016](#)). Previous laboratory studies have shown that ERT is suitable for characterizing moisture content dynamics and tracer breakthrough in the unsaturated zone (e.g. [Koestel et al., 2008](#); [Wehrer and Slater, 2015](#)).

To translate resistivities to moisture content, a petrophysical relationship needs to be determined. (Note that although the root “petro” implies an application related to rocks [as in this study], similar physical laws applies to soils as well.) One common method is to take core samples from the field for laboratory testing ([Amidu and Dunbar, 2007](#)) using well-established procedures (see [Hen-Jones et al., 2017](#); [Jayawickreme et al., 2008](#)). The samples are often oven dried and re-wetted, and their resistivities are then repeatedly measured as their saturation changes. Although hysteresis has been reported in the wetting-drying behavior of samples, laboratory testing is usually only applied to a single drying or wetting regime. Another method is to calibrate field-based inverted resistivity from ERT with in situ measurements of soil moisture, for example, using time domain reflectometry (TDR) probes. Several studies have compared moisture content estimates from TDR and ERT ([Brunet et al., 2010](#)), and in recent years it has become increasingly popular to use such field-derived petrophysical relationships. The local TDR-derived moisture content is taken as error-free, and this is typically used to calibrate against inverted resistivities using Archie's, Waxman–Smits ([Cassiani et al., 2009](#); [Garré et al., 2013](#); [Lehmann et al., 2013](#); [Michot et al., 2003](#)), or data-driven models ([Brillante et al., 2014](#)). More recently, calibration methods have been developed for apparent electrical conductivity from EMI against TDR-derived moisture content ([Robinet et al., 2018](#)). The repeated EMI-moisture content monitoring study of [Martini et al. \(2017\)](#) shows that this is not as straightforward as the relationship between electrical conductivity and moisture content can change with time. [Whalley et al. \(2017\)](#) compared the change in electrical conductivity from EMI and ERT with changes in water content from neutron probe measurements. The third (and perhaps most common) option is to simply use literature values for petrophysical parameters (e.g., [Friedman, 2005](#)). Regardless of the method for the assignment of petrophysical relationships, errors will be present in some form. Laboratory measurements assume the observed relationship and errors from small samples taken at a few locations can be applied to the entire resistivity model. Field-based petrophysical relationships, on the other hand, assume the inverted resistivity model having insignificant and uncorrelated errors so that they can be used

to calibrate against in situ soil moisture data. In other words, the resistivity model uncertainty is implicitly counted twice.

The uncertainty of the moisture content estimates from electrical geophysics not only stems from the uncertainty in the resistivity model, but it also propagates through from any constitutive relationships linking geophysical and hydrological properties, and yet these relationships are frequently assumed to be precise and error-free (Binley et al., 2015), in part due to the time and effort required to measure petrophysical parameters in the lab. In fact, they are known to be uncertain due to the competing properties of the pore fluids, pore geometry, and pore surface area on resistivity measurements (Weller et al., 2013). Petrophysical model uncertainty is also one of the primary factors limiting the utility of coupled inversion approaches (i.e., joint estimation of geophysical and hydraulic properties; Singha et al., 2015). While some stochastic modeling approaches (e.g. Hermans et al., 2015; Hinnell et al., 2010; Wiese et al., 2018) allow some modifications so that petrophysical model uncertainty can be accounted for, resolving issues caused by such uncertainty remains an area of research. Recent coupled inversion approaches allow the option to jointly estimate petrophysical parameters. Kuhl et al. (2018) devised a coupled inversion approach to jointly estimate soil hydraulic parameters, petrophysical parameters, and root parameters simultaneously. Such methods are promising, but there are concerns over the non-uniqueness in the inverse problem formulation and that the petrophysical parameters obtained may merely be “effective” ones. In summary, research is needed to investigate the extent of the impact on moisture content estimates due to uncertain petrophysical relationships.

The oil and gas industry, from where many of the foundational petrophysical relationships used in hydrogeophysics are borrowed, or originate, has been aware of the potential impact of petrophysical uncertainty. For example, Glover (2017) highlighted that various sources of uncertainties in Archie parameters can lead to 20–40% error in hydrocarbon saturation. For instance, even an uncertainty of 0.01 in a saturation exponent of 2 (i.e., 0.5% or 2 ± 0.01) would result in an error in global oil reserves of about USD ± 254.36 billion based on figures in December 2015. While it is

difficult to put a monetary value on many near-surface applications, the above calculation underscores the highly sensitive nature of petrophysical parameters, and one should anticipate a similar scale of error in soil water content estimation from electrical hydrogeophysics.

It is not until recently that the issues associated with petrophysical uncertainty have been investigated. The pioneering work of [Brunetti et al. \(2018\)](#) considered the effect of petrophysical uncertainty on using ground penetrating radar (GPR) data for Bayesian hydrological model selection. There has also been some study on the parameter uncertainty of petrophysical models. For instance, [Laloy et al. \(2011\)](#) tested five “pedo-electrical” models for the reproduction of electrical resistivity (determined by ERT) in a silt loam soil sample across a range of moisture and bulk density values. They were inverted within a Bayesian framework, thereby identifying not only the optimal parameter set but also the parameter uncertainty and its effect on model prediction. However, to date, there has not been any study on how the uncertainty of petrophysical relationships affects the quantitative estimation of soil water in the vadose zone using electrical geophysics. The findings on this question are relevant to many applications mentioned above.

In this work, we present a first attempt to investigate the extent to which moisture content estimates are affected by uncertainty in petrophysical models. Our aims are to understand the likely variability in petrophysical models and to develop a method for petrophysical uncertainty propagation, which can be used to explore contributions to uncertainty in the estimation of soil moisture. We review time-lapse ERT monitoring data of a controlled infiltration experiment and the rock core data collected in the same formation. We test the two types of petrophysical models on the core data and apply it to the inverted resistivity model, while keeping track of the uncertainty propagation quantitatively. The methods and data used in this work are detailed in section 2. We report results from our analysis in section 3. Finally, we discuss our findings in section 4 and provide our conclusions in section 5.

2) Materials and methods

Our study focuses on data from earlier comprehensive field and laboratory investigations, at Hatfield (near Doncaster, South Yorkshire, UK) and Eggborough (near Selby, North Yorkshire, UK). Two field sites, 17 km apart from each other, were instrumented to study recharge processes to a Sherwood Sandstone aquifer. Tracer injection experiments, monitored by both ERT and GPR, were performed at both sites. At Eggborough, ERT and GPR surveys were conducted in 1999 (Binley et al., 2002a; Cassiani and Binley, 2005), and the data were used to study the utility of joint inversion of ERT and GPR data (Bouchedda et al., 2012; Linde et al., 2006) and the influence of prior information on vadose zone parameters estimation in stochastic inversion (Scholer et al., 2011). Similarly, both ERT and GPR surveys were conducted during tracer injection at Hatfield, and they have been used in a series of studies to improve the monitorability and predictability of vadose zone processes using geophysical measurements (Binley et al., 2004, 2002a, 2002b, 2001; Binley and Beven, 2003). Two radar and four ERT boreholes were drilled around an injector to monitor tracer injection. Each ERT borehole consists of 16 stainless steel mesh electrodes equally spaced at 0.733 m between 2 and 13 m depth. The borehole electrodes were supplemented with eight surface electrodes. Two cored boreholes were drilled close to the tracer injection area to obtain a depth profile of grain size distribution. Note that the top 2 meters is topsoil while its underlying material is weakly cemented sandstone. A similar borehole ERT and GPR setup was applied for the monitoring experiment at the Arreneas infiltration plant in Denmark (Haarder et al., 2012; Looms et al., 2008).

In this study, we fitted the Archie relationships for the cores collected at Eggborough and used them as realizations of petrophysical models. We then simulated the ERT response of a water injection experiment, assuming a baseline petrophysical relationship. We then inverted the ERT response and use each of the realizations of petrophysical models to estimate moisture content with uncertainty bounds, which we compared against the simulated value. We summarize the workflow of our approach in Figure 1.

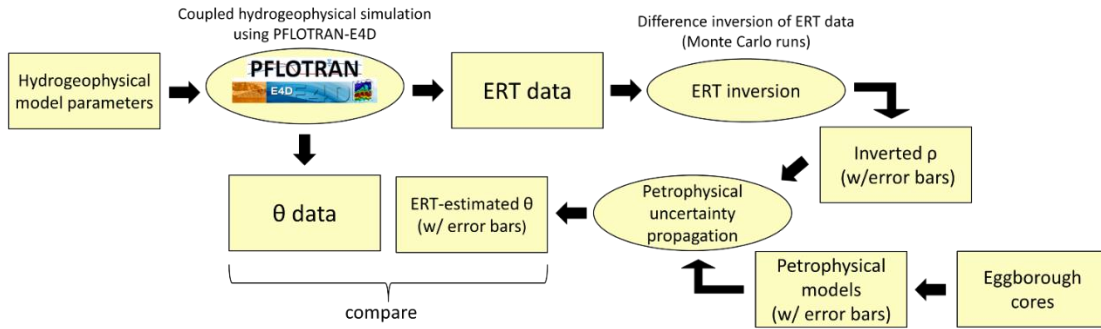


Figure 1 Moisture content (θ) estimation and petrophysical uncertainty propagation workflow used in this study. Rectangles indicate model inputs or data, while ovals represent modeling or analysis steps. We obtained synthetic ERT and θ data using PFLOTRAN-E4D. Then we inverted the ERT data and used the Eggborough cores as different petrophysical models. They were passed through the moisture content estimation and uncertainty estimation framework to obtain ERT-estimated θ , which were compared against the θ data. ERT = electrical resistivity tomography.

2.1. Eggborough Core Samples

Core samples collected at Eggborough were used to measure the spectral induced polarization responses at various saturations (Binley et al., 2005), and they are compared with various physical and hydraulic properties (Supporting Information Table S2). They found a strong correlation between mean relaxation time and hydraulic conductivity and showed that the former is affected by saturation. Binley et al. (2005) did not include the data showing the direct current (DC) resistivity and hydraulic properties were not published. Also, they focused their analysis on only three of the samples extracted. In this work, we examine the DC resistivity–saturation behavior of all the samples to understand its variability and the impact of such variability on estimating moisture content from ERT.

The grain size distribution of the Eggborough cores and blocks are plotted as percentiles (Figure 2a). Also, the percentages of sand, silt, and clay at Eggborough are plotted as depth profiles (Figure 2b). Note that the cores are not repacked sample but instead they are weakly cemented core plugs. In this work, we use the Eggborough data to obtain petrophysical relationships for predicting moisture content in a water injection simulation.

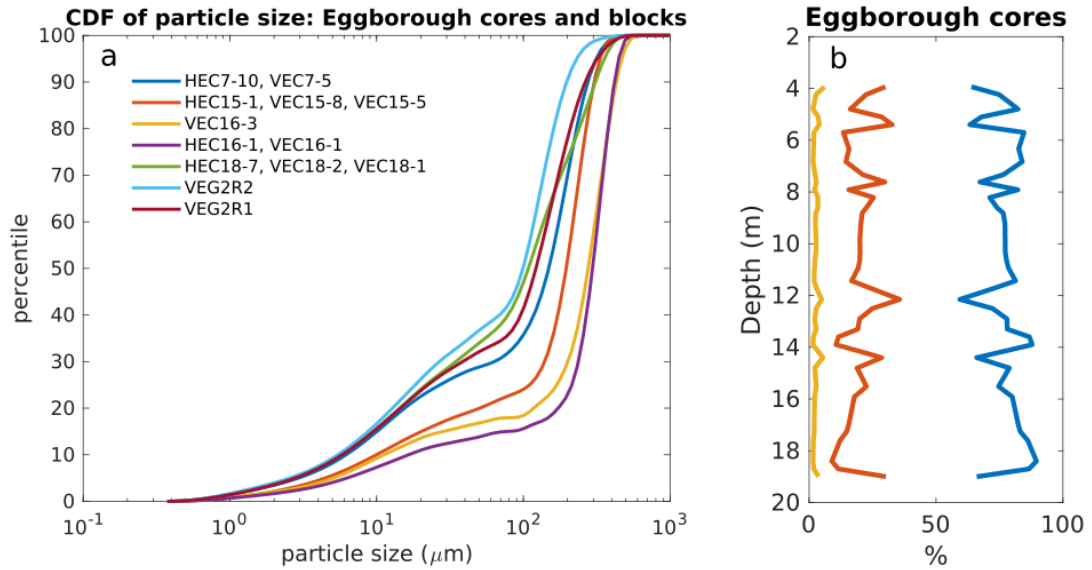


Figure 2 (a) Cumulative density functions of grain size distribution of Eggborough cores and blocks. The legend shows the core or block ID. (b) Depth profiles of sand (blue), silt (red), and clay (yellow) percentages for Eggborough cores.

2.2. Water Injection Simulation

The March 2003 tracer infiltration experiment at Hatfield (Binley, 2003; Winship et al., 2006) used a tracer that consisted of 1,200 L (or 1.2 m^3) of water, dosed with NaCl to give an σ_f of $2,200 \mu\text{S}/\text{cm}$ (groundwater σ_f was $650 \mu\text{S}/\text{cm}$). The tracer was injected over a period of 3 days, from 14 March 2003 to 17 March 2003 at a steady rate of 17 L/hr. The tracer injection port was screened between 3 and 3.5 m below ground surface. The water table was at 10 m below ground surface. The layout of the electrodes is shown in Figure 5.

Since our focus here is the change in moisture content, we numerically repeat the Hatfield 2003 injection experiment with groundwater instead of a conductive tracer. We used the parallel coupled hydrogeophysics code PFLOTRAN-E4D (Johnson et al., 2017) to simulate the flow and transport of the water injection and to obtain the corresponding ERT response. PFLOTRAN (Hammond et al., 2014) is a subsurface flow and reactive transport code, and we use the Richards model to simulate variably saturated flow. E4D (Johnson et al., 2010) is a 3-D modeling and inversion code designed for subsurface imaging and monitoring using static and time-lapse 3-D electrical resistivity or spectral induced polarization data, which we use here as a

forward ERT simulator. The PFLOTTRAN grid consists of 129,600 cells that are 0.25 to 1 m wide and 0.5 m thick. The E4D mesh is an unstructured tetrahedral mesh generated by tetgen (Si, 2015). The resultant mesh comprises 8,124 nodes and 46,842 elements. PFLOTTRAN-E4D interpolates and maps the PFLOTTRAN outputs to electrical resistivity on the E4D mesh given element-wise petrophysical transform. ERT snapshots are taken on Days 7, 9, 10, 15, 18, 21, 27, and 41. We assume a 2% measurement error in each of the 3,108 measurements taken in each frame. An additional 2.5% is added to the data errors in the inversions to account for forward modeling errors. The hydraulic conductivity field is assumed uniform and uses the values reported in Binley et al. (2002a). The parameters used in the simulation can be found in Table 1. The assumed petrophysical parameters are also plotted in Figure 4.

Parameters	Value	Parameters	Value
Initial water saturation	0.375	Water fluid conductivity	650 $\mu\text{S}/\text{cm}$
Injector depth interval	3-3.5 m	Assumed n	1.35
Water injection Rate	0.408 m^3/d	Assumed ρ_s (at 650 $\mu\text{S}/\text{cm}$)	44 $\Omega \text{ m}$
Injection period	Day 8-11	Assumed ERT data errors	4.5%
Hydraulic conductivity	0.4 m/d	van Genuchten α	10 m^{-1}
Porosity	0.32	van Genuchten n	2.5

Table 1 Parameters used for the water injection experiment.

2.3. Petrophysical models

2.3.1. Archie's Law

Assuming a minimal contribution from electrical conductivity on the grain surface, Archie's law relates bulk electrical resistivity ρ (1/conductivity) to fluid saturation S . It is given by

$$\rho = \sigma_f^{-1} \phi^{-m} S^{-n} \quad (1)$$

where m is the cementation factor, σ_f is the fluid conductivity, ϕ is the porosity, and n is the saturation exponent. Assuming constant material and fluid properties (e.g., m , n , and σ_f), Archie's law can be re-written in terms of the electrical resistivity at saturation (i.e., $S = 1$), which is given by

$$S = \left(\frac{\rho_s}{\rho} \right)^{\frac{1}{n}} \quad (2)$$

where $\rho_s = \sigma_f^{-1} \phi^{-m}$. To obtain best-fit estimates of Archie parameters, a straight line is fitted for $\log_{10}(S)$ and $\log_{10}(\rho_s)$ using the least-squares criterion. The fitting routine returns the covariance structure of the model estimates, which can be used to determine the 68% confidence interval (1 standard deviation) of the model estimates. Note that ρ_s corresponds to a particular σ_f . Therefore, it needs to be scaled when applied to a different σ_f using equation 1. We note that constant fluid conductivity may not be appropriate in a range of environments (e.g., Altdorff et al., 2017). Because the clay content in the cores is low, the results from fitting the Waxman–Smits model are not reported. Note that saturation and moisture content θ are related by $S = \theta/\phi$. The total amount of moisture Vw within a volume V is given by ϕVS .

The fractional change of θ , or equivalently that of S , is given by

$$\frac{\theta_t}{\theta_0} = \left(\frac{\rho_t \sigma_{f,t}}{\rho_0 \sigma_{f,0}} \right)^{-\frac{1}{n}} \quad (3)$$

where the subscripts t and 0 represent the variable at time t and at baseline.

2.4. ERT modelling and inversion

We use the code R3t version 1.8 (www.es.lancs.ac.uk/people/amb/Freeware/R3t/R3t.htm) for ERT inversion. To obtain the resistivity variation, we seek to find a model solution that minimizes the following objective function:

$$\Phi = \Phi_d + \Phi_m = (d - F(m))^T W_d^T W_d (d - F(m)) + \alpha m^T R m \quad (4)$$

where d is the data (e.g., measured apparent resistivities), $F(m)$ is the set of simulated data using the forward model and estimated parameters m . W_d is a data weight matrix, which, if we consider the case of uncorrelated measurement error and ignore forward model errors, is a diagonal matrix with entries equal to the reciprocal of the errors of each measurement. Forward modeling errors are also added to the diagonal of W_d . α

is the scalar regularization factor, while R is a roughness matrix that describes the spatial connectedness of the parameter cell values. α is selected via a line search, and isotropic smoothing is applied.

Using a Gauss–Newton procedure, the above is solved iteratively using the following solution:

$$(J^T W_d^T W_d J + \alpha W_m^T W_m) \Delta m = J^T W_d (d - F(m)) - \alpha R m_k \quad (5)$$

$$m_{k+1} = m_k + \Delta m$$

where J is the Jacobian (or sensitivity) matrix, given by $J_{i,j} = \partial d_i / \partial m_j$; m_k is the parameter set at iteration k ; and Δm is the parameter update at iteration k . For the DC resistivity case, the inverse problem is typically parameterized using log-transformed resistivities.

For analysis of time-lapse ERT, we follow the difference inversion approach (Labrecque and Yang, 2001) to invert on the change in ERT data. Its model penalty function seeks to minimize model variation relative to a reference mode m_{ref} :

$$\Phi_m = \alpha (m - m_{ref})^T R (m - m_{ref}) \quad (6)$$

Again, using a Gauss-Newton procedure, the objective function can be solved iteratively by:

$$(J^T W_m^T W_m J + \alpha R) \Delta m = J^T W_d \left([(d - d_{ref}) - (F(m) - F(m_{ref}))] \right) - \alpha R (m - m_{ref})$$

$$m_{k+1} = m_k + \Delta m \quad (7)$$

where d_{ref} is the baseline data vector. This approach, which has been proven to be effective in removing the effect of systematic errors (e.g., artifacts), has been applied to numerous time-lapse imaging studies (Doetsch et al., 2012b; LaBrecque et al., 2004). Note that the same mesh is used for both ERT forward modeling and inversion.

2.5. Uncertainty propagation and moisture content estimation

After inverting the electrical resistivity models, we can obtain the corresponding element-wise moisture content using the petrophysical relationships.

The quantity of water within a certain volume is given by the spatial integral of the moisture content within the volume.

Rules of analytical uncertainty propagation (Chen and Fang, 1986; Taylor, 1982) were followed to propagate petrophysical uncertainty to moisture content estimates at each element. The uncertainty of saturation estimated from Archie's law is given by the following equation (see Appendix A for details):

$$\sigma_S^2 = \left(\frac{\partial S}{\partial \rho}\right)^2 \sigma_\rho^2 + \left(\frac{\partial S}{\partial \rho_s}\right)^2 \sigma_{\rho_s}^2 + \left(\frac{\partial S}{\partial n}\right)^2 \sigma_n^2 \quad (8)$$

where σ^2 is the variance of parameters. $\sigma_{\rho_s}^2$ and σ_n^2 are determined by the parameter fitting procedures. σ_ρ^2 are determined by running Monte Carlo simulations of ERT inversion (Aster et al., 2005; Tso et al., 2017). This procedure, in essence, samples the measurement errors based on the prescribed error levels and obtains a distribution of inverted resistivity at each cell due to the perturbed measurements. The first term in the above equation can be viewed as the variance contribution from the variance of ERT inversion, while the other terms are the contributions from the uncertainty in the petrophysical fits. When evaluating the difference in saturation between two survey times, it is important to take account of the fact that their uncertainties may be correlated. Therefore, the variance of the difference in saturation ΔS is given by

$$\sigma_{\Delta S} = \sqrt{\sigma_S^2 + \sigma_{S_0}^2 - 2\text{cov}(S, S_0)} \quad (9)$$

where S_0 is saturation at baseline and $\text{cov}(S, S_0)$ is approximated by all the S values in the model domain at the two times. The variance of saturation can be converted to that of the total amount of water (V_w) within a volume by

$$\sigma_{V_w}^2 = \left(\frac{\partial V_w}{\partial \phi}\right)^2 \sigma_\phi^2 + \left(\frac{\partial V_w}{\partial S}\right)^2 \sigma_S^2 = (VS)^2 \sigma_\phi^2 + (V\phi)^2 \sigma_S^2 \quad (10)$$

If porosity ϕ is assumed to be known and constant, the first term is dropped. For a finite element domain consisting of many elements, the total variance is simply the sum of variances of all the elements.

3) Results

3.1. Fitting Archie models

Figure 3 shows the water saturation–electrical resistivity relationship of 12 of the Eggborough cores and blocks. Note that some sample exhibits rather large scatter, and in a few occasions, the resistivity shows a decrease with decreasing saturation. Archie's law is fitted on the data. The best-fit line and the corresponding ± 1 standard deviation envelope are also plotted. Both ρ_s (27.45–64.35 Ω m) and n (0.513–2.174) show significant variability. As observed in Table S1, the variability in Archie parameters does not tend to correlate with texture-related properties. In most previous studies literature-based estimates of Archie parameters are adopted, and where laboratory analysis is carried out, only a few samples are used. The significant variability (within the same unit) and lack of correlation with other properties presented here illustrate the challenge of constraining Archie parameters in the field. Our data show two distinct groups of clay contents ($\sim 2\%$ and $\sim 3.5\%$), and the corresponding Archie parameters show slightly different ranges. Figure 3 also shows the Archie's parameter estimation of all Eggborough cores and blocks. The predictions using the best estimate of the parameters are shown in solid lines, while the 68% (i.e., ± 1 standard deviation) confidence intervals are shown in dashed lines. It shows that when fitting all of the cores and blocks together, the resultant standard deviation is low, leaving some data points outside the ± 1 standard deviation envelope. We have also included the fit for Hatfield cores reported in [Binley et al. \(2002b\)](#) and summarize all the Archie models in Figure 4. Further details, including hydraulic and surface area measurements, of the Eggborough cores and blocks can be found in Table S2.

Results

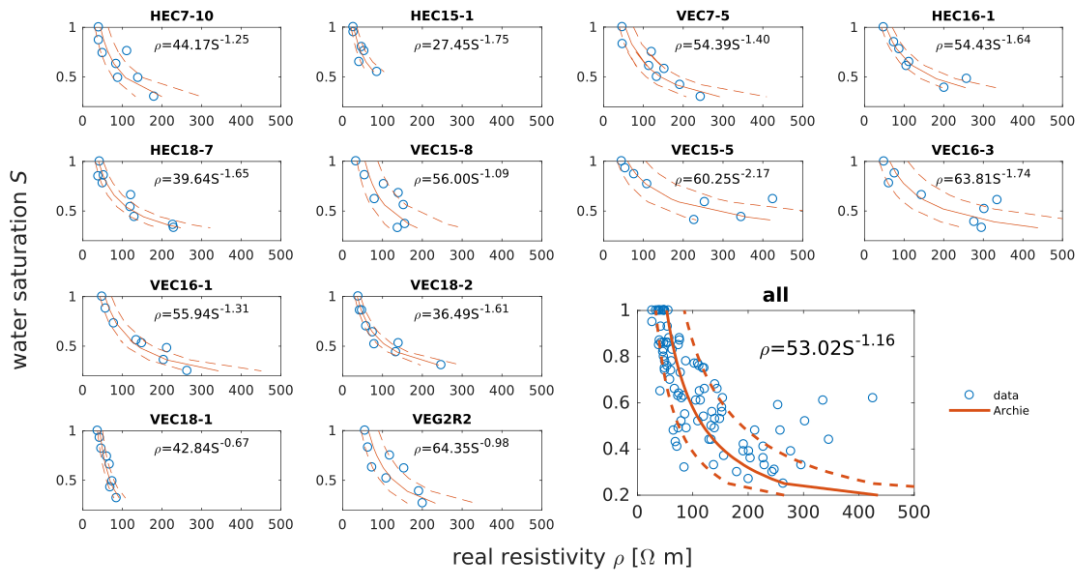


Figure 3 Archie's parameter estimation of individual Eggborough cores and blocks. The predictions using the best estimate of the parameters are shown in solid lines, while the 68% (i.e., ± 1 standard deviation) confidence intervals are shown in dashed lines. Note that the measurements are made at $\sigma_f = 1000 \mu\text{S cm}^{-1}$. Note that ρ , which is the dependent variable, is shown on the x-axis.

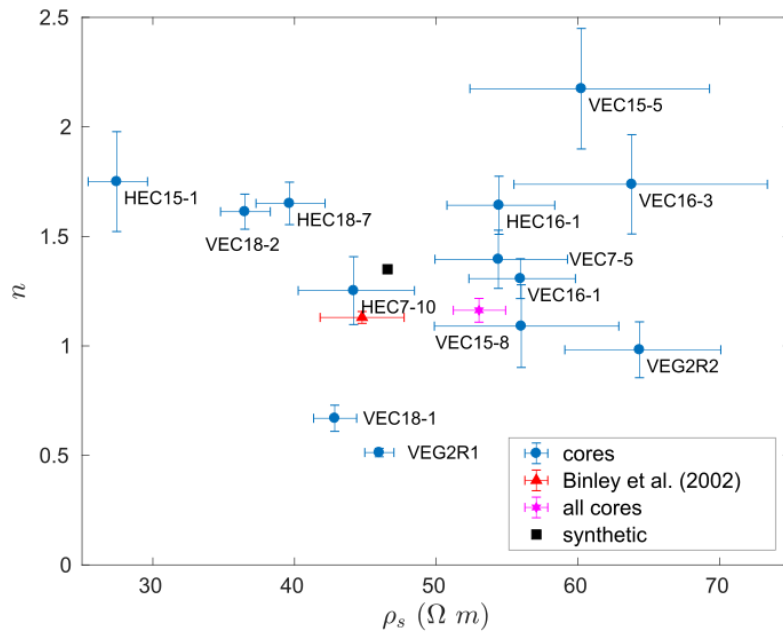


Figure 4 Summary of Archie model fits for the Eggborough/Hatfield cores and blocks. Note that values correspond to $\sigma_f = 1000 \mu\text{S cm}^{-1}$. The point label "synthetic" is the "true" solution considered in the synthetic study in section 3.2.

3.2. Moisture content estimation for the water injection simulation

The time-lapse ERT monitoring data during the water injection simulation was inverted using a difference inversion as described above. The iso-surfaces in Figure S1 show a volume that has 5.5% reduction of resistivity relative to baseline (Day 7). The inversion results capture the geometry and the swell-shrink dynamics of the plume very well. The plume expanded gradually once the injection commenced and then migrated downward within a few days after the injection finished.

Our subsequent results focus on an ERT snapshot 10 days after the injection (Day 18). Figures 5a and 5b show the resultant mean and standard deviation of electrical resistivities obtained from Monte Carlo runs of ERT inversion. Since we have assumed uniform initial saturation, the variation of resistivity is within the same order of magnitude. The center region of the ERT array shows reduced resistivity due to injection. The standard deviation is higher around the electrodes and is lower in the center region because the resolution of ERT decreases away from electrodes. Conceptually, however, the uncertainty in the center region through which the water plume evolves should be higher. This issue is not addressed in this study. Based on the Monte Carlo inversion results, Figure 5c shows the volume extracted from the ERT inversion domain where there is at least a 5.5% reduction in resistivity on Day 18 relative to the pre-injection baseline (Day 7). Such a threshold is used so that the effects of inversion artifacts are minimized. The size of this volume is 79.97 m³. The total amount of water in this volume at Days 7 and 18 are 9.65 and 10.68 m³, respectively. The resistivities on the nodes of the extracted volume were converted to saturation using the different petrophysical relationships (i.e., Archie model fits) discussed above, while a Monte Carlo experiment was run to estimate the uncertainty in the inverted resistivities.

Results

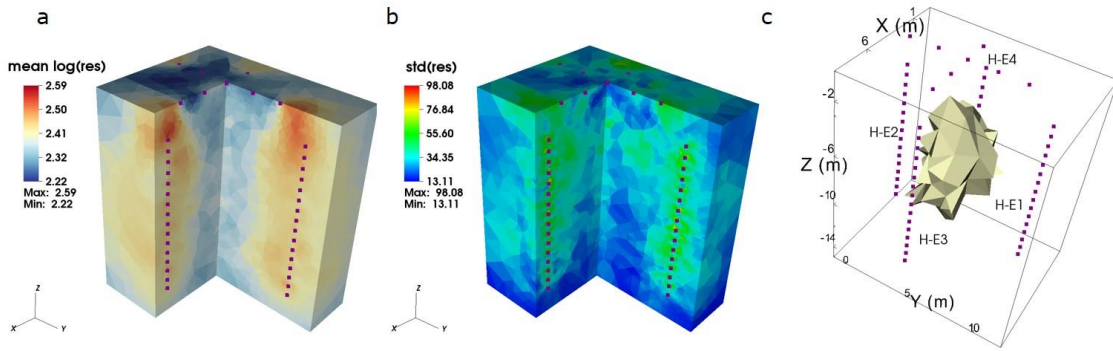


Figure 5 (a) Mean (\log_{10}) and (b) standard deviation (linear) of electrical resistivity for Day 18 obtained from Monte Carlo runs of electrical resistivity tomography inversion. (c) Extracted volume where there was a 5.5% reduction of resistivity relative to baseline on Day 18. The purple cubes are electrode locations.

For each of the petrophysical models, we then integrate the moisture contents over the extracted volume to estimate the total water volume (V_w) in it. At the same time, we derive error bars for the total water volume estimates using equations 8 and 9. Figure 6a shows the mean and uncertainty bounds for the amount of water within the extracted volume, assuming a constant porosity of 0.32. For Day 18 (post-injection), best estimates of total water volume among Archie models lie between 8.70 m^3 (Binley02) and 16.74 m^3 (VEC15-5), except for VEG2R1 and VEC18-1 that lie at 2.51 and 3.88 m^3 , respectively. The size of the error bars varies between $\pm 0.68 \text{ m}^3$ (VEG2R1) and $\pm 2.28 \text{ m}^3$ (VEG15-8), or between 9.59% (VEC18-2) and 27.01% (VEG2R1), depending on the Archie parameters estimates and their uncertainties. We observe similar results for Day 7 (pre-injection), yet we note that while the size of the error bars generally increases from Day 7 to Day 18, the increase ranges from 0.19 m^3 (HEC15-1) to 0.72 m^3 (“all”).

Results

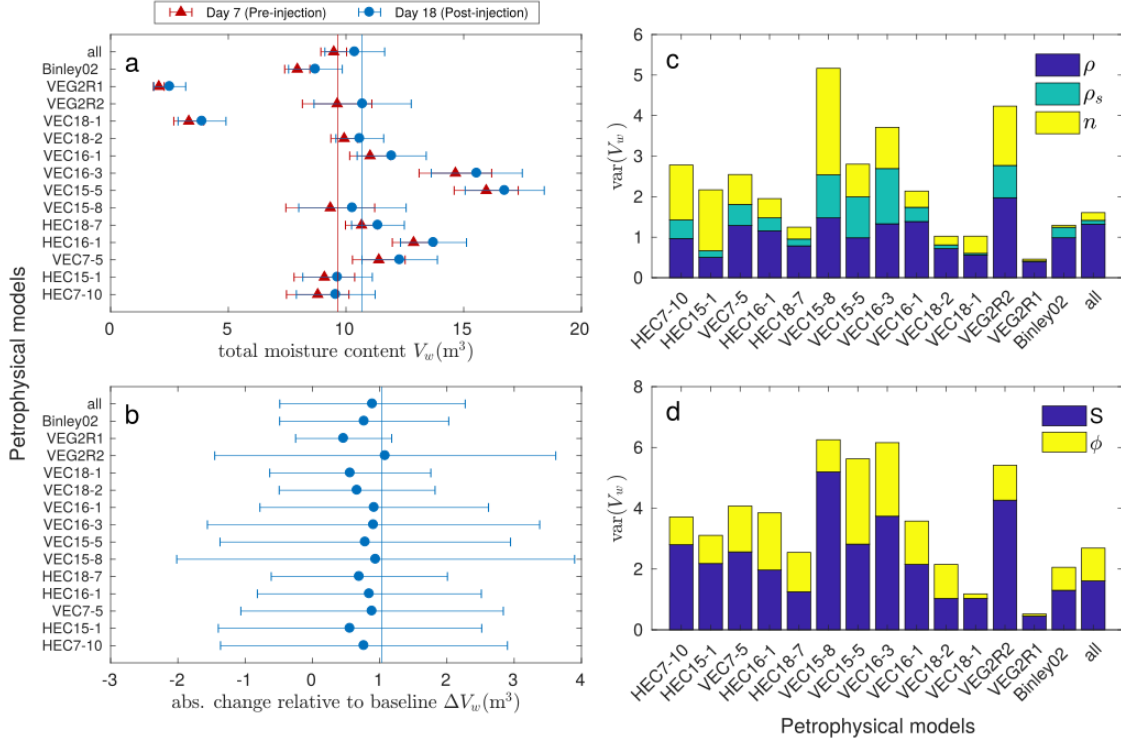


Figure 6 (a) Total water volume within the extracted volume (with uncertainty bounds) using the different petrophysical models. The uncertainty bounds correspond to ± 1 standard deviation. The vertical lines show the true total water volume. (b) The corresponding changes in the amount of moisture within the extracted volume relative to baseline. The vertical lines show the true change in total water volume. (c) The contribution of different variables to the variance of total moisture of each petrophysical models. (d) Additional variance (i.e., uncertainty) caused by uncertain porosity values (0.32 ± 0.032). The contribution from uncertain porosity is significant in most cases, especially when the variance in saturation is low.

Figure 6b shows the *change* in total water volume on Day 18 relative to baseline. The mean *change* is the difference between the total water volume at the two times. Using equation 10, the error bars shown here have accounted for potential correlation between total water volume estimates between the two times. As a result, when fluid conductivity is assumed constant, the uncertainty bounds for the change in total moisture would lie between one and two times of that of the total moisture. The Archie models estimate an increase in mean *change* in total water volume of 0.46 m^3 (VEG2R1) to 1.08 m^3 (VEG2R2). They are more consistent than the estimates of the absolute total water volume. Note that the total injection volume was 1.224 m^3 , meaning all the models have underestimated the addition of water due to injection. The uncertainty

bounds in Figure 6b are generally large, ranging from $\pm 0.71 \text{ m}^3$ (VEG2R1) to $\pm 2.96 \text{ m}^3$ (VEC15-8), or 154% (VEG2R1) to 350% (HEC15-1) of the mean value. This shows that even though the mean estimates for the change in total water volume using Archie models is consistent, they are nevertheless highly uncertain.

The size of the error bars in Figure 6a is determined by a combination of the uncertainty of the petrophysical parameters (ρ_s and n) and that of the inverted resistivities ρ . Based on equations 8 and 9, the variance of the total moisture estimates is the summation of the squared product of the partial derivative and standard deviation of the individual terms. We plot the terms as stacked bars for Day 18 (post-injection) in Figure 6c to show their contribution to the total variance. The square root of the total height of the bars equals the size of the error bars in Figure 6a. The contribution from inverted resistivities ρ is below $2 (\text{m}^3)^2$ for all the Archie models. For the Archie models with variance smaller than $2 (\text{m}^3)^2$, inverted resistivities can be an important source of errors; otherwise, the effects of uncertain petrophysical parameters dominate. Our results indicate that for the Archie models, n plays a more important role than ρ_s , with the exception of Binley02, which shows very low n error. n contributes 3.88% (VEG2R1) to 69.25% (HEC15-1) of the total variance, while ρ_s contributes 2.55% (VEG2R1) to 36.71% (VEC16-3) of the total variance.

So far we have assumed the porosity has a constant value of 0.32. Additional uncertainty is introduced if it is treated as uncertain. We consider the case where porosity is assumed to be 0.32 ± 0.032 . In Figure 6d, the height of the blue bars is the total height of the bars in Figure 6c. The height of the yellow bars shows the additional variance due to the uncertain porosity value, which ranges from $0.0631 (\text{m}^3)^2$ (VEG2R1) to $2.8026 (\text{m}^3)^2$ (VEC15-5). Percentage-wise, the uncertain porosity values lead to an increase in variance ranging from 13.7% (VEG2R1) to 108% (VEC18-2).

We have examined in Figure 6b the change in total moisture within the extracted volume. We examine in Figure 7 the change in volume of water within each finite element cell of the extracted volume. Figure 7a shows the estimated change in the volume of water (V_w) in four selected cells. It is observed that while the true change spans from 0 to 0.18 m^3 , the estimates for Archie models stay within the 0 to 0.05 m^3

range. Figure 7b shows the scatter plots for the ERT-estimated V_w using the 15 Archie models. For all of them, the fit at individual cells is unsatisfactory. Conversely, in Figure 6b the changes in total moisture within the extracted volume are fairly consistent across the petrophysical models, and they agree with the true value. We observe that within the extracted volume (the threshold was change in inverted resistivity greater than 5.5%), 101 of 219 cells show change in saturation of less than 0.01. This indicates the true water plume is much narrower than estimated by ERT inversion and highlights the detection limit of ERT, particularly in the context of smoothness-constrained inversion used here. The smoothing effect of the ERT inversion, however, roughly preserves mass balance in this case.

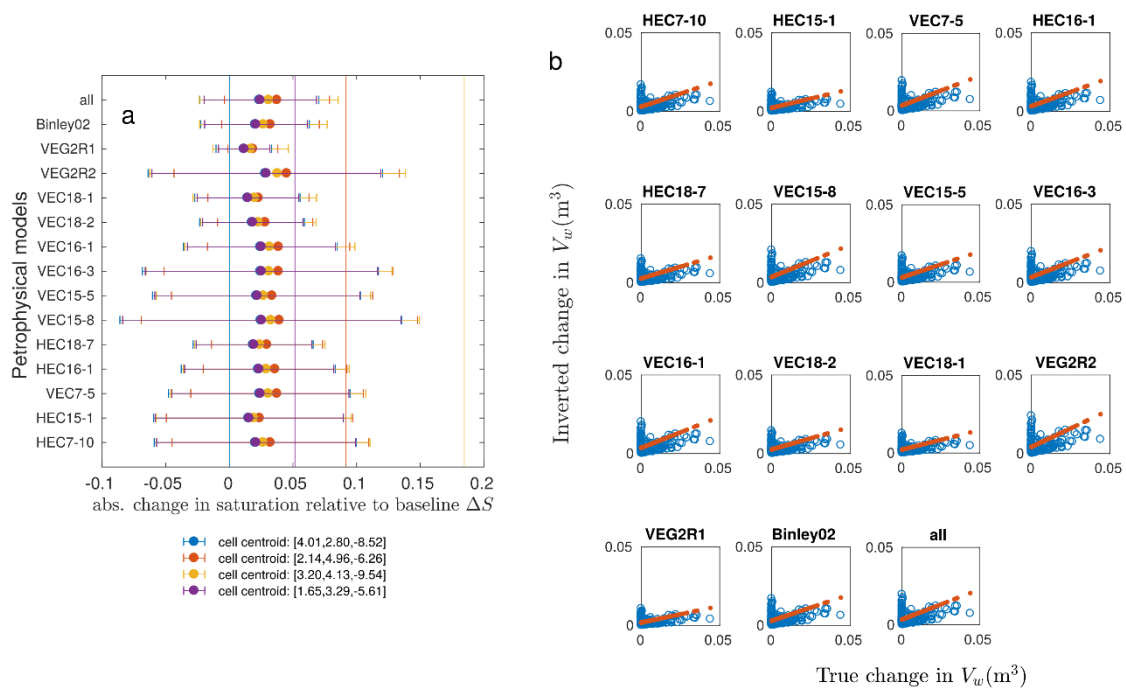


Figure 7 (a) Electrical resistivity tomography estimated changes in volume of water in four selected cells. The vertical lines indicate the true change. (b) Scatter plots showing the fit for change in volume of water at individual cells using the 15 Archie models. The red dashed line in each plot is the best-fit line of the scatter points.

4) Discussion and implications for future research

4.1. Fitting petrophysical models

Most previous studies have either fitted petrophysical models for up to a few cores or used petrophysical parameters based on literature values without assuming any errors or uncertainty. Our results from cores collected at a relatively uniform and clay-free sandstone unit suggest that in future studies, a wider range of petrophysical relationships or a larger uncertainty bound should be assumed. The n and ρ_s estimates do not appear to show significant correlation with other properties that were measured, making it difficult to constrain petrophysical relationships with more core samples. In fact, compared with previous studies at Hatfield and Eggborough, the use of more core data reveals greater petrophysical model uncertainty. The individual Archie model fits are good, but the concatenated data set shows a U-shaped $\theta(\rho)$ behavior, which suggests saturation is controlled by properties other than a saturation exponent or it implies a heterogeneous petrophysical parameter field.

4.2. The uncertainty propagation approach

We have proposed and demonstrated an effective procedure to propagate uncertainties in petrophysical relationships to uncertainties in the inferred moisture contents and the amount of water within the plume. The procedure requires mean and standard deviation of both the petrophysical parameters and the inverted resistivities. The application of this method on field data using two types of petrophysical models shows how uncertainty in petrophysical parameters and ERT data errors propagate through the modeling and inversion process and lead to uncertainty in moisture content estimates. Specifically, the inversion procedure smooths the resistivity profiles (a proxy of moisture content) spatially, while the uncertain petrophysical relationships add uncertainties to the quantitative conversion from resistivity to moisture content. These uncertainties, if untracked, can lead to significant bias and over-confidence in the moisture content estimates.

Part of our analysis has utilized a commonly employed smoothness-based inversion for our geophysical data to evaluate the impact of uncertain petrophysical

relationship. Other inversion algorithms may yield different uncertainty estimates. In fact, a limitation of this work is that our computation of the uncertainty contribution from inverted resistivity only considered the propagation of data errors through the inversion code. We have assumed no uncertainty contribution from the choice of the inverse model, its resolution, or its discretization, mainly because there is no standard procedure to compute the uncertainty of an inverted resistivity field yet. Some emerging techniques, such as trans-dimensional ERT (Galetti and Curtis, 2018), are attempts to address this issue. We also acknowledge Markov chain Monte Carlo sampling (Brunetti and Linde, 2018) may be more accurate and robust than the conventional MC sampling we use here.

Finally, we note that our approach follows the classical approach to error analysis (Taylor, 1982). The extent to which some of the underlying assumptions are valid, such as whether the uncertainties of petrophysical parameters and inverted resistivities are independent, is open to future investigation. Nevertheless, we highlight that the uncertainty propagation framework presented in this work is flexible and straightforward. It is potentially applicable to any type of petrophysical models and inversion methods, and it may be extended to consider the uncertainty of the inversion itself. It is independent of the inversion methods and petrophysical models used, and we expect it to be used widely in future studies.

4.3. Total moisture content estimation

The great variety of petrophysical models lead to a large range of total water volume estimates (Figure 6a). This shows that using only a single petrophysical model deterministically can give misleading results. It also shows that any applications wishing to quantify the absolute amount of moisture present must not rely on geophysics alone. The changes in moisture content estimated by Archie's law, however, are generally consistent (Figure 6b). This can be explained by the work of Lehmann et al. (2013), who show that the fractional changes in moisture content obtained from electrical resistivity are a scaling of the saturation exponent only. This means the other parameters in simple empirical models do not play a role in converting ratios of inverted resistivities to ratios of θ . Nevertheless, most applications are interested in at

least the difference of moisture content between two times, not just their relative change. We note the high uncertainty bounds associated with the change in θ obtained from most of the Archie petrophysical models. This shows that this scaling of n can lead to highly uncertain estimates of the amount of the change. This effect should be acknowledged and assumed when interpreting ERT-derived moisture contents. Moreover, other parameters in petrophysical models are still important in other frequently used methods. For example, coupled modeling of hydrogeophysics requires reliable petrophysical relationships. Examining the impact of the different uncertain petrophysical parameters and models remains an important research question.

Our uncertainty analysis shows that for most cases, the uncertainty in ERT-derived saturation is dominated by uncertain petrophysical parameters, not uncertain inverted resistivities due to data errors (Figure 6c). This presents a challenge because unlike inverted resistivities, petrophysical uncertainties cannot be straightforwardly reduced by good quality data or better inverse modeling approaches. Future studies should focus their efforts on better characterizing petrophysical uncertainties and incorporating them in moisture content estimation procedures. Figure 6d also shows that significant additional uncertainty can be caused by uncertain porosity values. Since porosity ultimately controls the volume of pore space for water to fill, better characterization of it can reduce the uncertainty of the moisture content estimates from ERT.

Our work has focused on a water injection experiment where there is no variation in fluid conductivity over time. Changes in fluid conductivity (e.g., in a saline tracer injection or leak of saline solute) will further complicate the estimation of moisture content changes since bulk resistivity is affected by both fluid conductivity and moisture content. When inverting time-lapse ERT data, the change relative to baseline is often set to be minimized. This setting works well in our water injection experiment but may give an insufficient change in resistivity to account for both changes in saturation and fluid conductivity.

Since laboratory petrophysical measurements are labor-intensive and time-consuming, many authors have used TDR data (in shallow vadose zone investigations) to fit field-based petrophysical relationships (e.g. Fan et al., 2015). The typical setup, for shallow investigations, consists of a trench with ERT, TDR, and temperature sensors installed. This *in situ* setup can be viewed as advantageous over lab measurements since it correctly represents pore water conductivity (given dynamic exchange of ions between particles and pore water) and avoids forced conditions in the lab. Despite its advantages, the range of ρ it considers is limited because only the range of the ERT-measured apparent ρ are evaluated. Given the large variability of petrophysical relationships observed in this study, perhaps the TDR data are best used to independently verify or constrain the inverted moisture contents (e.g. Beff et al., 2013). It is important to check independently whether the uncertainty bounds of ERT-predicted moisture content consistently capture the TDR data. While TDR or neutron probe can only be applied in shallow soil, radar can be used in deeper investigations. The joint use of ERT and radar measurements (e.g. Binley et al., 2002a; Linde et al., 2006) yields independent estimates of moisture contents and allows cross-validation.

We have examined the changes in total moisture content in the extracted volume and at selected locations obtained from ERT and their agreement with the simulation. Future uncertainty studies should consider the agreement by comparing ERT estimates and other (e.g., TDR and neutron probe) data in the field. Further work should also examine the extent to which the uncertainty in ERT-derived moisture content affects the decision making in specific applications, such as landslide monitoring or precision agriculture.

4.4. Strategy when petrophysical data is unavailable

With the increasing popularity of ERT or EMI studies for hydrological investigations, there will be an increasing number of studies that do not collect samples for petrophysical calibration, which is often more time-consuming than the geophysical survey itself. Conversely, a few depth profiles of grain size distributions are relatively easy to obtain (e.g., using a hand auger) in near-surface applications. Soil texture is commonly used to approximate unsaturated zone parameters through

pedotransfer functions (e.g., ROSETTA: Schaap et al., 2001; Zhang et al., 2016), and it will be useful if these functions can approximate the petrophysical parameters or models too. Future efforts should be devoted to building a global database on $\theta(\rho)$ and grain size distribution data, in order to formulate pedotransfer functions across sites. Data-driven methods such as multiple adaptive regression splines (Brillante et al., 2014) are particularly suitable for this task because they are capable of handling fairly large datasets (e.g., 105 observations and 100 variables). We attempted to apply some of these methods to fit the Eggborough data (not reported here), but we have too few samples to apply them reliably. Nevertheless, they are potentially powerful methods to apply in the future once there is a database for near-surface petrophysical measurements.

4.5. Relevance to EMI and other geophysical methods

We have focused mainly on the effect on ERT inversion results, but similar conclusions can be extended for EMI results or methods that use a combination of EMI and ERT results (von Hebel et al., 2014), as well as other applications in hydrogeophysics where petrophysical transforms are involved. Moreover, we recognize that there is a wealth of literature studying the spatial and temporal patterns of electrical conductivity and soil moisture in the Earth's near-surface. Similarly, there have been many recent studies on data assimilation of moisture content data across multiple spatial scales (e.g. Zhu et al., 2017). Hydrogeophysicists, while frequently working at the plot-scale and site-scale, should be involved in these developments. Closer collaboration between soil scientists, geostatisticians, geophysicists, and hydrologists are needed to tackle this grand challenge.

5) Conclusion

Our study showed the extent of petrophysical variability present at a field site and demonstrated an approach to computing uncertainty bounds of moisture content estimates due to uncertain petrophysical models. First, we showed that highly variable petrophysical relationships can be observed in field samples of a relatively uniform and clay-free sandstone unit. We then fitted and applied various petrophysical models

to convert ERT images to moisture content images. The different petrophysical models led to a wide range of total moisture content estimates of a plume, but their *changes* over time generally agreed. Using rules of error propagation, we were able to quantify the uncertainty bounds of the moisture content estimates and gained further insight by showing the individual contribution of the petrophysical parameters and inverted resistivities terms to the total uncertainty. We showed that, assuming the inverse model only smooths the resistivity field, the uncertainty is dominated by the petrophysical parameters. The total uncertainty was found to be 7.52–23.18% of the mean total water volume estimate. When translated to the *change* in time, the uncertainty can be as high as several multiples of the mean estimate—both uncertainties are higher than previously appreciated.

Our results have highlighted the potential danger of converting ERT images to moisture content from similar environments using a single petrophysical model deterministically. In particular, they should not be used to quantify the amount of moisture present independently of other data. Although the different Archie petrophysical models give consistent estimates of the change in total water volume, their relatively large uncertainty bounds highlight that even though electrical geophysics reliably determines the direction of the change in θ , its quantification of the amount of such change is highly uncertain. It is prudent to assume large uncertainties for θ and $\Delta\theta$ estimates where they have not been quantified. Data-driven methods (e.g., multiple adaptive regression splines) have the potential to be applied to build petrophysical models where such data are unavailable.

6) Acknowledgements

This paper is published with the permission of the Executive Director of the British Geological Survey (NERC) and UK Nuclear Decommissioning Authority (NDA). The first author is supported by a Lancaster University Faculty of Science and Technology PhD studentship and an NDA PhD Bursary. Peter Winship (deceased) and Melanie Fukes conducted the field experiments and the laboratory analysis, respectively. We thank Jared West (Leeds University) for supplying the Hatfield core analysis. We thank

Tim Johnson (Pacific Northwest National Laboratory) for assistance in using PFLOTRAN-E4D, access to the PNNL computing facilities, and hosting the first author's visits. We thank Keith Beven for commenting on an initial version of the manuscript. We are grateful to associate editor Sander Huisman, Sarah Garré, and an anonymous reviewer for their constructive comments. The data used in this paper are deposited at the Lancaster University's research data repository and is available for download (<https://dx.doi.org/10.17635/lancaster/researchdata/293>).

References

- Ahmed, M.A., Passioura, J., Carminati, A., 2018. Hydraulic processes in roots and the rhizosphere pertinent to increasing yield of water-limited grain crops: a critical review. *J. Exp. Bot.* 69, 3255–3265. <https://doi.org/10.1093/jxb/ery183>
- Altdorff, D., von Hebel, C., Borchard, N., van der Kruk, J., Bogena, H.R., Vereecken, H., Huisman, J.A., 2017. Potential of catchment-wide soil water content prediction using electromagnetic induction in a forest ecosystem. *Environ. Earth Sci.* 76, 111. <https://doi.org/10.1007/s12665-016-6361-3>
- Amidu, S.A., Dunbar, J.A., 2007. Geoelectric Studies of Seasonal Wetting and Drying of a Texas Vertisol. *Vadose Zo. J.* 6, 511. <https://doi.org/10.2136/vzj2007.0005>
- Aster, R., Borchers, B., Thurber, C.H., 2005. *Parameter estimation and inverse problems.* Elsevier, Burlington, Massachusetts, USA.
- Bass, B., Cardenas, M.B., Befus, K.M., 2017. Seasonal Shifts in Soil Moisture throughout a Semiarid Hillslope Ecotone during Drought: A Geoelectrical View. *Vadose Zo. J.* 0, 0. <https://doi.org/10.2136/vzj2016.11.0108>
- Beff, L., Günther, T., Vandoorne, B., Couvreur, V., Javaux, M., 2013. Three-dimensional monitoring of soil water content in a maize field using Electrical Resistivity Tomography. *Hydrol. Earth Syst. Sci.* 17, 595–609. <https://doi.org/10.5194/hess-17-595-2013>
- Binley, A., 2003. *Vadose Zone Tracer Testing in the UK Sherwood Sandstone: Hydrogeophysical Data Report.* Livermore, California.
- Binley, A., Beven, K., 2003. Vadose zone flow model uncertainty as conditioned on geophysical data. *Groundwater* 41, 119–127.

References

- Binley, A., Cassiani, G., Middleton, R., Winship, P., 2002a. Vadose zone flow model parameterisation using cross-borehole radar and resistivity imaging. *J. Hydrol.* 267, 147–159. [https://doi.org/10.1016/S0022-1694\(02\)00146-4](https://doi.org/10.1016/S0022-1694(02)00146-4)
- Binley, A., Cassiani, G., Winship, P., 2004. Characterization of heterogeneity in unsaturated sandstone using borehole logs and cross-borehole tomography, in: *Aquifer Characterization*, in: *Aquifer Characterization*. SEPM (Society for Sedimentary Geology), pp. 129–138. <https://doi.org/10.2110/pec.04.80.0129>
- Binley, A., Hubbard, S.S., Huisman, J.A., Revil, A., Robinson, D.A., Singha, K., Slater, L.D., 2015. The emergence of hydrogeophysics for improved understanding of subsurface processes over multiple scales. *Water Resour. Res.* 51, 3837–3866. <https://doi.org/10.1002/2015WR017016>
- Binley, A., Slater, L.D., Fukes, M., Cassiani, G., 2005. Relationship between spectral induced polarization and hydraulic properties of saturated and unsaturated sandstone. *Water Resour. Res.* 41, W12417. <https://doi.org/10.1029/2005WR004202>
- Binley, A., Winship, P., Middleton, R., Pokar, M., West, J., 2001. High-resolution characterization of vadose zone dynamics using cross-borehole radar. *Water Resour. Res.* 37, 2639–2652. <https://doi.org/10.1029/2000WR000089>
- Binley, A., Winship, P., West, L.J., Pokar, M., Middleton, R., 2002b. Seasonal variation of moisture content in unsaturated sandstone inferred from borehole radar and resistivity profiles. *J. Hydrol.* 267, 160–172. [https://doi.org/10.1016/S0022-1694\(02\)00147-6](https://doi.org/10.1016/S0022-1694(02)00147-6)
- Bouchedda, A., Chouteau, M., Binley, A., Giroux, B., 2012. 2-D joint structural inversion of cross-hole electrical resistance and ground penetrating radar data. *J. Appl. Geophys.* 78, 52–67. <https://doi.org/10.1016/j.jappgeo.2011.10.009>
- Brillante, L., Bois, B., Mathieu, O., Bichet, V., Michot, D., Lévêque, J., 2014. Monitoring soil volume wetness in heterogeneous soils by electrical resistivity. A field-based pedotransfer function. *J. Hydrol.* 516, 56–66. <https://doi.org/10.1016/j.jhydrol.2014.01.052>
- Brillante, L., Mathieu, O., Bois, B., Van Leeuwen, C., Lévêque, J., 2015. The use of soil electrical resistivity to monitor plant and soil water relationships in vineyards. *Soil* 1, 273–286. <https://doi.org/10.5194/soil-1-273-2015>
- Brunet, P., Clément, R., Bouvier, C., 2010. Monitoring soil water content and deficit using Electrical Resistivity Tomography (ERT) - A case study in the Cevennes area, France. *J. Hydrol.* 380, 146–153. <https://doi.org/10.1016/j.jhydrol.2009.10.032>

References

- Brunetti, C., Linde, N., 2018. Impact of petrophysical uncertainty on Bayesian hydrogeophysical inversion and model selection. *Adv. Water Resour.* 111, 346–359. <https://doi.org/10.1016/j.advwatres.2017.11.028>
- Cassiani, G., Binley, A., 2005. Modeling unsaturated flow in a layered formation under quasi-steady state conditions using geophysical data constraints. *Adv. Water Resour.* 28, 467–477. <https://doi.org/10.1016/j.advwatres.2004.12.007>
- Cassiani, G., Godio, A., Stocco, S., Villa, A., Deiana, R., Frattini, P., Rossi, M., 2009. Monitoring the hydrologic behaviour of a mountain slope via time-lapse electrical resistivity tomography. *Near Surf. Geophys.* 7, 475–486. <https://doi.org/10.3997/1873-0604.2009013>
- Chambers, J.E., Wilkinson, P.B., Uhlemann, S., Sorensen, J.P.R., Roberts, C., Newell, A.J., Ward, W.O.C., Binley, A., Williams, P.J., Gooddy, D.C., Old, G., Bai, L., 2014. Derivation of lowland riparian wetland deposit architecture using geophysical image analysis and interface detection. *Water Resour. Res.* 50, 5886–5905. <https://doi.org/10.1002/2014WR015643>
- Chen, H.C., Fang, J.H., 1986. Sensitivity analysis of the parameters in Archie's water saturation equation. *Log Anal.* 27, 39–44. <https://doi.org/SPWLA-1986-vXXVIIIn5a3>
- Doetsch, J., Linde, N., Vogt, T., Binley, A., Green, A.G., 2012. Imaging and quantifying salt-tracer transport in a riparian groundwater system by means of 3D ERT monitoring. *Geophysics* 77, B207. <https://doi.org/10.1190/geo2012-0046.1>
- Fan, J., Scheuermann, A., Guyot, A., Baumgartl, T., Lockington, D.A., 2015. Quantifying spatiotemporal dynamics of root-zone soil water in a mixed forest on subtropical coastal sand dune using surface ERT and spatial TDR. *J. Hydrol.* 523, 475–488. <https://doi.org/10.1016/j.jhydrol.2015.01.064>
- Friedman, S.P., 2005. Soil properties influencing apparent electrical conductivity: a review. *Comput. Electron. Agric.* 46, 45–70. <https://doi.org/10.1016/j.compag.2004.11.001>
- Galetti, E., Curtis, A., 2018. Transdimensional Electrical Resistivity Tomography. *J. Geophys. Res. Solid Earth.* <https://doi.org/10.1029/2017JB015418>
- Garré, S., Coteur, I., Wongleecharoen, C., Kongkaew, T., Diels, J., Vanderborght, J., 2013. Noninvasive Monitoring of Soil Water Dynamics in Mixed Cropping Systems: A Case Study in Ratchaburi Province, Thailand. *Vadose Zo. J.* 12, 0. <https://doi.org/10.2136/vzj2012.0129>

References

- Garré, S., Javaux, M., Vanderborght, J., Pagès, L., Vereecken, H., 2011. Three-Dimensional Electrical Resistivity Tomography to Monitor Root Zone Water Dynamics. *Vadose Zo. J.* 10, 412. <https://doi.org/10.2136/vzj2010.0079>
- Glover, P.W.J., 2017. A new theoretical interpretation of Archie's saturation exponent. *Solid Earth* 8, 805–816. <https://doi.org/10.5194/se-8-805-2017>
- Glover, P.W.J., 2015. Geophysical Properties of the Near Surface Earth: Electrical Properties, in: *Treatise on Geophysics*. Elsevier, pp. 89–137. <https://doi.org/10.1016/B978-0-444-53802-4.00189-5>
- Green, C.T., Liao, L., Nolan, B.T., Juckem, P.F., Shope, C.L., Tesoriero, A.J., Jurgens, B.C., 2018. Regional Variability of Nitrate Fluxes in the Unsaturated Zone and Groundwater, Wisconsin, USA. *Water Resour. Res.* 54, 301–322. <https://doi.org/10.1002/2017WR022012>
- Haarder, E.B., Binley, A., Looms, M.C., Doetsch, J., Nielsen, L., Jensen, K.H., 2012. Comparing Plume Characteristics Inferred from Cross-Borehole Geophysical Data. *Vadose Zo. J.* 11, 1–40. <https://doi.org/10.2136/vzj2012.0031>
- Hammond, G.E., Lichtner, P.C., Mills, R.T., 2014. Evaluating the performance of parallel subsurface simulators: An illustrative example with PFLOTRAN. *Water Resour. Res.* 50, 208–228. <https://doi.org/10.1002/2012WR013483>
- Hen-Jones, R.M., Hughes, P.N., Stirling, R.A., Glendinning, S., Chambers, J.E., Gunn, D.A., Cui, Y.J., 2017. Seasonal effects on geophysical–geotechnical relationships and their implications for electrical resistivity tomography monitoring of slopes. *Acta Geotech.* 12, 1159–1173. <https://doi.org/10.1007/s11440-017-0523-7>
- Hermans, T., Nguyen, F., Caers, J., 2015. Uncertainty in training image-based inversion of hydraulic head data constrained to ERT data: Workflow and case study. *Water Resour. Res.* 51, 5332–5352. <https://doi.org/10.1002/2014WR016259>
- Hinnell, A.C., Ferr, T.P.A., Vrugt, J.A., Huisman, J.A., Moysey, S., Rings, J., Kowalsky, M.B., 2010. Improved extraction of hydrologic information from geophysical data through coupled hydrogeophysical inversion. *Water Resour. Res.* 46, 1–14. <https://doi.org/10.1029/2008WR007060>
- Hübner, R., Heller, K., Günther, T., Kleber, A., 2015. Monitoring hillslope moisture dynamics with surface ERT for enhancing spatial significance of hydrometric point measurements. *Hydrol. Earth Syst. Sci.* 19, 225–240. <https://doi.org/10.5194/hess-19-225-2015>

References

- Jayawickreme, D.H., van Dam, R.L., Hyndman, D.W., 2008. Subsurface imaging of vegetation, climate, and root-zone moisture interactions. *Geophys. Res. Lett.* 35, 1–5. <https://doi.org/10.1029/2008GL034690>
- Johnson, T.C., Hammond, G.E., Chen, X., 2017. PFLOTRAN-E4D: A parallel open source PFLOTRAN module for simulating time-lapse electrical resistivity data. *Comput. Geosci.* 99, 72–80. <https://doi.org/10.1016/j.cageo.2016.09.006>
- Johnson, T.C., Versteeg, R.J., Ward, A., Day-Lewis, F.D., Revil, A., 2010. Improved hydrogeophysical characterization and monitoring through parallel modeling and inversion of time-domain resistivity and induced-polarization data. *Geophysics* 75, WA27. <https://doi.org/10.1190/1.3475513>
- Jonard, F., Bogena, H., Caterina, D., Garré, S., Klotzsche, A., Monerris, A., Schwank, M., von Hebel, C., 2018. Ground-Based Soil Moisture Determination, in: Li, X., Vereecken, H. (Eds.), *Observation and Measurement of Ecohydrological Processes*. Springer, pp. 1–42. https://doi.org/10.1007/978-3-662-47871-4_2-1
- Koestel, J., Kemna, A., Javaux, M., Binley, A., Vereecken, H., 2008. Quantitative imaging of solute transport in an unsaturated and undisturbed soil monolith with 3-D ERT and TDR. *Water Resour. Res.* 44, 1–17. <https://doi.org/10.1029/2007WR006755>
- LaBrecque, D.J., Heath, G., Sharpe, R., Versteeg, R., 2004. Autonomous Monitoring of Fluid Movement Using 3-D Electrical Resistivity Tomography. *J. Environ. Eng. Geophys.* 9, 167–176. <https://doi.org/10.4133/JEEG9.3.167>
- Labrecque, D.J., Yang, X., 2001. Difference inversion of ERT data: a fast inversion method for 3-D in situ monitoring. *J. Environ. Eng. Geophys.* 6, 83–89. <https://doi.org/dx.doi.org/10.4133/JEEG6.2.83>
- Laloy, E., Javaux, M., Vanclooster, M., Roisin, C., Bielders, C.L., 2011. Electrical Resistivity in a Loamy Soil: Identification of the Appropriate Pedo-Electrical Model. *Vadose Zo. J.* 10, 1023. <https://doi.org/10.2136/vzj2010.0095>
- Lehmann, P., Gambazzi, F., Suski, B., Baron, L., Askarinejad, A., Springman, S.M., Holliger, K., Or, D., 2013. Evolution of soil wetting patterns preceding a hydrologically induced landslide inferred from electrical resistivity survey and point measurements of volumetric water content and pore water pressure. *Water Resour. Res.* 49, 7992–8004. <https://doi.org/10.1002/2013WR014560>
- Lesmes, D.P., Friedman, S.P., 2005. Relationships between the Electrical and Hydrogeological Properties of Rocks and Soils, in: Rubin, Y., Hubbard, S.S. (Eds.),

References

- Hydrogeophysics. Springer Netherlands, Dordrecht, pp. 87–128.
https://doi.org/10.1007/1-4020-3102-5_4
- Linde, N., Binley, A., Tryggvason, A., Pedersen, L.B., Revil, A., 2006. Improved hydrogeophysical characterization using joint inversion of cross-hole electrical resistance and ground-penetrating radar traveltime data. *Water Resour. Res.* 42, WR005131. <https://doi.org/10.1029/2006WR005131>
- Looms, M.C., Binley, A., Jensen, K.H., Nielsen, L., Hansen, T.M., 2008. Identifying Unsaturated Hydraulic Parameters Using an Integrated Data Fusion Approach on Cross-Borehole Geophysical Data. *Vadose Zo. J.* 7, 238. <https://doi.org/10.2136/vzj2007.0087>
- Martini, E., Werban, U., Zacharias, S., Pohle, M., Dietrich, P., Wollschläger, U., 2017. Repeated electromagnetic induction measurements for mapping soil moisture at the field scale: validation with data from a wireless soil moisture monitoring network. *Hydrol. Earth Syst. Sci.* 21, 495–513. <https://doi.org/10.5194/hess-21-495-2017>
- Michot, D., Benderitter, Y., Dorigny, A., Nicoullaud, B., King, D., Tabbagh, A., 2003. Spatial and temporal monitoring of soil water content with an irrigated corn crop cover using surface electrical resistivity tomography. *Water Resour. Res.* 39, 1–20. <https://doi.org/10.1029/2002WR001581>
- Miller, C.R., Routh, P.S., Brosten, T.R., McNamara, J.P., 2008. Application of time-lapse ERT imaging to watershed characterization. *Geophysics* 73, G7. <https://doi.org/10.1190/1.2907156>
- Oldenborger, G.A., LeBlanc, A.M., 2015. Geophysical characterization of permafrost terrain at Iqaluit International Airport, Nunavut. *J. Appl. Geophys.* 123, 36–49. <https://doi.org/10.1016/j.jappgeo.2015.09.016>
- Ray, R.L., Jacobs, J.M., 2007. Relationships among remotely sensed soil moisture, precipitation and landslide events. *Nat. Hazards* 43, 211–222. <https://doi.org/10.1007/s11069-006-9095-9>
- Robinet, J., von Hebel, C., Govers, G., van der Kruk, J., Minella, J.P.G., Schlesner, A., Ameijeiras-Mariño, Y., Vanderborght, J., 2018. Spatial variability of soil water content and soil electrical conductivity across scales derived from Electromagnetic Induction and Time Domain Reflectometry. *Geoderma* 314, 160–174. <https://doi.org/10.1016/j.geoderma.2017.10.045>
- Robinson, D.A., Lebron, I., Kocar, B., Phan, K., Sampson, M., Crook, N., Fendorf, S., 2009. Time-lapse geophysical imaging of soil moisture dynamics in tropical

References

- deltaic soils: An aid to interpreting hydrological and geochemical processes. *Water Resour. Res.* 45, n/a-n/a. <https://doi.org/10.1029/2008WR006984>
- Scaini, A., Audebert, M., Hissler, C., Fenicia, F., Gourdol, L., Pfister, L., Beven, K.J., 2017. Velocity and celerity dynamics at plot scale inferred from artificial tracing experiments and time-lapse ERT. *J. Hydrol.* 546, 28–43. <https://doi.org/10.1016/J.JHYDROL.2016.12.035>
- Schaap, M.G., Leij, F.J., van Genuchten, M.T., 2001. rosetta: a computer program for estimating soil hydraulic parameters with hierarchical pedotransfer functions. *J. Hydrol.* 251, 163–176. [https://doi.org/10.1016/S0022-1694\(01\)00466-8](https://doi.org/10.1016/S0022-1694(01)00466-8)
- Scholer, M., Irving, J., Binley, A., Holliger, K., 2011. Estimating vadose zone hydraulic properties using ground penetrating radar: The impact of prior information. *Water Resour. Res.* 47, 1–14. <https://doi.org/10.1029/2011WR010409>
- Shanahan, P.W., Binley, A., Whalley, W.R., Watts, C.W., 2015. The Use of Electromagnetic Induction to Monitor Changes in Soil Moisture Profiles beneath Different Wheat Genotypes. *Soil Sci. Soc. Am. J.* <https://doi.org/10.2136/sssaj2014.09.0360>
- Si, H., 2015. TetGen, a Delaunay-Based Quality Tetrahedral Mesh Generator. *ACM Trans. Math. Softw.* 41, 1–36. <https://doi.org/10.1145/2629697>
- Singha, K., Day-Lewis, F.D., Johnson, T., Slater, L.D., 2015. Advances in interpretation of subsurface processes with time-lapse electrical imaging. *Hydrol. Process.* 29, 1549–1576. <https://doi.org/10.1002/hyp.10280>
- Taylor, J.R., 1982. *An Introduction to Error Analysis: The Study of Uncertainties in Physical Measurements.* University Science Books.
- Tso, C.-H.M., Kuras, O., Wilkinson, P.B., Uhlemann, S., Chambers, J.E., Meldrum, P.I., Graham, J., Sherlock, E.F., Binley, A., 2017. Improved characterisation and modelling of measurement errors in electrical resistivity tomography (ERT) surveys. *J. Appl. Geophys.* 146, 103–119. <https://doi.org/10.1016/J.JAPPGEO.2017.09.009>
- Turkeltaub, T., Jia, X., Zhu, Y., Shao, M.-A., Binley, A., 2018. Recharge and Nitrate Transport Through the Deep Vadose Zone of the Loess Plateau: A Regional-Scale Model Investigation. *Water Resour. Res.* 54, 4332–4346. <https://doi.org/10.1029/2017WR022190>
- Uhlemann, S., Chambers, J., Wilkinson, P., Maurer, H., Merritt, A., Meldrum, P., Kuras, O., Gunn, D., Smith, A., Dijkstra, T., 2017. Four-dimensional imaging of moisture

References

- dynamics during landslide reactivation. *J. Geophys. Res. Earth Surf.* 122, 398–418. <https://doi.org/10.1002/2016JF003983>
- Uhlemann, S., Sorensen, J.P.R., House, A.R., Wilkinson, P.B., Roberts, C., Goody, D.C., 2016. Integrated time-lapse geoelectrical imaging of wetland hydrological processes. *Water Resour. Res.* 52, 1607–1625. <https://doi.org/10.1002/2015WR017932>
- von Hebel, C., Rudolph, S., Mester, A., Huisman, J.A., Kumbhar, P., Vereecken, H., van der Kruk, J., 2014. Three-dimensional imaging of subsurface structural patterns using quantitative large-scale multiconfiguration electromagnetic induction data. *Water Resour. Res.* 50, 2732–2748. <https://doi.org/10.1002/2013WR014864>
- Wehrer, M., Slater, L.D., 2015. Characterization of water content dynamics and tracer breakthrough by 3-D electrical resistivity tomography (ERT) under transient unsaturated conditions. *Water Resour. Res.* 51, 97–124. <https://doi.org/10.1002/2014WR016131>
- Weller, A., Slater, L., Nordsiek, S., 2013. On the relationship between induced polarization and surface conductivity: Implications for petrophysical interpretation of electrical measurements. *Geophysics* 78, D315–D325. <https://doi.org/10.1190/geo2013-0076.1>
- Whalley, W.R., Binley, A., Watts, C.W., Shanahan, P., Dodd, I.C., Ober, E.S., Ashton, R.W., Webster, C.P., White, R.P., Hawkesford, M.J., 2017. Methods to estimate changes in soil water for phenotyping root activity in the field. *Plant Soil* 415, 407–422. <https://doi.org/10.1007/s11104-016-3161-1>
- Wiese, B., Wagner, F., Norden, B., Maurer, H., Schmidt-Hattenberger, C., 2018. Fully coupled inversion on a multi-physical reservoir model - Part I: Theory and concept. *Int. J. Greenh. Gas Control*.
- Winship, P., Binley, A., Gomez, D., 2006. Flow and transport in the unsaturated Sherwood Sandstone: characterization using cross-borehole geophysical methods. *Geol. Soc. London, Spec. Publ.* 263, 219–231. <https://doi.org/10.1144/GSL.SP.2006.263.01.12>
- Yamakawa, Y., Kosugi, K., Katsura, S., Masaoka, N., Mizuyama, T., 2012. Spatial and Temporal Monitoring of Water Content in Weathered Granitic Bedrock Using Electrical Resistivity Imaging. *Vadose Zo. J.* 11, 0. <https://doi.org/10.2136/vzj2011.0029>

Yonggen, Z., Schaap, M.G., Guadagnini, A., Neuman, S.P., 2016. Inverse modeling of unsaturated flow using clusters of soil texture and pedotransfer functions. *Water Resour. Res.* 52, 7631–7644. <https://doi.org/10.1002/2016WR019016>

Zhu, P., Shi, L., Zhu, Y., Zhang, Q., Huang, K., Williams, M., 2017. Data assimilation of soil water flow via ensemble Kalman filter: Infusing soil moisture data at different scales. *J. Hydrol.* 555, 912–925. <https://doi.org/10.1016/j.jhydrol.2017.10.078>

Appendix A: petrophysical uncertainty propagation

Following the analytical sensitivity analysis of [Chen and Fang \(1986\)](#) and [Taylor \(1982\)](#), we can obtain the uncertainty contributions of the various terms in Archie's law (equation 2). Assuming they have uncorrelated errors, by laws of error propagation, the variance of saturation is given by

$$\sigma_{S_w}^2 = \left(\frac{\partial S_w}{\partial \rho_s}\right)^2 \sigma_{\rho_s}^2 + \left(\frac{\partial S_w}{\partial \rho}\right)^2 \sigma_{\rho}^2 + \left(\frac{\partial S_w}{\partial n}\right)^2 \sigma_n^2$$

where

$$\begin{aligned}\frac{\partial S_w}{\partial \rho_s} &= \frac{1}{n\rho_s} S_w \\ \frac{\partial S_w}{\partial \rho} &= \frac{1}{n\rho} S_w \\ \frac{\partial S_w}{\partial n} &= \frac{\ln(\rho/\rho_s)}{n^2} S_w\end{aligned}$$

So

$$\begin{aligned}\left(\frac{\partial S_w}{\partial \rho_s}\right)^2 \sigma_{\rho_s}^2 &= \left(\frac{S_w}{n}\right)^2 \left(\frac{\sigma_{\rho_s}}{\rho_s}\right)^2 \\ \left(\frac{\partial S_w}{\partial \rho}\right)^2 \sigma_{\rho}^2 &= \left(\frac{S_w}{n}\right)^2 \left(\frac{\sigma_{\rho}}{\rho}\right)^2 \\ \left(\frac{\partial S_w}{\partial n}\right)^2 \sigma_n^2 &= \left(\frac{S_w}{n}\right)^2 \left(\frac{\ln(\rho/\rho_s)}{n} \sigma_n\right)^2\end{aligned}$$

Supplementary information

Text S1.

Monte Carlo ERT inversion runs

Given the data errors of the ERT measurements, the Monte Carlo uncertainty propagation procedure of Aster et al. (2005) (as used in Tso et al. (Tso et al., 2017)) can be used and is outlined below:

8. Propagate the inverse solution $\bar{\mathbf{m}}$ into an assumed noise-free baseline $j \times 1$ data vector \mathbf{d} (where j is the size of number of measurements) using the forward model \mathbf{G} :

$$\mathbf{G}\bar{\mathbf{m}} = \mathbf{d} \quad (11)$$

9. Generate q realizations ($i = 1, \dots, q$) of noisy data about $\bar{\mathbf{m}}$ using the error model

$$\mathbf{d}_i = \mathbf{d}_b + \boldsymbol{\varepsilon}.*\mathbf{Z} \quad (12)$$

where $\boldsymbol{\varepsilon}$ is the $j \times 1$ vector of error levels predicted by the error model and \mathbf{Z} is the standard normal distribution variable and $.*$ is element-wise multiplication.

10. Invert the q realizations ($i = 1, \dots, q$) of noisy data using the inverse model

$$\mathbf{G}\mathbf{m}_i = \mathbf{d}_b + \boldsymbol{\varepsilon}_i \quad (13)$$

11. Let \mathbf{A} be a $q \times m$ matrix where the i -th row contains the departure of the i -th model from the baseline inverse solution $\bar{\mathbf{m}}$

$$\mathbf{A}_i = \mathbf{m}_i^T - \bar{\mathbf{m}}^T \quad (14)$$

12. An empirical estimate of the model covariance matrix is given by

$$\text{cov}(\bar{\mathbf{m}}) = \frac{\mathbf{A}^T\mathbf{A}}{q} \quad (15)$$

13. 95% confidence interval about $\bar{\mathbf{m}}$ is given by

$$\bar{\mathbf{m}} \pm 1.96 \cdot \text{diag}(\text{cov}(\bar{\mathbf{m}}))^{1/2} \quad (16)$$

14. Similarly, the coefficient of variation of the estimate is given by

$$\text{diag}(\text{cov}(\bar{\mathbf{m}}))^{1/2} ./ \bar{\mathbf{m}}^T \quad (17)$$

where $./$ is element-wise division.

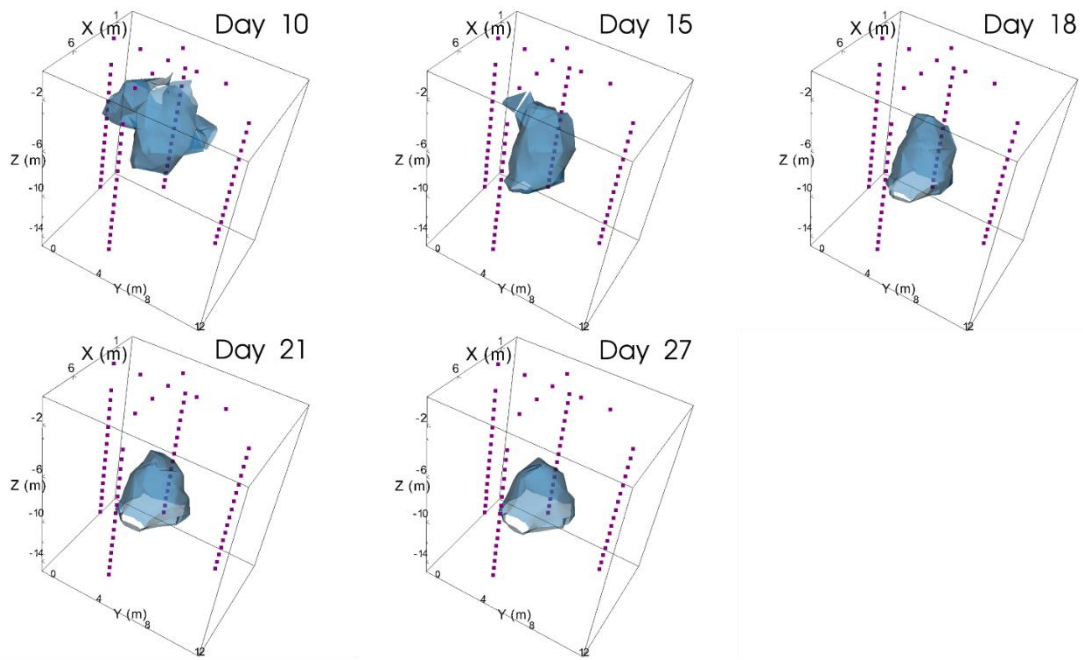


Figure S1. Inverted ERT images from the Hatfield controlled infiltration experiment. The electrode locations are shown in purple squares. The iso-surfaces show area that has 5.5% reduction of resistivity relative to baseline (Day 7).

Table S1. Relationship between Archie's parameters with clay content, cation exchange capacity (CEC), and surface area to pore volume ratio (Spor). Note that Spor data is not available for some cores.

R^2	Clay content (%)	CEC (meq/100g)	Spor (μm^{-1})
ρ_s ($\Omega \text{ m}$)	0.2655	0.2913	0.6301
n (-)	0.0017	0.0871	0.2018

7. Discussion summary

A primary goal of this thesis is to identify the sources of uncertainty in ERT data collection, modelling, inversion, and interpretation. In the introduction section, I outlined a 5-step workflow (Figure 1.1) for ERT and argued that information and uncertainty propagates through it. I then identified three specific research areas to address in chapters 4-6 of this thesis. I have reviewed in chapter 2 the geophysical methods that have been used extensively for nuclear site characterisation (particularly in the USA). Uncertainty and risk assessment is a recurring topic in these work because of the management decisions that are made at these sites. A comprehensive review of the sources of uncertainties in the ERT workflow was given in chapter 3, which provides an overview of existing work on handling uncertainty at specific stages of the workflow. Most of the work reviewed focused on inversion, with a few exceptions that considers the remaining aspects. Summaries of the findings of this thesis can be found below and in Figure 1.

Chapter 4 reviewed the various aspects of measurement errors in ERT. I compared the three common type of errors obtained during data acquisition—stacking errors, repeatability errors, and reciprocal errors and assessed the statistical distribution and correlation. Using data from two long-term monitoring dataset provided by the British Geological Survey, it was found that stacking errors are consistently an order of magnitude lower than others while repeatability and reciprocal errors tend to agree and show little auto-correlation. Since errors obtained in the field is only an instance in the assumed Gaussian distribution for noise, they need to be modelled before being fed to inversion. Linear models are commonly used to account for proportionality effects. It was found that each electrode used for making a ERT measurement has a secondary effect on errors. Such effect is incorporated using a new linear mixed effect model and it leads to superior inversion results in cases where certain electrodes are of significantly lower quality than others.

In some applications, the goal of using ERT is to predict some quantities of interests while the ERT images themselves are not directly relevant. Chapter 5 assessed the benefit of leak parameter estimation using ERT data directly (i.e. without inversion).

It provided a first attempt to combine steps 3-5 of the ERT workflow (Figure 1, see also chapter 1) to estimate leak parameters directly from raw ERT data. This can be achieved by combining coupled hydrogeophysical modelling and data assimilation, where the ERT data misfits update the distribution of flow model parameters. The reduction of model uncertainty upon conditioning on ERT data can be visualised in reduced spread in model parameters as well as mass discharge curves over a user-defined plane. The proposed method is promising as it offers a way to estimate leak parameters from ERT data, but care should be taken in model proposals and interpreting the posterior. For leak detection and similar problems, the proposed method can provide additional insights that complements ERT inversion. It is particularly relevant to nuclear sites because most of them have undergone series of site investigation over the past decades and has a wealth of prior site characterisation information. It should be noted such framework is not limited to geophysical data but can be used in any site characterisation work. The key idea is to use data to constrain one's prior understand of the site conceptualization.

Geophysics are also frequently used in the unsaturated zone to infer changes in spatial distribution of moisture content with time. This is important because higher moisture content can mean more water available for crop growth or faster solute transport from near-surface sources to aquifers. However, the spatially varying resolution of geophysical inversion as well as the uncertainties in the petrophysical relationships relating moisture content and geophysical properties can complicate the inference of moisture content from geophysical data. Chapter 6 addressed a classic problem in the interpretation of ERT image—the quantification of an imaged moisture plume. The chapter examined the extent to which uncertain petrophysical relationships affect the estimation of soil water content (and its temporal changes). These effects were quantified and compared for the first time using an uncertainty propagation framework for resistivity-derived moisture content estimates. It was shown that natural variability of petrophysical models can be high and as a consequence the moisture content estimates can vary significantly. It was also shown that it is possible that petrophysical parameters to be a more significant source of uncertainty than ERT measurement errors and inversion. The original goal in chapter

6 was to quantify the uncertainty in the volume of a solute plume. However, there is no straightforward way to disentangle the contribution of saturation and solute concentration to resistivity. An analysis like the one in chapter 6 to solutes is highly relevant, but some major adaptations need to be made.

The workflow for geophysical studies in site characterization is conceptualized as a pipeline for information and uncertainty propagation.

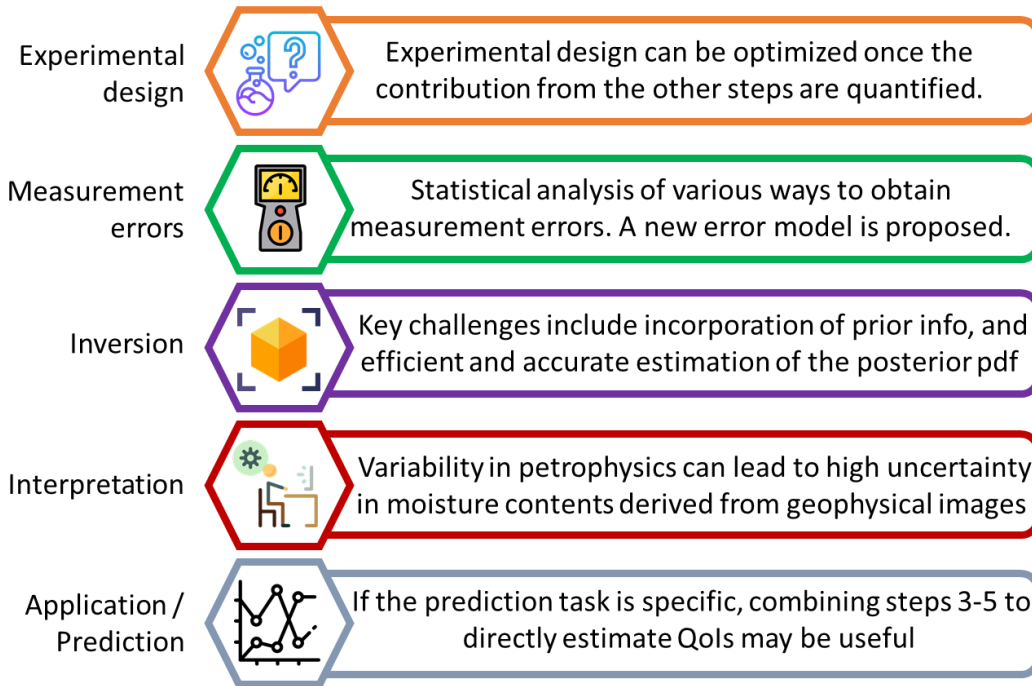


Figure 1 A diagram summarizing the major findings in this thesis and their relation to the ERT workflow.

Long-term ERT monitoring has provided a new dimension to the wealth of geophysical data available. For example, in the Sellafield data, daily data for about 1.5 years is available. An initial ambition that was not materialized is to make use of the full time series of the ERT data such as to make "live" leak/no-leak calls based on raw ERT data and to automatically flag "interesting" time slices for inversion. In this thesis, however, full time series are only used in the measurement error characterisation chapter. Others have only used data from a few selected time slices available in order to save computation time (note that the observation ensemble is $((n_d \times n_t) \times (n_e))$, where n_d , n_t and n_e are number of measurements, number of time slices, and size of the ensemble respectively. Recently, I have come across statistical methods for changepoint detection (i.e. mean and/or variance shifts in time series) (Killick et al.,

2012) to automatically identify features of interest from ERT data with both online and offline modes. It has been used in an increasing number of environmental applications and they have potential to be used for geophysical monitoring data.

In this thesis, a deliberate decision was made not to focus on ERT inversion so that other sources of uncertainties can be considered. However, inversion remains an integral part of the ERT workflow and UQ in ERT and it will remain an important area of research. To obtain inversion uncertainty, we have used traditional Monte Carlo sampling for simplicity. There exist other alternatives such as Bootstrap inversion (Schnaidt and Heinson, 2015) that can improve the efficiency, accuracy, and robustness of such sampling. We also recognize that the uncertainty estimates from the above procedures do not represent the uncertainty of the parameter space, but rather the effect of parameter uncertainty due to data errors (i.e. how data errors are propagated through inversion). Some of the inversion approaches listed in the following are perhaps more suitable for this task.

Because Markov chain Monte Carlo (MCMC) methods conditionally accept and reject model proposals, it is argued that they provide more robust and accurate uncertainty estimates. In particular, it provides the full posterior parameter probability distribution, which can be multi-modal in highly uncertain regions such as interfaces. At the start of the PhD, I decided not to use MCMC because of its very high computation cost. This high cost is in part due to computation needed to generate model proposals, and in part due to parameterization (i.e. very fine parameterization is used), among other factors. Significant progress has been made on MCMC in both areas. For example, graph cuts (Zahner et al., 2016) allow rapid generation of many model proposals with the same characteristic features using training images. Trans-dimensional ERT (Galetti and Curtis, 2018) allows estimation of unstructured parameter cell sizes and shapes alongside with their resistivity values. Recently, a two-step methodology based on area-to-point kriging is proposed to generate fine-scale multi-Gaussian realizations from smooth tomographic images (Nussbaumer et al., 2019).

Even though there are many inversion strategies available, our understanding on the topology of the ERT inverse problem or the parameter space uncertainty behaviour is limited. One piece of work I have started during my PhD is to investigate whether we can use gradient-based approach to locate regions of global minima. The concept here is to randomly sample the parameter space with particles and calculate their local gradient. Then starting with one of the particles, look for the next closest particle that is downhill of the current one. The process will continue until the search path reaches a valley, where it will either bounce between two particle locations, or it will form an orbit that joins several particle locations that outlines the boundary of the valley. An example is shown in Figure 2. This approach, first proposed by [Curtis and Spencer \(1999\)](#), is not itself an inversion method, but it can improve the modeller's understanding of the structure of the inverse problem they are facing, with a much smaller computational cost than an uncertainty analysis that uses a fully Bayesian McMC inversion.

Although McMC inversions are promising and advance rapidly, more efficient methods (e.g. 3-D problems that can be calculated on a laptop) for ERT inversion with uncertainty quantification and more flexible parameterization to account for spatial scales are needed to aid enhancing the information content of geophysical data and its uncertainty quantification. My leak detection work is one of the first that uses data assimilation for raw ERT data. Such methods should also be considered, where appropriate, for ERT inversion. There is potential for data assimilation methods to be combined with level set or multi-point geostatistics (MPS) parameterization to estimate a multi-scale heterogeneous resistivity field efficiently and provides approximation of its uncertainty. Such methods allow target features that do not have a constant length scale and normally not well recovered by smoothness-constrained or traditional covariance-based (i.e. two-point) geostatistical inversion to be resolved reasonably well.

The simulation of some hydrological problems can require a very long run time, which makes it prohibitive to use them directly for uncertainty quantification. Examples include regional-scale modelling of surface water-groundwater exchange or

predicting the fate of radionuclides decades or centuries into the future. In these cases, building surrogate models that approximate the behaviour of the full forward model will be useful. It ensures that the the uncertainty quantification methods described in this thesis is applicable to all hydrogeophysical problems.

Big data and machine learning methods have brought about radical changes in many fields. Application of data-driven methods has emerged in recent hydrogeophysical studies (Laloy et al., 2017; Nguyen et al., 2016). Bayesian evidential learning (Hermans et al., 2018) has also been applied, where it provides an incremental framework for characterisation to inform site management decisions. Specifically, before data acquisition, Monte Carlo simulations and global sensitivity analysis are used to assess the information content of the data to reduce the uncertainty of the prediction. After data acquisition, prior falsification and machine learning based on the same Monte Carlo simulations are used to directly assess uncertainty on key prediction variables from observations. A big challenge of applying machine learning methods is the availability of training data. For example, I have attempted to train a data-driven model for petrophysical relationships but the data I had access to was insufficient to build a robust model. The hydrogeophysics community can work together to build databases of laboratory and field data for building machine learning models. Recent work in surface water hydrology has also explored the use of deep learning methods (Shen, 2018), which has begun to show potential in hydrogeophysical studies (Laloy et al., 2017).

Forty years ago, Lytle and Dines (1978) developed the so-called “impedance camera”, which can be considered as one of the earliest work on ERT. They noted *“Items worthy of future research include an assessment of the influence of noise in the data, a study of the accuracy of the reconstruction and its spatial dependence, and evaluation of the degree of dependence of various measurement configurations, an analytic study of the resolution limit, and a determination of the extent to which the use of a priori knowledge affects the interpretation.”* As addressed in this thesis, the challenges these pioneers highlighted are more far-reaching and relevant than they were then and 40 years on we are getting there.

Discussion summary

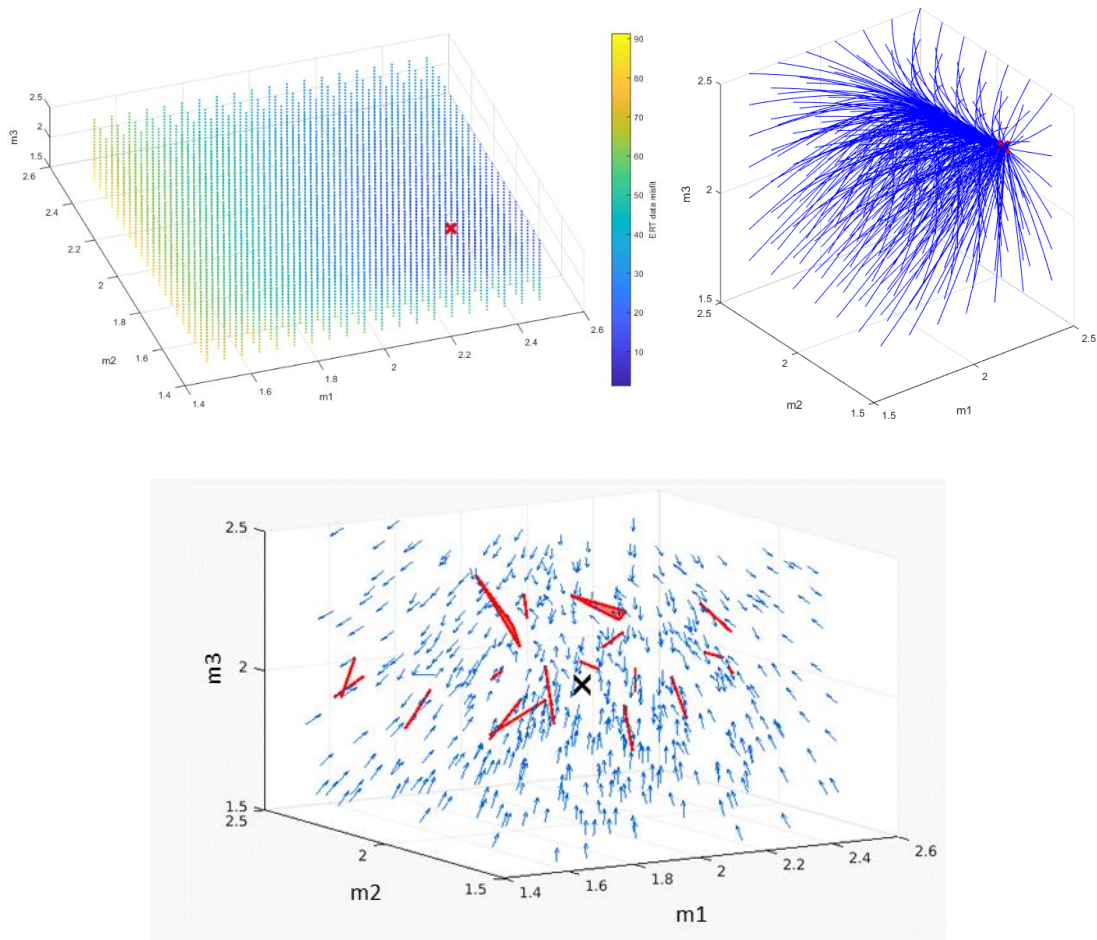


Figure 2 (Top) Parameter space of a 3-parameter layered ERT problem using 24 surface electrodes in dipole-dipole configuration. The axis represents the uniform parameter value of each layer in log scale. The true resistivity for all three layers are $100 \Omega \text{ m}$. The red cross indicate the true parameter value. The data misfit surface (left) and the derived streamlines to the data misfit minima (right) are plotted. (bottom) Gradient fields using 500 samples. The red polygons are the loops and the black cross is the true values. The gradient field somewhat point towards the true minima. 9 loops are identified, spanning a large fraction of the parameter space.

8. Conclusions and recommendations

8.1 Conclusions

Geophysical methods have been a suite of valuable tools to provide information for site characterisation. This thesis has formalised the ERT workflow as a pipeline for information/uncertainty propagation. It has focused on the sources of uncertainties in the various aspects of the ERT workflow while making contribution in better understanding several of its less explored aspects.

Through literature review and new analysis included here, we now better understand the behaviour of the various sources of uncertainties in ERT. We have also investigated how uncertainties at a given stage of the workflow propagates downstream. Using rules of error propagation, the impact of uncertainties that stemmed at any stage of the workflow can be approximated using Monte Carlo analysis. This provides a powerful design and evaluation framework to quantify, rank, and in some cases reduce the sources of uncertainties in an ERT study.

Statistical analysis of ERT measurement errors from long-term monitoring datasets shows that the use of reciprocal and repeatability errors are preferred and they have negligible correlation in time. Variations in electrode quality may have a minor effect on measurement errors and a new error model is proposed to account for such effects. Similarly, detailed examination of field samples allows us to better understand the variability of petrophysical relationships in real-world settings. The impact of such variability to moisture content estimates as it is propagated down the ERT workflow is then assessed, which is found to be consistent but with larger error bars than previously appreciated. A method that combined the inversion and prediction steps together to bypass the typical workflow is also developed. It is suitable for situations where there is abundant prior site information and a clear list of non-geophysical parameters to be estimated. This approach is applied to leak detection problems and estimated leak parameters from ERT data (with the help of prior hydrogeological model) directly, which is not achievable from typical ERT inversion.

The findings in this thesis are highly relevant to nuclear site characterisation. A literature review in the thesis shows geophysics is widely applied in nuclear sites and the industry has been used to dealing with uncertainties. The methods developed in the thesis not only can improve the reliability of using ERT in general but also provides a wealth of information for decision making at a nuclear site.

This thesis contributes to a growing number of studies which aims to extract additional meaningful information from ERT datasets (e.g. see PhD work of Crestani, 2013; Robinson, 2015; Wagner, 2016; Ward, 2018). The results from the work presented here demonstrates both the capability to extract more information from ERT, while the linked issue to better track and quantify uncertainties in ERT studies is highlighted. This thesis presents an uncertainty propagation framework that can serve as a basis for further development of methods that seek to extract additional information from ERT data for site characterisation.

8.2 Future work

Due to the limited scope of this thesis, many of the aspects on the information content and uncertainty for geophysical data for site characterization have not been fully investigated. An area of research that has not been addressed in this work is to track and quantify the amount of information and uncertainty that propagate through the entire ERT workflow. This can be investigated further using both synthetic examples and real-world problems. Once we have estimated the contribution of uncertainty and information in each step and the way they propagate throughout the pipeline, we can optimize each step for experimental design. This thesis focuses on ERT only, but the approach developed in it are applicable to other geophysics or site characterisation methods. Future work should also investigate the uncertainty propagation where there is fusion of data types and multiple modalities, e.g. fusion of satellite, air-borne, surface, and ground-based measurements. Similar uncertainty quantification methods can be extended the related concept of value of information (VOI), which computes the expected monetary return of a characterisation option. Such calculations can rank characterisation methods in terms of their cost-effectiveness and show the added value of including each additional method. An alternative to VOI

calculations is information content calculations (JafarGandomi and Binley, 2013; Nearing and Gupta, 2015), where the marginal gain in information from various characterisation options can be compared. Finally, a vision has been proposed recently to perform integrated modelling and uncertainty analysis in virtual laboratories using cloud computing platforms (Blair et al., 2019, 2018). One use of collaborative workspaces is that it allows users to perform individual modelling tasks and specify a workflow to compute uncertainty propagation across all components, which is well-suited for the ERT workflow described in this thesis.

This thesis has considered the behaviour and detection of a single leak event with a single source of assumed constant loading under “clean” antecedent conditions. Of course, these assumptions do not always hold in real-world applications. There is limited existing work that consider multiple source identification, most of them are based on Bayesian formulation. It is my hope that my work presented here can be generalized to handle more complex conditions that are present in some of the most complex environmental sites in the world.

Part of this thesis uses data assimilation methods on ERT data to estimate leak parameters and uniform hydro geophysical parameters. Some recent work has used data assimilation from head, concentration, or ERT data (in some cases, their combination) to estimate hydraulic parameter fields or plume geometry. Future work should explore the development of a more generalized framework to estimate parameters of both categories jointly. Likewise, the use of these methods for hydrogeological parameter using multiple injection (or leak) or abstraction events (i.e. as in hydraulic tomography or tracer tomography) (e.g. Tso et al., 2016; Zha et al., 2019) have potential to improve characterisation of environmental sites.

Bibliography

Aalstad, K., Westermann, S., Schuler, T.V., Boike, J., Bertino, L., 2018. Ensemble-based assimilation of fractional snow-covered area satellite retrievals to estimate the snow distribution at Arctic sites. *Cryosphere* 12, 247–270. <https://doi.org/10.5194/tc-12-247-2018>

Abdulsamad, F., Revil, A., Soueid Ahmed, A., Coperey, A., Karaoulis, M., Nicaise, S.,

Bibliography

- Peyras, L., 2019. Induced polarization tomography applied to the detection and the monitoring of leaks in embankments. *Eng. Geol.* 254, 89–101. <https://doi.org/10.1016/J.ENGGEOL.2019.04.001>
- Aghasi, A., Mendoza-Sanchez, I., Miller, E.L., Ramsburg, C.A., Abriola, L.M., 2013. A geometric approach to joint inversion with applications to contaminant source zone characterization. *Inverse Probl.* 29, 115014. <https://doi.org/10.1088/0266-5611/29/11/115014>
- Ahlbom, K., Carlsson, L., Olsson, O., 1983. Final disposal of spent nuclear fuel - geological, hydrogeological and geophysical methods for site characterization. Stockholm.
- Ahlstrom, S.W., Foote, H.P., Arnett, R.C., Cole, C.R., Serne, R.J., 1977. Multicomponent mass transport model: theory and numerical implementation (discrete-parcel-random-walk version). Richland, Washington.
- Ahmed, M.A., Passioura, J., Carminati, A., 2018. Hydraulic processes in roots and the rhizosphere pertinent to increasing yield of water-limited grain crops: a critical review. *J. Exp. Bot.* 69, 3255–3265. <https://doi.org/10.1093/jxb/ery183>
- Alpak, F., Torres-Verdín, C., Habashy, T.M., 2004. Joint inversion of transient pressure and dc resistivity measurements acquired with in-situ permanent sensors: A numerical study. *Geophysics* 69, 1173–1191. <https://doi.org/10.1190/1.1801935>
- Altdorff, D., von Hebel, C., Borchard, N., van der Kruk, J., Bogen, H.R., Vereecken, H., Huisman, J.A., 2017. Potential of catchment-wide soil water content prediction using electromagnetic induction in a forest ecosystem. *Environ. Earth Sci.* 76, 111. <https://doi.org/10.1007/s12665-016-6361-3>
- Alumbaugh, D.L., Newman, G.A., 2000. Image appraisal for 2-D and 3-D electromagnetic inversion. *Geophysics* 65, 1455. <https://doi.org/10.1190/1.1444834>
- Amidu, S.A., Dunbar, J.A., 2007. Geoelectric Studies of Seasonal Wetting and Drying of a Texas Vertisol. *Vadose Zo. J.* 6, 511. <https://doi.org/10.2136/vzj2007.0005>
- Andersen, K.E., Brooks, S.P., Hansen, M.B., 2003. Bayesian inversion of geoelectrical resistivity data. *J. R. Stat. Soc. Ser. B Stat. Methodol.* 65, 619–642. <https://doi.org/10.1111/1467-9868.00406>
- Artiola, J.F., Pepper, I.L., Brusseau, M.L., 2004. Environmental Monitoring and Characterization. Elsevier. <https://doi.org/10.1016/B978-0-12-064477-3.X5000-0>
- Asch, T., Morrison, H.F., 1989. Mapping and monitoring electrical resistivity with surface and subsurface electrode arrays. *Geophysics* 54, 235–244.
- Asher, M.J.J., Croke, B.F.W.F.W., Jakeman, A.J.J., Peeters, L.J.M.J.M., 2015. A review of surrogate models and their application to groundwater modeling. *Water Resour. Res.* 51, 5957–5973. <https://doi.org/10.1002/2015WR016967>
- Aster, R., Borchers, B., Thurber, C.H., 2005. Parameter estimation and inverse problems.

Bibliography

Elsevier, Burlington, Massachusetts, USA.

- Audebert, M., Clément, R., Touze-Foltz, N., Günther, T., Moreau, S., Duquennoi, C., 2014. Time-lapse ERT interpretation methodology for leachate injection monitoring based on multiple inversions and a clustering strategy (MICS). *J. Appl. Geophys.* 111, 320–333. <https://doi.org/10.1016/j.jappgeo.2014.09.024>
- Back, P.-E., 2007. A model for estimating the value of sampling programs and the optimal number of samples for contaminated soil. *Environ. Geol.* 52, 573–585. <https://doi.org/10.1007/s00254-006-0488-6>
- Backus, G.E., Gilbert, F., 1970. Uniqueness in the Inversion of inaccurate Gross Earth Data. *Philos. Trans. R. Soc. London A* 266, 123–192.
- Backus, G.E., Gilbert, F., 1968. The Resolving power of Gross Earth Data. *Geophys. J. R. Astron. Soc.* 16, 169–205.
- Balbarini, N., Rønde, V., Maurya, P., Fiandaca, G., Møller, I., Erik Klint, K., Christiansen, A. V., Binning, P.J., Bjerg, P.L., 2018. Geophysics Based Contaminant Mass Discharge Quantification Downgradient of a Landfill and a Former Pharmaceutical Factory. *Water Resour. Res.* <https://doi.org/10.1029/2017WR021855>
- Barker, J.A., 1991. The reciprocity principle and an analytical solution for Darcian flow in a network. *Water Resour. Res.* 27, 743–746. <https://doi.org/10.1029/91WR00258>
- Barnett, D.B., Gee, G.W., Sweeney, M.D., 2002. Results of Tank-Leak Detection Demonstration Using Geophysical Techniques at the Hanford Mock Tank Site – Fiscal Year 2001. Richland, Washington.
- Barnett, D.B., Gee, G.W., Sweeney, M.D., Johnson, M.D., Medina, V.F., Khan, F., 2003. Results of Performance Evaluation Testing of Electrical Leak-Detection Methods at the Hanford Site Mock Tank – FY 2002-2003. Richland, Washington.
- Bass, B., Cardenas, M.B., Befus, K.M., 2017. Seasonal Shifts in Soil Moisture throughout a Semiarid Hillslope Ecotone during Drought: A Geoelectrical View. *Vadose Zo.* J. 0, 0. <https://doi.org/10.2136/vzj2016.11.0108>
- Bates, D., Maechler, M., Bolker, B.M., Walker, S., 2015. Fitting Linear Mixed-Effects Models using {lme4}. *J. Stat. Softw.* 67, 1–48. <https://doi.org/10.18637/jss.v067.i01>
- Bayliss, C.R., Langley, K.F., 2003. Nuclear Decommissioning, Waste Management, and Environmental Site Remediation, Nuclear Decommissioning, Waste Management, and Environmental Site Remediation. Elsevier. <https://doi.org/10.1016/B978-075067744-8/50027-8>
- Bazin, S., Pfaffhuber, A.A., 2013. Mapping of quick clay by electrical resistivity tomography under structural constraint. *J. Appl. Geophys.* 98, 280–287. <https://doi.org/10.1016/J.JAPPGEO.2013.09.002>
- Beff, L., Günther, T., Vandoorne, B., Couvreur, V., Javaux, M., 2013. Three-dimensional

Bibliography

- monitoring of soil water content in a maize field using Electrical Resistivity Tomography. *Hydrol. Earth Syst. Sci.* 17, 595–609. <https://doi.org/10.5194/hess-17-595-2013>
- Begg, S., Bratvold, R., Campbell, J., 2013. The value of flexibility in managing Uncertainty in oil and gas investments, in: *SPE Annual Technical Conference and Exhibition*. Society of Petroleum Engineers. <https://doi.org/10.2118/77586-MS>
- Beskardes, G.D., Weiss, C.J., 2018. Modelling dc responses of 3-D complex fracture networks. *Geophys. J. Int.* 214, 1901–1912. <https://doi.org/10.1093/gji/ggy234>
- Beven, K., 2006. A manifesto for the equifinality thesis. *J. Hydrol.* 320, 18–36. <https://doi.org/10.1016/j.jhydrol.2005.07.007>
- Beven, K., Westerberg, I., 2011. On red herrings and real herrings: disinformation and information in hydrological inference. *Hydrol. Process.* 25, 1676–1680. <https://doi.org/10.1002/hyp.7963>
- Bickel, E.J., Bratvold, R.B., 2008. From uncertainty quantification to decision making in the oil and gas industry. *Energy, Explor. Exploit.* 26, 311–325. <https://doi.org/10.1260/014459808787945344>
- Binley, A., 2015a. *Tools and Techniques: Electrical Methods*, Treatise on Geophysics. Elsevier B.V. <https://doi.org/10.1016/B978-0-444-53802-4.00192-5>
- Binley, A., 2015b. *Tools and techniques: Electrical methods*. Treatise Geophys. <https://doi.org/10.1016/B978-0-444-53802-4.00192-5>
- Binley, A., 2003. *Vadose Zone Tracer Testing in the UK Sherwood Sandstone : Hydrogeophysical Data Report*. Livermore, California.
- Binley, A., Beven, K., 2003. Vadose zone flow model uncertainty as conditioned on geophysical data. *Groundwater* 41, 119–127.
- Binley, A., Cassiani, G., Middleton, R., Winship, P., 2002a. Vadose zone flow model parameterisation using cross-borehole radar and resistivity imaging. *J. Hydrol.* 267, 147–159. [https://doi.org/10.1016/S0022-1694\(02\)00146-4](https://doi.org/10.1016/S0022-1694(02)00146-4)
- Binley, A., Cassiani, G., Winship, P., 2004. Characterization of heterogeneity in unsaturated sandstone using borehole logs and cross-borehole tomography, in: *Aquifer Characterization*, in: *Aquifer Characterization*. SEPM (Society for Sedimentary Geology), pp. 129–138. <https://doi.org/10.2110/pec.04.80.0129>
- Binley, A., Daily, W., Ramirez, A., 1997. Detecting leaks from environmental barriers using electrical current imaging. *J. Environ. Eng. Geophys.* 2 (March), 11–19. <https://doi.org/10.4133/JEEG2.1.11>
- Binley, A., Hubbard, S.S., Huisman, J.A., Revil, A., Robinson, D.A., Singha, K., Slater, L.D., 2015. The emergence of hydrogeophysics for improved understanding of subsurface processes over multiple scales. *Water Resour. Res.* 51, 3837–3866. <https://doi.org/10.1002/2015WR017016>

Bibliography

- Binley, A., Ramirez, A.L., Daily, W., 1995. Regularised image reconstruction of noisy electrical resistance data, in: Proceedings of the 4th Workshop of the European Concerted Action on Process Tomography,. Bergen, pp. 401–410.
- Binley, A., Slater, L.D., Fukes, M., Cassiani, G., 2005. Relationship between spectral induced polarization and hydraulic properties of saturated and unsaturated sandstone. *Water Resour. Res.* 41, W12417. <https://doi.org/10.1029/2005WR004202>
- Binley, A., Winship, P., Middleton, R., Pokar, M., West, J., 2001. High-resolution characterization of vadose zone dynamics using cross-borehole radar. *Water Resour. Res.* 37, 2639–2652. <https://doi.org/10.1029/2000WR000089>
- Binley, A., Winship, P., West, L.J., Pokar, M., Middleton, R., 2002b. Seasonal variation of moisture content in unsaturated sandstone inferred from borehole radar and resistivity profiles. *J. Hydrol.* 267, 160–172. [https://doi.org/10.1016/S0022-1694\(02\)00147-6](https://doi.org/10.1016/S0022-1694(02)00147-6)
- Blair, G.S., Henrys, P., Leeson, A., Watkins, J., Eastoe, E., Jarvis, S., Young, P.J., 2019. Data Science of the Natural Environment: A Research Roadmap. *Front. Environ. Sci.* 7. <https://doi.org/10.3389/fenvs.2019.00121>
- Blair, G.S., Watkins, J., August, T., Bassett, R., Brown, M., Ciar, D., Dean, G., Henrys, P., Edwards, L., Nundloll, V., Samreen, F., Simm, W., Towe, R., 2018. Virtual Data Labs: Technological Support for Complex, Collaborative Research in the Environmental Sciences, in: CMWR Conference (Computational Methods in Water Resources). St Malo, France.
- Blome, M., Maurer, H., Greenhalgh, S., 2011. Geoelectric experimental design – Efficient acquisition and exploitation of complete pole-bipole data sets. *GEOPHYSICS* 76, F15–F26. <https://doi.org/10.1190/1.3511350>
- Booth, P.M., 1997. Sellafield site characterisation project: an appraisal of site investigation techniques previously untried at BNFL's sites. Risley, United Kingdom.
- Bouchedda, A., Chouteau, M., Binley, A., Giroux, B., 2012. 2-D joint structural inversion of cross-hole electrical resistance and ground penetrating radar data. *J. Appl. Geophys.* 78, 52–67. <https://doi.org/10.1016/j.jappgeo.2011.10.009>
- Bouchedda, A., Giroux, B., Gloaguen, E., 2015. Bayesian ERT Inversion using Non-Stationary Inverse Matérn Covariance Matrix, in: SEG Annual Meeting. New Orleans.
- Bowden, R.A., Bumpus, C., Littleboy, A.K., 1998. An overview and update of the site characterization studies at Sellafield. *Proc. Yorksh. Geol. Soc.* 52, 125–137. <https://doi.org/10.1144/pygs.52.2.125>
- Bratvold, R.B., Begg, S., 2010. Making good decisions. Society of Petroleum Engineers, Richardson, Texas, USA.
- Brillante, L., Bois, B., Mathieu, O., Bichet, V., Michot, D., Lévêque, J., 2014. Monitoring

Bibliography

- soil volume wetness in heterogeneous soils by electrical resistivity. A field-based pedotransfer function. *J. Hydrol.* 516, 56–66. <https://doi.org/10.1016/j.jhydrol.2014.01.052>
- Brillante, L., Mathieu, O., Bois, B., Van Leeuwen, C., Lévêque, J., 2015. The use of soil electrical resistivity to monitor plant and soil water relationships in vineyards. *Soil* 1, 273–286. <https://doi.org/10.5194/soil-1-273-2015>
- Bruggeman, G.A., 1972. The reciprocity principle in flow through heterogeneous porous media, in: *Fundamentals of Transport Phenomena in Porous Media*, Elsevier, New York, p. 136.
- Brunet, P., Clément, R., Bouvier, C., 2010. Monitoring soil water content and deficit using Electrical Resistivity Tomography (ERT) - A case study in the Cevennes area, France. *J. Hydrol.* 380, 146–153. <https://doi.org/10.1016/j.jhydrol.2009.10.032>
- Brunetti, C., 2019. Bayesian model selection in hydrogeophysics and hydrogeology. Université de Lausanne.
- Brunetti, C., Linde, N., 2018. Impact of petrophysical uncertainty on Bayesian hydrogeophysical inversion and model selection. *Adv. Water Resour.* 111, 346–359. <https://doi.org/10.1016/j.advwatres.2017.11.028>
- Brusseau, M.L., Guo, Z., 2014. Assessing contaminant-removal conditions and plume persistence through analysis of data from long-term pump-and-treat operations. *J. Contam. Hydrol.* 164, 16–24. <https://doi.org/10.1016/j.jconhyd.2014.05.004>
- Cai, Z., Wilson, R.D., Cardiff, M.A., Kitanidis, P.K., 2011. Increasing Confidence in Mass Discharge Estimates Using Geostatistical Methods. *Ground Water* 49, 197–208. <https://doi.org/10.1111/j.1745-6584.2010.00709.x>
- Calendine, S., Rucker, D.F., Fink, J.B., Levitt, M.T., 2011. Automated leak detection of buried tanks using geophysical methods at the Hanford nuclear site, in: *SAGEEP 2011. Annual Meeting of the Environmental and Engineering Geophysical Society*. Charleston, South Carolina.
- Camporese, M., Cassiani, G., Deiana, R., Salandin, P., 2011. Assessment of local hydraulic properties from electrical resistivity tomography monitoring of a three-dimensional synthetic tracer test experiment. *Water Resour. Res.* 47, 1–15. <https://doi.org/10.1029/2011WR010528>
- Camporese, M., Cassiani, G., Deiana, R., Salandin, P., Binley, A., 2015. Coupled and uncoupled hydrogeophysical inversions using ensemble Kalman filter assimilation of ERT-monitored tracer test data. *Water Resour. Res.* 51, 3277–3291. <https://doi.org/10.1002/2014WR016017>
- Carey, A.M., Paige, G.B., Carr, B.J., Dogan, M., 2017. Forward modeling to investigate inversion artifacts resulting from time-lapse electrical resistivity tomography during rainfall simulations. *J. Appl. Geophys.* 145, 39–49. <https://doi.org/10.1016/J.JAPPGEO.2017.08.002>

Bibliography

- Carrassi, A., Bocquet, M., Bertino, L., Evensen, G., 2018. Data assimilation in the geosciences: An overview of methods, issues, and perspectives. *Wiley Interdiscip. Rev. Clim. Chang.* 9, e535. <https://doi.org/10.1002/wcc.535>
- Carrigan, C.R., Yang, X., LaBrecque, D.J., Larsen, D., Freeman, D., Ramirez, A.L., Daily, W., Aines, R., Newmark, R., Friedmann, J., Hovorka, S., 2013. Electrical resistance tomographic monitoring of CO₂ movement in deep geologic reservoirs. *Int. J. Greenh. Gas Control* 18, 401–408. <https://doi.org/10.1016/j.ijggc.2013.04.016>
- Cassiani, G., Binley, A., 2005. Modeling unsaturated flow in a layered formation under quasi-steady state conditions using geophysical data constraints. *Adv. Water Resour.* 28, 467–477. <https://doi.org/10.1016/j.advwatres.2004.12.007>
- Cassiani, G., Bruno, V., Villa, A., Fusi, N., Binley, A.M., 2006. A saline tracer test monitored via time-lapse surface electrical resistivity tomography. *J. Appl. Geophys.* 59, 244–259. <https://doi.org/10.1016/j.jappgeo.2005.10.007>
- Cassiani, G., Godio, A., Stocco, S., Villa, A., Deiana, R., Frattini, P., Rossi, M., 2009. Monitoring the hydrologic behaviour of a mountain slope via time-lapse electrical resistivity tomography. *Near Surf. Geophys.* 7, 475–486. <https://doi.org/10.3997/1873-0604.2009013>
- Caterina, D., Beaujean, J., Robert, T., Nguyen, F., 2013. A comparison study of different image appraisal tools for electrical resistivity tomography. *Near Surf. Geophys.* 11, 639–657. <https://doi.org/10.3997/1873-0604.2013022>
- Caterina, D., Hermans, T., Nguyen, F., 2014. Case studies of incorporation of prior information in electrical resistivity tomography: comparison of different approaches. *Near Surf. Geophys.* 12, 451–465. <https://doi.org/10.3997/1873-0604.2013070>
- Chada, N.K., Iglesias, M.A., Roininen, L., Stuart, A.M., 2018. Parameterizations for ensemble Kalman inversion. <https://doi.org/10.1088/1361-6420/aab6d9>
- Chambers, J.E., Gunn, D.A., Wilkinson, P.B., Meldrum, P.I., Haslam, E., Holyoake, S., Kirkham, M., Kuras, O., Merritt, A., Wragg, J., 2014a. 4D electrical resistivity tomography monitoring of soil moisture dynamics in an operational railway embankment. *Near Surf. Geophys.* 12, 61–72. <https://doi.org/10.3997/1873-0604.2013002>
- Chambers, J.E., Kuras, O., Meldrum, P.I., Ogilvy, R.D., Hollands, J., 2006. Electrical resistivity tomography applied to geologic, hydrogeologic, and engineering investigations at a former waste-disposal site. *Geophysics* 71, B231–B239. <https://doi.org/10.1190/1.2360184>
- Chambers, J.E., Wilkinson, P.B., Penn, S., Meldrum, P.I., Kuras, O., Loke, M.H., Gunn, D.A., 2013. River terrace sand and gravel deposit reserve estimation using three-dimensional electrical resistivity tomography for bedrock surface detection. *J. Appl. Geophys.* 93, 25–32. <https://doi.org/10.1016/j.jappgeo.2013.03.002>

Bibliography

- Chambers, J.E., Wilkinson, P.B., Uhlemann, S., Sorensen, J.P.R., Roberts, C., Newell, A.J., Ward, W.O.C., Binley, A., Williams, P.J., Gooddy, D.C., Old, G., Bai, L., 2014b. Derivation of lowland riparian wetland deposit architecture using geophysical image analysis and interface detection. *Water Resour. Res.* 50, 5886–5905. <https://doi.org/10.1002/2014WR015643>
- Chambers, J.E., Wilkinson, P.B., Wardrop, D., Hameed, A., Hill, I., Jeffrey, C., Loke, M.H., Meldrum, P.I., Kuras, O., Cave, M., Gunn, D.A., 2012. Bedrock detection beneath river terrace deposits using three-dimensional electrical resistivity tomography. *Geomorphology* 177–178, 17–25. <https://doi.org/10.1016/j.geomorph.2012.03.034>
- Chen, H.C., Fang, J.H., 1986. Sensitivity analysis of the parameters in Archie's water saturation equation. *Log Anal.* 27, 39–44. <https://doi.org/SPWLA-1986-vXXVIIIn5a3>
- Chen, J., Hubbard, S., Peterson, J., Williams, K., Fienen, M., Jardine, P., Watson, D., 2006. Development of a joint hydrogeophysical inversion approach and application to a contaminated fractured aquifer. *Water Resour. Res.* 42, 1–13. <https://doi.org/10.1029/2005WR004694>
- Chen, J., Hubbard, S.S., Williams, K.H., 2013. Data-driven approach to identify field-scale biogeochemical transitions using geochemical and geophysical data and hidden Markov models: Development and application at a uranium-contaminated aquifer. *Water Resour. Res.* 49, 6412–6424. <https://doi.org/10.1002/wrcr.20524>
- Chen, J., Hubbard, S.S., Williams, K.H., Ficklin, D.L., 2016. Estimating groundwater dynamics at a Colorado River floodplain site using historical hydrological data and climate information. *Water Resour. Res.* n/a-n/a. <https://doi.org/10.1002/2015WR017777>
- Chen, J.S., Hubbard, S.S., Gaines, D., Korneev, V., Baker, G., Watson, D., 2010. Stochastic estimation of aquifer geometry using seismic refraction data with borehole depth constraints. *Water Resour. Res.* 46, 16. <https://doi.org/W1153910.1029/2009wr008715>
- Chen, X., Hammond, G.E., Murray, C.J., Rockhold, M.L., Vermeul, V.R., Zachara, J.M., 2013. Application of ensemble-based data assimilation techniques for aquifer characterization using tracer data at Hanford 300 area. *Water Resour. Res.* 49, 7064–7076. <https://doi.org/10.1002/2012WR013285>
- Chen, X., Murakami, H., Hahn, M.S., Hammond, G.E., Rockhold, M.L., Zachara, J.M., Rubin, Y., 2012. Three-dimensional Bayesian geostatistical aquifer characterization at the Hanford 300 Area using tracer test data. *Water Resour. Res.* 48, W06501. <https://doi.org/10.1029/2011WR010675>
- Chen, Z., Gómez-Hernández, J.J., Xu, T., Zanini, A., 2018. Joint identification of contaminant source and aquifer geometry in a sandbox experiment with the restart ensemble Kalman filter. *J. Hydrol.* 564, 1074–1084.

Bibliography

<https://doi.org/10.1016/J.JHYDROL.2018.07.073>

- Christ, J.A., Ramsburg, C.A., Pennell, K.D., Abriola, L.M., 2010. Predicting DNAPL mass discharge from pool-dominated source zones. *J. Contam. Hydrol.* <https://doi.org/10.1016/j.jconhyd.2010.02.005>
- Christ, J.A., Ramsburg, C.A., Pennell, K.D., Abriola, L.M., 2006. Estimating mass discharge from dense nonaqueous phase liquid source zones using upscaled mass transfer coefficients: An evaluation using multiphase numerical simulations. *Water Resour. Res.* 42, 1–13. <https://doi.org/10.1029/2006WR004886>
- Christakos, G., 2000. *Modern Spatiotemporal Geostatistics*. Oxford University Press, New York.
- Christensen, S., Doherty, J., 2008. Predictive error dependencies when using pilot points and singular value decomposition in groundwater model calibration. *Adv. Water Resour.* 31, 674–700. <https://doi.org/10.1016/J.ADVWATRES.2008.01.003>
- Cooper, S., 1997. *Assessment of the potential for downhole geophysics within the BHP boreholes*. Risley, United Kingdom.
- Cooper, S., Ross, M.O., 2005. *Application and comparative assessment of non-intrusive site characterisation techniques*. Daresbury, United Kingdom.
- Coscia, I., Greenhalgh, S.A., Linde, N., Doetsch, J., Marescot, L., Günther, T., Vogt, T., Green, A.G., 2011. 3D crosshole ERT for aquifer characterization and monitoring of infiltrating river water. *Geophysics* 76, G49–G59. <https://doi.org/10.1190/1.3553003>
- Crestani, E., 2013. *Tracer Test Assimilation Data for the Assessment of Local Hydraulic Properties in Heterogeneous Aquifers*. University of Padua.
- Crestani, E., Camporese, M., Salandin, P., 2015. Assessment of hydraulic conductivity distributions through assimilation of travel time data from ERT-monitored tracer tests. *Adv. Water Resour.* 84, 23–36. <https://doi.org/10.1016/j.advwatres.2015.07.022>
- Curtis, A., Lomax, A., 2001. Prior information, sampling distributions, and the curse of dimensionality. *GEOPHYSICS* 66, 372–378. <https://doi.org/10.1190/1.1444928>
- Curtis, A., Spencer, C., 1999. Survey design strategies for linearized nonlinear inversion, in: *SEG Technical Program Expanded Abstracts 1999*. Society of Exploration Geophysicists, pp. 1775–1778. <https://doi.org/10.1190/1.1820882>
- Dahlin, T., 2000. Short note on electrode charge-up effects in DC resistivity data acquisition using multi-electrode arrays. *Geophys. Prospect.* 48, 181–187. <https://doi.org/10.1046/j.1365-2478.2000.00172.x>
- Dahlin, T., Dalsegg, E., Sandstrom, T., 2013. Data quality quantification for time domain IP data acquired along a planned tunnel near Oslo, Norway, in: *Near Surface Geoscience 2013--19th European Meeting of Environmental and*

Bibliography

Engineering Geophysics. Bochum, Germany.

- Daily, W., Ramirez, A., 1995. Electrical resistance tomography during in-situ trichloroethylene remediation at the Savannah River Site. *J. Appl. Geophys.* 33, 239–249. [https://doi.org/10.1016/0926-9851\(95\)90044-6](https://doi.org/10.1016/0926-9851(95)90044-6)
- Daily, W., Ramirez, A., Binley, A., 2004. Remote monitoring of leaks in storage tanks using electrical resistance tomography: Application at the Hanford Site. *J. Environ. Eng. Geophys.* 9, 11–24. <https://doi.org/10.4133/jeeeg9.1.11>
- Daily, W., Ramirez, A., Binley, A., LaBrecque, D., 2005. 17. Electrical resistance tomography – theory and practice, in: Butler, D.K. (Ed.), *Near-Surface Geophysics*. Society of Exploration Geophysicists, Tulsa, Oklahoma, USA, pp. 525–550. <https://doi.org/10.1190/1.9781560801719.ch17>
- Daily, W., Ramirez, A., LaBrecque, D., Nitao, J., 1992. Electrical resistivity tomography of vadose water movement. *Water Resour. Res.* 28, 1429–1442. <https://doi.org/10.1029/91WR03087>
- Datta, B., Chakrabarty, D., Dhar, A., 2009. Simultaneous identification of unknown groundwater pollution sources and estimation of aquifer parameters. *J. Hydrol.* 376, 48–57. <https://doi.org/10.1016/J.JHYDROL.2009.07.014>
- Day-Lewis, F.D., Johnson, C.D., Singha, K., Lane Jr, J.W., 2008. Best practices in electrical resistivity imaging: Data collection and processing, and application to data from Corinna, Maine. EPA report, Boston, MA.
- Day-Lewis, F.D., Lane, J.W., 2004. Assessing the resolution-dependent utility of tomograms for geostatistics. *Geophys. Res. Lett.* 31, 2–5. <https://doi.org/10.1029/2004GL019617>
- Day-Lewis, F.D., Singha, K., Binley, A.M., 2005. Applying petrophysical models to radar travel time and electrical resistivity tomograms: Resolution-dependent limitations. *J. Geophys. Res. B Solid Earth* 110, 1–17. <https://doi.org/10.1029/2004JB003569>
- de Barros, F.P.J., Ezzedine, S., Rubin, Y., 2012. Impact of hydrogeological data on measures of uncertainty, site characterization and environmental performance metrics. *Adv. Water Resour.* 36, 51–63. <https://doi.org/10.1016/j.advwatres.2011.05.004>
- de Barros, F.P.J., Rubin, Y., 2008. A risk-driven approach for subsurface site characterization. *Water Resour. Res.* 44, 1–14. <https://doi.org/10.1029/2007WR006081>
- de Pasquale, G., Linde, N., Doetsch, J., Holbrook, W.S., 2019. Probabilistic inference of subsurface heterogeneity and interface geometry using geophysical data. *Geophys. J. Int.* <https://doi.org/10.1093/gji/ggz055>
- Deceuster, J., Kaufmann, O., Camp, M. Van, 2013. Automated identification of changes in electrode contact properties for long-term permanent ERT monitoring

- experiments. *Geophysics* 78, E79–E94. <https://doi.org/10.1190/GEO2012-0088.1>
- Delay, F., Ackerer, P., Guadagnini, A., 2011. Theoretical analysis and field evidence of reciprocity gaps during interference pumping tests. *Adv. Water Resour.* 34, 592–606. <https://doi.org/10.1016/j.advwatres.2011.02.006>
- Deman, G., Konakli, K., Sudret, B., Kerrou, J., Perrochet, P., Benabderrahmane, H., 2016. Using sparse polynomial chaos expansions for the global sensitivity analysis of groundwater lifetime expectancy in a multi-layered hydrogeological model. *Reliab. Eng. Syst. Saf.* 147, 156–169. <https://doi.org/10.1016/j.res.2015.11.005>
- Demirel, S., Irving, J., Roubinet, D., 2019. Comparison of REV size and tensor characteristics for the electrical and hydraulic conductivities in fractured rock. *Geophys. J. Int.* 216, 1953–1973. <https://doi.org/10.1093/gji/ggy537>
- Diggle, P.J., Heagerty, P., Liang, K.-Y., Zeger, S., 2015. *Analysis of Longitudinal Data*, 2nd ed. Oxford University Press.
- Doetsch, J., 2011. Joint and constrained inversion of geophysical data for improved imaging of aquifer structure and processes. ETH Zurich.
- Doetsch, J., Coscia, I., Greenhalgh, S., Linde, N., Green, A., Gunther, T., 2010a. The borehole-fluid effect in electrical resistivity imaging. *Geophysics* 75, F107–F114. <https://doi.org/10.1190/1.3467824>
- Doetsch, J., Kowalsky, M.B., Doughty, C., Finsterle, S., Ajo-Franklin, J.B., Carrigan, C.R., Yang, X., Hovorka, S.D., Daley, T.M., 2013. Constraining CO₂ simulations by coupled modeling and inversion of electrical resistance and gas composition data. *Int. J. Greenh. Gas Control* 18, 510–522. <https://doi.org/10.1016/j.ijggc.2013.04.011>
- Doetsch, J., Linde, N., Binley, A., 2010b. Structural joint inversion of time-lapse crosshole ERT and GPR traveltime data. *Geophys. Res. Lett.* 37, 1–6. <https://doi.org/10.1029/2010GL045482>
- Doetsch, J., Linde, N., Pessognelli, M., Green, A.G., Gunther, T., 2012a. Constraining 3-D electrical resistance tomography with GPR reflection data for improved aquifer characterization. *J. Appl. Geophys.* 78, 68–76. <https://doi.org/10.1016/j.jappgeo.2011.04.008>
- Doetsch, J., Linde, N., Vogt, T., Binley, A., Green, A.G., 2012b. Imaging and quantifying salt-tracer transport in a riparian groundwater system by means of 3D ERT monitoring. *Geophysics* 77, B207. <https://doi.org/10.1190/geo2012-0046.1>
- Dumont, G., Pilawski, T., Dzaomuh-Lenieregue, P., Hiligsmann, S., Delvigne, F., Thonart, P., Robert, T., Nguyen, F., Hermans, T., 2016. Gravimetric water distribution assessment from geoelectrical methods (ERT and EMI) in municipal solid waste landfill. *Waste Manag.* 55, 129–140. <https://doi.org/10.1016/J.WASMAN.2016.02.013>
- Dumont, G., Pilawski, T., Hermans, T., Nguyen, F., Garré, S., 2018. The effect of initial water distribution and spatial resolution on the interpretation of ERT monitoring

Bibliography

- of water infiltration in a landfill cover. *Hydrol. Earth Syst. Sci. Discuss.* 1–26. <https://doi.org/10.5194/hess-2018-163>
- Eddy-Dilek, C.A., Looney, B.B., Hoekstra, P., Harthill, N., Blohm, M., Phillips, D.B., 1997. Definition of a critical confining zone using surface geophysical methods. *Groundwater* 35, 451–462.
- Edwards, L.S., 1977. A modified pseudosection for resistivity and IP. *Geophysics* 42, 1020–1036. <https://doi.org/10.1190/1.1440762>
- Eidsvik, J., Mukerji, T., Bhattacharjya, D., 2015. Value of information in the earth sciences: Integrating spatial modeling and decision analysis. Cambridge University Press, Cambridge.
- Elwaseif, M., Slater, L., 2012. Improved Resistivity Imaging of Targets with Sharp Boundaries Using an Iterative Disconnect Procedure. *J. Environ. Eng. Geophys.* 17, 89–101. <https://doi.org/10.2113/JEEG17.2.89>
- Emerick, A.A., Reynolds, A.C., 2013. Ensemble smoother with multiple data assimilation. *Comput. Geosci.* 55, 3–15. <https://doi.org/10.1016/j.cageo.2012.03.011>
- Enescu, N., Ahokas, T., Heikkinen, E., Cosma, C., 2004. Integrated Geophysical Characterization of a Hard Rock Site, in: EAGE 66th Conference & Exhibition. Paris, France, pp. 7–10.
- Environment Agency, 2011. Geophysical surveying techniques to characterise a site for a geological disposal facility: A review of recent developments and NDA's proposals.
- Eslick, J.C., Ng, B., Gao, Q., Tong, C.H., Sahinidis, N. V., Miller, D.C., 2014. A framework for optimization and quantification of uncertainty and sensitivity for developing carbon capture systems. *Energy Procedia* 63, 1055–1063. <https://doi.org/10.1016/j.egypro.2014.11.113>
- Evensen, G., 2018. Analysis of iterative ensemble smoothers for solving inverse problems. *Comput. Geosci.* 22, 885–908. <https://doi.org/10.1007/s10596-018-9731-y>
- Falade, G.K., 1981. Analysis of the reciprocity concept in a porous medium. *Water Resour. Res.* 17, 918–920. <https://doi.org/10.1029/WR017i004p00918>
- Falzone, S., Robinson, J., Slater, L., 2018. Characterization and Monitoring of Porous Media with Electrical Imaging: A Review. *Transp. Porous Media* 1–26. <https://doi.org/10.1007/s11242-018-1203-2>
- Fan, J., Scheuermann, A., Guyot, A., Baumgartl, T., Lockington, D.A., 2015. Quantifying spatiotemporal dynamics of root-zone soil water in a mixed forest on subtropical coastal sand dune using surface ERT and spatial TDR. *J. Hydrol.* 523, 475–488. <https://doi.org/10.1016/j.jhydrol.2015.01.064>
- Farquharson, C.G., 2008. Constructing piecewise-constant models in multidimensional

Bibliography

- minimum-structure inversions. *GEOPHYSICS* 73, K1–K9.
<https://doi.org/10.1190/1.2816650>
- Fernández-Martínez, J.L., Fernández-Muñiz, Z., Xu, S., Cernea, A., Sirieix, C., Riss, J., 2019. Efficient uncertainty analysis of the 3D electrical tomography inverse problem. *GEOPHYSICS* 1–62. <https://doi.org/10.1190/geo2017-0729.1>
- Fernández-Muñiz, Z., Khaniani, H., Fernández-Martínez, J.L., 2019. Data kit inversion and uncertainty analysis. *J. Appl. Geophys.* 161, 228–238. <https://doi.org/10.1016/j.jappgeo.2018.12.022>
- Feyen, L., Gorelick, S.M., 2005. Framework to evaluate the worth of hydraulic conductivity data for optimal groundwater resources management in ecologically sensitive areas. *Water Resour. Res.* 41, 1–13. <https://doi.org/10.1029/2003WR002901>
- Fiandaca, G., Doetsch, J., Vignoli, G., Auken, E., 2015. Generalized focusing of time-lapse changes with applications to direct current and time-domain induced polarization inversions 1101–1112. <https://doi.org/10.1093/gji/ggv350>
- Flores-Orozco, A., Kemna, A., Zimmermann, E., 2012. Data error quantification in spectral induced polarization imaging. *Geophysics* 77, E227. <https://doi.org/10.1190/geo2010-0194.1>
- Flores-Orozco, A., Williams, K.H., Kemna, A., 2013. Time-lapse spectral induced polarization imaging of stimulated uranium bioremediation. *Near Surf. Geophys.* 11, 531–544. <https://doi.org/10.3997/1873-0604.2013020>
- Flores-Orozco, A., Williams, K.H., Long, P.E., Hubbard, S.S., Kemna, A., 2011. Using complex resistivity imaging to infer biogeochemical processes associated with bioremediation of an uranium-contaminated aquifer. *J. Geophys. Res. Biogeosciences* 116, 1–17. <https://doi.org/10.1029/2010JG001591>
- Frangos, W., Ter-Saakian, S., 1996. Resistivity and induced polarization survey at a Russian nuclear waste site. Berkeley, California, United States. <https://doi.org/10.1149/1.2221597>
- French, H.K., Kästner, M., van der Zee, S.E.A.T.M., 2014. New approaches for low-invasive contaminated site characterization, monitoring and modelling. *Environ. Sci. Pollut. Res.* 21, 8893–8896. <https://doi.org/10.1007/s11356-014-2840-9>
- Friedel, S., 2003. Resolution, stability and efficiency of resistivity tomography estimated from a generalized inverse approach. *Geophys. J. Int.* 153, 305–316. <https://doi.org/10.1046/j.1365-246X.2003.01890.x>
- Friedman, S.P., 2005. Soil properties influencing apparent electrical conductivity: a review. *Comput. Electron. Agric.* 46, 45–70. <https://doi.org/10.1016/j.compag.2004.11.001>
- Fu, J., Jaime Gómez-Hernández, J., 2009. Uncertainty assessment and data worth in groundwater flow and mass transport modeling using a blocking Markov chain

Bibliography

- Monte Carlo method. *J. Hydrol.* 364, 328–341.
<https://doi.org/10.1016/j.jhydrol.2008.11.014>
- Furman, A., Ferré, T.P.A., Heath, G.L., 2007. Spatial focusing of electrical resistivity surveys considering geologic and hydrologic layering. *Geophysics* 72, F65.
<https://doi.org/10.1190/1.2433737>
- Furman, A., Ferré, T.P.A., Warrick, A.W., 2004. Optimization of ERT Surveys for Monitoring Transient Hydrological Events Using Perturbation Sensitivity and Genetic Algorithms. *Vadose Zo. J.* 3, 1230. <https://doi.org/10.2136/vzj2004.1230>
- Galetti, E., Curtis, A., 2018. Transdimensional Electrical Resistivity Tomography. *J. Geophys. Res. Solid Earth.* <https://doi.org/10.1029/2017JB015418>
- Gallardo, L.A., Meju, M.A., 2011. Structure-coupled multiphysics imaging in geophysical sciences. *Rev. Geophys.* 49, RG1003.
<https://doi.org/10.1029/2010RG000330>
- Gan, Y., Duan, Q., Gong, W., Tong, C., Sun, Y., Chu, W., Ye, A., Miao, C., Di, Z., 2014. A comprehensive evaluation of various sensitivity analysis methods: A case study with a hydrological model. *Environ. Model. Softw.* 51, 269–285.
<https://doi.org/10.1016/j.envsoft.2013.09.031>
- Garré, S., Coteur, I., Wongleecharoen, C., Kongkaew, T., Diels, J., Vanderborght, J., 2013. Noninvasive Monitoring of Soil Water Dynamics in Mixed Cropping Systems: A Case Study in Ratchaburi Province, Thailand. *Vadose Zo. J.* 12, 0.
<https://doi.org/10.2136/vzj2012.0129>
- Garré, S., Javaux, M., Vanderborght, J., Pagès, L., Vereecken, H., 2011. Three-Dimensional Electrical Resistivity Tomography to Monitor Root Zone Water Dynamics. *Vadose Zo. J.* 10, 412. <https://doi.org/10.2136/vzj2010.0079>
- Gasperikova, E., Hubbard, S.S., Watson, D.B., Baker, G.S., Peterson, J.E., Kowalsky, M.B., Smith, M., Brooks, S., 2012. Long-term electrical resistivity monitoring of recharge-induced contaminant plume behavior. *J. Contam. Hydrol.* 142–143, 33–49. <https://doi.org/10.1016/j.jconhyd.2012.09.007>
- Gelhar, L., Axness, C., 1983. Three-dimensional stochastic analysis of macrodispersion in aquifers. *Water Resour. Res.* 19, 161–180.
- Gélis, C., Revil, A., Cushing, M.E., Jougnot, D., Lemeille, F., Cabrera, J., de Hoyos, A., Rocher, M., 2010. Potential of electrical resistivity tomography to detect fault zones in limestone and argillaceous formations in the experimental platform of Tournemire, France. *Pure Appl. Geophys.* 167, 1405–1418.
<https://doi.org/10.1007/s00024-010-0097-x>
- Gephart, R.E., 2010. A short history of waste management at the Hanford Site. *Phys. Chem. Earth, Parts A/B/C* 35, 298–306. <https://doi.org/10.1016/J.PCE.2010.03.032>
- Gephart, R.E., 2003. A short history of Hanford waste generation, storage, and release. *Pnnl-13605* 1–39.

Bibliography

- Ghorbanidehno, H., Kokkinaki, A., Li, J.Y., Darve, E., Kitanidis, P.K., 2015. Real-time data assimilation for large-scale systems: The spectral Kalman filter. *Adv. Water Resour.* 86, 260–272. <https://doi.org/10.1016/j.advwatres.2015.07.017>
- Glaser, D.R., Fink, J.B., Levitt, M.T., Rucker, D.F., 2008. A summary of recent geophysical investigations at the Department of Energy Hanford Nuclear Facility, in: 2008 Chapman Conference on Biogeophysics. Portland, Maine.
- Glover, P.W.J., 2017. A new theoretical interpretation of Archie's saturation exponent. *Solid Earth* 8, 805–816. <https://doi.org/10.5194/se-8-805-2017>
- Glover, P.W.J., 2015. Geophysical Properties of the Near Surface Earth: Electrical Properties, in: *Treatise on Geophysics*. Elsevier, pp. 89–137. <https://doi.org/10.1016/B978-0-444-53802-4.00189-5>
- Gottschalk, I.P., Hermans, T., Knight, R., Caers, J., Cameron, D.A., Regnery, J., McCray, J.E., 2017. Integrating non-colocated well and geophysical data to capture subsurface heterogeneity at an aquifer recharge and recovery site. *J. Hydrol.* 555, 407–419. <https://doi.org/10.1016/j.jhydrol.2017.10.028>
- Gouveia, W.P., Scales, J.A., 1997. Resolution of seismic waveform inversion: Bayes versus Occam. *Inverse Probl.* 13, 323–349. <https://doi.org/10.1088/0266-5611/13/2/009>
- Green, C.T., Liao, L., Nolan, B.T., Juckem, P.F., Shope, C.L., Tesoriero, A.J., Jurgens, B.C., 2018. Regional Variability of Nitrate Fluxes in the Unsaturated Zone and Groundwater, Wisconsin, USA. *Water Resour. Res.* 54, 301–322. <https://doi.org/10.1002/2017WR022012>
- Gunning, J., Glinsky, M.E., Hedditch, J., 2010. Resolution and uncertainty in 1D CSEM inversion: A Bayesian approach and open-source implementation. *Geophysics* 75, F151. <https://doi.org/10.1190/1.3496902>
- Günther, T., Rücker, C., Spitzer, K., 2006. Three-dimensional modelling and inversion of dc resistivity data incorporating topography - II. Inversion. *Geophys. J. Int.* 166, 506–517. <https://doi.org/10.1111/j.1365-246X.2006.03011.x>
- Haarder, E.B., Binley, A., Looms, M.C., Doetsch, J., Nielsen, L., Jensen, K.H., 2012. Comparing Plume Characteristics Inferred from Cross-Borehole Geophysical Data. *Vadose Zo. J.* 11, 1–40. <https://doi.org/10.2136/vzj2012.0031>
- Hadamard, J., 1902. Sur les problèmes aux dérivées partielles et leur signification physique. *Princet. Univ. Bull.* 13, 49–52.
- Hadley, P.W., Newell, C.J., 2012. Groundwater Remediation: The Next 30 Years. *Ground Water* 50, 669–678. <https://doi.org/10.1111/j.1745-6584.2012.00942.x>
- Hammond, G.E., Lichtner, P.C., 2010. Field-scale model for the natural attenuation of uranium at the Hanford 300 Area using high-performance computing. *Water Resour. Res.* 46, 1–31. <https://doi.org/10.1029/2009WR008819>

Bibliography

- Hammond, G.E., Lichtner, P.C., Mills, R.T., 2014. Evaluating the performance of parallel subsurface simulators: An illustrative example with PFLOTRAN. *Water Resour. Res.* 50, 208–228. <https://doi.org/10.1002/2012WR013483>
- Hayley, K., Pidlisecky, A., Bentley, L.R., 2011. Simultaneous time-lapse electrical resistivity inversion. *J. Appl. Geophys.* 75, 401–411. <https://doi.org/10.1016/j.jappgeo.2011.06.035>
- Hen-Jones, R.M., Hughes, P.N., Stirling, R.A., Glendinning, S., Chambers, J.E., Gunn, D.A., Cui, Y.J., 2017. Seasonal effects on geophysical–geotechnical relationships and their implications for electrical resistivity tomography monitoring of slopes. *Acta Geotech.* 12, 1159–1173. <https://doi.org/10.1007/s11440-017-0523-7>
- Hermans, T., Kemna, A., Nguyen, F., 2016a. Covariance-constrained difference inversion of time-lapse electrical resistivity tomography data. *GEOPHYSICS* 81, E311–E322. <https://doi.org/10.1190/geo2015-0491.1>
- Hermans, T., Nguyen, F., Caers, J., 2015. Uncertainty in training image-based inversion of hydraulic head data constrained to ERT data: Workflow and case study. *Water Resour. Res.* 51, 5332–5352. <https://doi.org/10.1002/2014WR016259>
- Hermans, T., Nguyen, F., Klepikova, M., Dassargues, A., Caers, J., 2018. Uncertainty Quantification of Medium-Term Heat Storage From Short-Term Geophysical Experiments Using Bayesian Evidential Learning. *Water Resour. Res.* 54, 2931–2948. <https://doi.org/10.1002/2017WR022135>
- Hermans, T., Nguyen, F., Robert, T., Revil, A., 2014. Geophysical methods for monitoring temperature changes in shallow low enthalpy geothermal systems. *Energies* 7, 5083–5118. <https://doi.org/10.3390/en7085083>
- Hermans, T., Oware, E., Caers, J., 2016b. Direct prediction of spatially and temporally varying physical properties from time-lapse electrical resistance data. *Water Resour. Res.* 52, 7262–7283. <https://doi.org/10.1002/2016WR019126>
- Hermans, T., Vandenbohede, A., Lebbe, L., Martin, R., Kemna, A., Beaujean, J., Nguyen, F., 2012. Imaging artificial salt water infiltration using electrical resistivity tomography constrained by geostatistical data. *J. Hydrol.* 438–439, 168–180. <https://doi.org/10.1016/J.JHYDROL.2012.03.021>
- Hinnell, A.C., Ferr, T.P.A., Vrugt, J.A., Huisman, J.A., Moysey, S., Rings, J., Kowalsky, M.B., 2010. Improved extraction of hydrologic information from geophysical data through coupled hydrogeophysical inversion. *Water Resour. Res.* 46, 1–14. <https://doi.org/10.1029/2008WR007060>
- Hu, L.Y., Chuginova, T., 2008. Multiple-point geostatistics for modeling subsurface heterogeneity: A comprehensive review. *Water Resour. Res.* 44, 1–14. <https://doi.org/10.1029/2008WR006993>
- Huang, H.-T., 2013. Radionuclide Migration in Low-level Radioactive Waste Disposal at Lan-Yu Site (in Chinese). National Cheng Kung University.

Bibliography

- Hübner, R., Heller, K., Günther, T., Kleber, A., 2015. Monitoring hillslope moisture dynamics with surface ERT for enhancing spatial significance of hydrometric point measurements. *Hydrol. Earth Syst. Sci.* 19, 225–240. <https://doi.org/10.5194/hess-19-225-2015>
- Huisman, J.A., Rings, J., Vrugt, J.A., Sorg, J., Vereecken, H., 2010. Hydraulic properties of a model dike from coupled Bayesian and multi-criteria hydrogeophysical inversion. *J. Hydrol.* 380, 62–73. <https://doi.org/10.1016/j.jhydrol.2009.10.023>
- Huntley, D., Bobrowsky, P., Hendry, M., Macciotta, R., Elwood, D., Sattler, K., Best, M., Chambers, J., Meldrum, P., 2019. Application of multi-dimensional electrical resistivity tomography datasets to investigate a very slow-moving landslide near Ashcroft, British Columbia, Canada. *Landslides* 16, 1033–1042. <https://doi.org/10.1007/s10346-019-01147-1>
- Iglesias, M., Yang, Y., n.d. A Computational efficient framework for ensemble Kalman inversion with applications to non-destructive testing and imaging. Prep.
- Iglesias, M.A., 2016. A regularizing iterative ensemble Kalman method for PDE-constrained inverse problems. *Inverse Probl.* 32, 025002. <https://doi.org/10.1088/0266-5611/32/2/025002>
- Iglesias, M.A., Lin, K., Stuart, A.M., 2014. Well-posed Bayesian geometric inverse problems arising in subsurface flow. *Inverse Probl.* 30, 114001. <https://doi.org/10.1088/0266-5611/30/11/114001>
- Iglesias, M.A., McLaughlin, D., 2011. Level-set techniques for facies identification in reservoir modeling. *Inverse Probl.* 27, 36. <https://doi.org/10.1088/0266-5611/27/3/035008>
- Iglesias, M.A., Stuart, A.M., 2014. Inverse problems and uncertainty quantification. *SIAM News* 2–3.
- Iooss, B., 2019. Package ‘sensitivity.’
- Irving, J., Singha, K., 2010. Stochastic inversion of tracer test and electrical geophysical data to estimate hydraulic conductivities. *Water Resour. Res.* 46, W11514. <https://doi.org/10.1029/2009WR008340>
- ITRC, 2010. Use and Measurement of Mass Flux and Mass Discharge, Use and Measurement of Mass Flux and Mass Discharge. Washington DC.
- JafarGandomi, A., Binley, A., 2013. A Bayesian trans-dimensional approach for the fusion of multiple geophysical datasets. *J. Appl. Geophys.* 96, 38–54. <https://doi.org/10.1016/j.jappgeo.2013.06.004>
- Jardani, A., Revil, A., Dupont, J.P., 2013. Stochastic joint inversion of hydrogeophysical data for salt tracer test monitoring and hydraulic conductivity imaging. *Adv. Water Resour.* 52, 62–77. <https://doi.org/10.1016/j.advwatres.2012.08.005>
- Jayawickreme, D.H., van Dam, R.L., Hyndman, D.W., 2008. Subsurface imaging of

Bibliography

- vegetation, climate, and root-zone moisture interactions. *Geophys. Res. Lett.* 35, 1–5. <https://doi.org/10.1029/2008GL034690>
- Johnson, T., Triplett, M., Wellman, D., Northwest, P., 2014. Modeling of electrical resistivity data in the presence of electrically conductive well casings and waste storage tanks, in: WM2014 Conference, March 2 – 6. Phoenix, Arizona, USA, p. 7.
- Johnson, T.C., Hammond, G.E., Chen, X., 2017. PFLOTRAN-E4D: A parallel open source PFLOTRAN module for simulating time-lapse electrical resistivity data. *Comput. Geosci.* 99, 72–80. <https://doi.org/10.1016/j.cageo.2016.09.006>
- Johnson, T.C., Rucker, D.F., Glaser, D.R., 2015a. Near-Surface Geophysics at the Hanford Nuclear Site, the United States, in: *Treatise on Geophysics*. Elsevier, pp. 571–595. <https://doi.org/10.1016/B978-0-444-53802-4.00205-0>
- Johnson, T.C., Slater, L.D., Ntarlagiannis, D., Day-Lewis, F.D., Elwaseif, M., 2012a. Monitoring groundwater-surface water interaction using time-series and time-frequency analysis of transient three-dimensional electrical resistivity changes. *Water Resour. Res.* 48, 1–13. <https://doi.org/10.1029/2012WR011893>
- Johnson, T.C., Versteeg, R., Thomle, J., Hammond, G., Chen, X., Zachara, J., 2015b. Four-dimensional electrical conductivity monitoring of stage-driven river water intrusion: Accounting for water table effects using a transient mesh boundary and conditional inversion constraints. *Water Resour. Res.* 51, 6177–6196. <https://doi.org/10.1002/2014WR016129>
- Johnson, T.C., Versteeg, R.J., Day-Lewis, F.D., Major, W., Lane, J.W., 2015c. Time-Lapse Electrical Geophysical Monitoring of Amendment-Based Biostimulation. *Groundwater* 53, 920–932. <https://doi.org/10.1111/gwat.12291>
- Johnson, T.C., Versteeg, R.J., Huang, H., Routh, P.S., 2009. Data-domain correlation approach for joint hydrogeologic inversion of time-lapse hydrogeologic and geophysical data. *Geophysics* 74, F127. <https://doi.org/10.1190/1.3237087>
- Johnson, T.C., Versteeg, R.J., Rockhold, M., Slater, L.D., Ntarlagiannis, D., Greenwood, W.J., Zachara, J., 2012b. Characterization of a contaminated wellfield using 3D electrical resistivity tomography implemented with geostatistical, discontinuous boundary, and known conductivity constraints. *Geophysics* 77, EN85. <https://doi.org/10.1190/geo2012-0121.1>
- Johnson, T.C., Versteeg, R.J., Ward, A., Day-Lewis, F.D., Revil, A., 2010. Improved hydrogeophysical characterization and monitoring through parallel modeling and inversion of time-domain resistivity and induced-polarization data. *Geophysics* 75, WA27. <https://doi.org/10.1190/1.3475513>
- Johnson, T.C., Wellman, D., 2015. Accurate modelling and inversion of electrical resistivity data in the presence of metallic infrastructure with known location and dimension. *Geophys. J. Int.* 202, 1096–1108. <https://doi.org/10.1093/gji/ggv206>
- Johnson, T.C., Wellman, D.M., 2013. Re-inversion of surface electrical resistivity

tomography data from the Hanford Site B-Complex.

- Jonard, F., Bogena, H., Caterina, D., Garré, S., Klotzsche, A., Monerris, A., Schwank, M., von Hebel, C., 2018. Ground-Based Soil Moisture Determination, in: Li, X., Vereecken, H. (Eds.), *Observation and Measurement of Ecohydrological Processes*. Springer, pp. 1–42. https://doi.org/10.1007/978-3-662-47871-4_2-1
- Jordi, C., Doetsch, J., Günther, T., Schmelzbach, C., Robertsson, J.O., 2018. Geostatistical regularization operators for geophysical inverse problems on irregular meshes. *Geophys. J. Int.* 213, 1374–1386. <https://doi.org/10.1093/gji/ggy055>
- Ju, L., Zhang, J., Meng, L., Wu, L., Zeng, L., 2018. An adaptive Gaussian process-based iterative ensemble smoother for data assimilation. *Adv. Water Resour.* <https://doi.org/10.1016/j.advwatres.2018.03.010>
- Kaipio, J.P., Karjalainen, P.A., Somersalo, E., Vauhkonen, M., 1999. State estimation in time-varying electrical impedance tomography. *Ann. N. Y. Acad. Sci.* <https://doi.org/10.1111/j.1749-6632.1999.tb09492.x>
- Kaipio, J.P., Somersalo, E., 2006. *Statistical and computational inverse problems*. Springer-Verlag, New York.
- Kang, X., Shi, X., Deng, Y., Revil, A., Xu, H., Wu, J., 2018. Coupled hydrogeophysical inversion of DNAPL source zone architecture and permeability field in a 3D heterogeneous sandbox by assimilation time-lapse cross-borehole electrical resistivity data via ensemble Kalman filtering. *J. Hydrol.* 567, 149–164. <https://doi.org/10.1016/J.JHYDROL.2018.10.019>
- Kang, X., Shi, X., Revil, A., Cao, Z., Li, L., Lan, T., Wu, J., 2019. Coupled hydrogeophysical inversion to identify non-Gaussian hydraulic conductivity field by jointly assimilating geochemical and time-lapse geophysical data. *J. Hydrol.* <https://doi.org/10.1016/j.jhydrol.2019.124092>
- Karaoulis, M., Kim, J.-H., Tsourlos, P.I., 2011a. 4D active time constrained resistivity inversion. *J. Appl. Geophys.* 73, 25–34. <https://doi.org/10.1016/j.jappgeo.2010.11.002>
- Karaoulis, M., Revil, A., Werkema, D.D., Minsley, B.J., Woodruff, W.F., Kemna, A., 2011b. Time-lapse three-dimensional inversion of complex conductivity data using an active time constrained (ATC) approach. *Geophys. J. Int.* 187, 237–251. <https://doi.org/10.1111/j.1365-246X.2011.05156.x>
- Kemna, A., 2000. *Tomographic inversion of complex resistivity*. Ruhr-Universität Bochum.
- Kemna, A., Binley, A.M., Slater, L., 2004. Cross-borehole IP imaging for engineering and environmental applications. *Geophysics* 69, 97–107. <https://doi.org/10.1190/1.1649379>
- Key, K.T., 1977. Nuclear waster tank and pipeline external leak detection systems.

Bibliography

Richland, Washington.

- Killick, R., Fearnhead, P., Eckley, I.A., 2012. Optimal Detection of Changepoints With a Linear Computational Cost. *J. Am. Stat. Assoc.* 107, 1590–1598. <https://doi.org/10.1080/01621459.2012.737745>
- Kim, J.-H., Yi, M.-J., Park, S.-G., Kim, J.G., 2009. 4-D inversion of DC resistivity monitoring data acquired over a dynamically changing earth model. *J. Appl. Geophys.* 68, 522–532. <https://doi.org/10.1016/j.jappgeo.2009.03.002>
- Kim, J., Supper, R., Ottowitz, D., Jochum, B., Yi, M., 2016. A new measurement protocol of direct current resistivity data. *Geophysics* 81.
- Kimbell, G.S., 1994. The interpretation of gravity and aeromagnetic data for the geological investigation of the Sellafield area, west Cumbria. *Proc. Yorksh. Geol. Soc.* 50, 103–112. <https://doi.org/10.1144/pygs.50.1.103>
- Kitanidis, P.K., 2015a. Three-dimensional ERT imaging by the geostatistical approach, in: American Geophysical Union Fall Meeting. San Francisco, California.
- Kitanidis, P.K., 2015b. Persistent questions of heterogeneity, uncertainty, and scale in subsurface flow and transport. *Water Resour. Res.* 51, 5888–5904. <https://doi.org/10.1002/2015WR017639>
- Kitanidis, P.K., 2011. Bayesian and Geostatistical Approaches to Inverse Problems, in: Biegler, L., Biros, G., Ghattas, O., Heinkenschloss, M., Keyes, D., Mallick, B., Marzouk, Y., Tenorio, L., van Bloemen Waanders, B., Willcox, K. (Eds.), *Large-Scale Inverse Problems and Quantification of Uncertainty*. John Wiley & Sons, Ltd, Chichester, UK, pp. 71–85. <https://doi.org/10.1002/9780470685853>
- Kitanidis, P.K., 1995. Quasi-linear geostatistical theory for inversing. *Water Resour. Res.* 31, 2411–2419.
- Koch, J., Nowak, W., 2016. Identification of contaminant source architectures—A statistical inversion that emulates multiphase physics in a computationally practicable manner. *Water Resour. Res.* 52. <https://doi.org/10.1002/2014WR015716>
- Koestel, J., Kemna, A., Javaux, M., Binley, A., Vereecken, H., 2008. Quantitative imaging of solute transport in an unsaturated and undisturbed soil monolith with 3-D ERT and TDR. *Water Resour. Res.* 44, 1–17. <https://doi.org/10.1029/2007WR006755>
- Köpke, C., Elsheikh, A.H., Irving, J., 2019. Hydrogeophysical Parameter Estimation Using Iterative Ensemble Smoothing and Approximate Forward Solvers. *Front. Environ. Sci.* 7, 34. <https://doi.org/10.3389/fenvs.2019.00034>
- Kowalsky, M.B., Finsterle, S., Peterson, J., Hubbard, S., Rubin, Y., Majer, E., Ward, A., Gee, G., 2005. Estimation of field-scale soil hydraulic and dielectric parameters through joint inversion of GPR and hydrological data. *Water Resour. Res.* 41, n/a-n/a. <https://doi.org/10.1029/2005WR004237>

Bibliography

- Kowalsky, M.B., Gasperikova, E., Finsterle, S., Watson, D., Baker, G., Hubbard, S.S., 2011. Coupled modeling of hydrogeochemical and electrical resistivity data for exploring the impact of recharge on subsurface contamination. *Water Resour. Res.* 47, W02509. <https://doi.org/10.1029/2009WR008947>
- Kuras, O., Pritchard, J.D., Meldrum, P.I., Chambers, J.E., Wilkinson, P.B., Ogilvy, R.D., 2009. Monitoring hydraulic processes with Automated time-Lapse Electrical Resistivity Tomography (ALERT). *Comptes Rendus Geosci.* 351, 868–885.
- Kuras, O., Wilkinson, P.B., Meldrum, P.I., Oxby, L.S., Uhlemann, S., Chambers, J.E., Binley, A., Graham, J., Smith, N.T., Atherton, N., 2016. Geoelectrical monitoring of simulated subsurface leakage to support high-hazard nuclear decommissioning at the Sellafield Site, UK. *Sci. Total Environ.* 566–567, 350–359. <https://doi.org/10.1016/j.scitotenv.2016.04.212>
- Kuras, O., Wilkinson, P.B., Meldrum, P.I., Oxby, L.S., Uhlemann, S., Chambers, J.E., Binley, A.M., Graham, J., Dewey, G., Atherton, N., 2014. A trial of 4D Cross-hole electrical resistivity tomography (ERT) for detecting and monitoring subsurface leakage and contaminant transport, supporting the decommissioning of legacy silos at the Sellafield Site, UK, in: WM2014 Conference, March 2 – 6. Phoenix, Arizona, USA.
- Kuras, O., Wilkinson, P.B., Meldrum, P.I., Uhlemann, S., Chambers, J.E., 2015. Results of the GEMS ERT trial and extended baseline measurements at Sellafield. Keyworth.
- Kuras, O., Wilkinson, P.B., White, J.C., Chambers, J.E., Meldrum, P.I., Ogilvy, R.D., 2011. MSSS leak mitigation-leak detection phase 3: Desk study for ERT technology. Keyworth.
- Kwong, S., Fowler, L., 2014. Technical Memorandum: MSSS Electrical Resistivity Tomography (ERT): TRAFFIC modelling of the ERT trial.
- LaBrecque, D.J., Heath, G., Sharpe, R., Versteeg, R., 2004. Autonomous Monitoring of Fluid Movement Using 3-D Electrical Resistivity Tomography. *J. Environ. Eng. Geophys.* 9, 167–176. <https://doi.org/10.4133/JEEG9.3.167>
- LaBrecque, D.J., Mletto, M., Daily, W., Ramirez, A.L., Owen, E., 1996a. The effects of noise on Occam's inversion of resistivity tomography data. *Geophysics* 61, 538. <https://doi.org/10.1190/1.1443980>
- LaBrecque, D.J., Ramirez, A.L., Daily, W.D., Binley, A.M., Schima, S.A., 1996b. ERT monitoring on environmental remediation processes. *Meas. Sci. Technol.* 7, 375–383. <https://doi.org/10.1088/0957-0233/7/3/019>
- LaBrecque, D.J., Yang, X., 2001. Difference inversion of ERT data: a fast inversion method for 3-D in situ monitoring. *J. Environ. Eng. Geophys.* 6, 83–89. <https://doi.org/dx.doi.org/10.4133/JEEG6.2.83>
- Laloy, E., Hérault, R., Jacques, D., Linde, N., 2017. Efficient training-image based

Bibliography

- geostatistical simulation and inversion using a spatial generative adversarial neural network 1–44.
- Laloy, E., Javaux, M., Vanclooster, M., Roisin, C., Biielders, C.L., 2011. Electrical Resistivity in a Loamy Soil: Identification of the Appropriate Pedo-Electrical Model. *Vadose Zo. J.* 10, 1023. <https://doi.org/10.2136/vzj2010.0095>
- Lan, T., Shi, X., Jiang, B., Sun, Y., Wu, J., 2018. Joint inversion of physical and geochemical parameters in groundwater models by sequential ensemble-based optimal design. *Stoch. Environ. Res. Risk Assess.* 5. <https://doi.org/10.1007/s00477-018-1521-5>
- Last, G. V., Horton, D.G., 2000. Review of geophysical characterization methods used at the Hanford Site.
- Le, D.H., Emerick, A.A., Reynolds, A.C., 2016. An Adaptive Ensemble Smoother With Multiple Data Assimilation for Assisted History Matching. *SPE J.* 21, 2195–2207. <https://doi.org/10.2118/173214-PA>
- Lean, C., 1998a. The use of surface geophysics in the geological characterisation of Sellafield. Risley, United Kingdom.
- Lean, C., 1998b. TerraDat geophysical site investigation at the buried channel area of Sellafield. Risley, United Kingdom.
- Lee, J., Kitanidis, P.K., 2014. Large-scale hydraulic tomography and joint inversion of head and tracer data using the Principal Component Geostatistical Approach (PCGA). *Water Resour. Res.* 50. <https://doi.org/10.1002/2014WR015483>
- Lee, J., Liu, X., Kitanidis, P.K., Kim, U., Parker, J., Bloom, A., Lyon, R., 2012. Cost optimization of DNAPL remediation at Dover Air Force Base Site. *Groundw. Monit. Remediat.* 48–56. <https://doi.org/10.1111/j1745>
- Lehikoinen, A., Finsterle, S., Voutilainen, A., Kowalsky, M.B., Kaipio, J.P., 2009. Dynamical inversion of geophysical ERT data: state estimation in the vadose zone. *Inverse Probl. Sci. Eng.* 17, 715–736. <https://doi.org/10.1080/17415970802475951>
- Lehmann, P., Gambazzi, F., Suski, B., Baron, L., Askarinejad, A., Springman, S.M., Holliger, K., Or, D., 2013. Evolution of soil wetting patterns preceding a hydrologically induced landslide inferred from electrical resistivity survey and point measurements of volumetric water content and pore water pressure. *Water Resour. Res.* 49, 7992–8004. <https://doi.org/10.1002/2013WR014560>
- Lelièvre, P.G., Farquharson, C.G., 2013. Gradient and smoothness regularization operators for geophysical inversion on unstructured meshes. *Geophys. J. Int.* 195, 330–341. <https://doi.org/10.1093/gji/ggt255>
- Lesmes, D.P., Friedman, S.P., 2005. Relationships between the Electrical and Hydrogeological Properties of Rocks and Soils, in: Rubin, Y., Hubbard, S.S. (Eds.), *Hydrogeophysics*. Springer Netherlands, Dordrecht, pp. 87–128. https://doi.org/10.1007/1-4020-3102-5_4

Bibliography

- Lesparre, N., Nguyen, F., Kemna, A., Robert, T., Hermans, T., Daoudi, M., Flores-Orozco, A., 2017. A new approach for time-lapse data weighting in electrical resistivity tomography. *GEOPHYSICS* 82, E325–E333. <https://doi.org/10.1190/geo2017-0024.1>
- Leube, P.C., Geiges, A., Nowak, W., 2012. Bayesian assessment of the expected data impact on prediction confidence in optimal sampling design. *Water Resour. Res.* 48, 1–16. <https://doi.org/10.1029/2010WR010137>
- Li, J.Y., Kokkinaki, A., Ghorbanidehno, H., Darve, E.F., Kitanidis, P.K., 2015. The compressed state Kalman filter for nonlinear state estimation: Application to large-scale reservoir monitoring. *Water Resour. Res.* 51, 9942–9963. <https://doi.org/10.1002/2015WR017203>
- Li, L., Puzel, R., Davis, A., 2018. Data assimilation in groundwater modelling: ensemble Kalman filter versus ensemble smoothers. *Hydrol. Process.* 32, 2020–2029. <https://doi.org/10.1002/hyp.13127>
- Li, Y.J., Kokkinaki, A., Darve, E.F., 2016. Smoothing-based compressed state Kalman filter for joint state-parameter estimation : applications in reservoir characterization and CO₂ storage monitoring. *Water Resour. Res.* 53, 7190–7207. <https://doi.org/10.1002/2016WR020168>
- Linde, N., 2014. Falsification and corroboration of conceptual hydrological models using geophysical data. *Wiley Interdiscip. Rev. Water* 1, 151–171. <https://doi.org/10.1002/wat2.1011>
- Linde, N., Binley, A., Tryggvason, A., Pedersen, L.B., Revil, A., 2006. Improved hydrogeophysical characterization using joint inversion of cross-hole electrical resistance and ground-penetrating radar traveltime data. *Water Resour. Res.* 42, WR005131. <https://doi.org/10.1029/2006WR005131>
- Linde, N., Doetsch, J., 2016. Joint Inversion in Hydrogeophysics and Near-Surface Geophysics, in: Moorkamp, M., Lelievre, P., Linde, N., Khan, A. (Eds.), *Integrated Imaging of the Earth*. John Wiley & Sons, Inc., Hoboken, New Jersey, pp. 117–135. <https://doi.org/10.1002/9781118929063.ch7>
- Linde, N., Ginsbourger, D., Irving, J., Nobile, F., Doucet, A., 2017. On uncertainty quantification in hydrogeology and hydrogeophysics. *Adv. Water Resour.* 110, 166–181. <https://doi.org/10.1016/j.ADVWATRES.2017.10.014>
- Linde, N., Lochbühler, T., Dogan, M., Van Dam, R.L., 2015a. Tomogram-based comparison of geostatistical models: Application to the Macrodispersion Experiment (MADE) site. *J. Hydrol.* 531, 543–556. <https://doi.org/10.1016/j.jhydrol.2015.10.073>
- Linde, N., Renard, P., Mukerji, T., Caers, J., 2015b. Geological Realism in Hydrogeological and Geophysical Inverse Modeling: a Review. *Adv. Water Resour.* 86, 86–101. <https://doi.org/10.1016/j.advwatres.2015.09.019>

Bibliography

- Liu, X., Lee, J., Kitanidis, P.K., Parker, J., Kim, U., 2012. Value of information as a context-specific measure of uncertainty in groundwater remediation. *Water Resour. Manag.* 26, 1513–1535. <https://doi.org/10.1007/s11269-011-9970-3>
- Lochbühler, T., Doetsch, J., Brauchler, R., Linde, N., 2013. Structure-coupled joint inversion of geophysical and hydrological data. *Geophysics* 78, ID1–ID14. <https://doi.org/10.1190/geo2012-0460.1>
- Loke, M.H., Barker, R.D., 1996. Practical techniques for 3D resistivity surveys and data inversion. *Geophys. Prospect.* 44, 499–523. <https://doi.org/10.1111/j.1365-2478.1996.tb00162.x>
- Loke, M.H., Wilkinson, P.B., Uhlemann, S.S., Chambers, J.E., Oxby, L.S., 2014. Computation of optimized arrays for 3-D electrical imaging surveys. *Geophys. J. Int.* 199, 1751–1764. <https://doi.org/10.1093/gji/ggu357>
- Looms, M.C., Binley, A., Jensen, K.H., Nielsen, L., Hansen, T.M., 2008. Identifying Unsaturated Hydraulic Parameters Using an Integrated Data Fusion Approach on Cross-Borehole Geophysical Data. *Vadose Zo. J.* 7, 238. <https://doi.org/10.2136/vzj2007.0087>
- Lytle, R.J., Dines, K.A., 1978. An impedance camera : A system for determining the spatial variation of electrical conductivity. Lawrence Livermore Natl. Lab. Distrib. 16.
- Manoli, G., Rossi, M., Pasetto, D., Deiana, R., Ferraris, S., Cassiani, G., Putti, M., 2015. An iterative particle filter approach for coupled hydro-geophysical inversion of a controlled infiltration experiment. *J. Comput. Phys.* 283, 37–51. <https://doi.org/10.1016/J.JCP.2014.11.035>
- Mariethoz, G., Caers, J., 2014. *Multiple-Point Geostatistics*. John Wiley & Sons, Ltd, Chichester, UK.
- Mariethoz, G., Renard, P., Straubhaar, J., 2010. The direct sampling method to perform multiple-point geostatistical simulations. *Water Resour. Res.* 46, 1–14. <https://doi.org/10.1029/2008WR007621>
- Martini, E., Werban, U., Zacharias, S., Pohle, M., Dietrich, P., Wollschläger, U., 2017. Repeated electromagnetic induction measurements for mapping soil moisture at the field scale: validation with data from a wireless soil moisture monitoring network. *Hydrol. Earth Syst. Sci.* 21, 495–513. <https://doi.org/10.5194/hess-21-495-2017>
- Maurer, H., Boerner, D.E., Curtis, A., 2000. Design strategies for electromagnetic geophysical surveys. *Inverse Probl.* 16, 1097–1117. <https://doi.org/10.1088/0266-5611/16/5/302>
- Maurer, H., Curtis, A., Boerner, D.E., 2010. Recent advances in optimized geophysical survey design. *Geophysics* 75, A177--A194. <https://doi.org/10.1190/1.3484194>
- Maurya, P.K., Rønde, V.K., Fiandaca, G., Balbarini, N., Auken, E., Bjerg, P.L.,

Bibliography

- Christiansen, A.V., 2017. Detailed landfill leachate plume mapping using 2D and 3D electrical resistivity tomography - with correlation to ionic strength measured in screens. *J. Appl. Geophys.* 138, 1–8. <https://doi.org/10.1016/j.jappgeo.2017.01.019>
- McLachlan, P.J., Chambers, J.E., Uhlemann, S.S., Binley, A., 2017. Geophysical characterisation of the groundwater–surface water interface. *Adv. Water Resour.* 109, 302–319. <https://doi.org/10.1016/j.advwatres.2017.09.016>
- Menke, W., 1989. *Geophysical Data Analysis: Discrete Inverse Theory*. Academic Press.
- Michalak, A.M., Shlomi, S., 2007. A geostatistical data assimilation approach for estimating groundwater plume distributions from multiple monitoring events. pp. 73–88. <https://doi.org/10.1029/171GM08>
- Michot, D., Benderitter, Y., Dorigny, A., Nicoullaud, B., King, D., Tabbagh, A., 2003. Spatial and temporal monitoring of soil water content with an irrigated corn crop cover using surface electrical resistivity tomography. *Water Resour. Res.* 39, 1–20. <https://doi.org/10.1029/2002WR001581>
- Millard, S.P., 2013. Designing a Sampling Program. *EnvStats An R Packag. Environ. Stat.* 25–61. <https://doi.org/10.1007/978-1-4614-8456-1>
- Miller, C.R., Routh, P.S., 2007. Resolution analysis of geophysical images: Comparison between point spread function and region of data influence measures. *Geophys. Prospect.* 55, 835–852. <https://doi.org/10.1111/j.1365-2478.2007.00640.x>
- Miller, C.R., Routh, P.S., Brosten, T.R., McNamara, J.P., 2008. Application of time-lapse ERT imaging to watershed characterization. *Geophysics* 73, G7. <https://doi.org/10.1190/1.2907156>
- Minsley, B.J., Sogade, J., Morgan, F.D., 2007. Three-dimensional self-potential inversion for subsurface DNAPL contaminant detection at the Savannah River Site, South Carolina. *Water Resour. Res.* 43, 1–13. <https://doi.org/10.1029/2005WR003996>
- Mitchell, M.A., Oldenburg, D.W., 2016. Data quality control methodology for large , non-conventional DC resistivity datasets. *J. Appl. Geophys.* 3, 948–953. <https://doi.org/10.1016/j.jappgeo.2016.09.018>
- Mitchell, V., Knight, R., Pidlisecky, A., 2011. Inversion of time-lapse electrical resistivity imaging data for monitoring infiltration. *Lead. Edge* 140–144.
- Moghadas, D., Badorreck, A., 2019. Machine learning to estimate soil moisture from geophysical measurements of electrical conductivity. *Near Surf. Geophys.* <https://doi.org/10.1002/nsg.12036>
- Morelli, G., LaBrecque, D.J., 1996. Advances in ERT inverse modeling. *Eur. J. Environ. Eng. Geophys.* 1, 171–186.
- Morris, M.D., 1991. *Factorial Sampling Plans for Preliminary Computational*

Bibliography

Experiments, *Technometrics*.

- Morrison, H.F., Beckers, A., Lee, K.H., 1987. Measurements of electrical conductivity for characterizing and monitoring nuclear waste repositories. Berkeley, California, United States.
- Mosegaard, K., 1999. Resolution analysis of general inverse problems through inverse Monte Carlo sampling. *Inverse Probl.* 14, 405–426. <https://doi.org/10.1088/0266-5611/14/3/004>
- Mosegaard, K., Tarantola, A., 1995. Monte Carlo sampling of solutions to inverse problems. *J. Geophys. Res. (Solid Earth)* 100, 12431–12448. <https://doi.org/10.1029/94JB03097>
- Moysey, S., Singha, K., Knight, R., 2005. A framework for inferring field-scale rock physics relationships through numerical simulation. *Geophys. Res. Lett.* 32, 1–4. <https://doi.org/10.1029/2004GL022152>
- Murakami, H., Chen, X., Hahn, M.S., Liu, Y., Rockhold, M.L., Vermeul, V.R., Zachara, J.M., Rubin, Y., 2010. Bayesian approach for three-dimensional aquifer characterization at the Hanford 300 Area. *Hydrol. Earth Syst. Sci.* 14, 1989–2001. <https://doi.org/10.5194/hess-14-1989-2010>
- Musgrave, H., Binley, A., 2011. Revealing the temporal dynamics of subsurface temperature in a wetland using time-lapse geophysics. *J. Hydrol.* 396, 258–266. <https://doi.org/10.1016/j.jhydrol.2010.11.008>
- Mwakanyamale, K., Slater, L., Binley, A., Ntarlagiannis, D., 2012. Lithologic imaging using complex conductivity: Lessons learned from the Hanford 300 Area. *Geophysics* 77, E397. <https://doi.org/10.1190/geo2011-0407.1>
- Myers, D.A., Cabbage, B., Brauchla, R., O'Brien, G., Bergeron, M., Henderson, C., 2008a. Surface geophysical exploration of TX-TY tank farms at the Hanford Site: Results of background characterization with ground penetrating radar. RPP-RPT-38104. Richland, Washington.
- Myers, D.A., Rucker, D.F., Levitt, M., Cabbage, B., Henderson, C., 2008b. Surface geophysical exploration of TX-TY tank farms at the Hanford Site: Results of background characterization with magnetics and electromagnetics. RPP-RPT-36893. Richland, Washington.
- Nearing, G.S., Gupta, H. V., 2015. The quantity and quality of information in hydrologic models. *Water Resour. Res.* 51, 524–538. <https://doi.org/10.1002/2014WR015895>
- Nenna, V., Knight, R., 2013. Demonstration of a value of information metric to assess the use of geophysical data for a groundwater application. *Geophysics* 79, E51–E60. <https://doi.org/10.1190/geo2012-0474.1>
- Nenna, V., Pidlisecky, A., Knight, R., 2011. Informed experimental design for electrical resistivity imaging. *Near Surf. Geophys.* 9, 469–482. [282](https://doi.org/10.3997/1873-</p></div><div data-bbox=)

0604.2011027

- Neuman, S.P., Xue, L., Ye, M., Lu, D., 2012. Bayesian analysis of data-worth considering model and parameter uncertainties. *Adv. Water Resour.* 36, 75–85. <https://doi.org/10.1016/j.advwatres.2011.02.007>
- Nguyen, F., Garambois, S., Jongmans, D., Pirard, E., Loke, M.H., 2005. Image processing of 2D resistivity data for imaging faults. *J. Appl. Geophys.* 57, 260–277. <https://doi.org/10.1016/j.jappgeo.2005.02.001>
- Nguyen, F., Kemna, A., Robert, T., Hermans, T., 2016. Data-driven selection of the minimum-gradient support parameter in time-lapse focused electric imaging. *GEOPHYSICS* 81, A1–A5. <https://doi.org/10.1190/geo2015-0226.1>
- Nimmer, R.E., Osiensky, J.L., Binley, A.M., Williams, B.C., 2008. Three-dimensional effects causing artifacts in two-dimensional, cross-borehole, electrical imaging. *J. Hydrol.* 359, 59–70. <https://doi.org/10.1016/j.jhydrol.2008.06.022>
- Nolet, G., Montelli, R., Virieux, J., 1999. Explicit, approximate expressions for the resolution and a posteriori covariance of massive tomographic systems. *Geophys. J. Int.* 138, 36–44. <https://doi.org/10.1046/j.1365-246X.1999.00858.x>
- Norton, M.G., Arthur, J.C.R., Dyer, K.J., 1997. Geophysical survey planning for the Dounreay and Sellafield geological investigations. *Geol. Soc. London, Eng. Geol. Spec. Publ.* 12, 335–343. <https://doi.org/10.1144/GSL.ENG.1997.012.01.31>
- Nowak, W., 2009. Best unbiased ensemble linearization and the quasi-linear Kalman ensemble generator. *Water Resour. Res.* 45. <https://doi.org/10.1029/2008WR007328>
- Nowak, W., Bode, F., Loschko, M., 2015. A Multi-objective Optimization Concept for Risk-based Early-warning Monitoring Networks in Well Catchments. *Procedia Environ. Sci.* 25, 191–198. <https://doi.org/10.1016/j.proenv.2015.04.026>
- Nowak, W., de Barros, F.P.J., Rubin, Y., 2010. Bayesian geostatistical design: Task-driven optimal site investigation when the geostatistical model is uncertain. *Water Resour. Res.* 46, 1–17. <https://doi.org/10.1029/2009WR008312>
- Nowak, W., Rubin, Y., de Barros, F.P.J., 2012. A hypothesis-driven approach to optimize field campaigns. *Water Resour. Res.* 48, W06509. <https://doi.org/10.1029/2011WR011016>
- Nussbaumer, R., Linde, N., Mariethoz, G., Holliger, K., 2019. Simulation of fine-scale electrical conductivity fields using resolution-limited tomograms and area-to-point kriging. *Geophys. J. Int.* 218, 1322–1335. <https://doi.org/10.1093/gji/ggz185>
- Oldenborger, G.A., Knoll, M.D., Routh, P.S., LaBrecque, D.J., 2007. Time-lapse ERT monitoring of an injection/withdrawal experiment in a shallow unconfined aquifer. *Geophysics* 72, F177–F187. <https://doi.org/10.1190/1.2734365>
- Oldenborger, G.A., LeBlanc, A.M., 2015. Geophysical characterization of permafrost

Bibliography

- terrain at Iqaluit International Airport, Nunavut. *J. Appl. Geophys.* 123, 36–49. <https://doi.org/10.1016/j.jappgeo.2015.09.016>
- Oldenborger, G.A., Routh, P.S., 2009. The point-spread function measure of resolution for the 3-D electrical resistivity experiment. *Geophys. J. Int.* 176, 405–414. <https://doi.org/10.1111/j.1365-246X.2008.04003.x>
- Oldenborger, G.A., Routh, P.S., Knoll, M.D., 2005. Sensitivity of electrical resistivity tomography data to electrode position errors. *Geophys. J. Int.* 163, 1–9. <https://doi.org/10.1111/j.1365-246X.2005.02714.x>
- Oldenburg, D.W., Li, Y., 2005. Inversion for Applied Geophysics: A Tutorial, in: *Near-Surface Geophysics*. Society of Exploration Geophysicists, pp. 89–150. <https://doi.org/10.1190/1.9781560801719.ch5>
- Oldenburg, D.W., Li, Y., 1999. Estimating depth of investigation in dc resistivity and IP surveys. *Geophysics* 64, 403. <https://doi.org/10.1190/1.1444545>
- Olsson, O., Anderson, P., Gustafsson, E., 1991. PROJECT 9118 Site Characterization and Validation - Monitoring of Saline Tracer Transport by Borehole Radar Measurements, Final Report.pdf. Stockholm.
- Olsson, O., Gale, J.E., 1995. Site assessment and characterization for high-level nuclear waste disposal; results from the Stripa Project, Sweden. *Q. J. Eng. Geol.* 28, 17–30.
- Oware, E.K., Moysey, S.M.J., Khan, T., 2013. Physically based regularization of hydrogeophysical inverse problems for improved imaging of process-driven systems. *Water Resour. Res.* 49, 6238–6247. <https://doi.org/10.1002/wrcr.20462>
- Pacific Northwest National Laboratory, 2016. An Award-Winning Subsurface Software [WWW Document]. URL <https://energyenvironment.pnnl.gov/highlights/highlight.asp?id=2556> (accessed 9.16.19).
- Parasnis, D.S., 1988. Reciprocity theorems in geoelectric and geoelectromagnetic work. *Geoexploration* 25, 177–198. [https://doi.org/10.1016/0016-7142\(88\)90014-2](https://doi.org/10.1016/0016-7142(88)90014-2)
- Park, H., Scheidt, C., Fenwick, D., Boucher, A., Caers, J., 2013. History matching and uncertainty quantification of facies models with multiple geological interpretations. *Comput. Geosci.* 17, 609–621. <https://doi.org/10.1007/s10596-013-9343-5>
- Parsekian, A.D., Claes, N., Singha, K., Minsley, B.J., Carr, B., Voytek, E., Harmon, R., Kass, A., Carey, A., Thayer, D., Flinchum, B., 2017. Comparing Measurement Response and Inverted Results of Electrical Resistivity Tomography Instruments. *J. Environ. Eng. Geophys.* 22, 249–266. <https://doi.org/10.2113/JEEG22.3.249>
- Parsekian, A.D., Singha, K., Minsley, B.J., Holbrook, W.S., Slater, L., 2015. Multiscale geophysical imaging of the critical zone. *Rev. Geophys.* 53, 1–26. <https://doi.org/10.1002/2014RG000465>

Bibliography

- Paté-Cornell, E., Cochran, J.J., Cox, L.A., Keskinocak, P., Kharoufeh, J.P., Smith, J.C., Assessment, F.R., 2010. An introduction to probabilistic risk analysis for engineered systems. Wiley Encycl. Oper. Res. Manag. Sci. <https://doi.org/10.1002/9780470400531.eorms0680>
- Pearson, E.S., Hartley, H.O. (Eds.), 1970. Biometrika tables for statisticians. Cambridge University Press.
- Pidlisecky, A., Singha, K., Day-Lewis, F.D., 2011. A distribution-based parametrization for improved tomographic imaging of solute plumes. *Geophys. J. Int.* 187, 214–224. <https://doi.org/10.1111/j.1365-246X.2011.05131.x>
- Pinheiro, J., Bates, D., 1988. Unconstrained parameterizations for variance-covariance matrices. *Stat. Comput.* 6, 289–296.
- Pollock, D., Cirpka, O.A., 2010. Fully coupled hydrogeophysical inversion of synthetic salt tracer experiments. *Water Resour. Res.* 46, W07501. <https://doi.org/10.1029/2009WR008575>
- Portniaguine, O., Zhdanov, M.S., 1999. Focusing geophysical inversion images. *GEOPHYSICS* 64, 874–887. <https://doi.org/10.1190/1.1444596>
- Power, C., Gerhard, J.I., Karaoulis, M., Tsourlos, P., Giannopoulos, A., 2014. Evaluating four-dimensional time-lapse electrical resistivity tomography for monitoring DNAPL source zone remediation. *J. Contam. Hydrol.* 162–163, 27–46. <https://doi.org/10.1016/j.jconhyd.2014.04.004>
- Ramirez, A., Daily, W., 1996. Detection of leaks in underground storage tanks using electrical resistance methods:1996 results. Livermore, California.
- Ramirez, A., Daily, W., Binley, A., Labrecque, D., Roelant, D., 1996. Detection of leaks in underground storage tanks using electrical resistance methods. *J. Environ. Eng. Geophys.* 1, 189–203. <https://doi.org/10.4133/JEEG1.3.189>
- Ramirez, A.L., Daily, W.D., Newmark, R.L., 1995. Electrical resistance tomography for steam injection monitoring and process control. *J. Environ. Eng. Geophys.* 1, 39. <https://doi.org/10.4133/JEEG1.A.39>
- Ramirez, A.L., Nitao, J.J., Hanley, W.G., Aines, R., Glaser, R.E., Sengupta, S.K., Dyer, K.M., Hickling, T.L., Daily, W.D., 2005. Stochastic inversion of electrical resistivity changes using a Markov Chain Monte Carlo approach. *J. Geophys. Res.* 110, B02101. <https://doi.org/10.1029/2004JB003449>
- Ray, A., Kaplan, S., Washbourne, J., Albertin, U., 2018. Low frequency full waveform seismic inversion within a tree based Bayesian framework. *Geophys. J. Int.* 212, 522–542. <https://doi.org/10.1093/gji/ggx428>
- Ray, A., Sekar, A., Hoversten, G.M., Albertin, U., 2016. Frequency domain full waveform elastic inversion of marine seismic data from the Alba field using a Bayesian trans-dimensional algorithm. *Geophys. J. Int.* 205, 915–937. <https://doi.org/10.1093/gji/ggw061>

Bibliography

- Ray, R.L., Jacobs, J.M., 2007. Relationships among remotely sensed soil moisture, precipitation and landslide events. *Nat. Hazards* 43, 211–222. <https://doi.org/10.1007/s11069-006-9095-9>
- Reichle, R.H., Crow, W.T., Keppenne, C.L., 2008. An adaptive ensemble Kalman filter for soil moisture data assimilation. *Water Resour. Res.* 44, 1–13. <https://doi.org/10.1029/2007WR006357>
- Revil, A., Skold, M., Hubbard, S.S., Wu, Y., Watson, D.B., Karaoulis, M., 2013a. Petrophysical properties of saprolites from the Oak Ridge Integrated Field Research Challenge site, Tennessee. *Geophysics* 78, D21–D40. <https://doi.org/10.1190/geo2012-0176.1>
- Revil, A., Wu, Y., Karaoulis, M., Hubbard, S.S., Watson, D.B., Epehimer, J.D., 2013b. Geochemical and geophysical responses during the infiltration of fresh water into the contaminated saprolite of the Oak Ridge Integrated Field Research Challenge site, Tennessee. *Water Resour. Res.* 49, n/a-n/a. <https://doi.org/10.1002/wrcr.20380>
- Reynolds, A.C., Zafari, M., Li, G., 2006. Iterative forms of the ensemble Kalman filter, in: *Proceedings of 10th European Conference on the Mathematics of Oil Recovery*. Amsterdam, The Netherlands.
- Robinet, J., von Hebel, C., Govers, G., van der Kruk, J., Minella, J.P.G., Schlesner, A., Ameijeiras-Mariño, Y., Vanderborcht, J., 2018. Spatial variability of soil water content and soil electrical conductivity across scales derived from Electromagnetic Induction and Time Domain Reflectometry. *Geoderma* 314, 160–174. <https://doi.org/10.1016/j.geoderma.2017.10.045>
- Robins, N.S., 1979. *Electrical resistivity survey at the Windscale Works, Cumbria. Oxfordshire, United Kingdom.*
- Robinson, D.A., Lebron, I., Kocar, B., Phan, K., Sampson, M., Crook, N., Fendorf, S., 2009. Time-lapse geophysical imaging of soil moisture dynamics in tropical deltaic soils: An aid to interpreting hydrological and geochemical processes. *Water Resour. Res.* 45, n/a-n/a. <https://doi.org/10.1029/2008WR006984>
- Robinson, J., 2015. *Improving characterization of fractured rock using 3D cross-borehole electrical resistivity tomography (ERT)*. Rutgers University. <https://doi.org/10.7282/T3DF6T3V>
- Robinson, J., Johnson, T., Slater, L., 2015. Challenges and opportunities for fractured rock imaging using 3D cross borehole electrical resistivity. *Geophysics* 80, E49–E61. <https://doi.org/10.1190/GEO2014-0138.1>
- Rojas, R., Feyen, L., Dassargues, A., 2008. Conceptual model uncertainty in groundwater modeling: Combining generalized likelihood uncertainty estimation and Bayesian model averaging. *Water Resour. Res.* 44, 1–16. <https://doi.org/10.1029/2008WR006908>
- Romero-Ruiz, A., Linde, N., Keller, T., Or, D., 2018. *A Review of Geophysical Methods*

Bibliography

- for Soil Structure Characterization. *Rev. Geophys.* 56, 672–697. <https://doi.org/10.1029/2018RG000611>
- Ross, M., 2004. Consideration of available geophysical techniques for non-intrusive survey of B291 trenches. Sellafield, United Kingdom.
- Rossi, M., Manoli, G., Pasetto, D., Deiana, R., Ferraris, S., Strobbia, C., Putti, M., Cassiani, G., 2015. Coupled inverse modeling of a controlled irrigation experiment using multiple hydro-geophysical data. *Adv. Water Resour.* 82, 150–165. <https://doi.org/10.1016/J.ADVWATRES.2015.03.008>
- Roubinet, D., Irving, J., 2014. Discrete-dual-porosity model for electric current flow in fractured rock. *J. Geophys. Res. Solid Earth* 119, 767–786. <https://doi.org/10.1002/2013JB010668>
- Routh, P.S., 2009. A practical strategy to interrogate resolution , uncertainty and value of information in geophysical inverse problem. *Geohorizons* 27–37.
- Rubin, Y., Chen, X., Murakami, H., Hahn, M., 2010. A Bayesian approach for inverse modeling, data assimilation, and conditional simulation of spatial random fields. *Water Resour. Res.* 46, 1–23. <https://doi.org/10.1029/2009WR008799>
- Rubin, Y., Hubbard, S.S. (Eds.), 2005. *Hydrogeophysics*. Springer.
- Rucker, D., Levitt, M., O'Brien, G., Henderson, C., 2007. Surface geophysical exploration of B , BX , and BY Tank Farms at the Hanford Site : Results of background characterization with ground penetrating radar.
- Rucker, D.F., 2012. Enhanced resolution for long electrode ERT. *Geophys. J. Int.* 191, 101–111. <https://doi.org/10.1111/j.1365-246X.2012.05643.x>
- Rucker, D.F., Myers, D.A., Cabbage, B., Levitt, M.T., Noonan, G.E., McNeill, M., Henderson, C., Lober, R.W., 2013. Surface geophysical exploration: Developing noninvasive tools to monitor past leaks around Hanford's tank farms. *Environ. Monit. Assess.* 185, 995–1010. <https://doi.org/10.1007/s10661-012-2609-x>
- Ruggeri, P., Gloaguen, E., Lefebvre, R., Irving, J., Holliger, K., 2014. Integration of hydrological and geophysical data beyond the local scale: Application of Bayesian sequential simulation to field data from the Saint-Lambert-de-Lauzon site, Québec, Canada. *J. Hydrol.* 514, 271–280. <https://doi.org/10.1016/J.JHYDROL.2014.04.031>
- Ruggeri, P., Irving, J., Gloaguen, E., Holliger, K., 2013. Regional-scale integration of multiresolution hydrological and geophysical data using a two-step Bayesian sequential simulation approach. *Geophys. J. Int.* 194, 289–303. <https://doi.org/10.1093/gji/ggt067>
- Salamon, P., Feyen, L., 2010. Disentangling uncertainties in distributed hydrological modeling using multiplicative error models and sequential data assimilation. *Water Resour. Res.* 46, 1–20. <https://doi.org/10.1029/2009WR009022>

Bibliography

- Sassen, D.S., Hubbard, S.S., Bea, S.A., Chen, J., Spycher, N., Denham, M.E., 2012. Reactive facies: An approach for parameterizing field-scale reactive transport models using geophysical methods. *Water Resour. Res.* 48, 1–20. <https://doi.org/10.1029/2011WR011047>
- Sato, K., 2011. Value of information analysis for adequate monitoring of carbon dioxide storage in geological reservoirs under uncertainty. *Int. J. Greenh. Gas Control* 5, 1294–1302. <https://doi.org/10.1016/j.ijggc.2011.07.010>
- Scaini, A., Audebert, M., Hissler, C., Fenicia, F., Gourdol, L., Pfister, L., Beven, K.J., 2017. Velocity and celerity dynamics at plot scale inferred from artificial tracing experiments and time-lapse ERT. *J. Hydrol.* 546, 28–43. <https://doi.org/10.1016/J.JHYDROL.2016.12.035>
- Scales, J.A., Snieder, R., 1997. To Bayes or not to Bayes? *GEOPHYSICS* 62, 1045–1046. <https://doi.org/10.1190/1.6241045.1>
- Schaap, M.G., Leij, F.J., van Genuchten, M.T., 2001. rosetta: a computer program for estimating soil hydraulic parameters with hierarchical pedotransfer functions. *J. Hydrol.* 251, 163–176. [https://doi.org/10.1016/S0022-1694\(01\)00466-8](https://doi.org/10.1016/S0022-1694(01)00466-8)
- Scheidt, C., Li, L., Caers, J., 2018. *Quantifying Uncertainty in Subsurface Systems, Geophysical Monograph Series*. John Wiley & Sons, Inc., Hoboken, NJ, USA. <https://doi.org/10.1002/9781119325888>
- Schmidt-Hattenberger, C., Bergmann, P., Labitzke, T., Wagner, F., Rippe, D., 2016. Permanent crosshole electrical resistivity tomography (ERT) as an established method for the long-term CO₂ monitoring at the Ketzin pilot site. *Int. J. Greenh. Gas Control* 52, 432–448. <https://doi.org/10.1016/j.ijggc.2016.07.024>
- Schmidt, F., Wainwright, H.M., Faybishenko, B., Denham, M., Eddy-Dilek, C., 2018. *In Situ Monitoring of Groundwater Contamination Using the Kalman Filter*. *Environ. Sci. Technol.* 52, 7418–7425. <https://doi.org/10.1021/acs.est.8b00017>
- Schnaidt, S., Heinson, G., 2015. Bootstrap resampling as a tool for uncertainty analysis in 2-D magnetotelluric inversion modelling. *Geophys. J. Int.* 203, 92–106. <https://doi.org/10.1093/gji/ggv264>
- Scholer, M., Irving, J., Binley, A., Holliger, K., 2011. Estimating vadose zone hydraulic properties using ground penetrating radar: The impact of prior information. *Water Resour. Res.* 47, 1–14. <https://doi.org/10.1029/2011WR010409>
- Scholer, M., Irving, J., Looms, M.C., Nielsen, L., Holliger, K., 2012. Bayesian Markov-chain-Monte-Carlo inversion of time-lapse crosshole GPR data to characterize the vadose zone at the Arrenaes site, Denmark. (Special Section: Model-data fusion in the vadose zone.). *Vadose Zo. J.* 11, 153. <https://doi.org/10.2136/vzj2011.0153>
- Schöniger, A., Nowak, W., Hendricks Franssen, H.-J., 2012. Parameter estimation by ensemble Kalman filters with transformed data: Approach and application to hydraulic tomography. *Water Resour. Res.* 48, W04502.

Bibliography

- <https://doi.org/10.1029/2011WR010462>
- Serco/Golder, 2010. Sellafield contaminated land and groundwater management project – geophysical survey – micro-gravity, downhole logging, EM61, GPR and ERI.
- Serco/Golder, 2009. Sellafield contaminated land and groundwater management project – Report for B291 Trench Area investigation.
- Serco/Golder, 2008a. Sellafield contaminated land and groundwater management project – geophysics survey – B291 Trench Area.
- Serco/Golder, 2008b. Sellafield contaminated land and groundwater management project – Geophysical data collection plan.
- Shanahan, P.W., Binley, A., Whalley, W.R., Watts, C.W., 2015. The Use of Electromagnetic Induction to Monitor Changes in Soil Moisture Profiles beneath Different Wheat Genotypes. *Soil Sci. Soc. Am. J.* <https://doi.org/10.2136/sssaj2014.09.0360>
- Shen, C., 2018. A Transdisciplinary Review of Deep Learning Research and Its Relevance for Water Resources Scientists. *Water Resour. Res.* 54, 8558–8593. <https://doi.org/10.1029/2018WR022643>
- Shi, L., Zeng, L., Tang, Y., Chen, C., Yang, J., 2013. Uncertainty quantification of contaminant transport and risk assessment with conditional stochastic collocation method. *Stoch. Environ. Res. Risk Assess.* 27, 1453–1464. <https://doi.org/10.1007/s00477-012-0682-x>
- Shi, W., 1998. Advanced modeling and inversion techniques for three-dimensional geoelectrical surveys. Massachusetts Institute of Technology.
- Shlomi, S., Michalak, A.M., 2007. A geostatistical framework for incorporating transport information in estimating the distribution of a groundwater contaminant plume. *Water Resour. Res.* 43. <https://doi.org/10.1029/2006WR005121>
- Si, H., 2015. TetGen, a Delaunay-Based Quality Tetrahedral Mesh Generator. *ACM Trans. Math. Softw.* 41, 1–36. <https://doi.org/10.1145/2629697>
- Sibbertt, L., Chambers, J.E., Li, B., Wilkinson, P.B., 2017. Total Generalised Variation: An improved regulariser for Electrical Resistivity Tomography inversion., in: *Geophysical Research Abstracts*. pp. EGU2017-14348.
- Singha, K., Day-Lewis, F.D., Johnson, T., Slater, L.D., 2015. Advances in interpretation of subsurface processes with time-lapse electrical imaging. *Hydrol. Process.* 29, 1549–1576. <https://doi.org/10.1002/hyp.10280>
- Singha, K., Gorelick, S.M., 2006. Effects of spatially variable resolution on field-scale estimates of tracer concentration from electrical inversions using Archie’s law. *Geophysics* 71, G83. <https://doi.org/10.1190/1.2194900>

Bibliography

- Singha, K., Moysey, S., 2006. Accounting for spatially variable resolution in electrical resistivity tomography through field-scale rock-physics relations. *Geophysics* 71, A25. <https://doi.org/10.1190/1.2209753>
- Skyles, J.F., Wilson, J.L., Andrews, R.W., 1985. Sensitivity analysis for steady state groundwater flow using adjoint operators. *Water Resour. Res.* 21, 359–371.
- Slater, L., Binley, A., 2006. Synthetic and field-based electrical imaging of a zerovalent iron barrier: Implications for monitoring long-term barrier performance. *Geophysics* 71, B129–B137. <https://doi.org/10.1190/1.2235931>
- Slater, L., Binley, A., 2003. Evaluation of permeable reactive barrier (PRB) integrity using electrical imaging methods. *Geophysics* 68, 911–921. <https://doi.org/10.1190/1.1581043>
- Slater, L., Binley, A.M., Daily, W., Johnson, R., 2000. Cross-hole electrical imaging of a controlled saline tracer injection. *J. Appl. Geophys.* 44, 85–102. [https://doi.org/10.1016/S0926-9851\(00\)00002-1](https://doi.org/10.1016/S0926-9851(00)00002-1)
- Slater, L.D., Binley, A., Brown, D., 1997. Electrical Imaging of Fractures Using Ground-Water Salinity Change. *Ground Water* 35, 436–442. <https://doi.org/10.1111/j.1745-6584.1997.tb00103.x>
- Slater, L.D., Ntarlagiannis, D., Day-Lewis, F.D., Mwakanyamale, K., Versteeg, R.J., Ward, A., Strickland, C., Johnson, C.D., Lane, J.W., 2010. Use of electrical imaging and distributed temperature sensing methods to characterize surface water-groundwater exchange regulating uranium transport at the Hanford 300 Area, Washington. *Water Resour. Res.* 46, 1–13. <https://doi.org/10.1029/2010WR009110>
- Sobol', I., 2001. Global sensitivity indices for nonlinear mathematical models and their Monte Carlo estimates. *Math. Comput. Simul.* 55, 271–280. [https://doi.org/10.1016/S0378-4754\(00\)00270-6](https://doi.org/10.1016/S0378-4754(00)00270-6)
- Song, X., Chen, X., Ye, M., Dai, Z., Hammond, G., Zachara, J.M., 2019. Delineating Facies Spatial Distribution by Integrating Ensemble Data Assimilation and Indicator Geostatistics With Level-Set Transformation. *Water Resour. Res.* 2018WR023262. <https://doi.org/10.1029/2018WR023262>
- Stenberg, L., 2008. Detailed ground magnetic and resistivity measurements for a potential deep geologic repository for spent nuclear fuel in Oskarshamn, in: Ahlbom, K., Stephens, M. (Eds.), *Investigations of Potential Repository Sites for Spent Nuclear Fuel at Forsmark and Laxemar-Simpevarp, Sweden*. SKB, Stockholm, p. 43.
- Stordal, A.S., Elsheikh, A.H., 2015. Iterative ensemble smoothers in the annealed importance sampling framework. *Adv. Water Resour.* 86, 231–239. <https://doi.org/10.1016/j.advwatres.2015.09.030>
- Stummer, P., Maurer, H.R., Green, A.G., 2004. Experimental design: Electrical resistivity data sets that provide optimum subsurface information. *Geophysics* 69,

Bibliography

120–139.

- Sun, A.Y., 2007. A robust geostatistical approach to contaminant source identification. *Water Resour. Res.* <https://doi.org/10.1029/2006WR005106>
- Sun, A.Y., Painter, S.L., Wittmeyer, G.W., 2006. A constrained robust least squares approach for contaminant release history identification. *Water Resour. Res.* 42. <https://doi.org/10.1029/2005WR004312>
- Sun, N.-Z., Sun, A., 2015. *Model Calibration and Parameter Estimation*. Springer New York, New York, NY. <https://doi.org/10.1007/978-1-4939-2323-6>
- Tai, X., Chan, T.F., 2004. A survey on multiple level set methods with applications for identifying piecewise constant functions. *Int. J. Numer. Anal. Model* 1, 25–48.
- Tang, G., D’Azevedo, E.F., Zhang, F., Parker, J.C., Watson, D.B., Jardine, P.M., 2010. Application of a hybrid MPI/OpenMP approach for parallel groundwater model calibration using multi-core computers. *Comput. Geosci.* 36, 1451–1460. <https://doi.org/10.1016/j.cageo.2010.04.013>
- Tarantola, A., 2006. Popper, Bayes and the inverse problem. *Nat. Phys.* 2, 492–494. <https://doi.org/10.1038/nphys375>
- Tarantola, A., 2005. *Inverse Problem Theory and Methods for Model Parameter Estimation*. SIAM.
- Tartakovsky, D.M., 2013. Assessment and management of risk in subsurface hydrology: A review and perspective. *Adv. Water Resour.* 51, 247–260. <https://doi.org/10.1016/j.advwatres.2012.04.007>
- Taylor, J.R., 1982. *An Introduction to Error Analysis: The Study of Uncertainties in Physical Measurements*. University Science Books.
- TERRADAT (UK) LTD., 2012. Geophysical survey to locate subsurface features and services at B38, Sellafield, Cumbria. Cardiff, United Kingdom.
- TERRADAT (UK) LTD., 2004. Geophysical investigations into the subsurface deposits and structures. Cardiff, United Kingdom.
- TERRADAT (UK) LTD., 1998. Geophysical survey trials carried out at Sellafield, West Boundary. Cardiff, United Kingdom.
- Trainor-Guitton, W.J., 2014. A geophysical perspective of value of information: Examples of spatial decisions for groundwater sustainability. *Environ. Syst. Decis.* 34, 124–133. <https://doi.org/10.1007/s10669-013-9487-9>
- Trainor-Guitton, W.J., Caers, J.K., Mukerji, T., 2011. A Methodology for Establishing a Data Reliability Measure for Value of Spatial Information Problems. *Math. Geosci.* 43, 929–949. <https://doi.org/10.1007/s11004-011-9367-0>
- Trainor-Guitton, W.J., Hoversten, G.M., Ramirez, A., Roberts, J., Juliusson, E., Key, K., Mellors, R., 2014. The value of spatial information for determining well placement:

Bibliography

- A geothermal example. *GEOPHYSICS* 79, W27–W41.
<https://doi.org/10.1190/geo2013-0337.1>
- Trainor-Guitton, W.J., Mukerji, T., Knight, R., 2013a. A methodology for quantifying the value of spatial information for dynamic Earth problems. *Stoch. Environ. Res. Risk Assess.* 27, 969–983. <https://doi.org/10.1007/s00477-012-0619-4>
- Trainor-Guitton, W.J., Ramirez, A., Yang, X., Mansoor, K., Sun, Y., Carroll, S., 2013b. Value of information methodology for assessing the ability of electrical resistivity to detect CO₂/brine leakage into a shallow aquifer. *Int. J. Greenh. Gas Control* 18, 101–113. <https://doi.org/10.1016/j.ijggc.2013.06.018>
- Tran, A.P., Dafflon, B., Hubbard, S.S., 2017. Coupled land surface–subsurface hydrogeophysical inverse modeling to estimate soil organic carbon content and explore associated hydrological and thermal dynamics in the Arctic tundra. *Cryosph.* 11, 2089–2109. <https://doi.org/10.5194/tc-11-2089-2017>
- Tran, A.P., Dafflon, B., Hubbard, S.S., Kowalsky, M.B., Long, P., Tokunaga, T.K., Williams, K.H., 2016. Quantifying shallow subsurface water and heat dynamics using coupled hydrological-thermal-geophysical inversion. *Hydrol. Earth Syst. Sci.* 20, 3477–3491. <https://doi.org/10.5194/hess-20-3477-2016>
- Trigo, F.C., Gonzalez-Lima, R., Amato, M.B.P., 2004. Electrical impedance tomography using the extended Kalman filter. *IEEE Trans. Biomed. Eng.* 51, 72–81. <https://doi.org/10.1109/TBME.2003.820389>
- Troldborg, M., Nowak, W., Lange, I. V., Santos, M.C., Binning, P.J., Bjerg, P.L., 2012. Application of Bayesian geostatistics for evaluation of mass discharge uncertainty at contaminated sites. *Water Resour. Res.* 48, 1–19. <https://doi.org/10.1029/2011WR011785>
- Troldborg, M., Nowak, W., Tuxen, N., Bjerg, P.L., Helmig, R., Binning, P.J., 2010. Uncertainty evaluation of mass discharge estimates from a contaminated site using a fully Bayesian framework. *Water Resour. Res.* 46, 1–19. <https://doi.org/10.1029/2010WR009227>
- Truex, M.J., 2018. Groundwater and Vadose Zone Remedy Management Strategies at DOE Sites, in: SERDP ESTCP Symposium. Washington, D.C.
- Truex, M.J., Johnson, T.C., Strickland, C.E., Peterson, J.E., Hubbard, S.S., 2013a. Monitoring Vadose Zone Desiccation with Geophysical Methods. *Vadose Zo. J.* 12, 0. <https://doi.org/10.2136/vzj2012.0147>
- Truex, M.J., Johnson, T.C., Strickland, C.E., Peterson, J.E., Hubbard, S.S., 2013b. Monitoring Vadose Zone Desiccation with Geophysical Methods. *Vadose Zo. J.* 12. <https://doi.org/10.2136/vzj2012.0147>
- Truex, M.J., Oostrom, M., Strickland, C.E., Chronister, G.B., Benecke, M.W., Johnson, C.D., 2012. Field-Scale Assessment of Desiccation Implementation for Deep Vadose Zone Contaminants. *Vadose Zo. J.* 11, 0.

Bibliography

<https://doi.org/10.2136/vzj2011.0144>

- Tsai, F.T.-C., Elshall, A.S., 2013. Hierarchical Bayesian model averaging for hydrostratigraphic modeling: Uncertainty segregation and comparative evaluation. *Water Resour. Res.* 49, 5520–5536. <https://doi.org/10.1002/wrcr.20428>
- Tsang, C.-F., Neretnieks, I., Tsang, Y., 2015. Hydrologic issues associated with nuclear waste repositories. *Water Resour. Res.* 51, 1–50. <https://doi.org/10.1002/2014WR016259>
- Tso, C.-H.M., Kuras, O., Binley, A., 2019. On the Field Estimation of Moisture Content Using Electrical Geophysics: The Impact of Petrophysical Model Uncertainty. *Water Resour. Res.* 55, 7196–7211. <https://doi.org/10.1029/2019WR024964>
- Tso, C.-H.M., Kuras, O., Wilkinson, P.B., Uhlemann, S., Chambers, J.E., Meldrum, P.I., Graham, J., Sherlock, E.F., Binley, A., 2017. Improved characterisation and modelling of measurement errors in electrical resistivity tomography (ERT) surveys. *J. Appl. Geophys.* 146, 103–119. <https://doi.org/10.1016/J.JAPPGEO.2017.09.009>
- Tso, C.-H.M., Zha, Y., Yeh, T.-C.J., Wen, J.-C., 2016. The relative importance of head, flux, and prior information in hydraulic tomography analysis. *Water Resour. Res.* 52, 3–20. <https://doi.org/10.1002/2015WR017191>
- Turkeltaub, T., Jia, X., Zhu, Y., Shao, M.-A., Binley, A., 2018. Recharge and Nitrate Transport Through the Deep Vadose Zone of the Loess Plateau: A Regional-Scale Model Investigation. *Water Resour. Res.* 54, 4332–4346. <https://doi.org/10.1029/2017WR022190>
- Uhlemann, S., Chambers, J., Wilkinson, P., Maurer, H., Merritt, A., Meldrum, P., Kuras, O., Gunn, D., Smith, A., Dijkstra, T., 2017. Four-dimensional imaging of moisture dynamics during landslide reactivation. *J. Geophys. Res. Earth Surf.* 122, 398–418. <https://doi.org/10.1002/2016JF003983>
- Uhlemann, S., Sorensen, J.P.R., House, A.R., Wilkinson, P.B., Roberts, C., Goody, D.C., 2016. Integrated time-lapse geoelectrical imaging of wetland hydrological processes. *Water Resour. Res.* 52, 1607–1625. <https://doi.org/10.1002/2015WR017932>
- Uhlemann, S., Wilkinson, P.B., Maurer, H., Wagner, F.M., Johnson, T.C., Chambers, J.E., 2018. Optimized survey design for Electrical Resistivity Tomography: combined optimization of measurement configuration and electrode placement. *Geophys. J. Int.*
- Varouchakis, E.A., Palogos, I., Karatzas, G.P., 2016. Application of Bayesian and cost benefit risk analysis in water resources management 534, 390–396.
- Vauhkonen, M., Karjalainen, P.A., Kaipio, J.P., 1998. A Kalman filter approach to track fast impedance changes in electrical impedance tomography. *IEEE Trans Biomed Eng* 45, 486–493. <https://doi.org/10.1109/10.664204>

Bibliography

- Vereecken, H., Binley, A., Cassiani, G., Revil, A., Titov, K. (Eds.), 2006. Applied Hydrogeophysics, NATO Science Series. Springer Netherlands, Dordrecht. <https://doi.org/10.1007/978-1-4020-4912-5>
- von Hebel, C., Rudolph, S., Mester, A., Huisman, J.A., Kumbhar, P., Vereecken, H., van der Kruk, J., 2014. Three-dimensional imaging of subsurface structural patterns using quantitative large-scale multiconfiguration electromagnetic induction data. *Water Resour. Res.* 50, 2732–2748. <https://doi.org/10.1002/2013WR014864>
- Vrugt, J.A., Robinson, B.A., 2007. Improved evolutionary optimization from genetically adaptive multimethod search. *Proc. Natl. Acad. Sci.* 104, 708–711. <https://doi.org/10.1073/pnas.0610471104>
- Vrugt, J.A., Robinson, B.A., Hyman, J.M., 2009. Self-Adaptive Multimethod Search for Global Optimization in Real-Parameter Spaces. *IEEE Trans. Evol. Comput.* 13, 243–259. <https://doi.org/10.1109/TEVC.2008.924428>
- Wagner, B.J., 1992. Simultaneous parameter estimation and contaminant source characterization for coupled groundwater flow and contaminant transport modelling. *J. Hydrol.* 135, 275–303. [https://doi.org/10.1016/0022-1694\(92\)90092-A](https://doi.org/10.1016/0022-1694(92)90092-A)
- Wagner, F.M., 2016. New developments in electrical resistivity imaging with applications to geological CO₂ storage. ETH-Zürich. <https://doi.org/10.3929/ethz-a-010636965>
- Wagner, F.M., Bergmann, P., Rücker, C., Wiese, B., Labitzke, T., Schmidt-Hattenberger, C., Maurer, H., 2015a. Impact and mitigation of borehole related effects in permanent crosshole resistivity imaging: An example from the Ketzin CO₂ storage site. *J. Appl. Geophys.* 123, 102–111. <https://doi.org/10.1016/j.jappgeo.2015.10.005>
- Wagner, F.M., Günther, T., Schmidt-Hattenberger, C., Maurer, H., 2015b. Constructive optimization of electrode locations for target-focused resistivity monitoring. *Geophysics* 80, E29–E40. <https://doi.org/10.1190/geo2014-0214.1>
- Wagner, F.M., Wiese, B.U., 2018. Fully coupled inversion on a multi-physical reservoir model – Part II: The Ketzin CO₂ storage reservoir. *Int. J. Greenh. Gas Control* 75, 273–281. <https://doi.org/10.1016/j.IJGGC.2018.04.009>
- Wainwright, H.M., Chen, J., Sassen, D.S., Hubbard, S.S., 2014a. Bayesian hierarchical approach and geophysical data sets for estimation of reactive facies over plume scales. *Water Resour. Res.* 50, 4564–4584. <https://doi.org/10.1002/2013WR013842>
- Wainwright, H.M., Finsterle, S., Jung, Y., Zhou, Q., Birkholzer, J.T., 2014b. Making sense of global sensitivity analyses. *Comput. Geosci.* 65, 84–94. <https://doi.org/10.1016/j.cageo.2013.06.006>
- Wainwright, H.M., Flores Orozco, A., Bucker, M., Dafflon, B., Chen, J., Hubbard, S.S., Williams, K.H., 2016. Hierarchical Bayesian method for mapping biogeochemical hot spots using induced polarization imaging. *Water Resour. Res.* 52, 533–551.

<https://doi.org/10.1002/2015WR017763>

- Wallin, E.L., Johnson, T.C., Greenwood, W.J., Zachara, J.M., 2013. Imaging high stage river-water intrusion into a contaminated aquifer along a major river corridor using 2-D time-lapse surface electrical resistivity tomography. *Water Resour. Res.* 49, 1693–1708. <https://doi.org/10.1002/wrcr.20119>
- Wang, J., Chen, L., Su, R., Zhao, X., 2018. The Beishan underground research laboratory for geological disposal of high-level radioactive waste in China: Planning, site selection, site characterization and in situ tests. *J. Rock Mech. Geotech. Eng.* 10, 411–435. <https://doi.org/10.1016/j.jrmge.2018.03.002>
- Ward, W.O.C., 2018. Development of machine learning techniques for characterising changes in time-lapse resistivity monitoring. University of Nottingham.
- Ward, W.O.C., Wilkinson, P.B., Chambers, J.E., Nilsson, H., Kuras, O., Bai, L., 2016. Tracking tracer motion in a 4-D electrical resistivity tomography experiment. *Water Resour. Res.* 52, 4078–4094. <https://doi.org/10.1002/2015WR017958>
- Ward, W.O.C., Wilkinson, P.B., Chambers, J.E., Oxby, L.S., Bai, L., 2014. Distribution-based fuzzy clustering of electrical resistivity tomography images for interface detection. *Geophys. J. Int.* 197, 310–321. <https://doi.org/10.1093/gji/ggu006>
- Watson, D.B., Doll, W.E., Gamey, T.J., Sheehan, J.R., Jardine, P.M., 2005. Plume and lithologic profiling with surface resistivity and seismic tomography. *Ground Water* 43, 169–77. <https://doi.org/10.1111/j.1745-6584.2005.0017.x>
- Webster, D.S., Proctor, J.F., Marine, I.W., 1970. Two -Well Tracer Test in Fractured Crystalline Two-Well Tracer Test in Fractured Crystalline. Washington DC.
- Wehrer, M., Slater, L.D., 2015. Characterization of water content dynamics and tracer breakthrough by 3-D electrical resistivity tomography (ERT) under transient unsaturated conditions. *Water Resour. Res.* 51, 97–124. <https://doi.org/10.1002/2014WR016131>
- Weller, A., Slater, L., Nordsiek, S., 2013. On the relationship between induced polarization and surface conductivity: Implications for petrophysical interpretation of electrical measurements. *Geophysics* 78, D315–D325. <https://doi.org/10.1190/geo2013-0076.1>
- West, B., Welch, K.E., Galecki, A.T., 2007. *Linear Mixed Models: a practical guide using statistical software*, 2nd ed. Chapman and Hall/CRC.
- Whalley, W.R., Binley, A., Watts, C.W., Shanahan, P., Dodd, I.C., Ober, E.S., Ashton, R.W., Webster, C.P., White, R.P., Hawkesford, M.J., 2017. Methods to estimate changes in soil water for phenotyping root activity in the field. *Plant Soil* 415, 407–422. <https://doi.org/10.1007/s11104-016-3161-1>
- Whiteley, J.S., Chambers, J.E., Uhlemann, S., Wilkinson, P.B., Kendall, J.M., 2019. Geophysical Monitoring of Moisture-Induced Landslides: A Review. *Rev. Geophys.* 57, 106–145. <https://doi.org/10.1029/2018RG000603>

Bibliography

- Wiese, B., Wagner, F., Norden, B., Maurer, H., Schmidt-Hattenberger, C., 2018. Fully coupled inversion on a multi-physical reservoir model - Part I: Theory and concept. *Int. J. Greenh. Gas Control*.
- Wilkinson, P., Chambers, J., Uhlemann, S., Meldrum, P., Smith, A., Dixon, N., Loke, M.H., 2016. Reconstruction of landslide movements by inversion of 4-D electrical resistivity tomography monitoring data. *Geophys. Res. Lett.* 43, 1166–1174. <https://doi.org/10.1002/2015GL067494>
- Wilkinson, P.B., Chambers, J.E., Lelliott, M., Wealthall, G.P., Ogilvy, R.D., 2008. Extreme sensitivity of crosshole electrical resistivity tomography measurements to geometric errors. *Geophys. J. Int.* 173, 49–62. <https://doi.org/10.1111/j.1365-246X.2008.03725.x>
- Wilkinson, P.B., Chambers, J.E., Meldrum, P.I., Gunn, D.A., Ogilvy, R.D., Kuras, O., 2010a. Predicting the movements of permanently installed electrodes on an active landslide using time-lapse geoelectrical resistivity data only. *Geophys. J. Int.* 183, 543–556. <https://doi.org/10.1111/j.1365-246X.2010.04760.x>
- Wilkinson, P.B., Loke, M.H., Meldrum, P.I., Chambers, J.E., Kuras, O., Gunn, D.A., Ogilvy, R.D., 2012. Practical aspects of applied optimized survey design for electrical resistivity tomography. *Geophys. J. Int.* 189, 428–440. <https://doi.org/10.1111/j.1365-246X.2012.05372.x>
- Wilkinson, P.B., Meldrum, P.I., Chambers, J.E., Kuras, O., Ogilvy, R.D., 2006. Improved strategies for the automatic selection of optimized sets of electrical resistivity tomography measurement configurations. *Geophys. J. Int.* 167, 1119–1126. <https://doi.org/10.1111/j.1365-246X.2006.03196.x>
- Wilkinson, P.B., Meldrum, P.I., Kuras, O., Chambers, J.E., Holyoake, S.J., Ogilvy, R.D., 2010b. High-resolution Electrical Resistivity Tomography monitoring of a tracer test in a confined aquifer. *J. Appl. Geophys.* 70, 268–276. <https://doi.org/10.1016/j.jappgeo.2009.08.001>
- Wilkinson, P.B., Uhlemann, S., Meldrum, P.I., Chambers, J.E., Carrière, S., Oxby, L.S., Loke, M.H.H., 2015. Adaptive time-lapse optimized survey design for electrical resistivity tomography monitoring. *Geophys. J. Int.* 203, 755–766. <https://doi.org/10.1093/gji/ggv329>
- Williams, B.A., Thompson, M.D., Miller, S.F., 2012a. Integrated surface geophysical investigation results at Liquid Effluent Retention Facility, 200 East Area, Washington. Richland, Washington.
- Williams, B.A., Thompson, M.D., Miller, S.F., 2012b. Interpretation and integration of seismic data in the Gable Gap. Richland, Washington.
- Williams, B.A., Thompson, M.D., Miller, S.F., 2012c. Land streamer and gimbaled geophones phase II-200 Areas: high-resolution seismic reflection survey at the Hanford Site. Richland, Washington.

Bibliography

- Williams, B.A., Thompson, M.D., Miller, S.F., 2012d. Seismic reflection investigation at the Liquid Effluent Retention Facility, 200 East Area, Hanford Site Richland, Washington. Richland, Washington.
- Williams, K.H., Kemna, A., Wilkins, M.J., Druhan, J., Arntzen, E., N'Guessan, A.L., Long, P.E., Hubbard, S.S., Banfield, J.F., 2009. Geophysical Monitoring of Coupled Microbial and Geochemical Processes During Stimulated Subsurface Bioremediation. *Environ. Sci. Technol.* 43, 6717–6723. <https://doi.org/10.1021/es900855j>
- Williams, M.D., Rockhold, M.L., Thorne, P.D., Chen, Y., 2008. Three-dimensional groundwater models of the 300 Area at the Hanford Site, Washington State. Richland, Washington.
- Winship, P., Binley, A., Gomez, D., 2006. Flow and transport in the unsaturated Sherwood Sandstone: characterization using cross-borehole geophysical methods. *Geol. Soc. London, Spec. Publ.* 263, 219–231. <https://doi.org/10.1144/GSL.SP.2006.263.01.12>
- Wu, W.M., Carley, J., Fienen, M., Mehlhorn, T., Lowe, K., Nyman, J., Luo, J., Gentile, M.E., Rajan, R., Wagner, D., Hickey, R.F., Gu, B., Watson, D., Cirpka, O. a., Kitanidis, P.K., Jardine, P.M., Criddle, C.S., 2006. Pilot-scale in situ bioremediation of uranium in a highly contaminated aquifer. 1. Conditioning of a treatment zone. *Environ. Sci. Technol.* 40, 3978–3985. <https://doi.org/10.1021/es051954y>
- Xu, T., Gómez-Hernández, J.J., 2018. Simultaneous identification of a contaminant source and hydraulic conductivity via the restart normal-score ensemble Kalman filter. *Adv. Water Resour.* 112, 106–123. <https://doi.org/10.1016/j.advwatres.2017.12.011>
- Xu, T., Gómez-Hernández, J.J., 2016. Joint identification of contaminant source location, initial release time, and initial solute concentration in an aquifer via ensemble Kalman filtering. *Water Resour. Res.* 52, 6587–6595. <https://doi.org/10.1002/2016WR019111>
- Xue, L., Zhang, D., 2014. A multimodel data assimilation framework via the ensemble Kalman filter. *Water Resour. Res.* 50, 4197–4219. <https://doi.org/10.1002/2013WR014525>
- Yamakawa, Y., Kosugi, K., Katsura, S., Masaoka, N., Mizuyama, T., 2012. Spatial and Temporal Monitoring of Water Content in Weathered Granitic Bedrock Using Electrical Resistivity Imaging. *Vadose Zo. J.* 11, 0. <https://doi.org/10.2136/vzj2011.0029>
- Yang, X., Chen, X., Carrigan, C.R., Ramirez, A.L., 2014. Uncertainty quantification of CO₂ saturation estimated from electrical resistance tomography data at the Cranfield site. *Int. J. Greenh. Gas Control* 27, 59–68. <https://doi.org/10.1016/j.ijggc.2014.05.006>
- Yang, X., Lassen, R.N., Jensen, K.H., Looms, M.C., 2015. Monitoring CO₂ migration in

Bibliography

- a shallow sand aquifer using 3D crosshole electrical resistivity tomography. *Int. J. Greenh. Gas Control* 42, 534–544. <https://doi.org/10.1016/J.IJGGC.2015.09.005>
- Yeh, T.-C.J., Liu, S., 2000. Hydraulic tomography : Development of a new aquifer test method. *Water Resour. Res.* 36, 2095–2105.
- Yeh, T.-C.J., Liu, S., Glass, R.J., Baker, K., Brainard, J.R., Alumbaugh, D., LaBrecque, D., 2002. A geostatistically based inverse model for electrical resistivity surveys and its applications to vadose zone hydrology. *Water Resour. Res.* 38, WR001204. <https://doi.org/10.1029/2001WR001204>
- Zahner, T., Lochbühler, T., Mariethoz, G., Linde, N., 2016. Image synthesis with graph cuts: a fast model proposal mechanism in probabilistic inversion. *Geophys. J. Int.* 204, 1179–1190. <https://doi.org/10.1093/gji/ggv517>
- Zeng, L., Shi, L., Zhang, D., Wu, L., 2012. A sparse grid based Bayesian method for contaminant source identification. *Adv. Water Resour.* 37, 1–9. <https://doi.org/10.1016/J.ADVWATRES.2011.09.011>
- Zha, Y., Yeh, T.-C.J., Illman, W.A., Mok, C.M.W., Tso, C.-H.M., Carrera, B.A., Wang, Y.-L., 2019. Exploitation of pump-and-treat remediation systems for characterization of hydraulic heterogeneity. *J. Hydrol.* 573, 324–340. <https://doi.org/10.1016/j.jhydrol.2019.03.089>
- Zhang, Y.-K., Neuman, S.P., 1990. A quasi-linear theory of non-Fickian and Fickian subsurface dispersion: 2. Application to anisotropic media and the Borden site. *Water Resour. Res.* 26, 903–913. <https://doi.org/10.1029/WR026i005p00903>
- Zhang, Y., Liu, N., Oliver, D.S., 2010. Ensemble filter methods with perturbed observations applied to nonlinear problems. *Comput. Geosci.* 14, 249–261. <https://doi.org/10.1007/s10596-009-9149-7>
- Zhang, Y., Schaap, M.G., Guadagnini, A., Neuman, S.P., 2016. Inverse modeling of unsaturated flow using clusters of soil texture and pedotransfer functions. *Water Resour. Res.* 52, 7631–7644. <https://doi.org/10.1002/2016WR019016>
- Zhao, Z., 2000. Application of geophysical exploration to site selection for waste disposal of the Guangdong nuclear power plant. *Geol. Prospect.* (in Chinese) 36, 51–53.
- Zheng, J., Zhang, Z., Dong, L., 2000. Environmental geophysics and its advance. *Adv. Earth Sci.* (in Chinese) 15, 40–47.
- Zheng, Q., Zhang, J., Xu, W., Wu, L., Zeng, L., 2018. Adaptive Multi-Fidelity Data Assimilation for Nonlinear Subsurface Flow Problems. *Water Resour. Res.* 2018WR023615. <https://doi.org/10.1029/2018WR023615>
- Zhou, B., Dahlin, T., 2003. Properties and effects of measurement errors on 2D resistivity imaging surveying. *Near Surf. Geophys.* 1, 105–117. <https://doi.org/10.3997/1873-0604.2003001>

Bibliography

- Zhou, H., Gómez-Hernández, J.J., Li, L., 2014. Inverse methods in hydrogeology: Evolution and recent trends. *Adv. Water Resour.* 63, 22–37. <https://doi.org/10.1016/j.advwatres.2013.10.014>
- Zhou, J., Revil, A., Jardani, A., 2016. Stochastic structure-constrained image-guided inversion of geophysical data. *Geophysics* 81, E89–E101. <https://doi.org/10.1190/geo2014-0569.1>
- Zhou, J., Revil, A., Karaoulis, M., Hale, D., Doetsch, J., Cuttler, S., 2014. Image-guided inversion of electrical resistivity data. *Geophys. J. Int.* 197, 292–309. <https://doi.org/10.1093/gji/ggu001>
- Zhu, P., Shi, L., Zhu, Y., Zhang, Q., Huang, K., Williams, M., 2017. Data assimilation of soil water flow via ensemble Kalman filter: Infusing soil moisture data at different scales. *J. Hydrol.* 555, 912–925. <https://doi.org/10.1016/j.jhydrol.2017.10.078>
- Zovi, F., Camporese, M., Hendricks Franssen, H.J., Huisman, J.A., Salandin, P., 2017. Identification of high-permeability subsurface structures with multiple point geostatistics and normal score ensemble Kalman filter. *J. Hydrol.* 548, 208–224. <https://doi.org/10.1016/j.jhydrol.2017.02.056>

Appendix 1: Instructions on using PFLOTRAN-E4D

A significant portion of this thesis uses the software PFLOTRAN-E4D (Johnson et al., 2017) for hydrogeophysical simulations. The software had been part of the PFLOTRAN releases but this feature is no longer supported by the end of 2018. The section documents an alternative procedure to run hydrogeophysical simulation by calling PFLOTRAN and E4D sequentially.

The approach documented in Johnson et al. (2017) runs PFLOTRAN and E4D in parallel by assigning a number of nodes to run the former and others to run the latter. When optimized, this can be advantageous in terms of run time, especially for very long hydrological simulations. An alternative and perhaps more straightforward and flexible approach is to run PFLOTRAN and then run E4D (each in parallel using all available resources). We can extract outputs from the PFLOTRAN output file (in HDF5 format) using a script, call the FORTRAN mapping subroutines in Johnson et al. (2017), and write to E4D input files. The scripts are available from the thesis author.

Steps (on a Linux-type machine):

1. Install PFLOTRAN and E4D (if not already)
2. Install `f2py` so that FORTRAN codes can be importable to python (if not already). After installation, load python in your terminal and type:

```
f2py -c -m test_interp2 test_interp2.f90
f2py -c -m mapit mapit.f90
```

Make sure the resultant executables are in the directory to run PFLOTRAN-E4D.

3. Now you can call two of the python scripts in the folder:

<code>build_pf_to_e4d_matrix.py</code>	It builds the interpolation matrix. You only need to call it once for each set of PFLOTRAN and E4D meshes.
<code>map_pf_to_e4d.py</code>	It maps PFLOTRAN outputs to E4D mesh and perform petrophysical transform (You can modify it

Appendix 1: Instructions on using PFLOTRAN-E4D

	to specify whatever model you like). It needs to be called whenever E4D needs to be run. Make sure you review the script and understand the mapping it uses.
--	--

You will also need to change these files, which are read by the scripts.

sim_times.txt (or equivalent)	Specifies the PFLOTRAN output times to which E4D is called (note: they must be specified in the PFLTORAN input file), the background conductivity file, and the petrophysical transform file.
background.sig	Specifies electrical conductivity for each cell in the E4D mesh. This value will be used if interpolation from PFLOTRAN is not available.
wax_smit.sig	Specifies petrophysical parameters (I.e. Waxman-Smit here) for each cell in the E4D mesh
All files required to run E4D mode 2 (forward model)	

An example bash script for running PFLOTRAN-E4D this way (hydrogeophysics.sh):

```
#!/bin/bash -l          ## Do not comment out this line. Must be
included for bash scripts
module load python

## run PFLOTRAN, for example:
$ mpirun -n 4 $PFLOTRAN_DIR/src/pflotran/pflotran -pflotranin
myinputfile.in
```

Appendix 1: Instructions on using PFLOTRAN-E4D

```
## build interpolation matrix
python build_pf_to_e4d_matrix.py

## map PF output to sigma files and run E4D for each specified
times.
python map_pf_to_e4d.py
```

Notes on the PFLOTRAN (.in) input file in order to run PFLOTRAN-E4D

1. The output time which E4D will call must be specified as PFLOTRAN output times
2. "Tracer" must be specified as a primary species

Appendix 2: A guide to performing global sensitivity analysis using the Morris (1991) method

The following is a excerpt of an interactive Jupyter Notebook with python codes included in the ResIPy distribution ([link](#)).

Global sensitivity analysis is a Monte Carlo based method to rank the importance of parameters in a given modelling problem. As opposed to local sensitivity analysis, it does not require the construction of the Jacobian, making it a flexible tool to evaluate complex problems.

Global sensitivity analysis is available in mainly uncertainty quantification packages, as well as some flow and transport programs (e.g. iTOUGH2). GSA is also very popular in catchment modelling and civil engineering/risk analysis problems.

Some GSA work in hydrogeophysics (mainly by Berkeley Lab):

- coupled hydrological-thermal-geophysical inversion ([Tran et al 2017](#))
- making sense of global sensitivity analysis ([Wainwright et al 2014](#))
- Sensitivity analysis of environmental models ([Pianosi et al 2014](#))
- hydrogeology of a nuclear site in the Paris Basin ([Deman et al 2016](#))
- Global Sensitivity and Data-Worth Analyses in iTOUGH2 User's Guide ([Wainwright et al 2016](#))

In this tutorial, we will see how to link the ResIPy API and SALib for sensitivity analysis. Two key elements of SA are (i) forward modelling (Monte Carlo runs) and (ii) specifying the parameter ranges. This notebook will showcase of the use of the Method of Morris, which is known for its relatively small computational cost. This tutorial is modified from the one posted on <https://github.com/SALib/SATut> to demonstrate its coupling with ResIPy

Morris sensitivity method

The Morris one-at-a-time (OAT) method (Morris, 1991) can be considered as an extension of the local sensitivity method. Each parameter range is scaled to the unit interval $[0, 1]$ and partitioned into $(p-1)(p-1)$ equally-sized intervals. The reference

Appendix 2: A guide to performing global sensitivity analysis using the Morris (1991) method

value of each parameter is selected randomly from the set $0, 1/(p-1), 2/(p-1), \dots, 1 - \Delta$. The fixed increment $\Delta = p/2(p-1)$ is added to each parameter in random order to compute the elementary effect (EE) of x_i

$$EE_i = \frac{1}{\tau_y} \frac{f(x_1^*, \dots, x_i^* + \Delta, \dots, x_k^*) - f(x_1^*, \dots, x_k^*)}{\Delta}$$

where x_i^* is the randomly selected parameter set, and τ_y is the output-scaling factor. To compute EE_i for k parameters, we need $(k + 1)$ simulations (called one “path”) in the same way as that of the local sensitivity method. By having multiple paths, we have an ensemble of EEs for each parameter. The total number of simulations is $r(k + 1)$, where r is the number of paths.

We compute three statistics: the mean EE , standard deviation (STD) of EE , and mean of absolute EE .

mean EE (μ) represents the average effect of each parameter over the parameter space, the mean EE can be regarded as a global sensitivity measure.

mean |EE| (μ^*) is used to identify the non-influential factors,

STD of EE (σ) is used to identify nonlinear and/or interaction effects. (The standard error of mean (SEM) of EE, defined as $SEM = STD/r^{0.5}$, is used to calculate the confidence interval of mean EE (Morris, 1991))

Importing libraries

```
%matplotlib inline
import warnings
warnings.filterwarnings('ignore')
import os
import sys
sys.path.append((os.path.relpath('./src'))) # add here the relative
path of the API folder

import numpy as np # numpy for electrode generation
import pandas as pd
from IPython.utils import io # suppress R2 outputs during MC runs
from resipy.R2 import R2
```

Appendix 2: A guide to performing global sensitivity analysis using the Morris (1991) method

```
API path = C:\Users\mtso\Downloads\pyr2-master\src\resipy
ResIPy version = 1.1.6
```

The SALib package

SALib is a **free open-source Python** library

If you use Python, you can install it by running the command

```
pip install SALib
```

[Documentation](#) is available online and you can also view the code on [Github](#).

The library includes:

- Sobol Sensitivity Analysis ([Sobol 2001](#), [Saltelli 2002](#), [Saltelli et al. 2010](#))
- Method of Morris, including groups and optimal trajectories ([Morris 1991](#), [Campolongo et al. 2007](#))
- Fourier Amplitude Sensitivity Test (FAST) ([Cukier et al. 1973](#), [Saltelli et al. 1999](#))
- Delta Moment-Independent Measure ([Borgonovo 2007](#), [Plischke et al. 2013](#))
- Derivative-based Global Sensitivity Measure (DGSM) ([Sobol and Kucherenko 2009](#))
- Fractional Factorial Sensitivity Analysis ([Saltelli et al. 2008](#))

[SALib Tutorial](#)

```
# import the packages
from SALib.sample import morris as ms
from SALib.analyze import morris as ma
from SALib.plotting import morris as mp
```

Create ERT forward problem with ResIPy

In the code below, created a R2 forward problem to be analyzed

```
k = R2()
elec = np.zeros((24,3))
elec[:,0] = np.arange(0, 24*0.5, 0.5) # with 0.5 m spacing and 24 electrodes
k.setElec(elec)
#print(k.elec)

# defining electrode array
```

Appendix 2: A guide to performing global sensitivity analysis using the Morris (1991) method

```
x = np.zeros((24, 3))
x[:,0] = np.arange(0, 24*0.5, 0.5)
k.setElec(elec)

# creating mesh
k.createMesh(res0=20)

# add region
k.addRegion(np.array([[2,-0.3],[2,-2],[3,-2],[3,-0.3],[2,-0.3]]), 50)
k.addRegion(np.array([[5,-2],[5,-3.5],[8,-3.5],[8,-2],[5,-2]]), 500)

# define sequence
k.createSequence(['dpdp1', 1, 10])

# forward modelling
k.forward(noise=0.025)

# read results
fwd_dir = os.path.relpath('../src/resipy/invdir/fwd')

obs_data = np.loadtxt(os.path.join(fwd_dir, 'R2_forward.dat'), skiprows=1)
obs_data = obs_data[:,6]

# plot
k.showMesh()
Working directory is: C:\Users\mtso\Downloads\pyr2-master\src\resipy\
invdir
clearing the dirname
computed DOI : -7.67
Using a quadrilateral mesh.
quad
written mesh.dat file to
C:\Users\mtso\Downloads\pyr2-master\src\resipy\invdir\mesh.dat
Writing .in file...
done

Writing protocol.dat ...
done

Running forward model
```

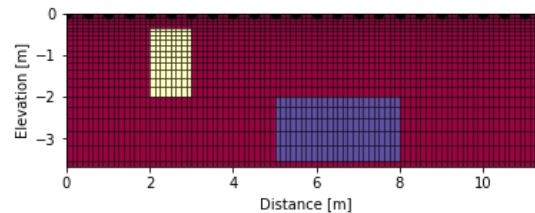
Appendix 2: A guide to performing global sensitivity analysis using the Morris (1991) method

```
>> R 2   R e s i s t i v i t y   I n v e r s i o n   v3.3 <<

>> D a t e : 21 - 08 - 2019
>> My beautiful survey
>> F o r w a r d   S o l u t i o n   S e l e c t e d <<
>> Determining storage needed for finite element conductance matrix
>> Generating index array for finite element conductance matrix
>> Reading start resistivity from resistivity.dat
```

```
Measurements read: 165   Measurements rejected: 0
```

```
>> Total Memory required is: 0.395 Gb
Inf or NaN: filterData: 0 / 165 quadrupoles removed.
strange quadrupoles: filterData: 0 / 165 quadrupoles removed.
165/165 reciprocal measurements NOT found.
0 measurements error > 20 %
computed DOI : -3.67
Forward modelling done.
Mesh plotted in 0.08826 seconds
```



Define a problem file

In the code below, a problem file is used to define the parameters and their ranges we wish to explore, which corresponds to the following table:

Parameter	Range	Description
rho0 [ohm m]	$10^{[0.5,3.5]}$	background
rho1 [ohm m]	$10^{[0.5,3.5]}$	inclusion A

Appendix 2: A guide to performing global sensitivity analysis using the Morris (1991) method

Parameter	Range	Description
-----------	-------	-------------

rho2 [ohm m]	10 ^[0.5,3.5]	inclusion B
--------------	-------------------------	-------------

```
morris_problem = {
  'num_vars': 3,
  # These are their names
  'names': ['rho1', 'rho2', 'rho3'], # can add z1 z2 etc.
  # Plausible ranges over which we'll move the variables
  'bounds': [[0.5,3.5], # log10 of rho (ohm m)
             [0.5,3.5],
             [0.5,3.5]#,
             # [-3,-1],
             # [-7,-4],
             ],
  # I don't want to group any of these variables together
  'groups': None
}
```

Generate a Sample

We then generate a sample using the `morris.sample()` procedure from the SALib package.

```
number_of_trajectories = 20
sample = ms.sample(morris_problem, number_of_trajectories, num_levels
=10)
len(sample)
print(sample[79,:])
[1.83333333 1.83333333 0.5          ]
```

Run the sample through the monte carlo procedure in R2

Great! You have defined your problem and have created a series of input files for forward runs. Now you need to run R2 for each of them to obtain their ERT responses.

For this example, each sample takes a few seconds to run on a PC.

```
##capture
```

Appendix 2: A guide to performing global sensitivity analysis using the Morris (1991) method

```
simu_ensemble = np.zeros((len(obs_data), len(sample)))
for ii in range(0, len(sample)):
    with io.capture_output() as captured:          # suppress inline
output from ResIPy
        # creating mesh
        k.createMesh(res0=10**sample[ii,0])      # need to use more effe
ctive method, no need to create mesh every time

        # add region
        k.addRegion(np.array([[2,-0.3],[2,-2],[3,-2],[3,-0.3],[2,-0.3
]], 10**sample[ii,1])
        k.addRegion(np.array([[5,-2],[5,-3.5],[8,-3.5],[8,-2],[5,-2]]
), 10**sample[ii,2])

        # forward modelling
        k.forward(noise=0.025, iplot = False)
        out_data = np.loadtxt(os.path.join(fwd_dir, 'R2_forward.dat')
, skiprows =1)
        simu_ensemble[:,ii] = out_data[:,6]
        print("Running sample",ii+1)
Running sample 1
Running sample 2
Running sample 3
...
Running sample 77
Running sample 78
Running sample 79
Running sample 80
```

Factor Prioritisation

We'll run a sensitivity analysis of the power module to see which is the most influential parameter.

The results parameters are called **mu**, **sigma** and **mu_star**.

- **Mu** is the mean effect caused by the input parameter being moved over its range.
- **Sigma** is the standard deviation of the mean effect.
- **Mu_star** is the mean absolute effect.

The higher the mean absolute effect for a parameter, the more sensitive/important it is*

Appendix 2: A guide to performing global sensitivity analysis using the Morris (1991) method

```

# Define an objective function: here I use the error weighted rmse
def obj_fun(sim,obs,noise):
    y = np.divide(sim-obs,noise) # weighted data misfit
    y = np.sqrt(np.inner(y,y))
    return y

output = np.zeros((1,len(sample)))
for ii in range(0, len(sample)):
    output[0,ii] = obj_fun(simu_ensemble[:,ii],obs_data,0.025*obs_data)
a) # assume 2.5% noise in the data

# Store the results for plotting of the analysis
Si = ma.analyze(morris_problem, sample, output, print_to_console=False)
print("{:20s} {:>7s} {:>7s} {:>7s}".format("Name", "mean(EE)", "mean(|EE|)", "std(EE)"))
for name, s1, st, mean in zip(morris_problem['names'],
                              Si['mu'],
                              Si['mu_star'],
                              Si['sigma']):
    print("{:20s} {:=7.3f} {:=7.3f} {:=7.3f}".format(name, s1, st, mean))
an)

```

Name	mean(EE)	mean(EE)	std(EE)
rho1	78050.042	78050.042	38362.374
rho2	2595.171	2738.277	4484.274
rho3	1594.958	1595.198	2568.473

```

# make a plot
import matplotlib.pyplot as plt
import numpy as np
fig, ax = plt.subplots()
ax.scatter(Si['mu_star'],Si['sigma'])
ax.plot(Si['mu_star'],2*Si['sigma']/np.sqrt(number_of_trajectories),'--',alpha=0.5)
ax.plot(np.array([0,Si['mu_star'][0]]),2*np.array([0,Si['sigma'][0]/np.sqrt(number_of_trajectories)]),'--',alpha=0.5)

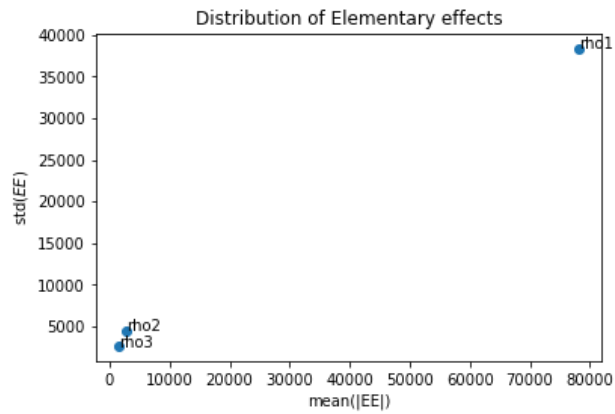
plt.title('Distribution of Elementary effects')
plt.xlabel('mean(|EE|)')
plt.ylabel('std($EE$)')

```

Appendix 2: A guide to performing global sensitivity analysis using the Morris (1991) method

```
for i, txt in enumerate(Si['names']):  
    ax.annotate(txt, (Si['mu_star'][i], Si['sigma'][i]))
```

```
# higher mean |EE|, more important factor  
# line within the dashed envelope means nonlinear or interaction effects dominant
```



Appendix 3: Annotated bibliography for related textbooks

1. Scheidt, C., Li, L., Caers, J., 2018. Quantifying Uncertainty in Subsurface Systems, Geophysical Monograph Series. John Wiley & Sons, Inc., Hoboken, NJ, USA.

This book (Scheidt et al., 2018) begins by stating its motivation—the earth resources challenge and the challenge to make decision under uncertainty. It then gives an excellent review of available data science tools that are relevant for UQ and introduces sensitivity analysis methods and Bayesianism. It is followed by a detailed review on geological priors and inversion, which is rarely found in other text. Subsequently, it introduces the concept of Bayesian evidential learning and provides several application example of UQ. Finally, this book provides an overview of available computer codes and an outlook for UQ in subsurface systems.

2. Sun, N.-Z., Sun, A., 2015. Model Calibration and Parameter Estimation. Springer New York, New York, NY.

This book (Sun and Sun, 2015) begins with a review both classical multi-objective and statistical parameter estimation methods. It is followed by a review for model differentiation, model dimension reduction, and model structure identification methods. Its final chapters reviewed goal-oriented modelling, uncertainty quantification and optimal experimental design methods for environmental inverse problems. The major strength of this books is its completeness and it links classical and statistical inverse problem formulation.

3. Eidsvik, J., Mukerji, T., and , Bhattacharjya, D. ,2015. Value of Information in the Earth Sciences. Cambridge University Press, Cambridge.

This book (Eidsvik et al., 2015) reviews the concept of value of information (VoI) analysis in subsurface characterisation, which is popular in petroleum and mining industry but also sees growing applications in groundwater protection and environmental conservation. It presents a unified framework for assessing the value of potential data gathering schemes by integrating spatial modelling and decision analysis, which is useful for site characterisation as it can be

applied to determine whether a proposed survey can provide sufficient information that justifies its cost. This book also describes relevant quantitative tools such as decision trees and influence diagrams, as well as models for continuous and discrete dependent spatial variables, including Bayesian networks, Markov random fields, Gaussian processes, and multiple-point geostatistics.

Vita

- 2007 Hong Kong Certificate of Education Examination: Queen's College,
Hong Kong
- 2012 BS in geosystems engineering and hydrogeology, The University
of Texas at Austin, Austin (TX), USA
- 2012 – 2015 Graduate research assistant, University of Arizona, Tucson (AZ),
USA
- 2015 MS in hydrology, University of Arizona, Tucson (AZ), USA
- 2015 – 2019 PhD student, Lancaster Environment Centre, Lancaster
University, Lancaster, UK
- 2019 – Research associate in environmental data science, Centre for
Ecology and Hydrology, Lancaster, UK